STUDIES OF NON-ADIABATIC PULSATIONS IN THE ATMOSPHERES OF THE roAp STARS

by

Rodney Medupe

Thesis presented to the Faculty of
Science at the University of Cape Town
for the Degree of Doctorate in SCIENCE

Supervisors: Professor Jørgen Christensen-Dalsgaard[1]

Professor D.W Kurtz[2]

Department of Astronomy
UNIVERSITY OF CAPE TOWN
April 2002

[1]Institute of Physics and Astronomy, Aarhus University, Denmark
[2]Astronomy Department, University of Lancashire, United Kingdom

Dedications,

I dedicate this thesis, to the love of my life **Winnie Medupe** and my dearest daughter **Bontle Medupe**, AND to my mother, **Dimakatso** and my father **Mothibi Medupe**.

Also to my brothers **Thapelo** and **Bassie**.

Ke le rata thata, I love you all.

Thank You,

With this Setswana saying **Mo ntsamaisa bosigo ke mo leboga bo sele** I wish to thank the following:

- **Jørgen Christensen-Dalsgaard**, my co-supervisor for his constant support and great supervision throughout. I have learnt so much from you Jørgen, you have showed me how fun theoretical astrophysics can be. I am looking forward to many more years of working with you!! Also thanks for your kind hospitality in Aarhus, and for making my dreams in Mmabatho come true. You are always welcome in Mmabatho!! Mange Tak.

- **Don Kurtz**, my co-supervisor, for rekindling my love for astronomy and for supporting many of my iniatiatives, in particular my quest to develop astronomy in Mmabatho. This means a lot to me. Thanks also for being such a great supervisor. I look forward to working with you many more times in the future as well.

- SAAO staff for the wonderful discussions and suggestions you have given to me, in particular, **Chris Koen** for helping with statistics, **Luis Balona** for going through chapter 3 and your incredible support for our Mmabatho initiative, and **John Menzies**.

- **Patricia Whitelock**, for your support and kindness and most of all for making my dream in Mmabatho possible.

- **Steve Katashaya**, for friendship and making my dream in Mmabatho possible to realise.

- **Carina Rubin** and **Anne Rogers** for the greatest fun we had in Egypt, Mali and Namibia on our Cosmic Africa journey, and for giving me different perspective to life. And for your support and creating such a great group of friends, the Cosmic Team.

- **Sebastian Dunn**, **Craig Foster**, **Damon Foster**, **Charles Standing** (Mr Sharlie!!), **Ian**, **Sheila van Zyl**, for great friendship and the fun we had last year. Mr Sharlie, we had the utmost fun and laughter under incredible situations. Seb, I hold great respect for you, we had good and interesting discussions together. The crazy brothers, you made me realise that astronomy can be even more interesting from very different angles. You have also brought back to me some of the creative parts of me that I thought I have lost in childhood. Ian, thanks for that humour. Sheila, it was great to know that there was always someone there for support, and for the great sense of humour.

- **Anne Druyan**, even though I haven't met you, thank you for your support of our initiative and for believing in us , and me in particular. You have helped make my dream come true.

- My many other friends, **Given Mabala**, **Nelson Toteng** and to all **African children** who are astronomers or scientists at heart but could not become professional because of circumstances. There's light at the end of the tunnel.

Abstract

The roAp stars are high overtone pulsators characterised by strong global magnetic fields with effective field strength of between a few hundred to a few thousand Gauss. They also show overabundances in rare-earths and iron peak element.

Multi-colour photometry of roAp stars shows that their pulsation amplitudes decrease more rapidly with increasing wavelength compared to other classically pulsating stars (*e.g.* Medupe & Kurtz 1998). In addition, this thesis shows that the pulsation phase can vary by up to 80° from Johnson U to V filters. In an attempt to explain the amplitude *vs* wavelength Kurtz & Medupe (1996) derived an analytic formula that indicated that the steep variation of the temperature eigenfunction with depth in the roAp atmospheres is the possible reason the rapid decrease of amplitude with wavelength. Even though Medupe & Kurtz (1998) showed that the analytical formula they derived in 1996 was a special form of a more general formula presented in Watson (1988), they found limitations in both formulae (see also Medupe, Christensen-Dalsgaard & Kurtz 1998 and chapter 3 of this thesis). This motivated me to attempt a numerical solution of the pulsation equations with consistent treatment of radiative transfer to investigate the multi-colour photometric data.

In this thesis, we report on the multi-colour pulsation amplitudes and phases for HD 128898, HD 101065, HD 134214 and HD 137949. We also report on the campaign undertaken in 1996 and 1998 to determine whether the HR 3831 amplitude and phase *vs* wavelength changes with rotation. No variations with rotation are found. We find that the pulsation phase varies by up to about 80° from Johnson U to V in HD 101065 and HR 3831.

We also report on the results of applying solutions to the grey non-adiabatic radial pulsation equations with consistent treatment of radiative transfer (Christensen-Dalsgaard & Frandsen 1983) to roAp stars. We find that for radial modes to have temperature, displacement and pressure nodes visible within 5000 km below the stellar surface their overtones must be larger than 20. No excited radial modes were found in the pulsation frequency range $\nu \epsilon [0.06, 7]$ mHz. The phase difference between relative temperature and radius variations, Ψ_T, shows variations from the stellar surface to the base of the photosphere of up to 285° in the roAp frequency regime. We suggest that this might explain the large photometric phases reported above.

We find evidence for chromospheric modes at $\nu = 2.5$ mHz, 3.7 mHz, 4.6 mHz and 5.7 mHz. Evidence for the presence of chromospheres in A stars has been observed in α Aql, α Cep and τ^3 Eri by Simon & Landsman (1997). Their analysis is based on ultra-violet spectra obtained from the HST/Goddard High Resolution Spectrograph. They were able to see Lα and Si III emission lines which are indicative of a chromosphere.

A comparison of the energy treatment that uses radiative transfer in the pulsation equations with the one that uses Eddington approximation in radiative equilibrium shows consistently

low damping rates for the latter approach compared to the former. The Eddington approximation in radiative equilibrium gives higher eigenfrequencies compared to the radiative transfer case. The Eddington approximation without the assumption of radiative equilibrium produces results that are almost indistinguishable from the consistent treatment of radiative transfer.

Preliminary non-grey results indicate that the amplitude *vs.* wavelength relationship becomes steeper with increasing pulsation frequency. The fact that the amplitude *vs.* wavelength relation for δ Scuti stars is less steep compared to that of the roAp stars (see chapter 2) seems to concur with these results. Another result is that the pulsation amplitudes increase with increasing wavelength in the near infrared region for low to high pulsation frequencies. This would be difficult to investigate observationally in roAp stars because of their low signal-to-noise ratio in that wavelength region. However, this could be investigated in high amplitude δ Scuti stars.

Investigation of node separation indicate that indeed modes with lower frequencies have larger node separation compared to those with higher frequencies. Modes with pulsation frequencies larger than acoustic cut-off frequencies show little variation of node separation with increasing pulsation frequency. With the current equilibrium models, it is difficult to compare the node separation for HR 3831 with that of α Cir since the first node for HR 3831 pulsation frequency occurs quite deep below the photosphere and therefore has no observable effects on radial velocities or photometry of this star. We therefore cannot suggest the reason why in the analysis of Baldry & Bedding (2000) they find similar bisector velocity pattern for both HR 3831 and α Cir even though α Cir has a larger pulsation frequency than HR 3831.

Contents

List of Tables

Chapter 1

Introduction

1.1 Introduction

It is more than 20 years since the short period pulsations were discovered in the chemically peculiar type 2 (CP2) class stars. The CP2 group stars are characterised by strong global dipole magnetic fields with effective strengths of a few hundred Gauss to 35 kG. Their spectra show enhanced lines of the Fe–peak elements and greatly enhanced lines of rare earth elements compared with spectra of normal stars. The number of the variable members of the CP2 class, now known as the rapidly oscillating Ap stars, roAp for short, has steadily increased to 32 today. However, not much is known about their pulsations because their low pulsation amplitudes (semi–amplitude of 8 mmag and below in Johnson B) and short periods of between 5.6 and 15 minutes make it difficult to study them both photometrically and spectroscopically. Their strong magnetic fields ranging between 100 to 3000 G and their peculiar abundances make it difficult to model their atmospheres, and thus their pulsations. However, there has been some progress as it will be shown in this section of the thesis.

This thesis is organised in the following manner. The first chapter introduces the problem this thesis addresses. Also presented in this chapter is the literature review. Chapter 2 presents the data obtained during the preparation of this thesis. Chapter 3 attempts to investigate the standard theoretical methods used to explain the data presented in chapter 2 and show that these methods fail. In chapter 4 we present the more improved theoretical approach of using non-adiabatic radial pulsation equations in order to understand the data in chapter 3. The results of the solution to the pulsation equations presented in chapter 4 are presented in chapter 5, followed by a summary of the conclusions in chapter 6. I make a tribute to my mother tongue, Setswana, by including a summary of my thesis in Setswana in chapter 7.

1.1.1 Motivation

Multi-colour photometric data of the roAp stars indicate a steeply decreasing amplitude with wavelength compared to other pulsating stars for the given mode (Weiss *et al.* 1991; Matthews, Wehlau & Walker 1991; Matthews *et al.* 1996). Analytical formulae which work well for other pulsating stars fail to explain this phenomenon well (Medupe, Kurtz & Christensen-Dalsgaard 1998). Matthews *et al.* (1996, 1990) sought to explain this in terms of a steeply wavelength-dependent limb-darkening. They noticed that for a dipole mode, the observed photometric pulsation amplitude increases with limb–darkening, therefore they reasoned that if limb-darkening drops sharply from shorter to longer wavelengths, the observed pulsation amplitude will do like- wise. This is only valid if limb-darkening has a dominant effect on the observed photometric amplitude. They then suggested a technique for obtaining limb-darkening coefficients by comparing the observed pulsation amplitudes with amplitudes calculated from models at different wavelengths. With the thus-obtained limb-darkening coefficients one could determine the atmospheric temperature structure in the same way as is done for the sun.

Matthews *et al.* (1996) applied their technique to HR 3831 to derive its limb–darkening coefficients as a function of wavelength. They obtained a $T(\tau)$ structure and showed that it is steeper than that of a normal A star, in accordance with Shibahashi & Saio's (1985) prediction. Shibahashi & Saio (1985) predicted a steep $T(\tau)$ for roAp stars in order to explain why some roAp stars pulsate with frequencies larger than their acoustic cut–off frequencies calculated from standard models. However, Kurtz & Medupe (1996) and Medupe & Kurtz (1998) showed that limb-darkening is too small an effect to explain the multi-colour data. Their results are based on a formula (henceforth called the KM formula) they derived that relates pulsation amplitude to wavelength, limb-darkening and relative temperature perturbations $\Delta T/T$ for a dipole mode. They assumed the intensity is described by the Planck function in the Wien approximation when deriving this formula. Medupe & Kurtz (1998) presented numerical models based on realistic treatment of the intensity spectrum from model atmospheres. Their results were consistent with the KM formula. Medupe & Kurtz (1998) also determined $\Delta T \cos\alpha$ as a function of depth in the atmosphere of HD 128898, where ΔT is the pulsational temperature semi-amplitude and α is the inclination of pulsation axis with respect to the observer line-of-sight. This suggested the presence of a temperature node high in the photosphere. This is discussed in detail in section 1.2.8. Baldry *et al.* (1998) also found a pulsation node in their investigation of the bisector velocities of the Hα line in HD 128898.

A more general formula that relates pulsation amplitude with five pulsation terms, namely, temperature, limb- darkening as a function of temperature and surface variations, geometry and pressure variations was presented by Watson (1988). We shall refer to it as the Watson formula. In chapter 3 of this thesis we present derivations and discussions of attempts to apply this formula to the roAp star data. Medupe & Kurtz (1998) showed that the Watson formula reduces to the KM formula when only the temperature term is included and other terms ignored. Medupe, Christensen-Dalsgaard & Kurtz (1998) applied the complete Wat-

son formula to the multi-colour photometry of α Cir hoping to fit the data and understand the amplitude *vs* wavelength. They found that the only way to fit Watson's formula to the amplitude *vs* wavelength was if the temperature effects on the brightness variations were less dominant than the pressure effects. According to Watson's formula, this happens when the oscillations are strongly non-adiabatic. However, when they made good fits to the data, the formula loses mode-discrimination ability, thus according to the formula all modes for $\ell < 4$ showed the same amplitude-wavelength trend. They also pointed out limitations in Watson's formula. This formula is revisited in detail in chapter 3. The above motivated us to calculate numerical solutions to non-adiabatic pulsation equations in the atmospheres of the roAp stars with consistent treatment of radiative transfer. The details of this are found in chapter 4.

1.2 Introducing the roAp stars

1.2.1 The chemically peculiar A–type stars

Lower main sequence stars of $T_{\rm eff} \leq 7000\,{\rm K}$ are remarkably homogeneous with respect to their rotation (which is uniformly slow) and their approximately solar chemical composition (Preston 1974). However, in the temperature range $7000\,{\rm K} \leq T_{\rm eff} \leq 30000\,{\rm K}$ lie several families of chemically peculiar (CP) stars. Preston (1974) distinguished four different groups based primarily on abundance anomalies amongst other criteria. The CP1 class contains non–magnetic and slowly rotating metallic line (Am) stars that occupy the temperature range $7400\,{\rm K} \leq T_{\rm eff} \leq 10200\,{\rm K}$. The subject of this thesis, the rapidly oscillating Ap stars are a sub–group of the CP2 class which occupy the temperature range $7400\,{\rm K} \leq T_{\rm eff} \leq 23000\,{\rm K}$. The rest of this section is devoted to the discussion of this class. The main sequence stars that show enhanced lines of Hg II and Mn II and no detectable magnetic fields are put in the CP3 class. They occupy the temperature domain $10000\,{\rm K} \leq T_{\rm eff} \leq 15000\,{\rm K}$ and are slow rotators as well. Preston's CP4 class contains He–weak stars in the temperature domain $13000\,{\rm K} \leq T_{\rm eff} \leq 20000\,{\rm K}$. Maitzen (1984) extended Preston's CP4 class to distinguish the magnetic He–weak stars (which he named CP4) and the non–magnetic He–weak stars (the CP5 class). He added two further classes: CP6, which contains the magnetic He–strong stars, and the CP7 class in which the non–magnetic He–strong stars belong.

The CP2 stars are for traditional reasons called Ap stars, even though they cover the spectral type B8p to F0p V-IV. Throughout this thesis I shall use the CP2 and Ap appellations interchangeably when referring to these stars. The rapidly oscillating stars are members of the cool SrCrEu subclass of the CP2 group.

The line strength anomalies observed in CP2 stars are generally accepted to be mostly due to atmospheric abundance anomalies (as a result of radiative diffusion) rather than abnormal atmospheric structure. Diffusion (developed by Michaud 1970) occurs in stars whose atmospheres are stable enough against turbulent mixing that radiation pressure pushes those elements that have many absorption lines near flux maximum to the surface of the star.

This is because photons have momentum, and as they get absorbed by an element (an atom or ion) they add to the net momentum of such an element. Thus the more absorption lines an element has the more momentum it will have (as it absorbs each photon) to move in the direction of radiation. Elements that have few absorption lines near flux maximum, or that are cosmically abundant so that their lines are saturated, sink under their own weight in a sea of hydrogen. Michaud (1970) points out that in the Ap stars the magnetic fields can help provide the stability needed in the atmosphere for diffusion processes to become important. Balmforth *et al.* (2001) also show that magnetic fields in Ap stars may suppress convection in their magnetic polar regions, but not near the magnetic equator.

The abundance anomalies are believed to be confined to a thin layer in the atmosphere for two reasons:

- Ap stars are observed to have only main sequence and subgiant luminosities, by the time Ap stars become giants, their line strength anomalies disappear.
- The abundances of certain rare earth elements (Eu for example, which is overabundant by a factor of 10^4 in some cases) are so great that a significant supply of such elements in the universe would be found in the Ap stars, if the observed abundances extended throughout the star.

Other attempts to explain the line strength anomalies involve the accretion of planetesimals, interior nuclear processes with mixing, surface nuclear processes and magnetic accretion from the interstellar medium. The diffusion hypothesis is most acceptable because of the following reasons:

- It can now account quantitatively for the observed abundance anomalies as shown in Turcotte, Richter & Michaud (1998) for F stars, Turcotte *et al.*(1998) for the sun and Turcotte *et al.* (2000) for A stars.
- It is consistent with the requirement that the abundance anomalies be confined to thin layers of the atmosphere.
- It allows patchy abundance distribution by invoking various magnetic field geometries.
- It explains why Ap stars rotate slowly. Rotation distorts the shape of the star and sets meridional currents in motion whose speed increases with increasing rotational speed. There is a critical rotational velocity above which the meridional currents become turbulent. Thus stars rotating faster than their critical frequency cannot support diffusion because they have turbulent atmospheres.

The diffusion hypothesis, however, has too many free parameters to explain the observations quantitatively. The presence of strong magnetic fields such as in Ap stars increases the number of free parameters in diffusion models (Alecian 1986). Another problem is that the diffusion velocities predicted are so small (10^{-4} to 1 cm s^{-1}) that they require the star to be

exceedingly stable against turbulence in the diffusion zones. Irrespective of these problems diffusion is the best hypothesis invoked to explain the Ap phenomenon so far.

Before I discuss the light variability in these stars I need to distinguish the mean light variations and the pulsational light variabilities. Throughout this thesis I will use the term 'mean light' to refer to light variability occurring on the time–scale of the rotation period, that varies from days to decades, in order to distinguish it from the light variations due to pulsation, which occur on time scales of minutes (for roAp stars).

Early last century some Ap stars were found to be spectrum variables. The nature of these variations is such that not all elements vary in phase, although the lines of a given ion always appear to vary together (Deutsch 1947). The variable lines usually include those strong features that are characteristic of peculiar stars, including Sr, Cr and Eu. The phase relationships of various elements are not the same from star to star. In those Ap stars for which spectrum variations have been studied for a long time no changes in the period and phase are detected. This implies that Ap stars are rigid rotators, unlike the sun which shows differential rotation. This rigid rotation has been used together with spectrum variations to model the distribution of spots or areas on the surface where the anomalously strong lines originate.

In the second decade of the last century light variations which are in phase (or antiphase) with spectrum variations were discovered in some Ap stars. It is now a well established fact that the majority of the Ap stars show these long–term light variations. The amplitudes range typically from 0.01 to 0.10 mag (Wolff 1983). Stepien (1968) compared his UBV measurements (of 16 Ap stars) with earlier measurements and found no evidence for long term changes in the periods, amplitudes or shapes of the light curves. Although the light variations are in phase with magnetic variations, the light variation amplitudes are not correlated with magnetic field strengths, periods of variation, spectral peculiarity, mean colours or line widths. The amplitude and character of the variations are wavelength dependent.

In the late 1940's H.W. Babcock (1947) discovered variable magnetic fields in some Ap stars. The measured fields varied in phase with the spectrum and light variations.

1.2.2 The oblique rotator model

The oblique rotator was proposed by Stibbs (1950) in order to account for the form of the magnetic, spectrum and light variations in the magnetic Ap stars. It was developed by Deutsch (1958). This model assumes the geometry shown in Fig. 1.1. The magnetic field is frozen–in to the stellar atmosphere and has an axis inclined by an angle β to the rotation axis. The rotation axis is inclined by an angle i to the line–of–sight.

Let us consider the magnetic variations. Until recently virtually all magnetic field observations in the literature were of the mean longitudinal or effective magnetic field $B_{\rm eff}$ (Borra Landstreet & Mestel 1982). The transverse component of the field is difficult to measure,

it requires the measurement of the linear polarization in the absorption lines, and linear polarization is small for typical stellar magnetic fields and line profiles. Earlier attempts by Polosukhina (1969), Serkovski & Chojnacki (1969), Kemp & Wolstencroft (1974) and Tuominen & Piirola (1978) to detect and measure broad band linear polarization (BBLP) were of limited success because of the small signals involved. Polarimeters with sensitivities of the order 10^{-4} are necessary to measure BBLP and these were only available about 20 years ago. Linear polarization measurements were used in the 1970s to measure magnetic fields in solar prominences by Leroy and others (see Leroy, Ratier & Bommier 1977 for example).

Recent interest in the study of BBLP in Ap stars were rekindled by Landolfi *et al.* (1993) when they re-investigated the method of determining magnetic and geometrical parameters of a star from BBLP measurements for dipolar and quadrupolar field configurations. They developed a method that can accurately describe (under the weak field approximation) the variation of the polarization with the rotation of a star. The BBLP measurements can provide angles i and β (see Fig. 1.1) which are otherwise difficult to determine with circular polarization measurements. One can determine magnetic structure from these measurement as well.

Leroy *et al.* (1993) applied Landolfi *et al.*'s 1993 method to the old BBLP measurements of HD 137909, HD 65339, HD 71866 and HD 115708. They were able to show that the BBLP analysis is consistent longitudinal field measurements. For these four stars the BBLP analysis is consistent with dipolar magnetic field. Bagnulo *et al.* (1995) presented a method that combines studies of both BBLP and circular polarization and applied it to HD 24712 and HD 71866. Their results for HD 24712 are consistent with a dipolar magnetic field even though their determination of rotation period is inconsistent with that obtained from photometry. The data for some stars are inconsistent with oblique dipole rotator. This could be due to the presence other magnetic components (*e.g.* quadrupole as in Bagnulo *et al.* 2000) in the magnetic configurations. The influence of local abundance inhomogeneities should not be ruled out (Leroy *et al.* 1995). Leroy (1995) present BBLP measurements of a large sample of Ap stars.

Mathys and his collaborators studied and measured mean longitudinal magnetic fields of Ap stars from 1986 until 1995 (see Mathys & Stenflo 1986, Mathys 1991, Mathys 1994, Mathys 1995a; 1995b and Mathys & Hubrig, 1997) by considering circular polarization in their spectral lines. During the course of the study, the magnetic field of 14 roAp stars were studied. Some of the roAp stars studied (HD 6532, HD 166473, HD 128898) do show the presence of quadratic field components. There are roAp stars that have magnetic fields so low that could not be detected in this survey by Mathys. If there are roAp stars that are not magnetic as is suspected by Mathys & Hubrig (1997), then we need to think of a different excitation mechanism for them, a mechanism different from that proposed by Balmforth *et al.* (2001). We would also have to explain why such 'non-magnetic' Ap stars have peculiarities similar to that of Ap stars (as explained by the oblique rotator model). A good review of magnetism in stars is presented by Borra, Landstreet & Mestel (1982).

The mean surface magnetic field is only measurable for stars which show Zeaman splitting in their spectral lines. The $B_{\rm eff}$ is related to the polar field strength H_p by:

$$B_{\rm eff} \propto H_p \, P_\ell \, (\cos \alpha) \tag{1.1}$$

where $P_\ell(\cos\alpha)$ is the Legendre polynomial appropriate to the magnetic field configuration, and α is the inclination of the magnetic field axis with respect to the line–of–sight (Fig. 1.1).

The cosine formula for spherical geometry, (see Smart 1977 for proof) when applied to the geometry in Fig. 1.1 gives

$$\cos \alpha = \cos \, i \cos \beta + \sin \, i \sin \beta \cos \Omega \, t \tag{1.2}$$

where $\Omega = 2\pi\nu_{rot}$ is the angular rotation frequency and phase zero is at the time of magnetic maximum.

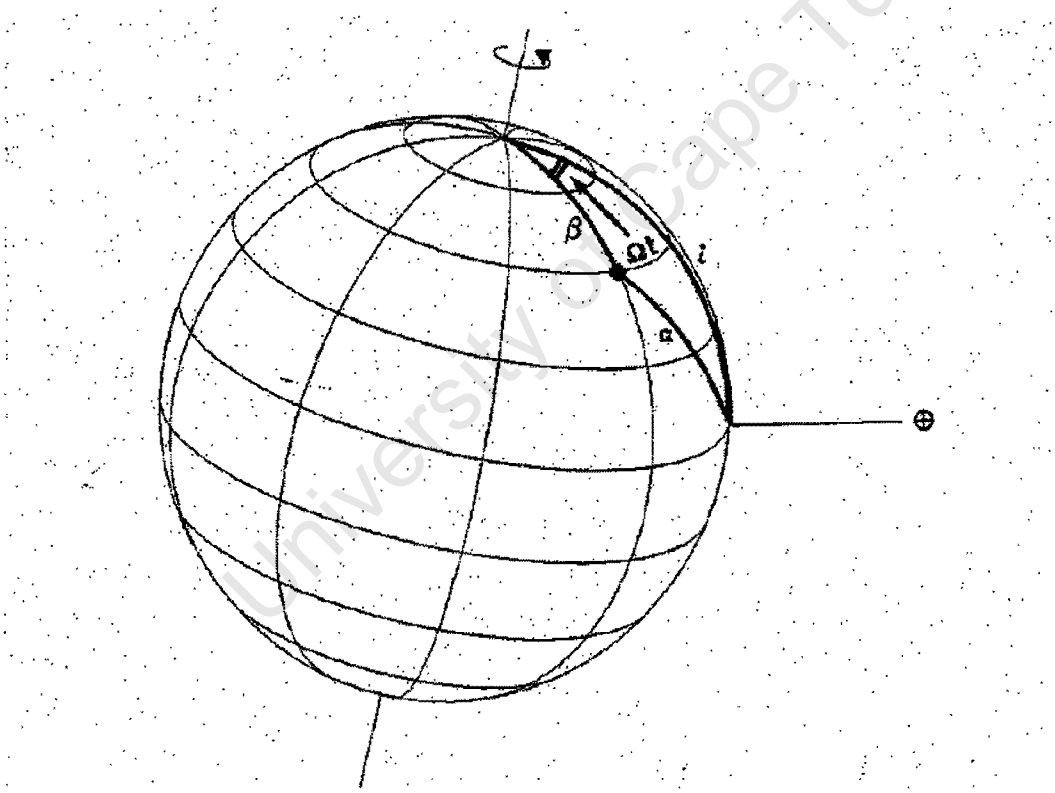

Figure 1.1: The geometry of an oblique rotator. The angle β (magnetic obliquity) is the inclination of the magnetic axis to the rotation axis, which is itself inclined to the line–of–sight by angle i. The angular rotation frequency is $\Omega = 2\pi\nu_{rot}$. Phase zero is taken to be at the magnetic maximum (from Martinez 1993).

For a dipole magnetic field $P_\ell(\cos\alpha) = \cos\alpha$, and equation (1.1) becomes

$$B_{\rm eff} \propto H_p \cos \alpha \tag{1.3}$$

Substituting equation (1.2) into equation (1.3) we get

$$B_{\rm eff} \propto H_p \cos i \cos\beta + H_p \sin i \sin\beta \cos\Omega t \tag{1.4}$$

Thus the field varies with the rotation period about a zero point proportional to $\cos i \cos\beta$ and an amplitude proportional to $\sin i \sin\beta$. It follows that studies of magnetic variations of an oblique rotator can constrain its i and β values. The magnetic field variations in Ap stars are often characterised by a parameter $r = B_{\rm eff}(\min)/B_{\rm eff}(\max)$ for $-1 \leq r \leq +1$. This, when applied to magnetic variations of the form of equation (1.4) gives $\tan i \tan\beta = (1-r)/(1+r)$. Thus measurement of r puts constraints on the i and β values.

Spectrum variations are explained by assuming that the elemental abundance anomalies are not uniformly distributed over the stellar surface. Many elements and ions are overabundant or deficient in spots or rings that are approximately centered on the magnetic poles. So these patches will come in and out of view as the star rotates. Thus when a particular spot comes into view the anomalous lines become stronger or weaker. As it moves out of view they become weaker or stronger. The oblique rotator does not specify the physical mechanism producing line strength anomalies.

The light variations are thought to result from spectrum variations (Wolff & Wolff 1971). Enhanced continuum and line opacity in the ultra–violet results in flux being distributed to longer wavelengths. Therefore, periodic changes in line blanketing as spots come in and out of view during rotation results in flux variations in the visible.

1.2.3 The oblique pulsator model

Pulsation frequency spectra of some roAp stars reveal frequency multiplets (usually triplets), composed of the principal frequency and its sidelobes. The sidelobes are separated from the principal frequency by precisely the same amount. This frequency separation is equal or nearly equal to the rotation frequency Ω of these stars. Six of the 32 known roAp stars show this behaviour. They are HR 3831 (Kurtz *et al.* 1997a), HD 128898 (Kurtz, Martinez & Ashley 1993), HR 1217 (Kurtz *et al.* 1989), HD 6532 (Kurtz *et al.* 1996), HD 80316 (Kurtz *et al.* 1997b) and HD 122970 (Handler *et al.* 2002).

At first one might think that the triplets discussed above are evidence of rotationally perturbed m-modes as discussed in Ledoux (1951). If that is the case, then for an external observer the frequencies of the sidelobes are given by:

$$\nu_m = \nu_0 + m\,(1 - C_{n\ell})\nu_{rot}, \tag{1.5}$$

for the principal frequency ν_0 and rotational frequency ν_{rot}, $C_{n\ell}$ is a constant that depends on the structure of a star, and n, ℓ, m are the three quantum numbers that describe a pulsation mode. Takata & Shibahashi (1995) calculated $C_{n\ell} = 0.003 - 0.01$ in the roAp star frequency range for A star models. However, when this value is used in equation (1.5) it does not match the frequency separations observed in roAp stars. As early as 1982 Kurtz

(1982) showed that $C_{n\ell}$ for HR 3831 is much smaller than that expected for A stars. Kurtz *et al.* (1992) calculated $C_{n\ell}$ using equation (1.5) and showed that $C_{n\ell} < 2 \times 10^{-5}$ at the 3σ level for HR 3831. It has also been found that the times of pulsation maxima coincide with those of the magnetic extrema (Kurtz 1990). The significant difference between the values of $C_{n\ell}$ determined from models and roAp data shows that eqn (1.5) cannot be applied to pulsations in roAp stars.

The following three points show that it is unlikely that the observed frequency triplet (at least in HR 3831) is due to rotationally perturbed $m-$ modes or three different modes:

- Firstly, photometric studies of HR 3831, taken over years (see Kurtz *et al.* 1990, 1993, 1994, 1997a) indicate that the frequency separation of the sidelobes is exactly or nearly equal to the rotation frequency.
- The same photometric studies of HR 3831 show that the amplitude ratios between the different members of the frequency triplet do not change with time.
- Detailed spectroscopic studies of HR 3831 by Baldry & Bedding (2000) indicate that the parameters (P_1 and P_2) that depend on amplitude ratios of the frequency triplet give the same values when obtained from photometry as when obtained spectroscopically. The two parameters are defined as:

$$P_1 = \frac{A_{+1} + A_{-1}}{A_0} = \tan\, i \, \tan\, \beta \tag{1.6}$$

and

$$P_2 = \frac{A_{+1} - A_{-1}}{A_{+1} + A_{-1}} = \frac{C_{n\ell}\, \nu_{\rm rot}}{\nu_1^{(1)mag} - \nu_0^{(1)mag}}, \tag{1.7}$$

where i the inclination of the magnetic axis to the line of sight, β is the angle between the magnetic axis and the rotation axis. The amplitudes of the sidelobes are A_{+1} and A_{-1}. The principal frequency has amplitude A_0 and frequency ν_0.

To explain the abovementioned frequency multiplets and the observed photometric amplitude modulation with rotation, Kurtz (1982) proposed a model where the pulsation axis of a mode coincides with the magnetic axis in the framework of the oblique rotator (*cf* 1.2.2). Kurtz (1982) called this the oblique pulsator model (OPM). The simple model of Kurtz (1982) has since been improved upon and put on more firm theoretical footing by Dziembowski & Goode (1985), Shibahashi and Takata (1993) and Takata & Shibahashi (1994, 1995). An improved OPM was found to be able to explain all of the abovementioned observations.

Of the roAp stars showing the signature of the OPM, only HD 128898 is a pure dipole oblique pulsator, *i.e.* its principal mode is described completely by a single spherical harmonic. The rest are distorted dipole oblique pulsators.

Thus, according to the OPM, since the star is an oblique rotator, as the magnetic axis points in different direction (relative to the observer), the pulsation amplitude varies. The pulsation amplitude is a maximum when the magnetic axis is facing the observer, and a minimum at quadrature. Also, a dipole mode will show a π radian jump in pulsation phase at quadrature as one pulsation pole disappears and another one reappears. This is demonstrated in Fig. 1.2.

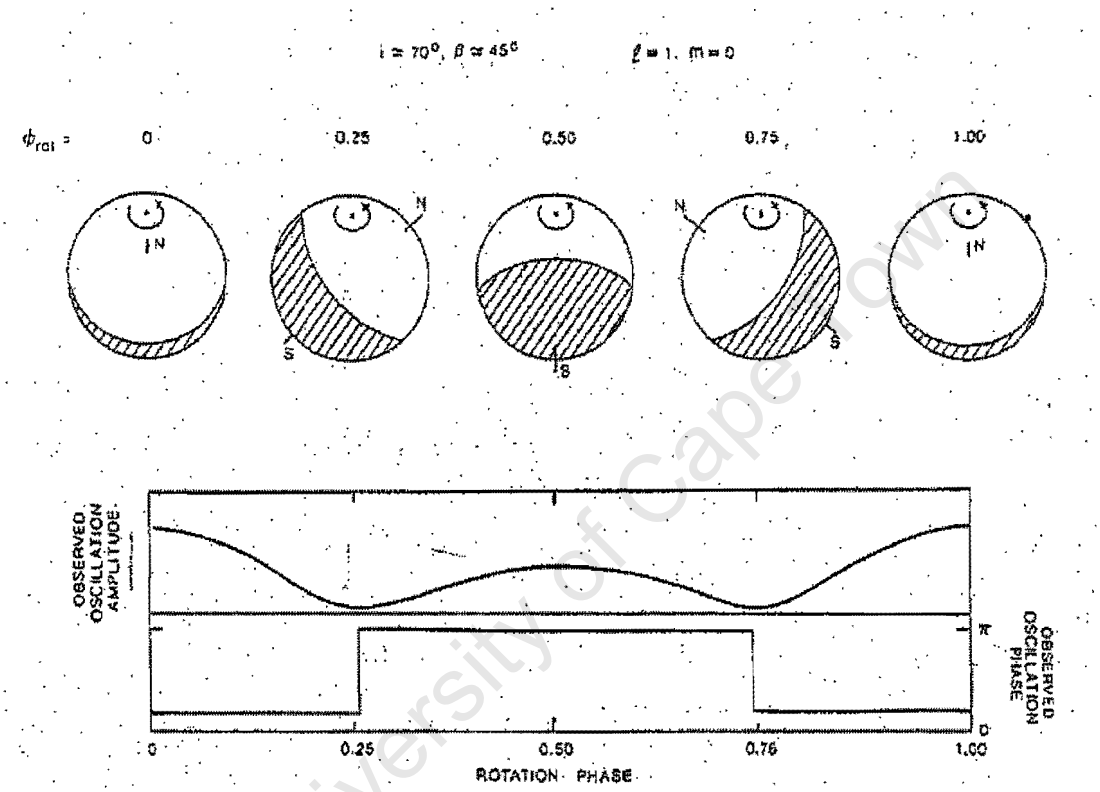

Figure 1.2: This diagram shows how the oblique pulsator model explains the pulsation amplitude modulation and phase reversal observed in dipole modes. The top diagram shows the geometry of the oblique pulsation at different rotation phases. The pulsation maximum occurs when the pulsation axis points towards the observer, and a minimum at quadrature. Also at quadrature there is a π radian jump as one pulsation pole disappears and another reappear. The magnetic poles are denoted by N and S. The diagram is taken from Matthews (1991).

The oblique model described so far takes into consideration the effects of the coriolis force, those of the centrifugal force are often regarded as negligible. One of the effects of the centrifugal force is to distort the shape of the star, for other effects of rotation in general see Wolff (1983) and Tassoul (1978). Another approximation used is to treat the effects of magnetism on pulsation as a small perturbation.

Bigot & Dziembowski (2002) discusses the suitability of applying the abovementioned ap-

proximations to the roAp stars. They show that the considerably large surface magnetic fields found in most roAp stars create magnetic pressures that are comparable to gas pressures in the atmoospheres of these stars. They therefore, argue that magnetic effects cannot be treated as a small perturbation. They suggested an improvement to the oblique pulsator model that treats the effects of surface magnetic field non-perturbatively. Studies of non-perturbative treatment of the effects of magnetic field in roAp stars are presented by Bigot *et al.* (2000), also see Dziembowski & Goode (1996) and Cunha & Gough (1998). One of the results of these studies is to show that the strong magnetic field distorts axi-symmetric pulsation modes so that their angular dependence is described by a linear combination of spherical harmonics of different ℓ with the same m value. As to the dominance of Coriolis force over the centrifugal force, Bigot & Dziembowski (2002) considered a more general form of equation (1.5) that includes the effects of centrifugal force on the observed pulsation frequency as well. As it is, the second term on equation (1.5) represents only the effect of the coriolis force on the frequencies. The effect of the centrifugal force is to introduce a term that is proportional to the square of the rotational frequency multiplied by the distortion factor ($D_{n\ell}$). For a non-magnetic star, the effect of the centrifugal force is to make the frequency separation between the sidelobes and the principal frequency (ν_0) unequal (Saio 1981). For low overtone pulsators, the effects of the coriolis force dominates those of the centrifugal force, but, the situation is reversed for high-order pulsators like the roAp stars. That is because for high overtone modes $D_{n\ell}\Omega^2 \propto n$ and $C_{n\ell}\Omega \propto 1/n$, where Ω is the angular rotational frequency and n is the overtone number. Bigot & Dziembowski (2002) find $D_{n\ell}\Omega^2 = 5.1\,\mu$Hz and $C_{n\ell}\Omega = 0.04\,\mu$Hz for HR 3831 for example.

Bigot & Dziembowski (2002) find, in their attempt to revise the oblique pulsator model to overcome its short-comings discussed above, that the difference in the amplitudes of the sidelobes is due to the dynamical effect of the coriolis force. Therefore, the treatment of the effects of coriolis force cannot be ignored over those of the centrifugal force. They also found that their revised model allows seismic determination of the magnetic obliquity (β) and the surface magnetic field strength. Their attempt to apply their revised model to HR 3831 data failed, and they attribute this to the fact the magnetic field of HR 3831 might be larger than they assumed (see Shavrina *et al.* 2000 for example). This would deform the dipole pulsation mode to such an extent that the mode cannot be represented by spherical harmonics with a single ℓ as Bigot & Dziembowski had assumed.

The spectroscopic evidence for the OPM is discussed in the next subsection.

1.2.4 Spectroscopic Evidence for and against the OPM

Mathys (1985) and Dolez & Gough (1982) challenged the main supposition of the OPM that the pulsation axis is aligned with the magnetic axis. Mathys proposed the spotted pulsator model as an alternative to the oblique pulsator model. This model was an attempt by him to show that it is not necessary to assume that the pulsation axis is aligned to the magnetic axis in order to describe the frequency spectrum and amplitude modulation of HR 3831. He

points out that the surface inhomogeneities may cause an inhomogeneous distribution in the ratio of the flux to radius variations, f, and in the phase lag ψ between the flux and radius variations. The contribution to luminosity variation is due to two factors; the flux variations and the surface area variations. The quantity f measures the relative importance of the flux variations compared to the surface area variations. Mathys showed that by varying f and ψ over the surface, within reasonable limits, the spotted pulsator model can describe the amplitudes in the frequency spectrum of HR 3831 with a single dipole mode aligned with the rotation axis.

The spotted pulsator model failed two observational tests. The first was the observation by Matthews *et al.* (1988) that the radial velocity in HR 1217 is amplitude modulated in phase with the light amplitude. The oblique pulsator model predicts exactly this, whereas the spotted pulsator does not. It is possible to have radial velocity amplitude modulation (by beating of the frequencies) in a spotted pulsator, if the star is multi–periodic (HR 1217 has six pulsation frequencies). However, Matthews *et al.* observed for 5 hours on each of the two nights, which should have averaged over many of the beat cycles of HR 1217's six frequencies. More recently, Baldry, Kurtz & Bedding (1998) presented the definite signature of the oblique pulsator from the radial velocity studies of HR 3831. The observed radial velocity amplitude modulation and the π-radian phase reversals that typify the OPM. The second piece of evidence that favours the oblique pulsator model is the fact that the time of pulsation maximum in HR 1217 (which coincides with the time of magnetic maximum) differs from the time of the mean light minimum by 3σ (Kurtz *et al.* 1989) and by 5σ for HR 3831 (Kurtz *et al.* 1992). In the spotted pulsator model the pulsation maximum should coincide with the mean light extremum because the variations in f and ψ are caused by the surface inhomogeneities.

Interestingly, there are some points of observations that are difficult to explain in terms of the OPM, these are pointed out by Baldry & Bedding (2000). They subdivided their spectra into wavelength intervals with the result that the wavelength interval that suffered the most from line blending had the lowest signal-to-noise (S/N) ratio than others. For the intervals with poor S/N they found that P_2 in equation (1.7) determined spectroscopically differed from the photometric one. They also found significant differences in pulsation phases determined at ν_{+1} and ν_{-1}. This introduces a shift in the amplitude maxima. They interpret this to indicate that the amplitudes and phases of a mode changes across the surface of a star as a result of spots or limb-darkening.

1.2.5 Limitations of the OPM

Although the OPM is very successful in describing the pulsation frequency multiplets, phase reversals and amplitude modulations observed in roAp stars, and can be used for determination of ℓ values, it suffers from several deficiencies:

1. It lacks the detailed physics of the stellar structure for it to be useful to explain or describe wavelength- dependent data. It is based on the geometry of the pulsating star.

2. It is only useful for stars that show frequency multiplets, *i.e.* it is very geometry dependent. However, stars not showing multiplets require other models. Unfortunately most of the known roAp stars belong to this latter category.

3. The detection of sidelobes often requires very low noise levels and reduced interference from aliasing effects. This can only be achieved over longer periods of observations and by multi-site observations.

1.2.6 The currently known roAp stars

Other than the sun, in 1990 only Ap stars were known to pulsate in high overtones. Martinez (1993) searched southern Ap stars for overtone pulsations in a survey that lasted from 1990 to 1993. Each Ap star was investigated based on looking at its Strömgren indices. The search for roAp stars is still on, and an updated list of the known roAp stars is shown in Tables 1.1 and 1.2 (courtesy of Peter Martinez).

1.2.7 Abundance analyses of roAp stars.

It is common to use photometric indices to determine parameters such as temperature and surface gravity in normal A stars. Handler & Paunzen (1999) show how problematic it is to do the same for chemically peculiar stars. It was therefore welcome when Werner Weiss and his group in Vienna undertook to do abundance analyses of the roAp stars in order to provide accurate fundamental parameters such as temperature and surface gravity for this group of stars. We summarise the results of their work so far in Table 1.3. Another great result of their work is that they have calculated model atmospheres based on the abundance analysis determined for each star. This is very useful for calculating pulsation models and determining the excitation mechanism in the roAp stars. Their published work spans 1996 until present. I will give their general results below:

1. The general abundance patterns for α Cir, HD 203932, γ Equ, 10 Aql, HD 122970 and HD 24712 indicate Iron and Nickel abundances that are similar to those of the sun. They find large overabundances in rare earth elements (REE), overabundance in Cr and Co, and underabundance in carbon and oxygen.

2. They find that the second ions of the REE in HD 166437, HD 176232 and HD 122970 are overabundant by a factor of 100 compared to the singly ionized REE. This anomaly is not found in the non-roAp stars.

3. Surface gravities obtained spectroscopically for HD 128898, HD 24712 and HD 201601 are systematically different from those obtained through asteroseismology and evolution.

4. There are indications in HD 128898, HD 203932, HD 201601 and HD 24712 that strong magnetic fields can suppress turbulent motions.

Table 1.1: The rapidly oscillating Ap stars

HD	HR Name	α (2000)	δ (2000)	V	Spectral Type	Period (min)	ΔB_{max} (mmag)
6532		01 05 56	-26 43 43	8.445	Ap SrCrEu	7.1	5
9289		01 31 15	-11 07 04	9.383	Ap SrEu	10.5	3.5
12098		02 00 40	+58 31 37				
12932		02 06 13	-19 07 16	10.235	Ap SrEuCr	11.6	4
19918		03 01 24	-81 54 00	9.336	Ap SrEuCr	14.5	2
24712	1217	03 55 16	-12 05 54	6.001	Ap SrEu(Cr)	6.2	10
42659		06 11 21	-15 47 32	6.768	Ap SrCrEu	9.7	0.8
60435		07 31 00	-58 00 00	8.891	Ap Sr(Eu)	11.4-23.5	16
80316		09 18 25	-20 22 13	7.782	Ap Sr(Eu)	7.4	2
83368	3831	09 36 25	-48 45 03	6.168	Ap SrEuCr	11.6	10
84041		09 41 34	-29 22 26	9.330	Ap SrEuCr	15.0	6
86181		09 54 54	-58 41 00	9.323	Ap Sr	6.2	4.6
99563		11 27 43	-08 55 01	8.16	—	10.7	2
101065	Przbylski's star	11 37 37	-46 43 00	7.994	Controversial	12.1	13
119027		13 41 19	-28 47 23	10.022	Ap SrEu(Cr)	8.7	2
122970		14 05 15	+05 22 21	8.31	—	11.1	2
128898	5463 α Cir	14 42 30	-64 58 00	3.198	Ap SrEu(Cr)	6.8	5
134214		15 09 03	-13 59 58	7.464	Ap SrEu(Cr)	5.6	7
137949	33 Lib	15 29 35	-17 26 27	6.673	Ap SrEuCr	8.3	3
150562		16 44 11	-48 39 16	9.816	A/F(p Eu)	10.8	0.8
161459		17 48 29	-51 55 02	10.326	Ap EuSrCr	12.0	1.3
166473		18 12 26	-37 45 06	7.923	Ap SrEuCr	8.8	2
176232	7167 10 Aql	18 58 47	+13 54 00	5.89	F0p SrEu	11.6	0.6
185256		19 39 24	-29 44 28	9.938	Ap Sr(EuCr)	10.2	3
190290		20 14 00	-78 52 00	9.912	Ap EuSr	7.3	2
193756		20 24 11	-51 43 25	9.195	Ap SrCrEu	13.0	0.9
196470		20 38 10	-17 30 06	9.721	Ap SrEu(Cr)	10.8	0.7
201601	8097 γEqu	21 10 21	+10 08 00	4.68	F0p	12.4	3
203932		21 26 04	-29 55 45	8.820	Ap SrEu	5.9	2
213637		22 33 14	-20 02 08	9.611	A(p EuSrCr)	11.5	1.5
217522		23 01 47	-44 50 25	7.525	Ap (Si)Cr	13.9	4
218495		23 09 30	-63 40 00	9.356	Ap EuSr	7.4	1

Notes:
[a] This is the typical peak-to-peak variation for a night when the star is "up" in amplitude.
[b] For multi-periodic stars the frequency of the mode with the highest amplitude is listed.
[c] The V magnitudes are as measured in the Cape Survey, except for the three stars, HD 128898, HD 176232 & HD 201601. For these stars, the V magnitudes from Table 1 of Kurtz's (1990) review were used.
[d] The spectral types listed are from the Michigan Spectral Catalogue (Houk & Cowley 1975, Houk 1978, 1982, Houk & Smith-Moore 1988)

Table 1.2: Strömgren indices, magnetic field strengths and rotation periods for the roAp stars.

HD	y	$b-y$	m_1	δm_1	c_1	δc_1	β	B_e (G)	P_{rot} (day)
6532	8.445	0.088	0.214	-0.014	0.879	-0.051	2.880		1.944973
9289	9.383	0.138	0.225	-0.018	0.826	-0.012	2.833		
12098									
12932	10.235	0.179	0.228	-0.024	0.765	-0.035	2.810		
19918	9.336	0.169	0.216	-0.010	0.822	-0.058	2.855		
24712	6.001	0.191	0.211	-0.023	0.626	-0.074	2.760	+400 to +1300	12.4572
42659	6.768	0.124	0.257	-0.050	0.765	-0.076	2.834		
60435	8.891	0.136	0.240	-0.034	0.833	-0.047	2.855	< 1000	7.6793
80316	7.782	0.118	0.324	-0.118	0.599	-0.283	2.856		2.1?
83368	6.168	0.159	0.230	-0.024	0.766	-0.062	2.825	-700 to +700	2.851982
84041	9.330	0.177	0.233	-0.026	0.797	-0.061	2.844		3.69
86181	9.323	0.172	0.205	0.001	0.757	-0.061	2.819		
99563	8.160	0.171	0.206	-0.001	0.745	-0.090	2.830		
101065	7.994	0.431	0.387	-0.204	0.002	-0.370	2.641	-2200	3.94?
119027	10.022	0.257	0.214	-0.034	0.557	-0.076	2.731		
122970	8.310	0.260	0.178	-0.005	0.540	-0.011	2.707		11.30?
128898	3.198	0.152	0.195	0.012	0.760	-0.077	2.831	-300	4.4790
134214	7.464	0.216	0.223	-0.029	0.620	-0.108	2.774		
137949	6.673	0.196	0.311	-0.105	0.580	-0.236	2.818	+1400 to +1800	
150562	9.816	0.301	0.212	-0.015	0.659	-0.087	2.783		
161459	10.326	0.245	0.246	-0.040	0.679	-0.141	2.820		
166473	7.923	0.208	0.321	-0.118	0.514	-0.268	2.801		
176232	5.89	0.150	0.208	-0.004	0.829	0.031	2.809	-315 to 440	
185256	9.938	0.277	0.185	-0.004	0.615	-0.039	2.738		
190290	9.912	0.289	0.293	-0.091	0.466	-0.306	2.796		
193756	9.195	0.181	0.213	-0.008	0.760	-0.040	2.810		
196470	9.721	0.211	0.263	-0.059	0.650	-0.144	2.807		
201601	4.68	0.147	0.238	-0.032	0.760	-0.058	2.819	-800 to +500	> 70 yr
203932	8.820	0.175	0.196	0.004	0.742	-0.020	2.791		
213637	9.611	0.298	0.206	-0.035	0.411	-0.031	2.670		
217522	7.525	0.289	0.227	-0.056	0.484	-0.015	2.691		
218495	9.356	0.114	0.252	-0.049	0.812	-0.098	2.870		

Notes:
[a] The photometric data in this Table were acquired as part of the Cape Survey for all but three stars, HD 128898, HD 176232 and HD 201601. For these stars, the photometric data in Table 1 of Kurtz's (1990) review were used.
[b] The magnetic field measurements tabulated here are from Table 2 of Kurtz's (1990) review.

5. In some cases (in HD 166473 for example) they have been able to reproduce observed photometric indices from model atmospheres by taking into account proper treatment of chemical abundances in the opacity distribution functions of their models.

6. They have found the abundance patterns of HD 166473 very peculiar (second only to HD 101065). The REE in this star are overabundant by +2.8 dex compared to the +4.0 dex in HD 101065.

7. In the abundance analysis of HD 203932, they found no evidence for strong magnetic field. The absence of strong magnetic field allows convection to be more important in this star compared to other roAp stars they investigated. Mathys & Hubrig (1997) also find no detection of magnetic field on this star.

Table 1.3: A summary of results obtained by the Vienna group.

Starname	$T_{\rm eff}$ (K)	log g	v sin i (km/s)	$B_{\rm eff}$ kG	v_{turb} (km/s)	**publication**
HD 128898	7900 ± 200	4.2 ± 0.15	12.5			Kupka *et al.* (1996)
HD 24712	7250	4.3	5.6 ± 2.3	4.4	1.0	Ryabchikova *et al.* (1997)
HD 166473	7550 ± 250	4.2 ± 0.2			1.0	Gelbmann *et al.* (2000)
HD 176232	7550	3.95 ± 0.25	4.5 - 5.5	≈ 1	0.0	Ryabchikova *et al.* (2000)
HD 122970	6930 ± 100	4.11 ± 0.1	5	2.0 - 2.3	0.85	Ryabchikova *et al.* (2000)
HD 201601	7700	4.20	NDR[1]		NDR	Ryabchikova *et al.* (1997)
HD 203932	7450 ± 100	4.2 ± 0.15	12.5		NDR	Gelbmann *et al.* (1997)

[1] Not determined reliably

1.2.8 Multi–colour photometry anomaly

Classical pulsators show a decrease in pulsation amplitude with wavelength which is consistent with that of a pulsating black–body (Matthews *et al.* 1996; Watson 1988). However, within few years of discovery of the roAp stars, multi–colour photometry (Weiss & Schneider 1984) showed that the pulsation amplitudes of roAp stars decline rapidly with increasing wavelength, more so than for classical pulsators. Subsequent multi-colour photometric studies of more of these stars by Matthews *et al.* (1990) and Kurtz & Medupe (1996) confirmed this. Matthews *et al.* (1990; 1996) sought to explain the precipitous decline of the amplitude with wavelength by weighting the dipole mode with the strongly wavelength dependent limb–darkening. This technique was motivated by the following observations:

1. In most of the roAp stars where mode identification has been successfully done, their principal pulsation mode is dipole (Kurtz 1990; Martinez 1993, 1996). As is shown by Kurtz & Medupe (1996) and Watson (1988), this makes it easy to model the pulsations

of roAp stars because dipole mode light variations are due entirely to temperature variations.

2. Irrespective of the inclination α of the dipole pulsation mode with respect to the line–of–sight, limb–darkening has the effect of increasing the pulsation amplitude. This does not apply for $\alpha = 90^{\circ}$ where the two hemispheres of the dipole mode vary in anti–phase to each other and (since they contribute equally on the visible disk) produce a net amplitude of zero. Matthews *et al.* (1990) supposed (reasonably so) that if limb–darkening has strong dependence on wavelength, the pulsation amplitude also has a strong dependence on wavelength. In particular, if limb– darkening drops steeply from the shorter wavelengths to longer wavelengths, then the observed pulsation amplitude will do like–wise. This can only be true if limb–darkening is a big effect on pulsations. We now know that this is not the case with roAp stars.

Matthews *et al.* (1990; 1996) sought to explain the precipitous decline of the amplitude with wavelength by weighting the dipole mode with the strongly wavelength dependent limb–darkening.

Matthews *et al.* (1990; 1996) measured limb–darkening coefficients for HR 3831 by measuring the pulsation amplitudes at various wavelengths, and comparing them with the results of a pulsating black–body model without limb–darkening. Their data were obtained from multi–colour photometry. The models involved numerical simulation of the light variations of a dipole mode inclined to an observer by an angle α.

They reported a steeper dependence of limb–darkening coefficients on wavelength for HR 3831 than that of the sun. A steeper limb–darkening dependence on wavelength implies a steeper $T(\tau)$ gradient. This result could not only explain the sharp decline of amplitude with wavelength, but was also consistent with the results of Shibahashi & Saio (1985) who suggested a steeper $T(\tau)$ in order to explain why some roAp stars have eigenfrequencies higher than the acoustic cut–off frequency.

Had this technique succeeded, it could have lead to advances in the understanding of the atmospheric structure of roAp stars. It could have provided a check for Ap model atmospheres and hence enable a more reliable determination of parameters such as effective temperatures and surface gravities, which are currently still difficult to determine accurately for Ap stars. Improved model atmospheres that could arise from this work would also make abundance analyses for Ap stars more accurate. The main source of continuous opacity can be deduced (as was done for the sun by Pierce & Waddell (1961) from the temperature gradient measurements. The effects of other physical processes such as convection and NLTE (which are poorly understood for Ap stars) could be investigated through comparison of the empirical $T(\tau)$ with those obtained from model atmospheres.

It was these exciting prospects that prompted Kurtz & Medupe (1996) to attempt to apply the above- mentioned technique to other large amplitude roAp stars. We were interested in stars that have the dipole pulsation mode as the dominant mode of pulsation in addition

to being large amplitude pulsators. We derived the following simple formula that relates observed pulsation amplitude to limb-darkening and temperature amplitude amongst other factors:

$$A_{\lambda obs} = 1.086 \frac{1}{4}\sqrt{\frac{3}{\pi}}\left(\frac{4-\beta_\lambda}{3-\beta_\lambda}\right)\cos\alpha \frac{hc}{\lambda k T_o}\frac{\Delta T}{T_o}, \tag{1.8}$$

where $A_{\lambda obs}$ is the observed photometric amplitude, β_λ is the limb-darkening coefficient based on the following linear limb-darkening function:

$$\frac{I_\lambda(\theta)}{I(0)} = 1 - \beta_\lambda(1-\cos\theta), \tag{1.9}$$

where hc is the product of Planck constant and speed of light, k the Boltzmann's constant, T_o is the equilibrium temperature of the stellar atmosphere, ΔT is the temperature semi-amplitude and $\mu = \cos\theta$. For quadratic limb-darkening Medupe & Kurtz (1998) derive the following formula:

$$A_{\lambda obs} = 1.086 \frac{1}{10}\sqrt{\frac{3}{\pi}}\left(\frac{20-5u_{1\lambda}-2u_{2\lambda}}{6-2u_{1\lambda}-u_{2\lambda}}\right)\cos\alpha \frac{hc}{\lambda k T_o}\frac{\Delta T}{T_o}, \tag{1.10}$$

where $u_{1\lambda}$ and $u_{2\lambda}$ are quadratic limb-darkening coefficients based on the following limb-darkening function:

$$\frac{I_\lambda(\theta)}{I_{0\lambda}} = 1 - u_{1\lambda}(1-\mu) - u_{2\lambda}(1-\mu)^2. \tag{1.11}$$

By comparing the formula with the data we showed that limb-darkening cannot account for the rapid decline of the observed photometric amplitude with wavelength, since limb–darkening is only a small effect. We also showed that $T(\tau)$ cannot be determined empirically, but that the amplitude *vs* wavelength data give us information about ΔT (the polar pulsational temperature semi–amplitude) as a function of atmospheric depth if $T(\tau)$ is known *a priori* (from model atmospheres).

Kurtz & Medupe (1998) determined $\Delta T \cos\alpha$ as a function of depth in the atmosphere of α Cir and HR 3831. We also showed that the formula derived by Kurtz & Medupe (1996) is a special form of the more general formula presented by Watson (1988). We showed that equation (1.8) is consistent with improved numerical models based on realistic Kurucz model atmospheres.

1.2.9 Mode identification

A mode of a vibrating string is described by a single integer number, a vibrating membrane requires two integer numbers to describe its surface mode and a three-dimensional spherical object such as an oscillating star requires three quantum numbers for its mode to be fully

described. Mode identification, therefore is a way of determining n, ℓ, m numbers that describe a mode from the data of a pulsating star.

Pulsation modes are identified from multi–colour photometry, single–colour pulsation frequency spectra, several spectroscopic techniques and techniques that combine spectroscopic and photometric data. The details of techniques that use photometric data alone are left to chapter 3. In our discussion of the oblique pulsator model in section 1.2.3 I showed how frequency splittings observed in some roAp stars are used to identify the spherical index ℓ. Stamford & Watson (1981) presented analytic expressions that combine photometric and radial velocity amplitudes to determine ℓ. As far as I know no such approach has been applied to roAp star data. I discuss the line profile variation technique in the next subsection.

Line profile variations

Line profiles of a star depend on the temperature of the line-forming region and surface velocity. Therefore, perturbations in temperature and velocity due to pulsation do affect the shape of the line. Indeed, periodic variations in the line profiles have been found in early-type stars like ζ Oph (Walker, Yang & Fahlman 1979), 53 Per variables (Smith & McCall 1978; Buta & Smith 1979; Smith *et al.* 1984) and β Cephei stars . The line profile variations (LPVs) take the form of travelling bumps that move across the line from the blue to the red part. At first they might be confused with the travelling bumps that result from spots on the surface of a rotating star. However, closer inspection reveals that the nature of these types of LPVs is quite different. For example, one expects to derive an estimate of the rotational velocity from the movements of the starspot-induced LPVs. On the other hand, if upon applying pulsation model the bumps we find that the number and the spacing of the bumps on the line depend on the spherical index ℓ and m, then it is likely that such travelling bumps are due to stellar pulsations. The fact that the rotational velocities derived from travelling bumps observed in the line profiles of ζ Oph variables are inconsistent with those determined by other independent means (modelling of line widths for example) as was shown by Vogt & Penrod (1983) favours the interpretation of pulsation as being their cause. Furthermore, Kambe & Osaki (1988) demonstrate with their models of pulsational line profile variations that the number of travelling bumps roughly equals $m/2$ and that they are spaced at regular intervals.

In order to understand how pulsational line profile variations can be used for mode identification we will briefly discuss how LPVs are modelled. See Kambe & Osaki (1988), Lee & Saio (1990, 1986) and Pesnell (1989) for more details. First one needs to specify parameters that describe the mode (this is where ℓ and m come in), its amplitude, and orientations of rotation and pulsation axes with respect to the observer. The latter come in the form of three angles; the inclination of the rotation axis to the observer, i, the magnetic obliquity, β, and the azimuth of the pulsation pole, α. The last two angles are most relevant when modelling an oblique pulsator. In particular, β is most relevant when magnetic pulsators are considered, it is therefore appropriate for roAp stars. When including the effects of pulsational velocity for $p-$ or g-modes, for example, one needs a parameter $\alpha_H = \frac{GM/R^3}{\omega^2}$,

the amplitude ratio of horizontal to radial motions. The reason for the inclusion of these terms becomes clearer when one considers an expression for pulsational velocity for $p-$ or g-modes:

$$v_{osc} = A\,\mathrm{Re}\{\left(1,\, \alpha_H \frac{\partial}{\partial\theta},\, \alpha_H \frac{1}{\sin\theta}\frac{\partial}{\partial\phi}\right) Y_\ell^m(\theta,\,\phi)\, e^{i\omega t}\} \tag{1.12}$$

where A is the velocity amplitude for the case when $\alpha_H \sim 0$ (as in roAp stars) and Re{} indicates that we are only interested in the real parts of the expressions inside the brackets. The LPVs are then modelled by dividing the visible surface of a star into a number of small surface elements, then Doppler shifting an intrinsic line profile assuming a velocity field of the form of equation (1.12) at each surface element. The resulting flux is integrated over the whole visible surface. Kambe & Osaki (1988) show the effect of changing different parameters on theoretical LPVs for which temperature effects were not included.

To compare the LPVs model with data, the above-mentioned parameters are selected by trial and error and adjusted until a fit is made with the data. As pointed out by Balona (1986a) this method works fine for stars with a single mode, but becomes more difficult when other modes of comparable amplitudes are present. That is why Balona (1986a, 1986b) proposed a method of characterising the shapes of line profile variations by a series of moments, these are then Fourier transformed to produce frequency spectra. From the relationships that exist between relative amplitudes and phases of moments one can determine the ℓ and m. This method also allows one to determine i and the projected rotational velocity $v \sin i$ and does not require profile modelling with its many parameters.

Baade & Weiss (1987) calculated theoretical LPVs for the roAp regime. Their calculations are for low (ℓ, m) modes because one does not expect to see high (ℓ, m) modes in narrow line stars such as the roAp stars. They are also based on rotational velocities of $10\,\mathrm{km\,s^{-1}}$ (typical of Ap stars), and had to use larger values of $10\,\mathrm{km\,s^{-1}}$ for pulsation velocity in order to see the effects clearly. Unfortunately the radial velocities for roAp stars are typically under $10\,\mathrm{km\,s^{-1}}$. We therefore require very high spectral and time resolution, and good signal-to-noise ratio. Baade & Weiss's calculations predict travelling bumps which are strongly dependent on the inclination angle i and the rotation phase. The dependence on the rotation phase is such that for the same given mode at one rotation phase the travelling bumps are visible, and at others not visible. The way the distortion in the line profile happens also changes with rotation phase. This dependence on rotation phase is a unique property of the oblique pulsator. These results are confirmed by Pesnell's 1989 calculations.

Attempts to detect LPVs in roAp stars

Schneider & Weiss (1989) presented results on their attempts to detect line profile variations in α Cir. Their data were collected with high temporal resolution, a signal-to-noise ratio of 30 per spectrum and consisted of 887 single spectra. The data were obtained with the 3.6-m CAT ESO telescope and Coudé Echelle Spectrograph with Reticon array. They found no convincing evidence of line profile variations on α Cir. Baldry, Bedding, Kurtz, Chapman

& myself obtained obtained high resolution spectroscopic data at the AAT in 1998 with the hope of detecting line profile variations in HR 3831 and HD 128898. This is still work in progress. Our data are a great improvement to the Schneider & Weiss data; our data have S/N of about 500 per spectra for α Cir, and 40-s exposure times.

More recently Kochukhov & Ryabchikova (2001) reported detection of line profile variation in Nd III lines in HR 3831 and α Cir. Their data are based on high resolution spectrograms (R=123 000) taken on the CES spectrograph attached to the ESO 3.6-m telescope. They also detected rotational modulation in the profile variations in both stars. This is the first successful detection of line profile variation in roAp stars. They however, have not reported mode identification based on this.

1.2.10 The question of excitation mechanism

Several causes of pulsations have been identified in several types of pulsating stars. In the sun the oscillations are induced by overstable convection in the upper part of the solar convection zones (Nordlund & Stein 1998, Osaki 1993, Balmforth 1992 and Goldreich & Keeley 1977). The $p-$ modes in δ Scuti stars are excited by κ mechanism acting in the He II ionisation zone (Chevalier 1971).

Several attempts to understand the excitation mechanism for the roAp stars in the past have failed. The roAp stars are found in the instability strip of the HR diagram close to the δ Scuti stars. They cover similar temperature and luminosity ranges, and therefore it was believed that their pulsations ought to be excited by the same mechanism as the δ Scuti stars. However, the fundamental difference between these two types of stars is that δ Scuti stars are low overtone pulsators whereas the roAp stars are high overtone pulsators. This means that their acoustic cavities extend over different depths, and that the δ Scuti oscillations are mostly confined in deeper layers of the stars, while the roAp oscillations occur mostly in the upper layers of the stars. Therefore, it is to be expected that the regions of excitation of the roAp stars would be shallower than those of the δ Scuti stars. In addition, the strong magnetic fields in roAp stars cannot be ignored when considering the excitation of pulsations in these stars. Matthews (1988) suggested the κ mechanism acting on the Si IV ionisation zone as another possible excitation mechanism in roAp stars. This is because the gravitational settling of Helium in the He II ionisation is thought to dampen the oscillation. He argued that the κ mechanism can apply to any element that has sufficient abundance on condition that its next ionisation stage results in significant drop in opacity. He showed that one such element is Si IV. The problem with his suggestion is that the Si IV ionisation zone occurs quite deep in the star where roAp oscillation amplitudes are very low.

The similarities in the pulsation periods between roAp stars and the sun might tempt some to think that the stochastic excitation might be responsible for the roAp pulsation. However, the large amplitudes of the roAp stars make it difficult to see how stochastic mechanism can sustain such oscillations (see Houdek *et al.* 1999).

Without evoking magnetism, Gautschy, Saio & Harzenmoser (1998) investigated excitation mechanism in roAp stars and found that in order to excite high overtones in their homogeneous equilibrium models, they needed to have a steeper T(τ) relation resulting from chromospheres in their equilibrium models. In addition, their equilibrium models have masses lower than those estimated by North *et al.* (1997).

Dolez & Gough (1982) investigated the possibility of the magnetic field effect on the excitation of the roAp oscillations. They calculated growth rates in chemically homogeneous stellar envelopes with strong magnetic fields in polar regions, and similar envelopes with weaker magnetic fields. They did not, however, find any excited high overtone modes in any of the envelopes they investigated. Dziembowski & Goode (1996) studied the driving of oscillations in homogeneous equilibrium models using non-adiabatic code. They found that for high overtones ($n > 20$) the κ mechanism acting in the hydrogen ionisation zone drives or excites the modes. They commented that the driving is not strong enough to compensate for the radiative damping beneath the hydrogen ionisation zone. They cautioned that their equilibrium models did not include magnetic effects, and that their treatment of the energy equation in their atmospheres is inadequate.

The latest attempt to look for excitation mechanism was conducted by Balmforth *et al.* (2001). They first showed that near the magnetic poles of roAp stars, the vertical magnetic field is able to suppress convection, whereas near the equator convection is unsuppressed. They therefore divided their equilibrium stellar models into chemically differentiated polar regions without convection and homogeneous equatorial regions with convection present. They show that their composite models are unstable against high order pulsation modes in polar regions and found no unstable modes in their equatorial regions. The work integrals they calculated indicated that the unstable modes are excited by the κ mechanism operating in the hydrogen ionisation zone of the polar regions. They also find that the presence of turbulent pressure in the equatorial regions helps stabilize the high overtone modes. The damping and growth rates they obtained for their composite model are shown in Fig. 1.3.

1.3 Summary of the pulsational properties of roAp stars.

In this subsection I summarise pulsational properties observed for roAp stars to date.
The roAp stars are high overtone, low degree non–radial p- mode pulsators with periods between 5.6 and 15 minutes. Their pulsation semi–amplitudes are under 8 mmag in Johnson B. Other pulsational properties are listed below:

1. some show frequency splittings that are explained by the oblique pulsator model.
2. some show frequency shifts over time scales of a few to several years.
3. some show amplitude modulation on time scales of the rotational periods.

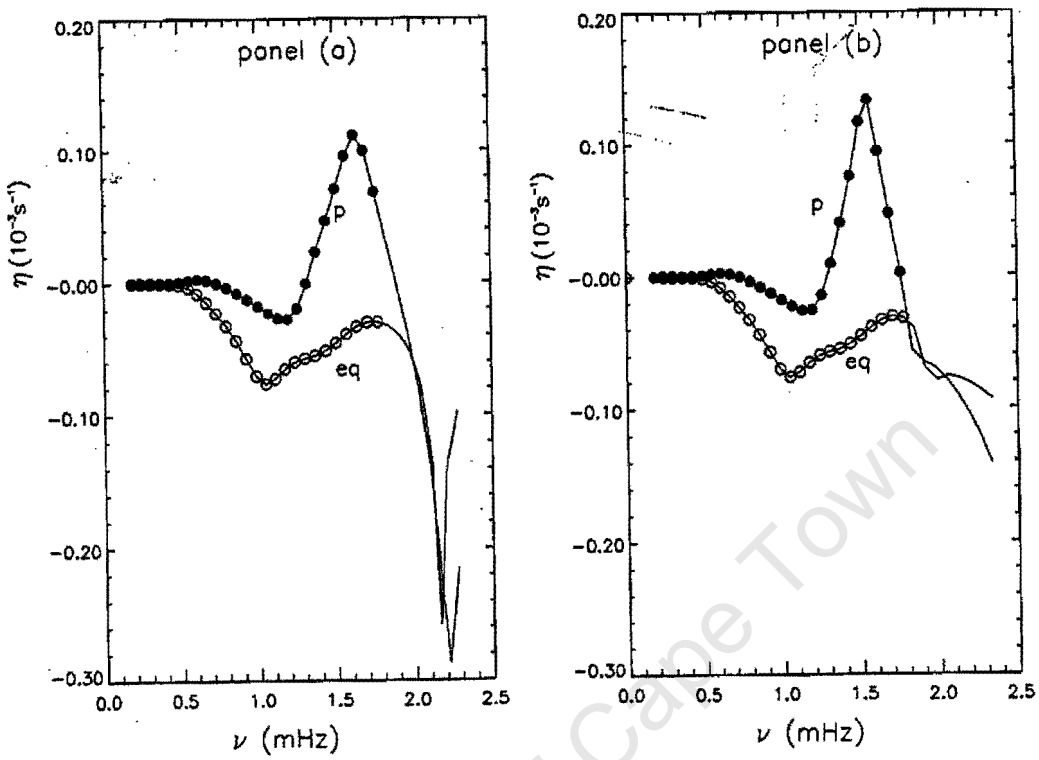

Figure 1.3: The damping or growth rates obtained for the composite model of Balmforth *et al.* (2001). The curve with solid line labelled "p" is for the polar regions and labelled "eq" is for equatorial region. The left panel uses the boundary condition that reflects all the modes back into the star, the right panel allows modes with frequencies larger than the acoustic cut-off frequencies to leak through the stellar surface. The "trough" at $\nu = 2.2$ mHz could be a signature of chromospheric mode.

4. some show pulsation phase reversal.

5. many show pulsation amplitudes that decrease steeply with increasing wavelength.

6. some show radial velocities that vary in amplitude and phase from one spectral line to the next.

7. some have bisector velocity of their Hα line varying with the depth of the line.

8. The pulsations in their atmospheres vary so much with depth that models that treat their atmosphere as a single point do not work.

I would like to list the major tools that are used in investigating the properties of roAp stars:

- The oblique pulsator model. This is used for determining the rotation periods and constraining the geometries of the stars and is also valuable for mode identification. This tool is only useful where rotational frequency splitting is observed in the pulsation amplitude spectrum. This often involves collecting good quality data through multi–site campaigns. I discuss this in detail in section 1.3.2.

- Some techniques of asteroseismology that are applicable to roAp stars, the primary one being the asymptotic relation (Tassoul 1980, 1990) for high overtone, low-order pulsators. This is used mainly for mode identification and potentially can be used as a mass and age indicator. The $T_{\rm eff}$ and the frequency spacing of the various independently excited modes enables asteroseismological luminosities of roAp to be determined (Martinez 1993; Matthews, Kurtz & Martinez 1999) (this is discussed in section 1.3.3).

- The O–C diagrams for determining the nature of frequency variations observed in some roAp stars (HR 3831, α Cir, HD 134214, HD 137949, HD 101065, HR 1217 and HD 12932). An O–C diagram is a plot of the observed pulsation phase minus the phase calculated on the basis of constant frequency as a function of time. The following observations can be made about such plots:

  1. If the frequency and phase are constant, then the O–C is a horizontal straight line.
  2. If too small a frequency is used then the O–C diagram is a straight line with negative slope.
  3. If too big a frequency is used then the O–C diagram is a straight line with positive slope.
  4. If the frequency is constant, but the phase changes discontinuously, the O–C lies along horizontal lines with discrete changes in zero points at the discontinuities.
  5. If frequency or phase (or both) are continuously variable, the O–C diagram is non–linear. It is not possible to distinguish between continuously variable phase and continuously variable frequency in the O–C diagram, however. To distinguish one has to look at the physics of the situation.

  Some of the possible physical causes of the frequency changes are stellar evolution (Heller & Kawaler 1988) which results in a quadratic curve in the O–C diagram, and the Doppler shift caused by binary motion which results in cyclic variation in the O–C. A circular orbit shows a sinusoid in the O–C diagram. Heller & Kawaler (1988) noted from the asymptotic relation for high overtone p mode pulsators that frequency changes due to stellar evolution can be measured. They also noted that frequency spacing is an age indicator, thus they show that measuring the secular frequency changes could identify the evolutionary stage of a star. Note that this assumes high overtone p- mode pulsators, so it should be applicable to roAp stars. However, for all the roAp stars which show frequency changes, the nature of such changes is such that either the frequency changes are cyclic as in HR 3831 (Kurtz *et al.* 1994a), α

Cir (Kurtz *et al.* 1994b) and HD 134214 (Kreidl *et al.* 1994), or for those that have secular frequency changes (such as that observed in HD 101065 (Martinez & Kurtz 1990)) the changes are several orders of magnitudes greater than those predicted by Heller & Kawaler's models. Stellar evolution should give rise to a constant rate of change in the pulsation period.

- Kurtz & Medupe (1996) have proposed a technique that enables one to study level effects on the pulsational temperature amplitude of roAp stars with dipole pulsation modes. This is the subject of this thesis. This technique arises out of an idea proposed by Matthews (1990) that the pulsation amplitude as a function of wavelength of roAp stars gives a measure of the empirical $T(\tau)$, an idea proved incorrect by Kurtz & Medupe (1996). The level effects can also be studied from bisector velocities of their Hα line as shown in Baldry & Bedding (2000) and Baldry *et al.* (1999).

1.4 Theoretical understanding of linear stellar pulsation

There are different treatments for small and large amplitude pulsating stars. Non-linear theory is used for large amplitude pulsators, and shall not be discussed here because roAp stars have small amplitudes. It is often adequate to use linear theory in the case of small amplitude pulsators. In the linear theory stellar pulsations are regarded as small perturbations around an equilibrium star. This is justifiable from the fact that observed pulsation amplitudes are small compared to characteristic distance scales in the sun. Even in stars where the observed pulsation amplitudes are large, most of the oscillation energy is in the regions of small amplitudes.

A star in equilibrium is composed of gas (a fluid), and can therefore be described by the hydrodynamic equations. The equilibrium star is also considered static, therefore time derivatives of equilibrium quantities are neglected, *i.e.* there are no equilibrium velocities for example. Hydrodynamic equations involve the statement of mass conservation, balance of all forces that act on the fluid and the thermodynamics of the fluid. These are discussed in detail below, and are summarised in Table 1.4.

Table 1.4: Equations of hydrodynamics for a non-viscous fluid.

Equation	**Description**
$\frac{\mathrm{d}\rho}{\mathrm{d}t} + \rho \,\mathrm{div}\,\vec{\mathrm{v}} = 0$	The continuity equation.
$\rho \frac{\mathrm{d}\vec{\mathrm{v}}}{\mathrm{d}t} = -\nabla \mathrm{P} + \rho \vec{\mathrm{f}}$	The equation of motion.
$\rho C_p \left(\frac{dT}{dt} - \nabla_{ad} \frac{T}{P} \frac{dP}{dt}\right) = \rho\epsilon - div\, \vec{F}$	The energy equation.

Mass conservation

The equation that describes mass conservation in a fluid is called the continuity equation, and states that the rate of change of total mass of the fluid equals the net inflow of fluid through the surface enclosing the fluid. It is often expressed in the following Lagrangian form:

$$\frac{d\rho}{dt} + \rho\, div\, \vec{v} = 0, \tag{1.13}$$

where ρ is the density, P the pressure and $\vec{v}$ the velocity of a fluid. The time derivative d/dt corresponds to what is seen by an observer who follows the motion of the fluid and is called the material or Lagrangian time derivative.

Equation of motion

Here the forces that act on the fluid are balanced using Newton's second law. Two kinds of forces can be identified; **body forces** that act throughout the whole fluid, and those that act only at the surface (**surface forces**). Examples of the former are gravity and magnetic forces, and the latter is exemplified by surface gas pressure forces. In words:

$$\text{mass} \times \text{acceleration} = \text{surface forces} + \text{body forces}, \tag{1.14}$$

or

$$\rho \frac{dv}{dt} = -\nabla P + \rho \vec{f} \tag{1.15}$$

where $\vec{f}$ is the body force per unit mass. Rotation introduces centrifugal force of the form $\vec{\Omega} \times \vec{\Omega} \times \vec{r}$ and Coriolis force ($\vec{\Omega} \times \vec{v}$) on the right-hand side of equation (1.15). Viscosity term of the form $\mu \nabla^2 \vec{v}$ also appears on the right-hand side of equation (1.15).

The order-of-magnitude estimate of the first coefficient of viscosity is ν is

$$\nu \approx 10^{-4} \frac{\mu T}{\rho} \tag{1.16}$$

The time-scale over which a motion is damped by friction is estimated as:

$$T_\nu \approx \frac{L^2}{\nu} \tag{1.17}$$

where L is the characteristic distance scale. The value of T_ν is of the order 10^{13} years for motions in the interior of a star. Therefore viscosity is a small in stellar interiors. Similar arguments for the stellar surface show that viscosity can be ignored on the stellar surface.

Large scale magnetic fields are usually too weak to affect the condition of hydrostatic equilibrium significantly. However, the effects may be localised in the sense that in small regions (such as as sunspots) the magnetic forces might be comparable to gas pressures. Magnetic fields introduce the term $(\nabla \times \vec{B}) \times \vec{B}$ on the right hand part of the momentum equation.

We avoid the complications by not including rotation, magnetic fields and viscosity. Neglecting viscosity in stellar atmospheres is not a bad assumption. Throughout this thesis, our body force consist of gravity, and possibly turbulent body force ($\vec{f_{turb}}$), so that $\vec{f} = \vec{g} - \vec{f_{turb}}$.

The energy equation

The thermodynamic properties of a fluid are described using the first law of thermodynamics:

$$\frac{dq}{dt} = \frac{dU}{dt} + P\frac{dV}{dt} \tag{1.18}$$

where U is the internal energy, V volume of the fluid, and $\frac{dq}{dt}$ is the rate of heat loss or gain. This relation states that the heat gain or loss goes partly into changing the internal energy and partly into expanding or compressing the gas. Equation (1.18) can be expressed, with the help of thermodynamic identities, into the following relations:

$$\begin{aligned}\frac{dq}{dt} &= \frac{1}{\rho(\Gamma_3 - 1)}\left(\frac{dP}{dt} - \Gamma_1\frac{P}{\rho}\frac{d\rho}{dt}\right) \\ &= c_P\left(\frac{dT}{dt} - \nabla_{ad}\frac{T}{P}\frac{dP}{dt}\right) \\ &= c_V\left(\frac{dT}{dt} - (\Gamma_3 - 1)\frac{T}{\rho}\frac{d\rho}{dt}\right)\end{aligned} \tag{1.19}$$

where $\nabla_{ad} = \frac{\Gamma_2 - 1}{\Gamma_2} = \left(\frac{\partial \ln T}{\partial \ln P}\right)_{ad}$ is the adiabatic temperature gradient, and Γ_2 and Γ_3 are adiabatic exponents.

The source of heat in stars is the nuclear reactions in their cores, and cooling takes place near surface where the energy is radiated into space. Therefore, we have the following:

$$\text{heat gain} = \text{energy generation rate} - \text{net flux out.} \tag{1.20}$$

Mathematically the above statement is expressed as:

$$\rho\frac{dq}{dt} = \rho\epsilon - div\,\vec{F}, \tag{1.21}$$

where ϵ is the energy generation rate per unit mass, it equals to zero in the stellar atmospheres, F is the energy flux. The flux $\vec{F}$ includes all forms of energy transport such as radiation and convection.

Combining equations (1.19) and (1.21) we obtain:

$$\rho C_p\left(\frac{dT}{dt} - \nabla_{ad}\frac{T}{P}\frac{dP}{dt}\right) = \rho\epsilon - div\,\vec{F} \tag{1.22}$$

The equations (1.13), (1.15) and (1.22) describe a star in equilibrium. These equations are then perturbed and only first-order terms retained. The resulting differential equations are then solved for perturbed quantities. The whole procedure is described in Christensen-Dalsgaard's notes available at http : //astro.ifa.au.dk/ $\sim$ jcd/oscilnotes.

1.5 Observational evidence for stellar pulsation

1.5.1 Seismology of the sun and stars

The solutions of adiabatic non-radial pulsation equations are of the form:

$$y(r,\,\theta,\,\phi) = A_{n\ell}(r)\,Y_\ell^m\,(\theta,\,\phi)\,\exp(-i\,\omega\,t) \tag{1.23}$$

for any perturbed quantity y. $A_n(r)$ gives the radial dependence of the eigenfunction and is obtained from numerical solutions of the pulsation equations. The function Y_ℓ^m is a spherical harmonic and gives the angular dependence of the surface pulsations. The quantum numbers n, ℓ, m mentioned in section 1.2.9 define a pulsation mode and are defined in detail below:

- n, **the overtone**, it gives the total number of nodal points along the radial direction. A mode with $n = 0$ is called fundamental, that with $n = 1$, the first overtone, $n = 2$, second overtone, *etc.*
- ℓ, **the degree**, it gives the total number of surface nodal lines.
- m, **the azimuthal order**, gives the number of surface nodal lines parallel to lines of longitude.

Three types of seismic waves are observed in pulsating stars:

- $p-$ **modes** where pressure force is the restoring force. They reach their maximum amplitude near the stellar surface. In the sun they are excited in the upper part of the convection zone. In other stars other excitation mechanisms such as the κ-mechanism come into play.
- **g- modes**, also called internal gravity waves, where negative buoyancy is the restoring force. They reach their maximum amplitude near the core and generally oscillate at frequencies lower than the $p-$ modes. No g-modes have been observed in the sun yet. However, other stars such as δ Scuti stars, SPB, sdB, γ Doradus stars, 53 Per stars, ζ Oph stars, DA, DB and DO white dwarfs do pulsate in g- modes.
- **f- modes**, these are horizontal surface waves, very similar to the ocean waves.

We demonstrate how acoustic cavities are set up in the sun (and other stars) in Fig. 1.4(**A**). Consider a $p-$ mode starting from the surface at some angle. As it propagates inward, it penetrates regions of increasing temperature, therefore its speed increases as $c_s \propto \sqrt{(\frac{T}{\mu})}$, where T is temperature, μ is mean molecular weight and c_s is the sound speed. It is hence refracted back towards the surface. When such a wave arrives at the surface it experiences a sharp drop in density and is reflected back towards the interior again. In Fig. 1.4(**A**) we show two such $p-$ modes, one inclined far from the vertical (which gets rapidly refracted, creating a shallower acoustic cavity), and another with relatively smaller inclination to the vertical. The latter penetrates deeper into the star. Modes that travel vertically (radial

modes) can go right through the centre. For a given n value, the depth of the acoustic cavity depends on the ℓ value. Small ℓ value modes create deeper cavities, while large ℓ-value modes have shallower acoustic cavities.

Modes that reach the centre of star can potentially provide valuable information about the core of a star, thus they might give us a clue to the solar neutrino problem for example. However, few waves reach the core. Another problem is that for a medium to influence the properties of a sound wave, the wave needs to spend some time in that medium. Since sound speed increases rapidly in the deep interior, the sound waves spend little time there. This requires extremely precise measurements of the frequencies. This problem does not apply to seismic studies of the earth (for example) because here the speed of seismic waves through the earth does not increase rapidly with depth.

In Fig. 1.4(**B**) we see that the g- modes are mostly confined to the regions below the convection zone, therefore the convection zone is the reflection point for them. This is because g- modes depend on negative buoyancy as a restoring force.

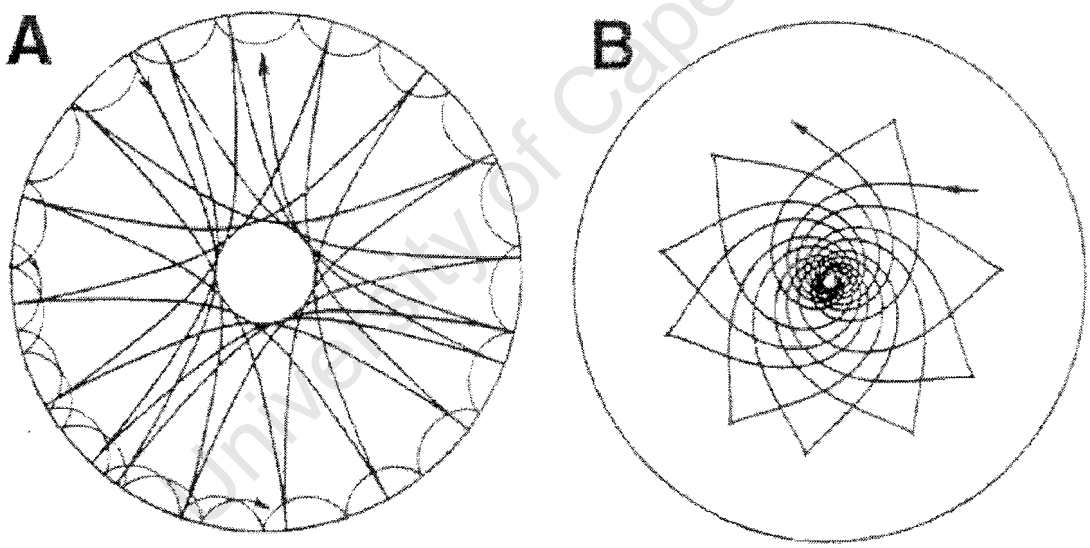

Figure 1.4: Examples of the paths that $p-$ modes (**A**) and g- modes (**B**) can trace in the interior of the sun. In **A** the paths of two modes are shown; the high ℓ value one that creates a shallow acoustic cavity confined to the atmosphere, and the more deeply penetrating mode corresponding to low ℓ value. Note that the g- mode is confined beneath the convection zone in the sun. The sketch is taken from Gough, Leibacher, Scherrer & Toomre (1996).

The acoustic cavities manifest themselves by

- raising surface gases up and down, thereby creating velocity fields. The wave amplitudes and phases can therefore be measured by Doppler shifts caused by such velocities on spectral lines of such a pulsating star.

- alternately rarifying and compressing surface gases, thereby perturbing surface temperature and gravity. Since the surface flux is defined by temperature and gravity, it is also perturbed. Here measurement of intensities and subsequent analysis should reveal amplitudes and phases. Therefore in this photometry is used.

The $p-$ mode oscillations observed in the sun have small amplitudes; individual modes have velocity amplitudes of $20\,\mathrm{cm\,s^{-1}}$, and their random superposition produces amplitudes of up to $500\,\mathrm{m\,s^{-1}}$, the g- mode amplitudes are expected to be 10 times smaller. Therefore very precise and stable spectrometers are necessary to measure velocities of individual modes in the sun. Vapour cell spectrometers such as the ones used by the Birmingham Solar Oscillation Network (BiSON) group (Brookes, Isaak & van der Raay 1978) are suitable. Because the oscillations often observed in other stars have larger amplitudes, standard astronomical spectrographs are used. Stability is still an important requirement, therefore for precise measurements it is still necessary to use very stable spectrograph like coudé and echelle spectrographs. Bouchy & Carrier (2001) demonstrate the stability of their echelle spectrograph by detecting pulsational radial velocity amplitudes in α Cen A to an accuracy of $1\,\mathrm{m\,s^{-1}}$.

Following the tremendous successes of helioseismology as will be shown in the next subsections, there have been attempts to see if helioseismological techniques can be applied to solar-like oscillations in other stars. The first step towards achieving this is to obtain a clear and unambiguous detection of these oscillations in other stars. The amplitudes are expected to be very small and therefore the effects associated with ground observations are a hindrance and make it difficult to detect signals. In spite of this, detection of solar-like oscillations have been reported in Procyon (Martic *et al.* 1999), β Hydri (Bedding *et al.* 2001; Carrier *et al.* 2001) and α Cen A (Kjeldsen & Bedding 1995). There are also future projects like MONS (http://www.obs.aau.dk/hans/mons/), MOST (http://www.astro.ubc.ca/MOST/), COROT (http : //www.astrsp_mrs.fr/projects/corot) and Eddington (http://sci.esa.int/home/eddington/index.cfm) that will attempt to detect and measure these oscillations from space.

1.5.2 Some of the results of helioseismology

The part of this section that deals with helioseismology is based on Gough *et al.* (1996a,b), Harvey *et al.* (1996), Christensen-Dalsgaard *et al.* (1996), Hill *et al.* (1996) and Thompson *et al.* (1996). A good introduction of astero- and helio-seismology presented in layman's terms can be found at http : //www.obs.aau.dk/helio_outreach/english.
Some of the important results obtained from helioseismology are

- **measurement of the depth of the solar convection zone**
- **measurement of the solar rotation profile**
- **constraints on the solar neutrino problem**

Each of the above results are briefly discussed in the following subsections.

The depth of the solar convection zone

It has been shown through numerical simulations by Gilman & Miller (1986) that the depth of the base of the convection zone could control the form of the differential rotation in the sun. This would have bearing on on the dynamo effect that is believed to be one of the possible source of the solar magnetism. It is therefore important to determine the depth of the base of the convection zone.

The history of determination of the depth of the extent of the solar convection zone goes back to the early days of helioseismology. The earlier methods were indirect in the sense that they were based on observations of high degree modes. These modes are trapped in the outer parts of the convection zone, but they allow a determination of the adiabat in the adiabatically stratified part of the convection zone. The depth of the convection zone was determined (then) by calculations of envelope models based on this determined adiabat. Gough (1977) was able to determine that the convection zone extends down to 0.3 of the solar radius from the surface using these indirect methods.

A more direct method of determining the depth of the base of the convection zone was suggested by Gough (1986) from noting that the sound speed gradient is closely related to the temperature gradient. Therefore, the base of the convection zone is marked by a transition from adiabatic temperature gradient (inside the convection zone) to radiative one (beneath the convection zone). This transition leads to a break in the gradient of the sound speed. Sound speed in the sun can be determined from helioseismic inversion of the observed pulsation frequencies. This break is shown clearly in the inset of Fig. 1.5 taken from Christensen-Dalsgaard, Gough & Thompson (1991), who applied this method to the data observed by Libbrecht & Kaufman(1988). The frequencies observed were of degree $\ell \geq 100$. They determined the depth of the convection zone to be 0.287 ± 0.003 $R_\odot$. They also found that the method seems to be independent of the physics of the solar interior. They caution that if large magnetic field (of the order megagauss) is present at the base of the convection zone, it would affect the value they determined. The latest value for the depth of the convection zone is 0.287 ± 0.001 $R_\odot$ obtained by Basu & Antia (1997). Their result is based on the asymptotic sound speed inversion taking into account the systematic errors introduced by the discontinuity composition gradient (resulting from diffusion of helium and heavy elements).

The Solar Rotation profile

That rotation causes frequency splittings was discussed in the section 1.2.3, and when one can observe the many million modes (10^7) observed in the sun and each of those modes sample different parts of the sun, one can end up with a map of rotation periods of much of the interior and atmosphere of the sun. Of course, since presently we only observe $p-$ modes and f- modes in the sun, we can only build such a map in regions of the sun where $p-$ modes can reach and are most sensitive to. This means we can have accurate rotation profile of much of the interior (the envelope and atmosphere), but not of the core and part of the envelope near the core. Such maps have been created, an example based on the results

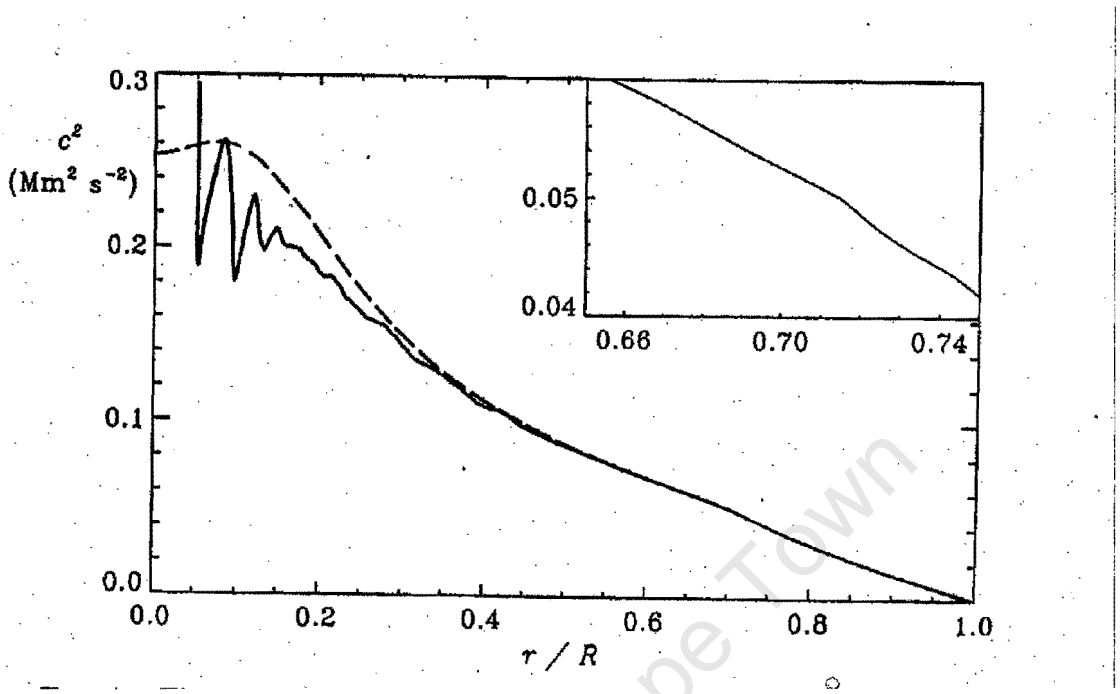

Figure 1.5: The solid curve shows the sound speed in the Sun as inferred by Christensen-Dalsgaard *et al.* (1985) compared to the sound speed calculated from a standard solar model shown as a dashed curve. The inset shows in detail the inferred sound speed near the base of the convection zone (Taken from Christensen- Dalsgaard, Gough & Thompson 1991).

from the low and intermediate-degree (LOWL) experiment operated by the High Altitude Observatory is shown in Fig. 1.6.

The first thing to observe from Fig. 1.6 is that the surface behaves as expected, *i.e.* the equator rotates faster (red) than the poles (blue). The dotted line marks the base of the convection zone, and also the end of the differentially rotating region. Areas below the convection zone show more uniformity in rotation which suggests that these regions are rotating rigidly. The results are confirmed by Kosovichev *et al.* (1997) on their analysis of the data obtained from MDI instrument of the SOHO satellite, and the GONG analysis by Thompson *et al.* (1996). The white shading in the core indicates our lack of knowledge of that part of the star. We know less about rotation of the core of the sun because $p-$ modes are less sensitive to conditions there and also relatively few of them reach there.

The Solar Neutrino Problem

All experiments that attempt to measure the flux of neutrino that result from nuclear (proton-proton) reactions occurring in the solar core, where hydrogen is converted to helium, have reported fluxes that are about a third of the theoretical predictions of the solar models. The results from three such experiments, Homestake, Gallex and Kamiokande are 2.32 ± 0.26 SNU, 78 ± 10 SNU and $2.9 \pm 0.4\,\mathrm{cm}^{-2}\mathrm{s}^{-1}$,respectively. As a comparison the neutrino flux

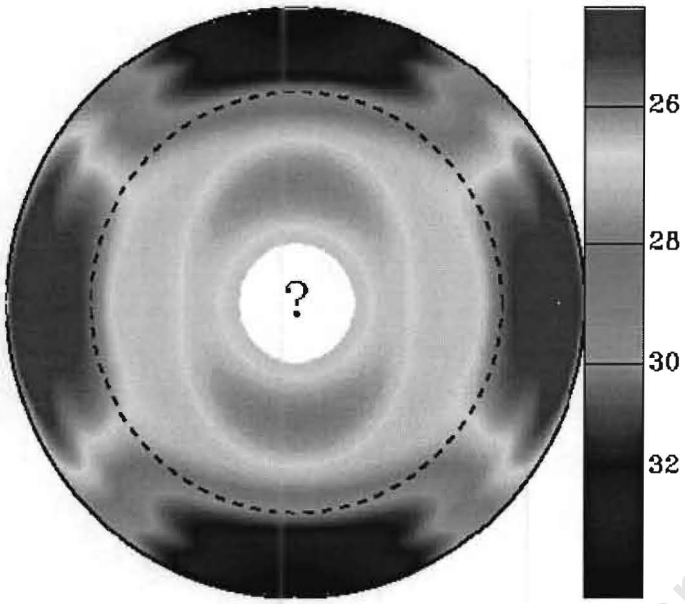

Figure 1.6: A colour-coded diagram showing the variation of solar rotation period with depth and latitude. The scaling is shown on the right. The dotted line represents the base of the convection zone. It is clear that the atmosphere and convection zone rotate differentially. However, the interior regions have more uniform (rigid body-like). This diagram was taken from http : //www.obs.aau.dk/helio_outreach/english.

predicted by Bahcall & Pinsonneault's (1992) model for Homestake, Gallex and Kamiokande are 8 ± 1 SNU, 132 ± 7 SNU and $5.7 \pm 0.8\,\mathrm{cm}^{-2}\mathrm{s}^{-1}$ respectively. A modern account of the solar neutrino problem is given by Bahcall, Pinsonneault & Basu (2001). See also Raghavan (1995).

Several proposals to reduce the discrepancies between theory and experiments have been made. Some of them involve processes that can lower the temperature of the solar core whilst maintaining its radius, and the total luminosity of the sun. The reasoning behind these proposals is based on the knowledge that the p-p reaction rates are very much temperature dependent. The ^7Be reactions go as T^8 and those for ^8B go as T^{18}. I list some of these here:

- A fast rotating solar core produces a centrifugal force that acts against gravity. A fast rotating core seems to be in contradiction with the helioseismologically inferred rotation profile discussed above. Also, it has been estimated that the core needs to rotate about a thousand times faster than the surface (Bahcall 1989).

- A strong magnetic field was suggested by Iben (1968) as a means to reduce the core temperature. This strong field in the core tends to increase the pressure gradient if the magnetic field increases from the surface towards the core. Interior magnetic field strengths of about 10^9 G are needed to affect the neutrino fluxes significantly. Moreover, the effect of such huge field strengths has been shown by Bahcall & Ulrich (1971) and Abraham & Iben (1971) to increase the predicted neutrino fluxes, making matters worse.

- A solar core with high hydrogen and lower helium abundances by mass. A test of this scenario is shown in Fig. 1.7 where a model with different helium abundances is compared with helioseismic data. It is clear from that sketch that low helium abundance in the core does not agree with helioseismic data. High helium abundance agrees well with the helioseismic data, but does not solve the solar neutrino problem.

- If neutrinos have non-negligible mass, then they can change from one type to another (the so called neutrino oscillations), then the electron-type neutrinos (which are the main neutrinos produced from the ^{8}B reactions in the solar core) will transform into other types (ν_τ and ν_μ) on their way from the sun. Therefore, when they reach the earth, the neutrino flux will contain a mixture of all types of neutrinos, the total sum of which will add to the original flux that left the solar core (which, if the solar models are correct should be the same as theoretical predictions).

For other suggested modifications to the standard solar physics and particle physics see Bahcall (1989). The fact that current models agree with helioseismic data, suggests that the disagreement between observed neutrino fluxes and theoretical predictions is not caused by errors in the standard solar models (Christensen-Dalsgaard *et al.* 1996). The topic on solar neutrino problem and helioseismology is also discussed by Roxburgh (1996).

The latest results from the Sudbury Neutrino Observatory (SNO) presented by Ahmad *et al.* (2001) (see http : //www.sno.phy.queensu.ca/sno/first_results) seem to provide evidence for neutrino oscillations. By taking taking neutrino oscillations into account, they were able to show that their solar neutrino flux measurements are in agreement with theoretical models. This is not a surprise since helioseismic measurements have shown many a times that convectional solar models are in agreement with helio-seismic data and do not need major revision (see Turck-Chièze *et al.* 2001 for example). In addition, helioseismic data have often led to refinements of the solar models. The experimental method employed by the SNO group involved comparing solar neutrino flux detected from charged current (CC) reactions on deuterium to that detected from elastic scattering (ES) of electrons. The logic behind this being that the CC reactions are exclusively sensitive to electron-type neutrinos (ν_e), while the ES reactions have small sensitivity to the ν_τ and ν_μ in addition to being sensitive to the ν_e. Therefore, if the charged current neutrino flux is found to be less than that detected from elastic scattering it shows the presence of other flavours of neutrinos. They found this to be the case in their measurements. They still are analysing the results from neutral charge (NC) reactions which are more sensitive to all neutrino types.

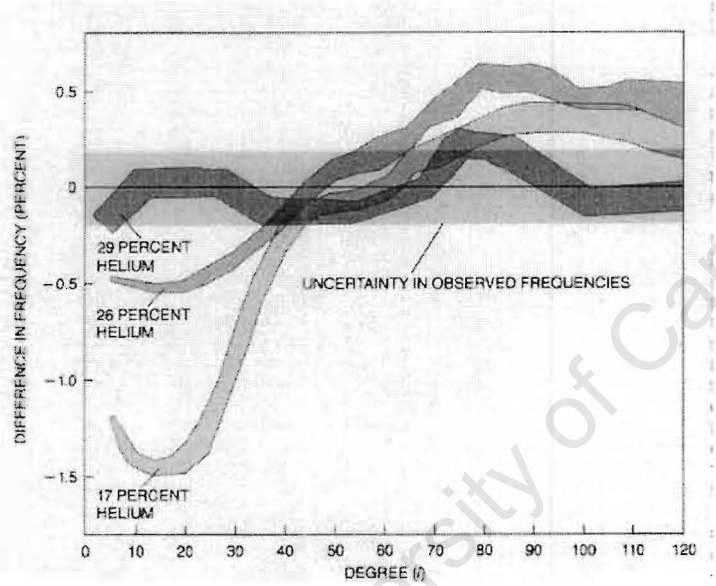

Figure 1.7: A graph for comparing the observed and theoretical frequencies as a function of the degree ℓ at constant overtone, taken from Leibacher *et al.* (1985). The graph shows how the solar models compare with helioseismic data when different core helium abundances are used. A high core helium abundance is in agreement with helio-seismic data, but does not solve the solar-neutrino problem. On the other hand a low helium abundance solves the solar neutrino problem but is inconsistent with helioseismic data.

Chapter 2

Data

2.1 Photometric data

2.1.1 Data presentation

Multi-colour photometric data of several roAp stars, HD 101065, HD 128898, HD 137949 and HD 134214, were obtained in 1995, the results (based on amplitudes) of which were used for my MSc thesis (Medupe 1996) and in Medupe & Kurtz (1998). In 1996 I obtained multi-colour photometric data on HR 3831 over fourteen nights, five of which were lost to bad weather. HR 3831 was observed again in 1998 by Yolanda van Niekerk and me for two full weeks. Again, we were able to obtain nine out of fourteen nights for the same reason as in 1996. The purpose for both the 1996 and 1998 campaigns was to look for the variations of amplitudes and phases with rotation phase. Before I go on to discuss the data, I discuss briefly of the data acquisition and analysis procedures, the details of which are in Medupe (1996).

Data acquisition

The data were acquired using the LUCY data acquisition program (Balona 1988). LUCY requires as input the colour equations, zero–points, extinction coefficients, star names and coordinates. These are used for on-line reductions. To specify the sequence of filters and the corresponding integration times, programs which contain integration time, flags to denote star or sky measurements and filter numbers are used. These programs can be arranged into a macro–program containing one or more programs. In our case, we included a star program (a program with flags set for star measurements) and a sky program (a program with flags set to sky measurements) in our macro–program. This allowed us to switch between the two programs whenever necessary. The results of each integration are displayed on the screen, stored on the hard disk drive of the PC and printed on the matrix printer (if so required). After every program a summary of the on–line reductions (Heliocentric Julian Date, magnitudes and colours) corresponding to the middle of integration is displayed on the screen. This is invaluable for tracking errors in the instruments, the presence of clouds and

can be used to check if the correct star is being observed. However, the on-line reductions are not used in the analysis, more detailed and accurate reductions procedures are followed.

All observations were obtained with 10 second integrations and 30 arcsec apertures. We found this aperture size to be optimal for avoiding light losses when the telescope tracking was not good or when the seeing is marginal or bad.

Sky measurements were taken at regular intervals of between 30 and 45 minutes to ensure proper monitoring of sky brightness variations. Extra care was exercised when there were rapid sky brightness variations, during moon–rise, moon–set, towards dawn, and just after evening twilight. During those times sky measurements were taken at shorter time intervals of 10 to 15 minutes.

Data reduction method

The first step in the data reduction was to visually inspect all the raw light curves to remove any obvious bad data points. The main source of bad points is thin cirrus clouds that are not easy to see. Electrical interference from radios and other electrical appliances in the observing dome could contribute as well. However, the observing domes at SAAO are properly shielded from electrical interference.

I then applied the following corrections to the data, in order: dead–time correction, sky–subtraction and atmospheric extinction correction. The times were converted to heliocentric Julian dates to an accuracy of 10^{-5} day. A full account of the corrections applied to the counts are given in Medupe (1996), also see Henden & Kaitchuk (1982).

Determination of amplitudes and phases

The discrete Fourier transform technique as suggested by Deeming (1975) and modified by Kurtz (1985) was applied to the reduced data, in order to obtain the Fourier spectrum. Normally after this step, low frequency peaks can be seen, in addition to the real signal. These low frequency peaks are then pre-whitened before the amplitudes and phases are refined by fitting (by linear least-squares) a function of the following form

$$y = A_\lambda \cos\left(2\,\pi\,\nu\,(t - t_0) + \phi_\lambda\right) \tag{2.1}$$

where the pulsation frequency ν is assumed to be known perfectly. A_λ is the amplitude in mmag, and ϕ_λ the phase in radians.

Kurtz & Medupe (1996) and Medupe & Kurtz (1998) published tables of the amplitudes for Johnson $U\ B\ V\ R\ I$ and Strömgren $uvby$ filters based on the 1995 data on HD 101065, HD 128898, HD 137949, HD 134214 and HR 3831. In this chapter we include the pulsation phases at different wavelengths as well in the tables published above. The data for HD 101065, HD 128898, HD 137949 and HD 134214 are listed in Table 2.1. These phases

Table 2.1: The pulsation amplitudes and phases obtained from a linear least squares fit to the May 1995 campaign data. The amplitudes were published in Medupe & Kurtz (1998). The zero point for the all phases presented here is 2449000.

Star	ν	**Filter**	λ	σ	**A(obs)**	**phase**
	mHz		Å	mmag	mmag	radians
HD 101065	1.3728660	U	3670	4.14	7.43 ± 0.25	-2.25 ± 0.03
		B	4360	2.39	6.59 ± 0.14	-2.03 ± 0.02
		V	5450	2.29	3.01 ± 0.13	-1.55 ± 0.04
		R	6380	2.56	1.72 ± 0.12	-1.51 ± 0.07
		I	7970	2.23	0.53 ± 0.11	-1.32 ± 0.20
HD 128898	2.4419999	U	3670	3.81	2.71 ± 0.18	-2.28 ± 0.07
		B	4360	3.49	2.03 ± 0.15	-2.27 ± 0.08
		V	5450	3.17	1.06 ± 0.14	-2.12 ± 0.13
		R	6380	3.76	0.54 ± 0.15	-2.46 ± 0.27
		I	7970	3.35	0.41 ± 0.13	-2.04 ± 0.33
HD 134214	2.949574	U	3670	2.93	4.25 ± 0.16	2.89 ± 0.04
		B	4360	2.15	4.13 ± 0.11	2.97 ± 0.03
		V	5450	2.55	1.94 ± 0.13	2.98 ± 0.07
		R	6380	2.35	1.27 ± 0.11	2.96 ± 0.08
		I	7970	2.61	0.73 ± 0.12	2.82 ± 0.16
HD 137949	2.014781	U	3670	2.59	1.37 ± 0.15	-0.47 ± 0.11
		B	4360	2.19	1.46 ± 0.13	-0.90 ± 0.09
		V	5450	2.09	0.82 ± 0.12	-0.56 ± 0.15
		R	6380	2.30	0.55 ± 0.12	-0.63 ± 0.22
		I	7970	2.50	0.24 ± 0.13	$+0.72 \pm 0.54$

and amplitudes were determined from data spanning over six hours for each star. This is equivalent to 0.06 of the α Cir rotation cycle for example, hence we expect rotational modulation to 'dilute' the amplitudes and phases determined for this star. We expect this to affect to all the five wavelength bands we consider for each star by the same amount. This effect of the rotational modulation is not expected in HD 134214 and HD 137949 since they do not show such modulations. To see the trends in the data, plots of normalised amplitudes and phases for Johnson U B V R I filters are shown in Figs 2.1, 2.2, 2.3 and 2.4.

Of the four stars, HD 101065 has the highest photometric amplitudes, even in the R and I filters. In addition, the night it was observed was of good photometric quality. The noise levels in U, B, V, R and I in its amplitude spectrum were around 0.5 mmag. It is for these reasons that the errors in amplitude and phase are small, and that the phases are well

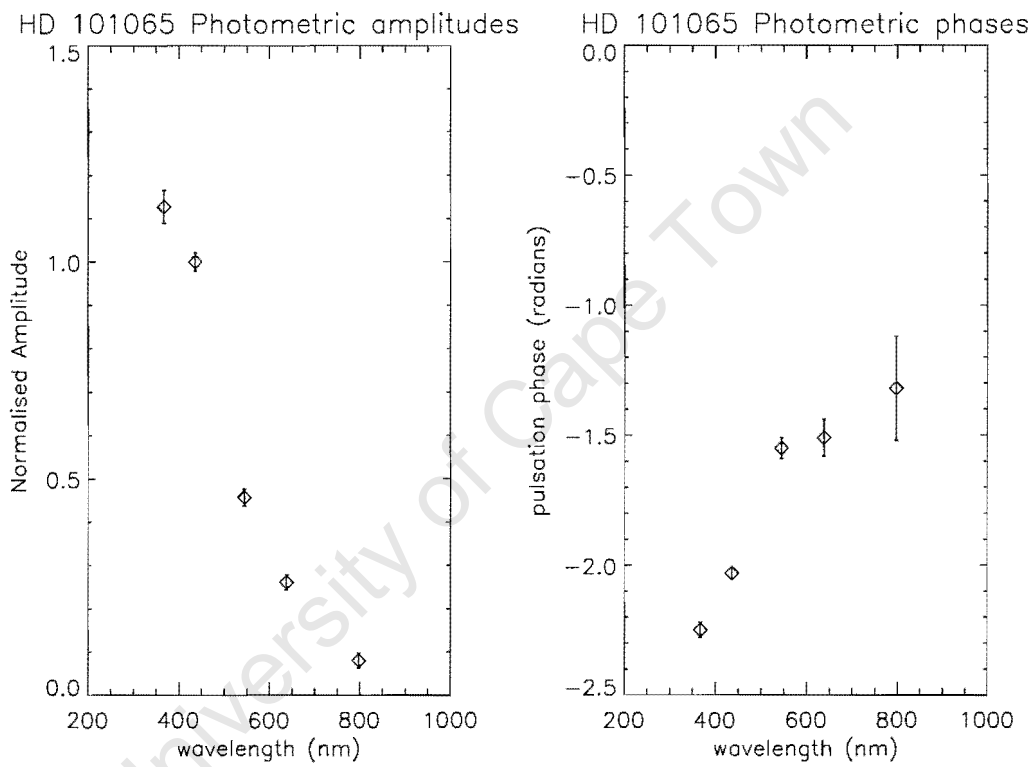

Figure 2.1: The left plot shows the variation of pulsation photometric amplitudes, normalised to 1 at Johnson B, with wavelength of observations. Notice the rapid decline of the normalised amplitude with wavelength. The variation of pulsation phase with wavelength is shown on the right. It is clear that for this star, HD 101065, the photometric pulsation phase increases with wavelength. This is the phenomenon that this thesis attempts to explain.

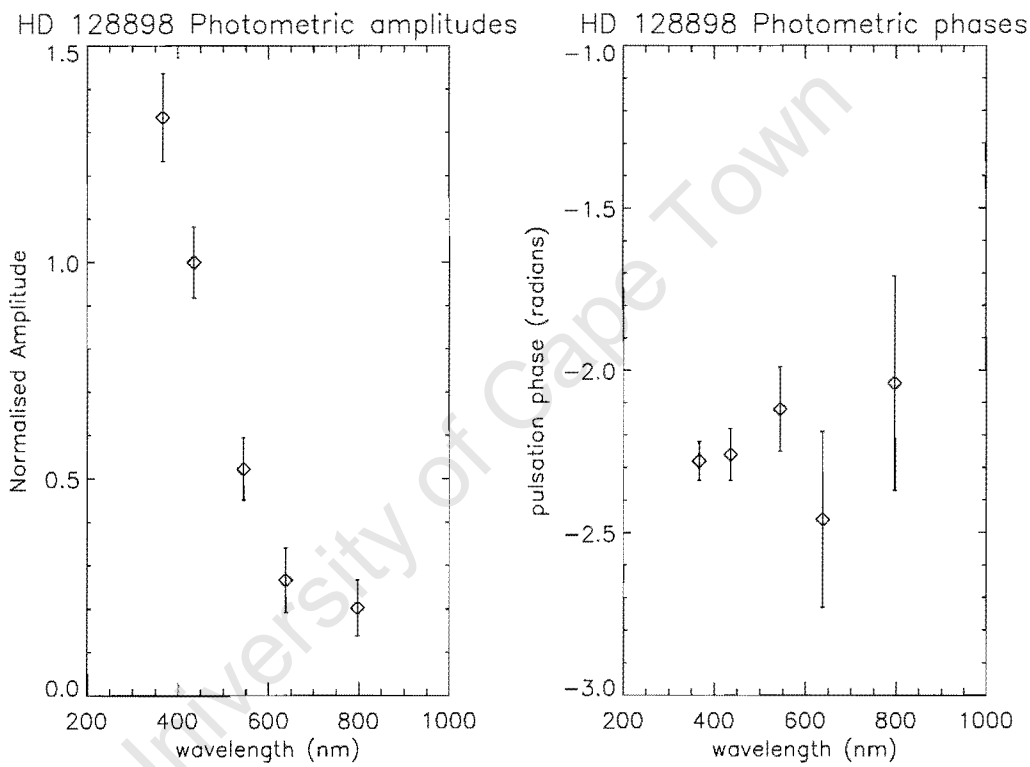

Figure 2.2: The multi-colour photometric data for HD 128898. The left plot shows the variation of pulsation photometric amplitudes, normalised to 1 at Johnson B, with wavelength of observations. The variation of pulsation phase with wavelength is shown on the right. Here there is no variation in the photometric pulsation phase.

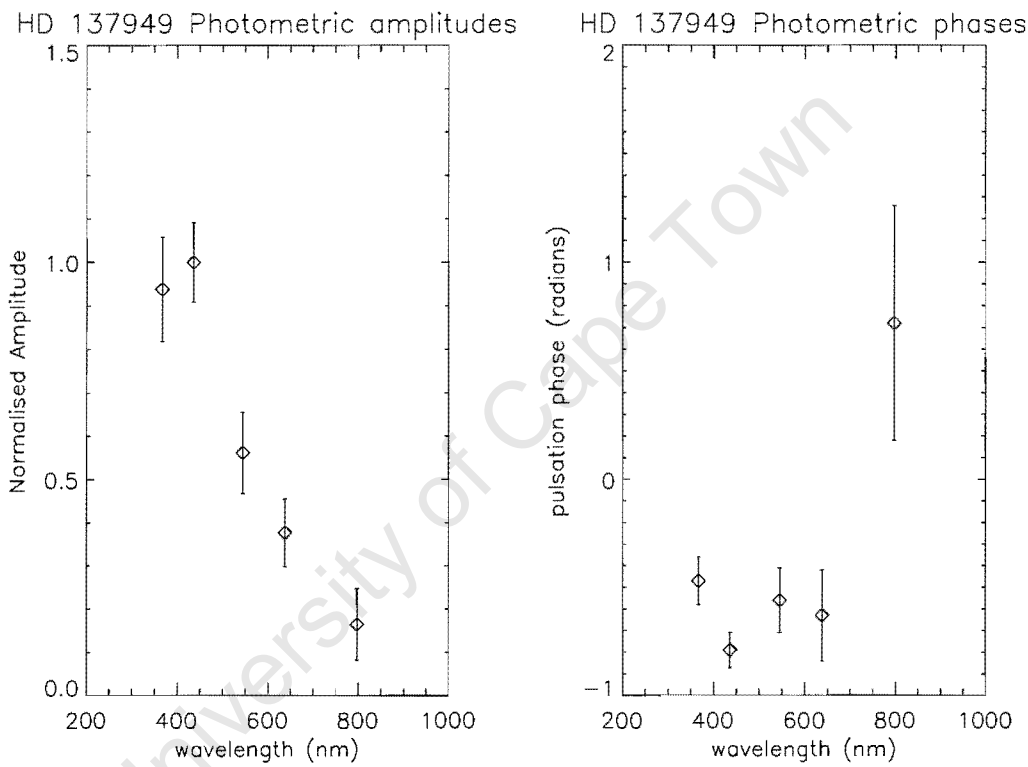

Figure 2.3: The multi-colour photometric data for HD 137949. The trend in the amplitude data is clear, but the errors on the phase data are such that it is difficult to tell if they have any wavelength dependence. The I phase is not well determined because the I amplitude is very small 0.24 ± 0.13, therefore compared to amplitudes in other filters, the signal-to-noise is quite small.

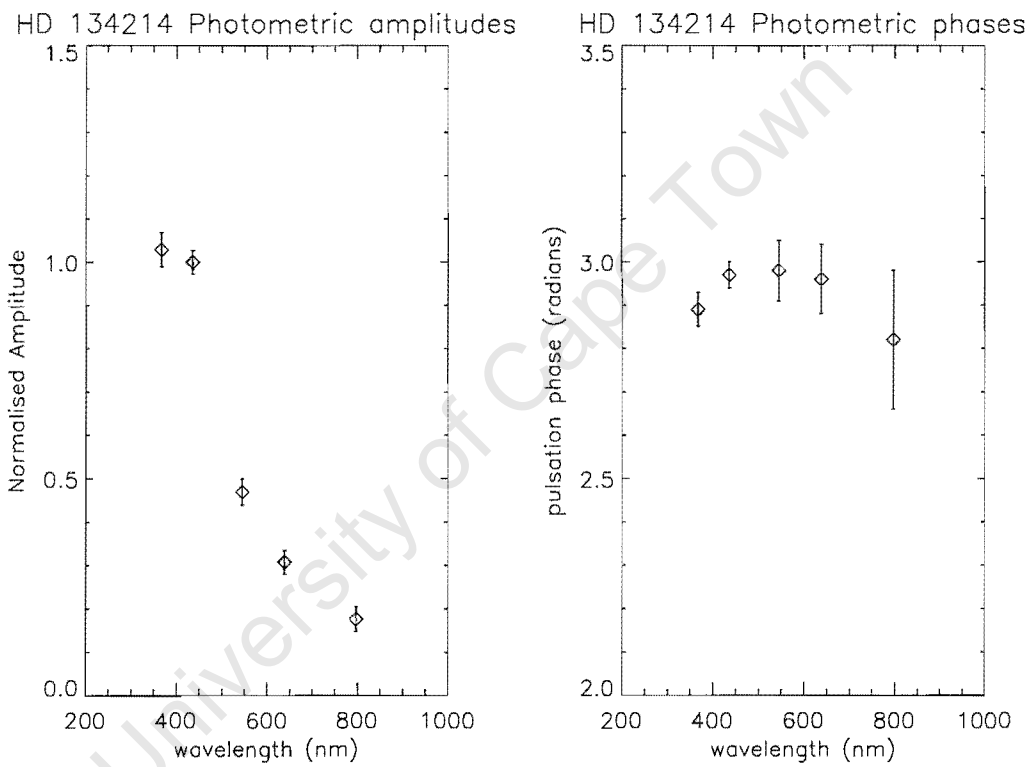

Figure 2.4: The multi-colour photometric data for HD 134214. Again we notice the rapid decrease of amplitude with wavelength. The pulsation phase shows no variation with wavelength.

Table 2.2: A table of coefficients obtained by linear least squares fits to the pulsation phases obtained in the May 1995 campaign. The HR 3831 data are from the 1996 campaign for rotation phase 0.58.

Star	**Coefficients**		χ^2_ν
	a	b	
HD 101065	-3.370 ± 0.005	$(3.10 \pm 0.01) \times 10^{-3}$	5.53
HD 128898	-2.4 ± 0.2	$(4.1 \pm 5.1) \times 10^{-4}$	0.57
HD 134214	$+2.9 \pm 0.1$	$(1.5 \pm 2.5) \times 10^{-4}$	1.06
HD 137949	-0.9 ± 0.3	$(6.7 \pm 6.8) \times 10^{-4}$	5.36
HR 3831	-2.2 ± 0.2	$(3.08 \pm 0.04) \times 10^{-3}$	4.17

determined.

Trends in the 1995 data

Here we try to look for trends in the pulsation phase data shown in Figs 2.1, 2.2, 2.3 and 2.4. We do this by fitting a linear function of the form:

$$y = a + b\,x \tag{2.2}$$

and a quadratic function of the form

$$y = a + b\,x + c\,x^2 \tag{2.3}$$

where the coefficients are obtained from the least squares fit method. Therefore, a good criterion for selecting linear over quadratic fit is to consider the coefficient of the second order term. Another approach is to consider the χ^2 of the fits given by

$$\chi^2 = \sum_i \left(\frac{[y_i - y(x_i)]^2}{\sigma_i^2} \right) \tag{2.4}$$

where (x_i, y_i) is a data point, $y(x_i)$ is a fitting function at x_i and σ_i the error in a data point (see Bevington & Robinson 1992). The statitic $\chi^2_\nu = \chi^2/NDF$, where NDF is the number of degrees of freedom, compares the variance of the residuals of the fit to the measurement errors so that $\chi^2_\nu \approx 1$ implies that the error in the fit is comparable to that in measurements. The results are shown in Tables 2.2 and 2.3, and in the plots in Figs 2.1, 2.2, 2.3 and 2.4.

The χ^2_ν shown in Tables 2.2 and 2.3 shows that neither linear nor quadratic functions make good fits to the HD 101065 data. In Fig. 2.1 we can clearly see that the phase for HD 101065 increases by about 60° from Johnson U to V. The relatively large errors in R and I make it difficult to tell whether the phase continues to increase from Johnson V to I or stays constant.

The errors in the Johnson V R I of HD 128898 are so large that one can also deduce no trend in the data as well. The noise level was under 0.7 mmag.

Table 2.3: A table of coefficients obtained by quadratic polynomial least squares fit to the pulsation phases obtained in the May 1995 campaign. The HR 3831 data are from the 1996 campaign for rotation phase 0.58.

Star	**Coefficients**			χ^2_ν
	a	b	c	
HD 101065	-4.4 ± 0.4	$(7.6 \pm 1.7) \times 10^{-3}$	$(-4.6 \pm 1.7) \times 10^{-6}$	4.75
HD 128898	-2.47 ± 0.04	$(5.5 \pm 0.9) \times 10^{-4}$	$(-1.4 \pm 1.8) \times 10^{-7}$	23.14
HD 134214	2.06 ± 1.05	$(3.4 \pm 0.4) \times 10^{-3}$	$(-3.1 \pm 0.4) \times 10^{-6}$	1.76
HD 137949	3.5 ± 1.4	$(-1.8 \pm 0.6) \times 10^{-2}$	$(1.7 \pm 0.5) \times 10^{-5}$	9.59
HR 3831	-5.1 ± 1.1	$(1.5 \pm 0.5) \times 10^{-2}$	$(-1.1 \pm 0.4) \times 10^{-5}$	1.11

The large errors in the HD 137949 data are mainly due to the fact that the amplitude of this star is the lowest of the stars investigated here. This can be seen in Fig. 2.3 where the error bars are almost equal to the actual point-by-point differences (with the exception of the I data). In addition to this, the linear and quadratic functions do not make good fits to its data, both fits result in large χ^2_ν values. Thus, there appears to be no phase variations with wavelength in the data.

At one sigma level however there appears to be no trend visible in the HD 134214 data as shown in Fig. 2.4. The noise level was well under 0.5 mmag in all five filters.

The HR 3831 phase data is best fit by a quadratic function. Tables 2.2 and 2.3 show that the phase data definitely does not depend linearly on wavelength.

As a comparison I show a plot of amplitudes and phases for five Johnson filters for a δ Scuti star HD 95321 (Koen *et al.* 1999) in Fig. 2.5. One thing to note is that the normalised amplitude decreases by half from Johnson B to I, compared to the steep decline observed in roAp stars. Here the temperature effects overwhelm other effects see chapter 3, Medupe & Kurtz (1998) show that the temperature term goes as $\frac{1}{\lambda}$. The pulsation phase of HD 95321 shows only a slight increase of about 17° from Johnson U to I. These phase changes are small compared to the 63° we saw in HD 101065, and over 80° we see in HR 3831 (see Fig. 2.6).

The 1996 observations of HR 3831 were done in the Johnson U B V R I, and through the Strömgren filters as well. The photometric amplitudes were published in Medupe & Kurtz (1998). In Table 2.4 both the amplitudes and phases are included. We used the following ephemeris derived by Kurtz *et al.* (1997a):

$$HJD_{max} = 2448312.23606 + (2.851976 \pm 0.00003)E, \tag{2.5}$$

to calculate the rotation phase for each day of observation. The plots of the data at various rotation phases are shown in Figs 2.6, 2.7 and 2.8.

The results of the 1998 campaign are shown in Table 2.5. The corresponding plots are shown in Figs 2.9, 2.10 and 2.11. Here the observations were obtained with the South

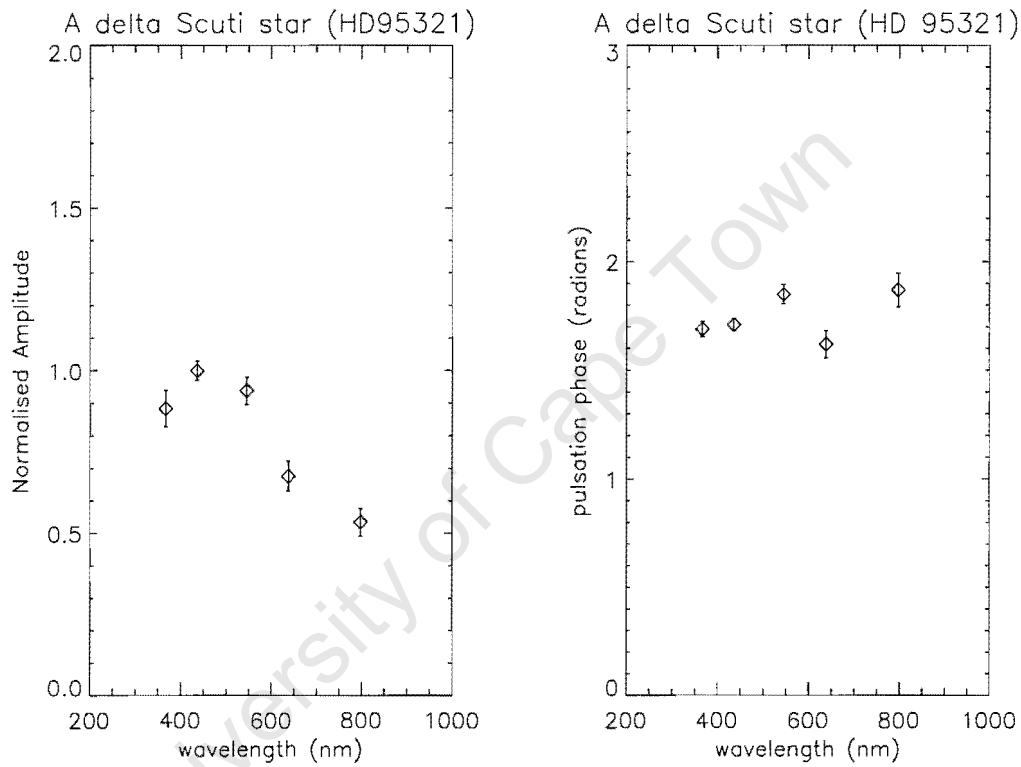

Figure 2.5: The data for a δ Scuti star HD 95321 as presented in Koen *et al.* (1999). The normalised amplitudes decrease by half from Johnson B to I. This is consistent with the temperature term (see section 3) dominating other pulsation terms. Watson's formula (Watson 1988) is applicable to this star, and was used by Koen *et al.* (1999) to determine $\ell = 2$ and $(R, \Psi_T) = (0.28, 187°)$ for the mode shown in these plots. Compare to the values of $(R, \Psi_T) = (0.01, 90°$ for HD 128898 obtained by Medupe, Christensen-Dalsgaard & Kurtz (1998) for $\ell = 1$.

Table 2.4: A Table of amplitudes for the February 1996 campaign on HR 3831. Notice the large σ values for the R and I amplitudes. These are largely due to the problems with the StAP photometer red tube. $\nu = 1.42801257\,\mathrm{mHz}$. The rotation phases were calculated using the ephemeris in equation (2.5). The pulsation phases were calculated with $t_0 = 2450000$.

Filter	λ	σ	**A(obs)**	**pulsation phase**	**rotation phase**
	$\mathring{A}$	mmag	mmag	radians	radians
U	3670	2.74	3.23 ± 0.22	-0.13 ± 0.068	0.58
B	4360	3.89	2.82 ± 0.33	$+0.45 \pm 0.13$	0.58
V	5450	3.91	2.21 ± 0.32	$+0.98 \pm 0.15$	0.58
R	6380	4.06	1.05 ± 0.33	$+1.26 \pm 0.31$	0.58
I	7970	4.23	0.58 ± 0.33	$+0.36 \pm 0.59$	0.58
U	3670	2.56	3.92 ± 0.20	-1.08 ± 0.05	0.93
B	4360	4.02	2.63 ± 0.32	-0.55 ± 0.12	0.93
V	5450	4.05	1.84 ± 0.32	-0.40 ± 0.18	0.93
R	6380	4.48	1.16 ± 0.36	-0.15 ± 0.32	0.93
I	7970	4.09	0.87 ± 0.33	-0.33 ± 0.38	0.93
u	3500	2.98	1.86 ± 0.26	0.60 ± 0.14	0.63
v	4110	2.84	2.66 ± 0.24	0.99 ± 0.09	0.63
b	4650	2.61	2.24 ± 0.22	1.75 ± 0.09	0.63
y	5500	2.58	1.81 ± 0.21	1.56 ± 0.12	0.63
R	6380	4.81	1.28 ± 0.40	1.30 ± 0.31	0.63
I	7970	4.76	0.49 ± 0.40	2.31 ± 0.81	0.63
u	3500	2.97	4.27 ± 0.23	-0.31 ± 0.05	0.98
v	4110	2.80	4.59 ± 0.22	$+0.08 \pm 0.05$	0.98
b	4650	2.60	2.96 ± 0.20	$+0.73 \pm 0.07$	0.98
y	5500	2.55	2.43 ± 0.20	$+0.89 \pm 0.08$	0.98
R	6380	4.50	1.13 ± 0.35	$+0.40 \pm 0.31$	0.98
I	7970	4.34	0.77 ± 0.34	$+1.02 \pm 0.44$	0.98
u	3500	2.56	0.88 ± 0.21	-1.26 ± 0.24	0.33
v	4110	2.36	1.69 ± 0.18	-0.03 ± 0.11	0.33
b	4650	2.15	1.03 ± 0.17	$+0.09 \pm 0.16$	0.33
y	5500	2.38	1.12 ± 0.19	$+0.17 \pm 0.16$	0.33
R	6380	3.48	0.99 ± 0.28	$+0.22 \pm 0.28$	0.33
I	7970	3.25	0.53 ± 0.27	-0.14 ± 0.50	0.33
u	3500	3.49	1.70 ± 0.48	-0.28 ± 0.29	0.38
v	4110	2.89	2.64 ± 0.40	$+0.29 \pm 0.15$	0.38
b	4650	3.03	1.72 ± 0.42	$+1.03 \pm 0.24$	0.38
y	5500	2.61	2.00 ± 0.37	$+1.06 \pm 0.18$	0.38
$\mathrm{H}\beta_{\mathrm{W}}$	4860	2.63	1.38 ± 0.37	$+1.24 \pm 0.26$	0.38
$\mathrm{H}\beta_{\mathrm{N}}$	4860	3.37	2.10 ± 0.43	$+0.85 \pm 0.22$	0.38

... continues from Table 2.4.

Filter	λ	σ	**A(obs)**	**rotation phase**	
	$\AA$	mmag	mmag	radians	radians
u	3500	3.10	0.45 ± 0.31	-3.08 ± 0.69	0.73
v	4110	2.87	0.41 ± 0.28	$+2.99 \pm 0.69$	0.73
b	4650	2.06	0.40 ± 0.20	$+3.08 \pm 0.52$	0.73
y	5500	2.04	0.34 ± 0.20	$+2.99 \pm 0.63$	0.73
$H\beta_W$	4860	2.23	0.36 ± 0.22	-2.97 ± 0.63	0.73
$H\beta_N$	4860	3.33	0.29 ± 0.34	$+2.45 \pm 1.15$	0.73
u	3500	2.73	3.11 ± 0.23	1.13 ± 0.07	0.09
v	4110	2.87	3.71 ± 0.24	1.60 ± 0.07	0.09
b	4650	2.29	2.58 ± 0.19	2.30 ± 0.07	0.09
y	5500	2.58	1.95 ± 0.22	2.60 ± 0.11	0.09
$H\beta_W$	4860	2.76	2.19 ± 0.22	2.47 ± 0.10	0.09
$H\beta_N$	4860	3.30	1.78 ± 0.28	2.40 ± 0.17	0.09
u	3500	4.18	2.04 ± 0.48	$+1.88 \pm 0.23$	0.14
v	4110	3.52	1.87 ± 0.39	$+2.10 \pm 0.21$	0.14
b	4650	3.44	0.81 ± 0.39	-2.37 ± 0.48	0.14
y	5500	3.24	1.25 ± 0.35	-2.95 ± 0.29	0.14
$H\beta_W$	4860	3.06	0.88 ± 0.34	-3.06 ± 0.39	0.14
$H\beta_N$	4860	4.10	0.89 ± 0.49	-1.85 ± 0.54	0.14

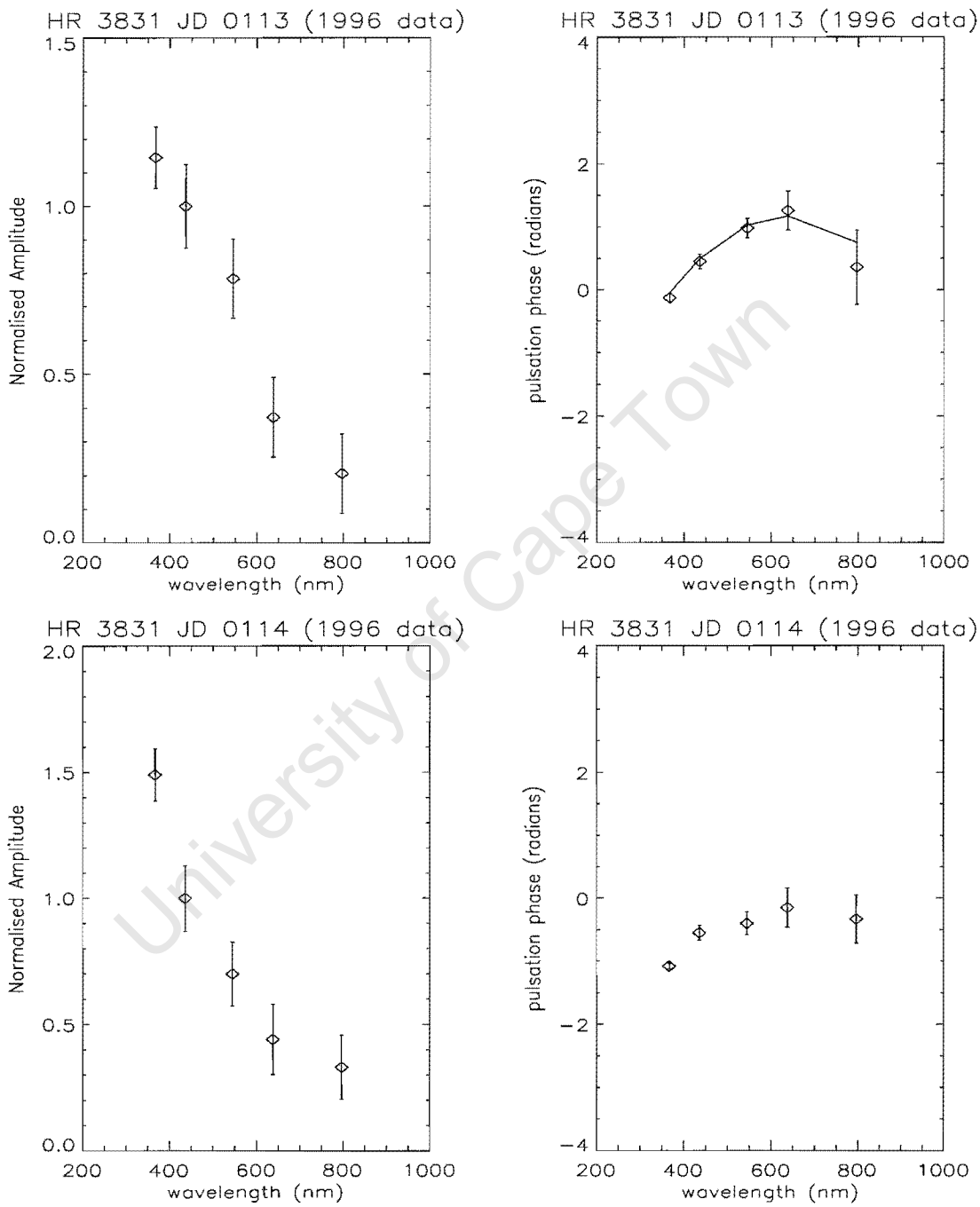

Figure 2.6: The Johnson U B V R and I data for HR 3831 at rotation phases 0.58 (the top panel), and 0.93 (the bottom panel). The data were obtained in 1996.

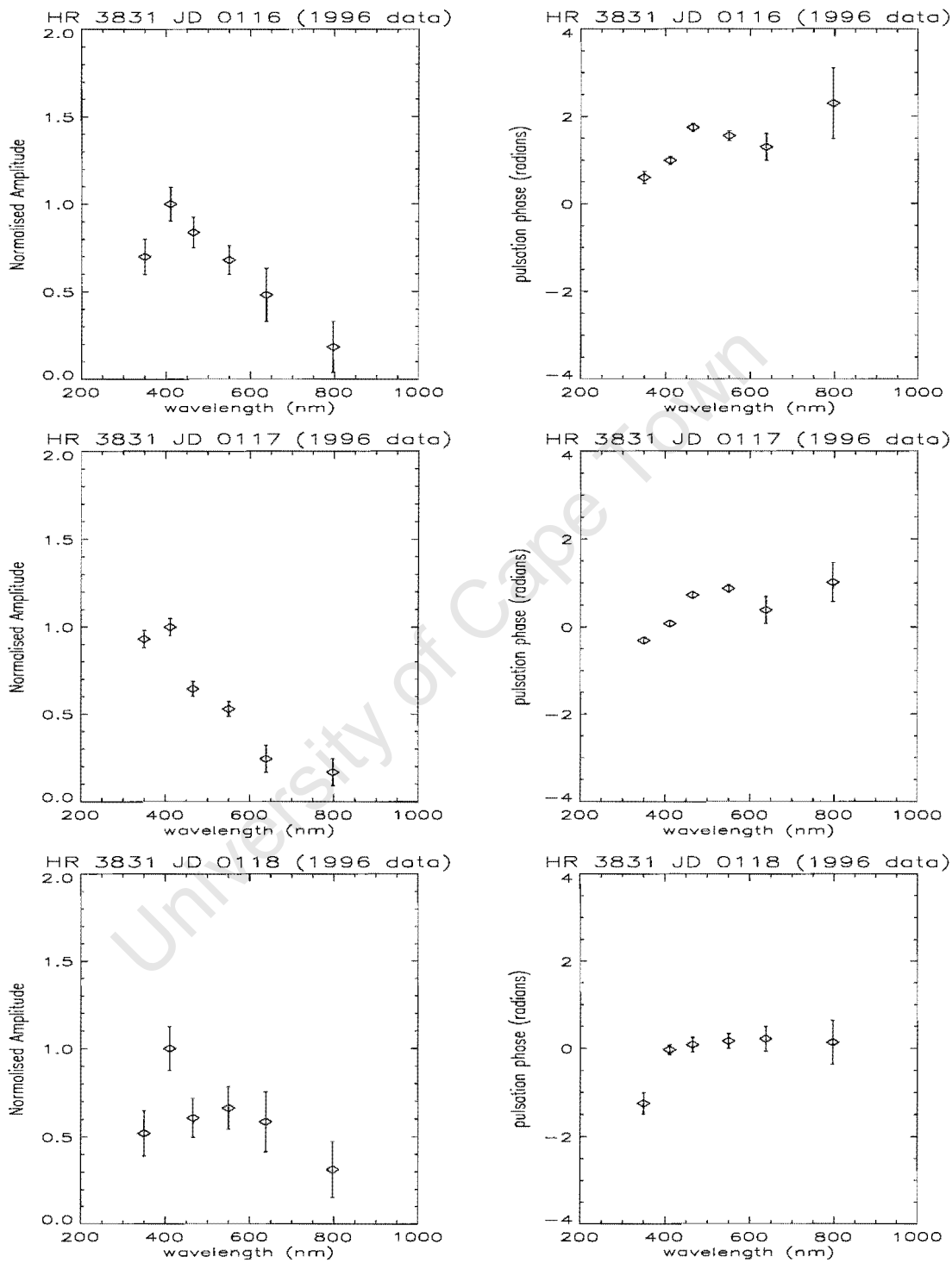

Figure 2.7: The Strömgren $u\ v\ b\ y$ and Johnson $R\ I$ data for HR 3831 at rotation phases 0.63, 0.98, and 0.33 (top to bottom panels), obtained in 1996.

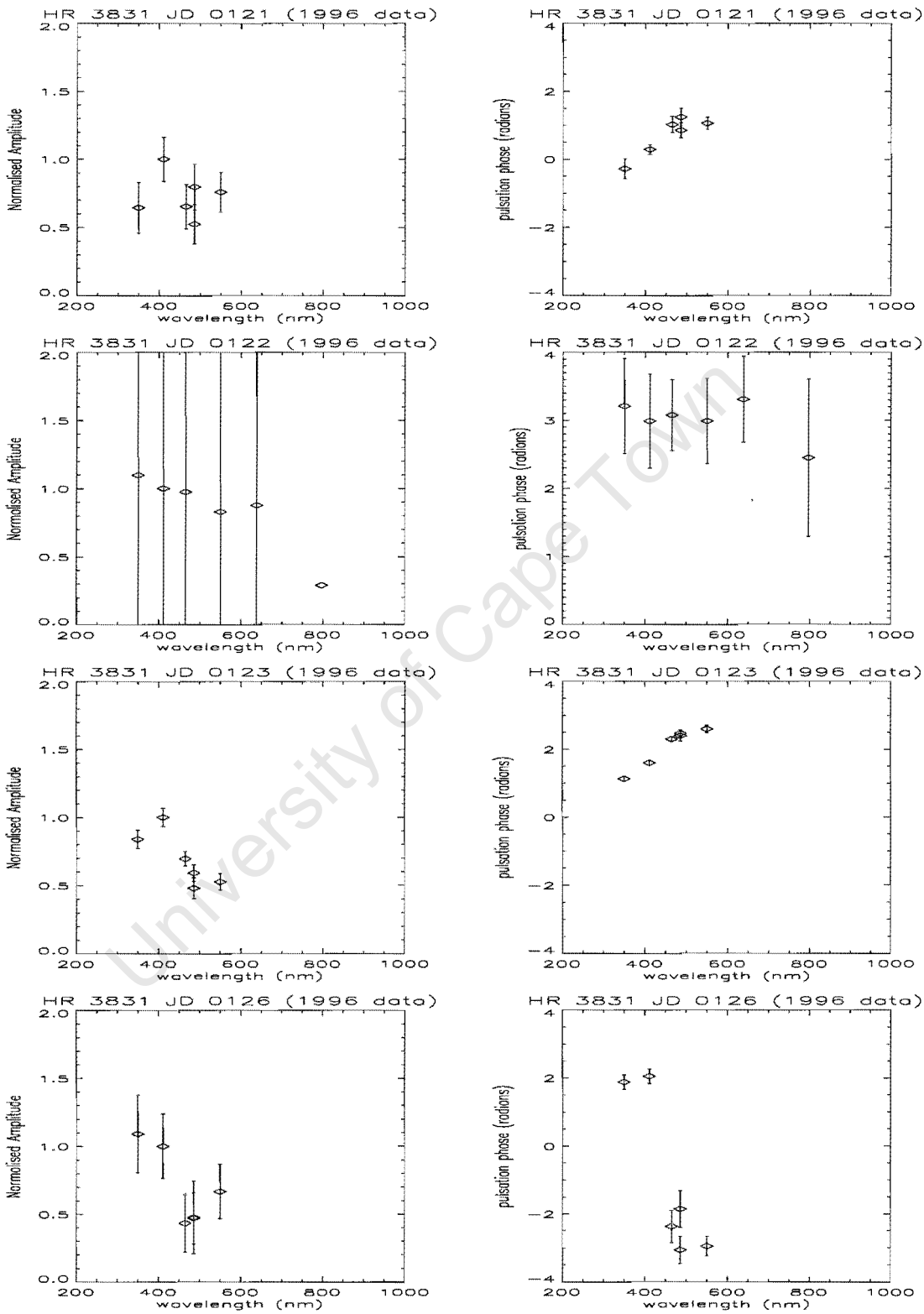

Figure 2.8: The Strömgren $uvby, H_\beta$ wide and narrow data for HR 3831 at rotation phases 0.38, 0.73, 0.08 and 0.14 (top to bottom), obtained in 1996.

Africa Astronomical Observatory 0.5-metre telescope. Only the Johnson U B V R and I data were used this time.

2.1.2 Data discussion

Amplitudes and phases

It is clear from the last section that the normalised photometric amplitudes of HD 101065, HD 128898, HD 137949, and HD 134214 uniformly decrease more steeply with wavelength than theoretically expected, and the pulsation phase *vs* wavelength curves differ greatly from one star to the next. HD 101065 shows a large increase of about 63° in phase from Johnson U to V. HD 128898 shows no phase variation with wavelength at one sigma level. HD 137949 seem to show a decrease from Johnson U to V, followed by an increase to Johnson U, the errors in phases are large though. This star could benefit from another observing run. In HD 134214 we see an increase in pulsation phase from Johnson U to V, followed by a decrease to I. However, here also the large error bars make it difficult to conclude on the shape of the curve. HR 3831 shows the same trend as HD 134214 more clearly with smaller errors, hence I am inclined to believe that HD 134214 shows a trend in phase *vs* wavelength. HR 3831 shows the largest phase changes with wavelength of about 80°.

Changes with rotation: HR 3831

Visual inspection

In this section, we try to see if the phase *vs* wavelength curves change as HR 3831 rotates. We do this first by visual representation of the data, then we apply a more rigorous statistical method.

For the 1996 data we compare the Johnson U, B, V, R and I data obtained during rotation phases 0.58 and 0.93 separately, the u, v, b, y, R, I data for the rotation phases 0.98 and 0.33 are also compared separately. These are displayed in Fig. 2.12.

In Figs 2.13 and 2.14 we compare the 1998 data for rotation phase 0.09 with those of other phases listed in Table 2.5. The pulsation phases are also a function of rotation phase (as explained by the oblique pulsator model), so for each data set corresponding to a different rotation phase we determined the difference between its Johnson B phase and that for the template data. This difference is then added to phases in U, V, R and I filters (of the same data set). This retains the shape of the phase *vs* wavelength curve. Visual inspection reveals no change in the B, V, R and I amplitudes with rotation. However, the U amplitudes and phases show clear variations with rotation.

Statistical Analysis

Here we try to investigate whether there are any significant night-to-night variations in the amplitude and phase *vs* wavelength curves. The hypothesis to be tested is:

Table 2.5: A table of amplitudes for the February 1998 campaign on HR 3831. The pulsation frequency of HR 3831 is $\nu = 1.42801257$ mHz. The rotation phases were calculated using the ephemeris given in equation (2.5). The pulsation phases where calculated with $t_0 = 2450000$. The observers were Yolanda van Niekerk & R. Medupe.

Filter	λ	σ	**A(obs)**	**pulsation phase**	**rotation phase**
	$\AA$	mmag	mmag	radians	radians
U	3670	3.18	0.32 ± 0.26	1.63 ± 0.79	0.74
B	4360	2.70	0.59 ± 0.21	1.04 ± 0.37	0.74
V	5450	2.60	0.35 ± 0.21	0.66 ± 0.59	0.74
R	6380	2.83	0.31 ± 0.33	1.26 ± 0.31	0.74
I	7970	3.00	0.36 ± 0.33	0.36 ± 0.59	0.74
U	3670	5.60	4.68 ± 0.39	$+3.05 \pm 0.08$	0.09
B	4360	4.94	3.98 ± 0.35	-2.71 ± 0.09	0.09
V	5450	3.59	2.10 ± 0.29	-2.09 ± 0.14	0.09
R	6380	2.91	1.57 ± 0.24	-2.19 ± 0.15	0.09
I	7970	3.34	1.19 ± 0.31	-2.71 ± 0.26	0.09
U	3670	5.13	3.92 ± 0.42	0.60 ± 0.14	0.44
B	4360	4.82	3.09 ± 0.40	0.99 ± 0.09	0.44
V	5450	4.93	2.76 ± 0.42	1.75 ± 0.09	0.44
R	6380	4.57	1.77 ± 0.41	1.30 ± 0.31	0.44
I	7970	4.76	1.46 ± 0.38	2.31 ± 0.81	0.44
U	3670	4.11	0.77 ± 0.31	-2.77 ± 0.41	0.79
B	4360	3.51	0.36 ± 0.28	-0.81 ± 0.76	0.79
V	5450	3.03	0.39 ± 0.24	-2.37 ± 0.62	0.79
R	6380	2.68	0.31 ± 0.23	-2.66 ± 0.73	0.79
I	7970	2.82	0.24 ± 0.24	-1.71 ± 0.94	0.79
U	3670	3.39	3.12 ± 0.25	$+2.84 \pm 0.08$	0.14
B	4360	2.96	2.06 ± 0.22	-2.77 ± 0.11	0.14
V	5450	2.27	0.91 ± 0.18	-1.99 ± 0.19	0.14
R	6380	2.13	0.32 ± 0.17	-2.93 ± 0.53	0.14
I	7970	0.29	0.53 ± 0.16	-2.40 ± 0.54	0.14
U	3670	5.54	4.29 ± 0.40	0.46 ± 0.09	0.49
B	4360	5.17	4.48 ± 0.37	1.06 ± 0.08	0.49
V	5450	4.16	2.51 ± 0.31	1.47 ± 0.12	0.49
R	6380	4.67	2.35 ± 0.34	1.34 ± 0.15	0.49
I	797	4.45	1.04 ± 0.35	1.18 ± 0.34	0.49

... continues from Table 2.5.

Filter	λ	σ	**A(obs)**	**pulsation phase**	**rotation phase**
	Å	mmag	mmag	radians	radians
U	3670	3.72	2.53 ± 0.38	-2.72 ± 0.15	0.84
B	4360	2.67	2.38 ± 0.28	-2.16 ± 0.12	0.84
V	5450	2.75	1.14 ± 0.29	-1.14 ± 0.26	0.84
R	6380	2.88	1.31 ± 0.29	-1.69 ± 0.23	0.84
I	7970	2.23	0.99 ± 0.33	-2.11 ± 0.33	0.84
U	3670	4.82	3.93 ± 0.36	-3.04 ± 0.09	0.89
B	4360	4.40	2.42 ± 0.33	-2.49 ± 0.14	0.89
V	5450	4.25	2.10 ± 0.32	-2.41 ± 0.15	0.89
R	6380	4.39	1.08 ± 0.33	-2.33 ± 0.30	0.89
I	7970	4.16	0.44 ± 0.29	-1.56 ± 0.68	0.89
U	3670	3.09	0.58 ± 0.31	$+1.87 \pm 0.53$	0.24
B	4360	2.92	0.42 ± 0.23	$+2.95 \pm 0.54$	0.24
V	5450	2.68	0.31 ± 0.22	-1.37 ± 0.70	0.24
R	6380	2.67	0.28 ± 0.20	-1.76 ± 0.71	0.24
I	7970	2.67	0.23 ± 0.20	-0.89 ± 0.88	0.24

- H_0: No night-to-night variation in pulsation phase ϕ_λ.
- H_1: There is night-to-night variation in pulsation phase ϕ_λ.

Under the null hypothesis we fit a model of the form:

$$y_{i,j} = \mu + \alpha_i + \beta_j + \epsilon_{i,j}, \tag{2.6}$$

where i is the wavelength subscript, j is denotes each night, $y_{i,j}$ is a fit to a data point, μ is the mean of $y_{i,j}$ estimated as:

$$\tilde{\mu} = \frac{1}{N\,M} \sum_{ij} y_{ij}, \tag{2.7}$$

where N is the total number of wavelength points and M the number of nights considered. The model parameters α_i represent the variation in wavelength and has the property:

$$\sum_{i=1}^{N} \alpha_i = 0, \tag{2.8}$$

and β_j represents the night to night variation and has the property:

$$\sum_{j=1}^{M} \beta_j = 0. \tag{2.9}$$

Therefore it can be shown that an estimate to α_i is:

$$\hat{\alpha_i} = \frac{1}{M}\sum_{j=1}^{M} y_{ij} - \tilde{\mu} \tag{2.10}$$

and an estimate to β_j is given as:

$$\hat{\beta_j} = \frac{1}{N}\sum_{i=1}^{N} y_{ij} - \tilde{\mu}. \tag{2.11}$$

The ϵ_{ij} in equation (2.6) is the error in the fit and is assumed to be Gaussian distributed with zero mean. It is estimated from:

$$\epsilon_{i,j} = y_{i,j} - \hat{\mu}. \tag{2.12}$$

For an alternative hypothesis we introduce the interaction term θ_{ij} to equation (2.6). The interaction term indicates that λ and ϕ_{rot} are not independent, *i.e.* $\phi = \phi(\lambda, \phi_{rot})$. Therefore, under H_1,

$$y_{i,j} = \mu + \alpha_i + \beta_j + \theta_{ij} + \epsilon_{i,j}. \tag{2.13}$$

Comparing equations (2.6) and (2.13), the hypothesis can be written in the concise form:

- H_0: $\theta = 0$.
- H_1: $\theta \neq 0$.

The test procedure consists of fitting eqn (2.6) to the data, and evaluating the fit. If eqn (2.6) fits well, we accept H_0; otherwise we reject it in favour of H_1. If σ_{ij} is the error in the data point y_{ij}, then $\frac{\epsilon_{ij}}{\sigma_{ij}}$ is also Gaussian distributed with zero mean and standard deviation equal 1. Therefore:

$$\Gamma = \sum_{ij}\left(\frac{\epsilon_{i,j}}{\sigma_{ij}}\right)^2 \sim \chi^2_{(N-1),(M-1)} \tag{2.14}$$

is distributed like χ^2 with the degree of freedom of $(M-1)(N-1)$. The value of the Γ thus obtained is checked against the table of percentage points of a chi-squared distribution to look for the probability that there are significant night-to-night changes. The table of percentage points give the probablity p that χ^2 is less than the measured value for a given degree of freedom. It really is the area under the χ^2 probability density function. The significance level is given by $100 \times (1-p)$ such that the smaller the $100 \times (1-p)$ the stronger is the evidence against the null hypothesis.

Fits of equation (2.6) to the 1998 pulsation phase data alone were done and are shown in Fig. (2.15). The fits to the amplitude data alone are shown in Fig. (2.16). The model (2.6) fits both amplitudes and phases quite well. The data sets corresponding to amplitude minimum were discarded since their pulsation phases are ill-defined. We obtain $\Gamma = 27.7$

Table 2.6: A table of Γ and its percentage points determined for the amplitude and phase data with degrees of freedom equal to 24.

observable	Γ	**Percentage**	**Significance level**
ϕ	27.7	0.73	27 %
ϕ^*	26.1	0.652	35 %
Δm	41.7	0.986	1.4 %
Δm^*	16.9	0.147	85 %

Notes:
* These are calculated with U data excluded.

in the phase data, and 41.7 for the normalised amplitude data. The standard error for the amplitude data is much larger than that for the phases, even though the amplitudes are generally better determined.

Since visual inspection suggest significant variation of the U amplitude with rotation, we calculated Γ with the Johnson U amplitude excluded from the data set. We obtained $\Gamma = 26.1$ for the phase data and $\Gamma = 16.9$ for the amplitude data with U excluded from the data set. Thus it appears that the U amplitude contributes a lot to the larger value of Γ. The Γ values and their corresponding percentage points are shown in Table 2.6. The conclusions we draw from this Table 2.6 are:

1. No significant night-to-night variation in $BVRI$ amplitude *vs* wavelength were detected. However, there is significant variations in U/B amplitudes with rotation.

2. No significant night-to-night variation in the pulsation phase *vs* wavelength were observed in the HR 3831 data.

However, a plot of the U amplitude compared with B amplitude at various rotation phases in Fig. 2.17 shows no significant variation of U amplitudes compared to the B amplitude except possibly at rotation phases 0.14 and 0.89. Note thatas expected from other HR 3831 measurements (see Kurtz *et al.* 1997) the size of the phase errors is inversely proportional to the size of the pulsation amplitude, *ie.* the small the errors in the pulsation phase correspond to theamplitude maximum.

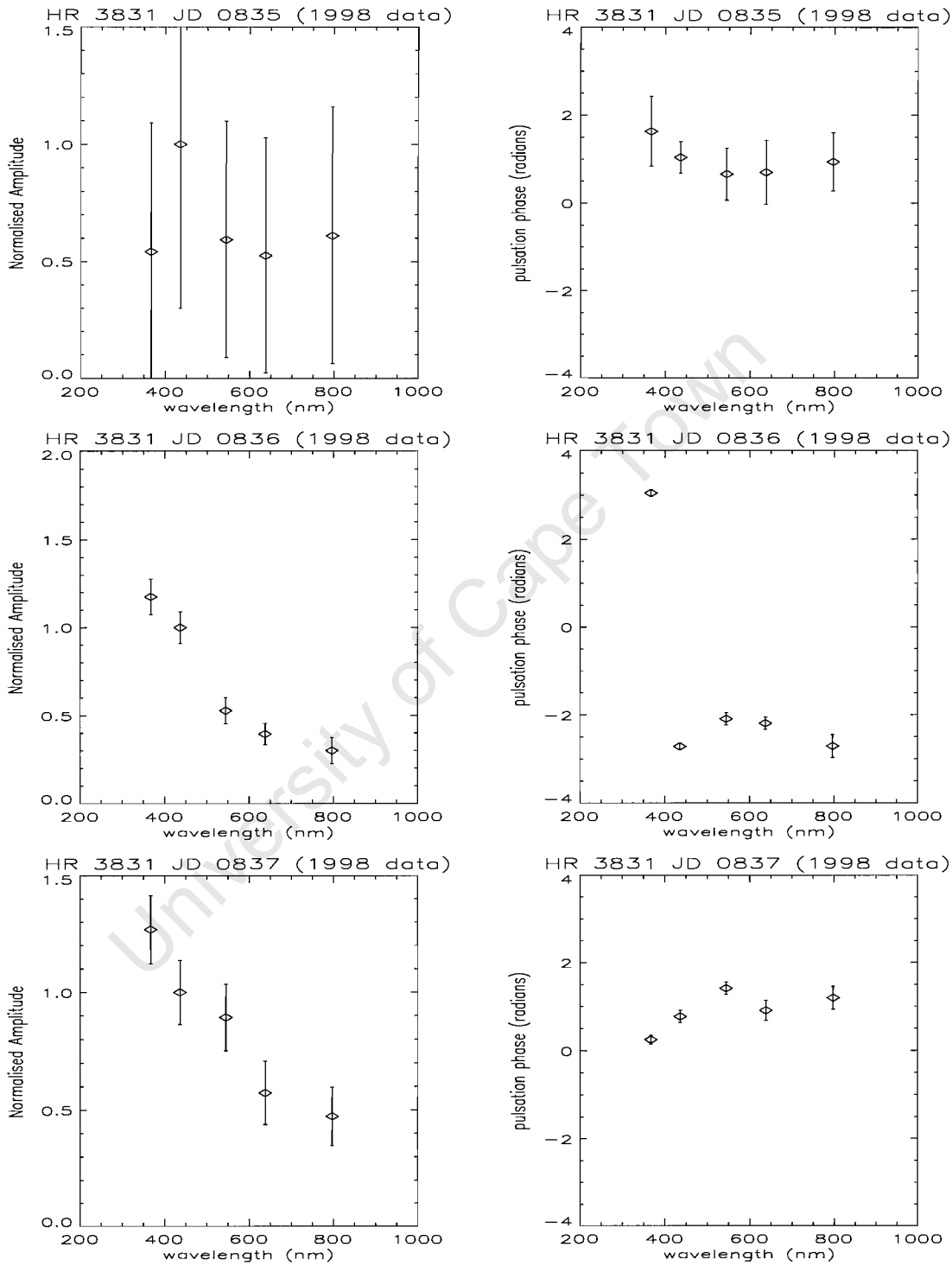

Figure 2.9: The Johnson U, B, V, R and I data for HR 3831 at rotation phase 0.74, 0.09 and 0.44 (from top to bottom) obtained in 1998.

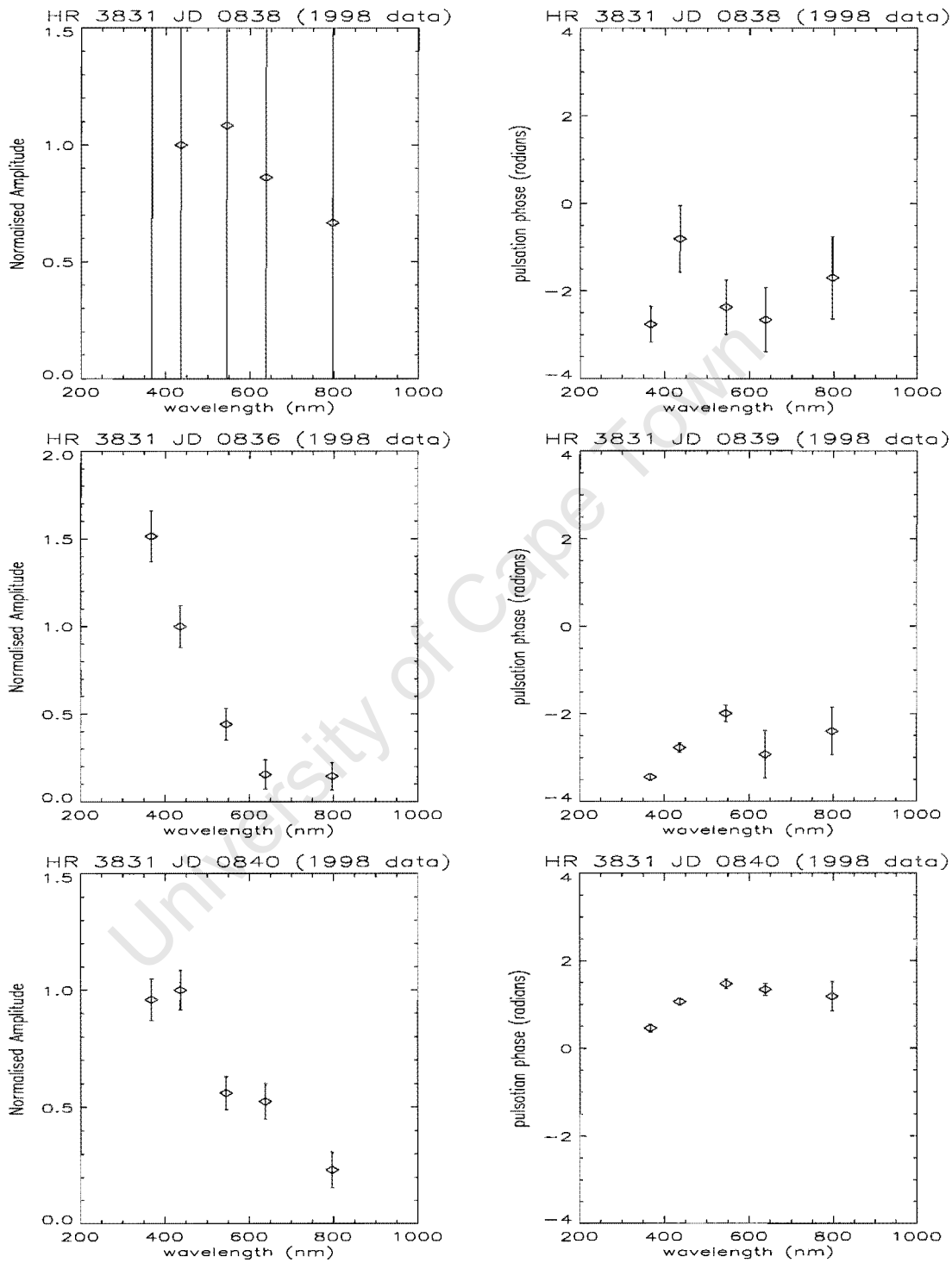

Figure 2.10: The Johnson U, B, V, R and I data for HR 3831 at rotation phase 0.79, 0.14 and 0.49.

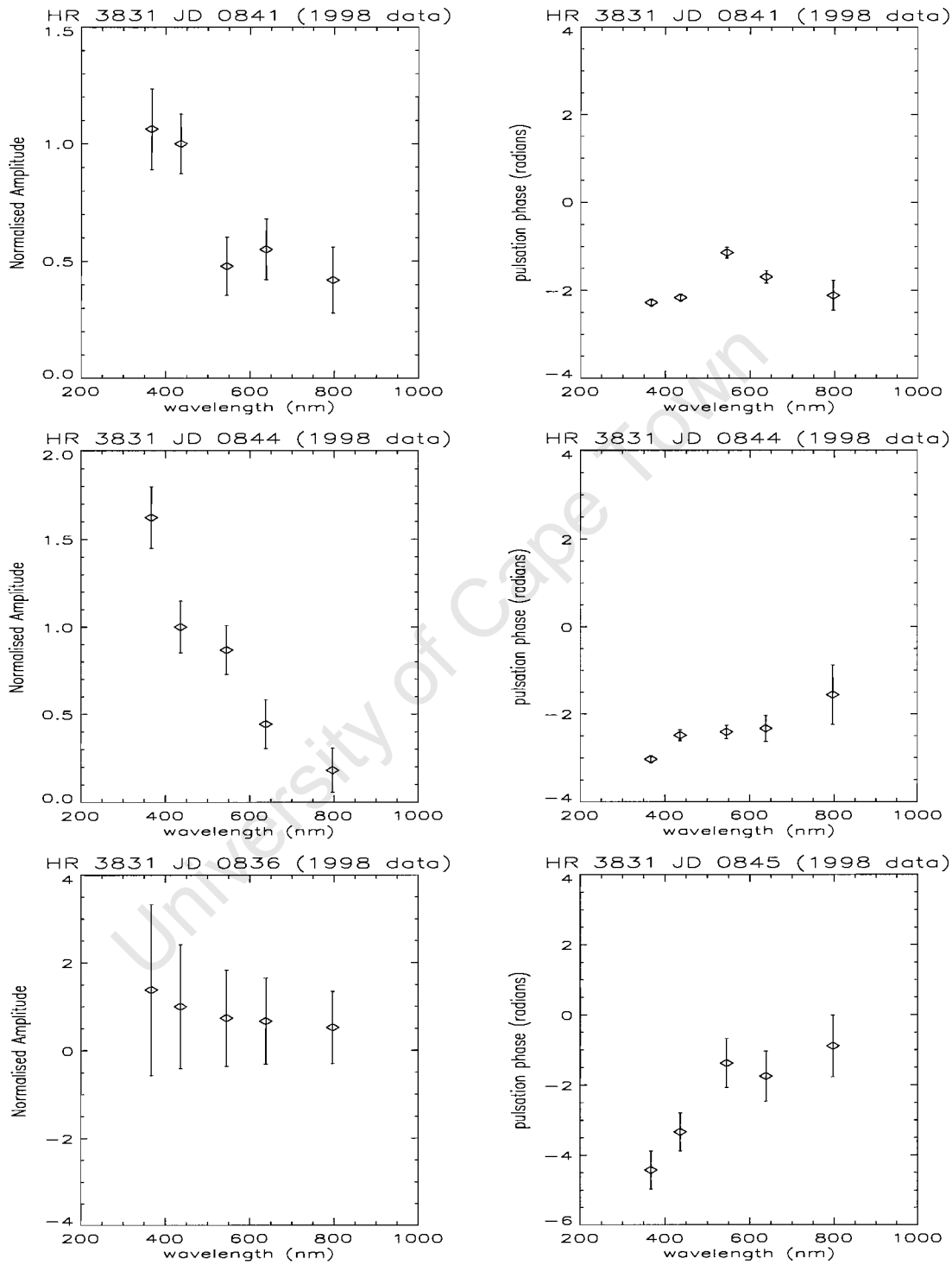

Figure 2.11: The Johnson U, B, V, R and I data for HR 3831 at rotation phases 0.84, 0.89 and 0.24 (top to bottom).

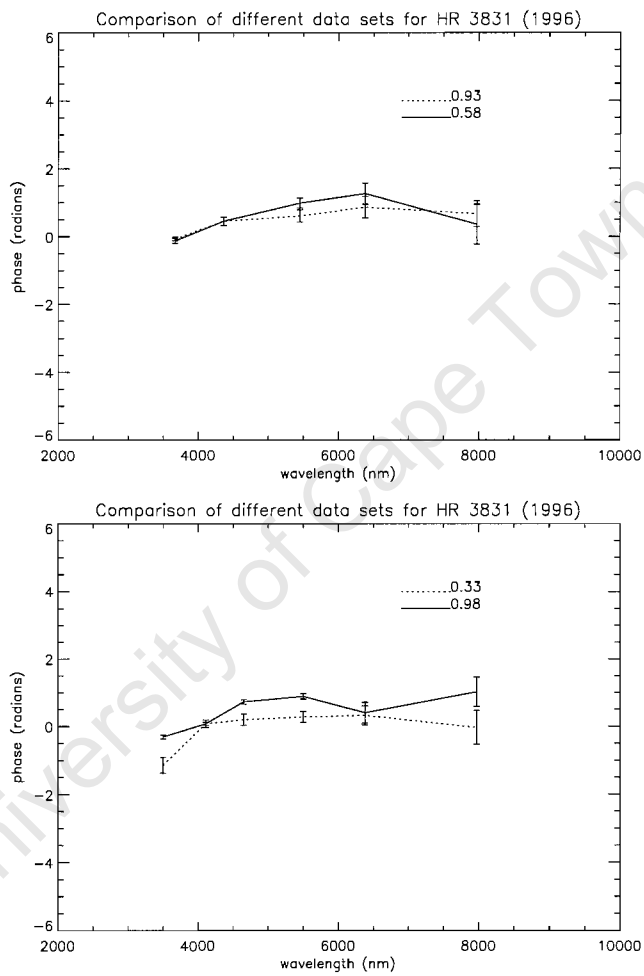

Figure 2.12: Comparisons of the variation of pulsation phase with wavelength at rotation phases 0.58 with that at phase 0.93 in the Johnson system (top panel). The Strömgren u, v, b, y and R and I data are shown in the bottom panel where rotation phases 0.98 and 0.33 are compared.

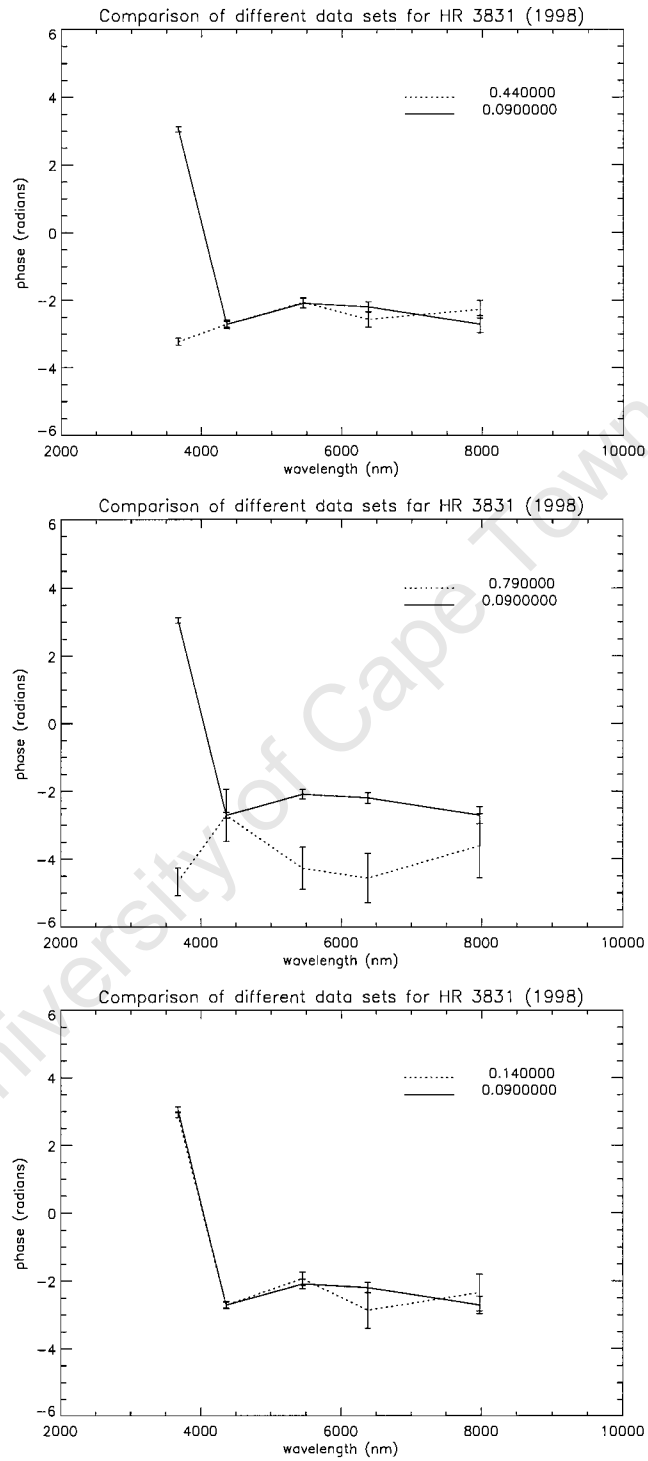

Figure 2.13: Comparisons of the variation of pulsation phase with wavelength at rotation phases 0.44, 0.79, 0.14 with that at phase 0.09. This is the Johnson U, B, V, R and I data for HR 3831.

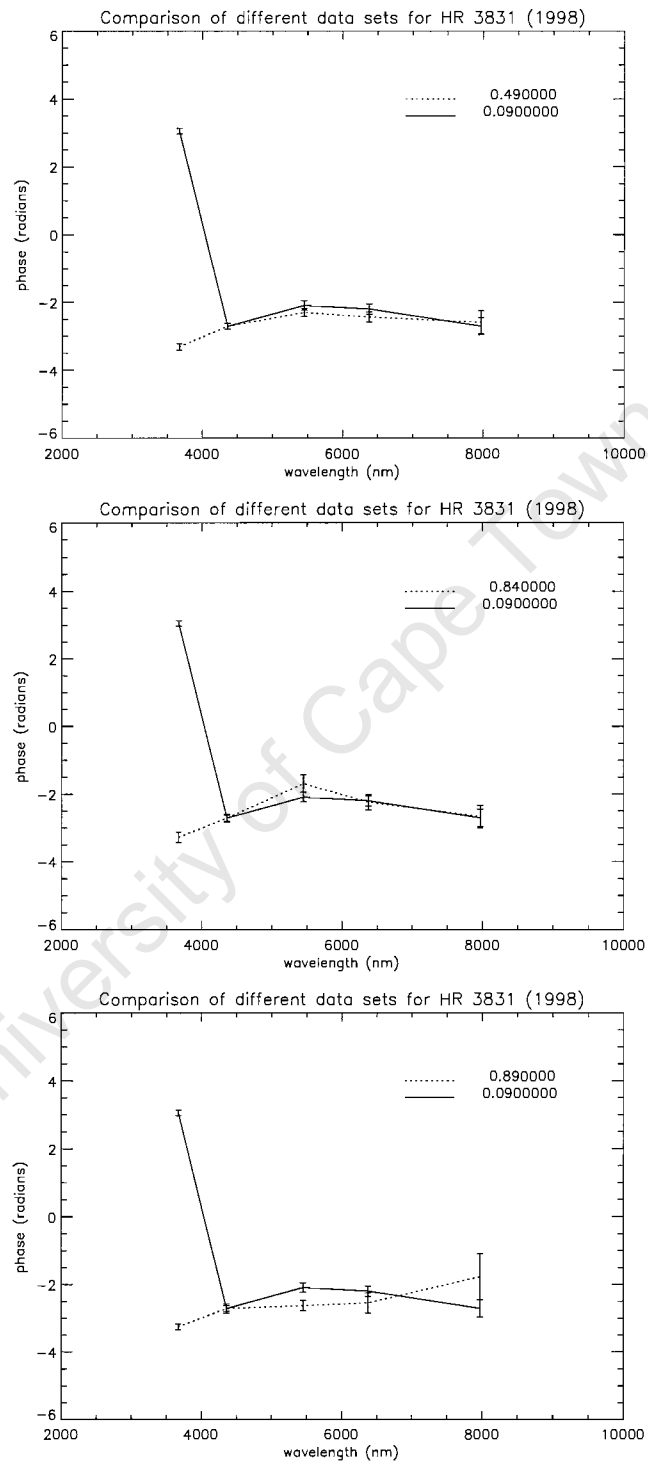

Figure 2.14: Comparisons of the variation of pulsation phase with wavelength at rotation phases 0.49, 0.84 and 0.89 with that at phase 0.09. This is the Johnson U, B, V, R and I data for HR 3831.

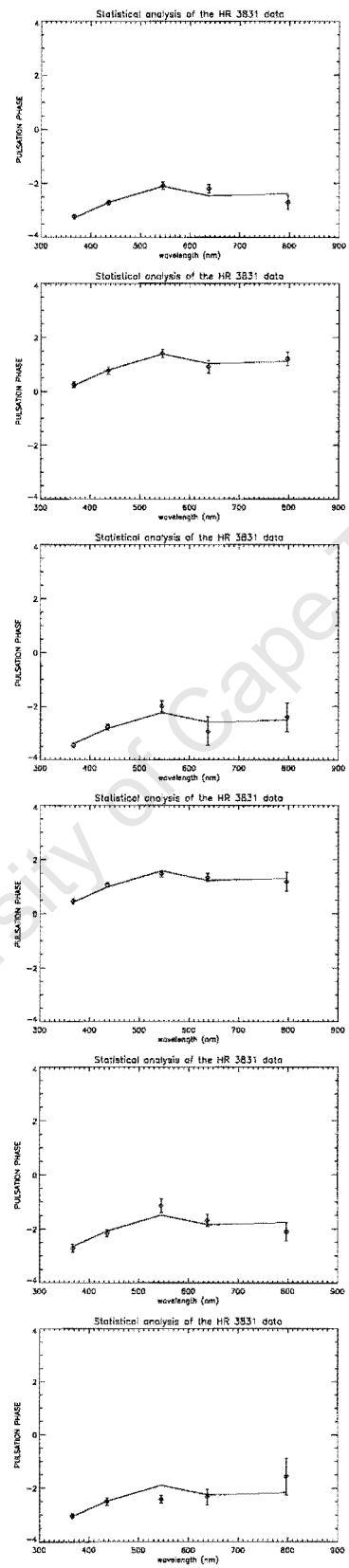

Figure 2.15: A fit to the statistical model (2.6) to the 1998 phase data for rotation phases 0.09, 0.44, 0.14, 0.49, 0.84 and 0.89. All the data obtained when the pulsation axis was at quadrature were excluded during the analysis since they are not well determined.

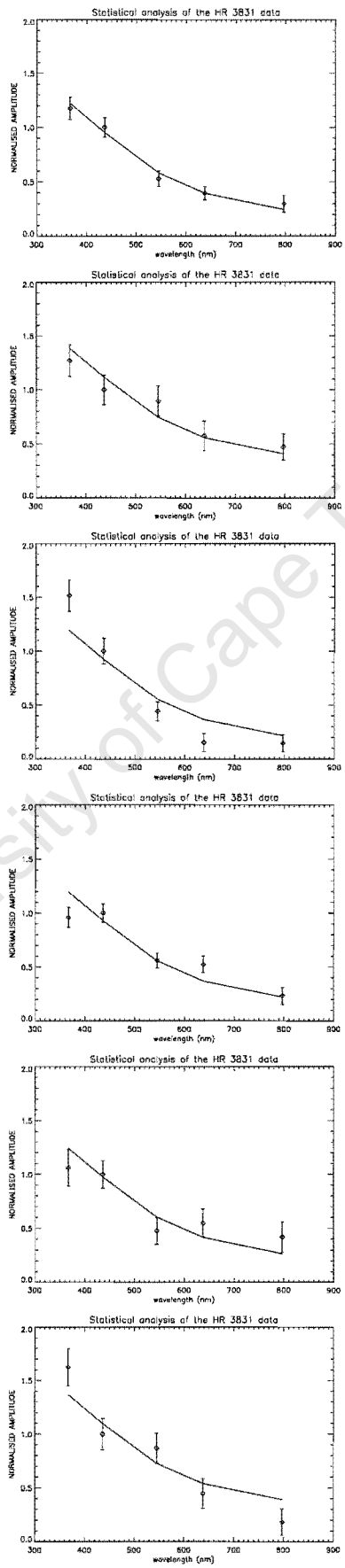

Figure 2.16: A fit to the statistical model (2.6) to the 1998 amplitude data for rotation phases 0.09, 0.44, 0.14, 0.49, 0.84 and 0.89.

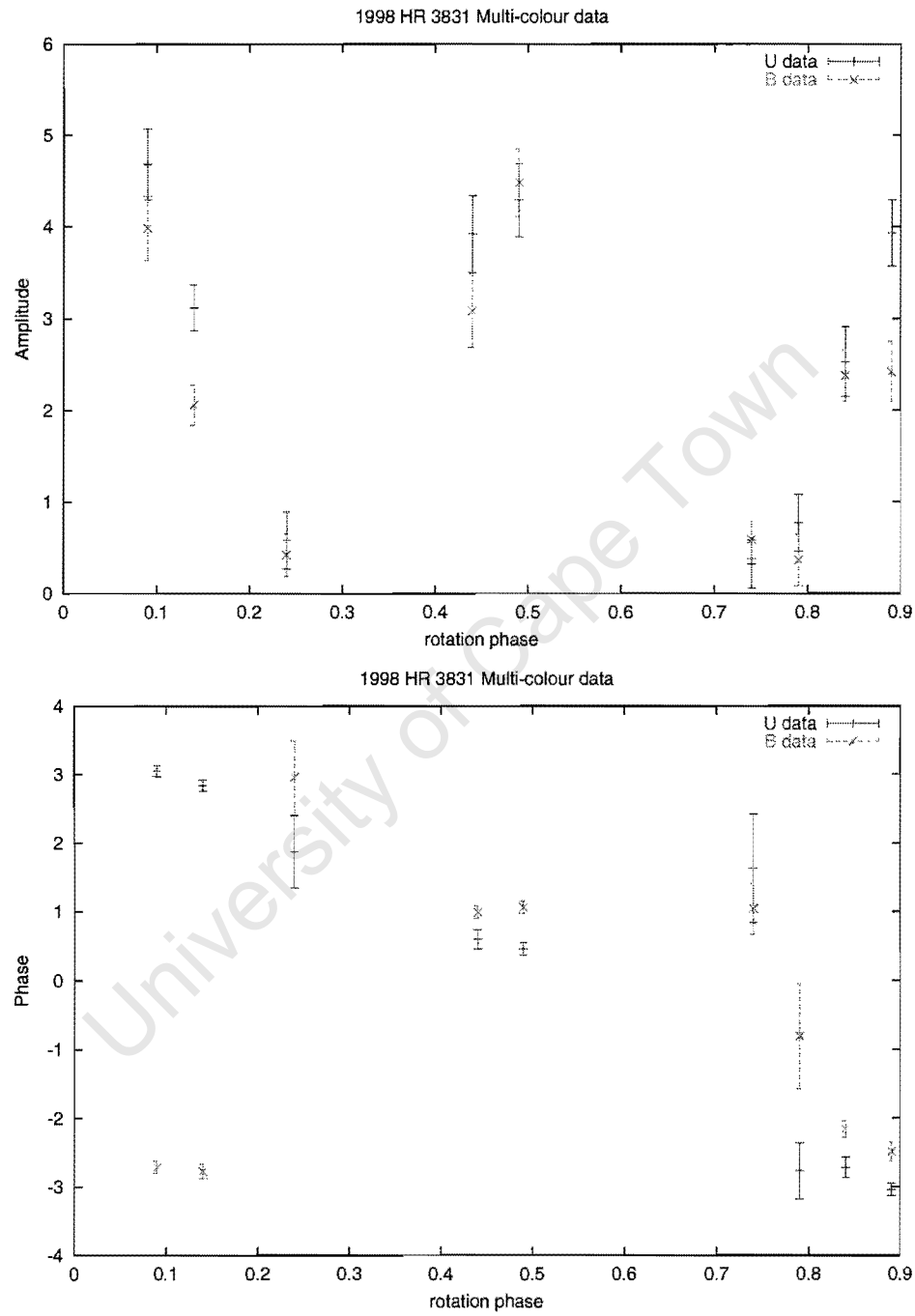

Figure 2.17: The top panel shows the variation of the Johnson U amplitude with rotation compared to the Johnson B. The bottom panel shows the variation of pulsation phase with rotation in the U and the B. Notice the inverse relation between the size of the phase error bar and that of the amplitude.

Chapter 3

Watson's formula

3.1 Introduction

In this section I will present key developments that led to Watson's formula. Dziembowski (1977) was the first to derive an expression to describe the variation of non-radial pulsation amplitude as a star pulsates. His formula could not be easily compared with data because it was in bolometric magnitude. It included the geometry effects (*i.e.* local surface normal and area variations) and surface brightness variations due to the effective temperature variations only, *i.e.*

$$\Delta m_\lambda = \Delta S_\lambda - 1.086 \frac{\Delta A}{A_0}, \tag{3.1}$$

where ΔS_λ is the variation in surface brightness due to pulsations, and $\frac{\Delta A}{A_0}$ is the geometric variation.

In order to compare Dziembowski's formula with data, Balona & Stobie (1979) assumed a linear relation between perturbed surface brightness ΔS_λ and some colour index $\Delta (m_{\lambda_1} - m_{\lambda_2})$. They thus obtained ΔS_λ from colour indices and could determine the degree ℓ, from photometric and radial velocity data and the knowledge of the radius of the star under study.

Buta & Smith (1979) calculated ΔS_λ theoretically by assuming that the intensity is distributed in wavelength like a black-body. Their $\frac{\Delta A}{A_0}$ is similar to Dziembowski's. So their formula was purely theoretical (like Dziembowski's), but it could be applied to observed data as they demonstrated with 53 Per data.

Stamford & Watson (1980) showed that the assumption of a single-valued relation between surface brightness changes and colour variations does not apply for $\ell > 1$. They also improved on the formalism of Dziembowski (1977) and Buta & Smith (1979) by noting that stellar flux is defined by effective temperature ($T_{\rm eff}$) and surface gravity ($\log g$). Therefore, in

their formula, ΔS_λ included perturbations in $T_{\rm eff}$ and log g. They coined the term pressure effect for surface pressure variations due to perturbations in log g. Another improvement they introduced is that the flux derivatives in ΔS_λ, and limb-darkening were calculated from model atmospheres. Since limb-darkening is derived from intensity, it follows that it, also is a function of $T_{\rm eff}$ and log g. Watson (1988) included these last two effects in a formula which is a subject of this chapter. Heynderickx, Waelkens & Smeyers (1994) included the effects of the non-radial components of the Lagrangian displacement on the local surface element in addition to all of the above effects. They then applied their formula (which is very similar to Watson's) to multi-colour photometric data of β Cephei stars to determine their ℓ values with some measure of success.

In this section the formula as presented by Watson (1988) is introduced, we then show how attempts to apply it to roAp stars fail. In order to improve on the formula so that in the future it can be made to work for roAp stars, we show how it is derived, then suggest improvements.

Watson (1988) presented the following formula for describing the dependence of the magnitude of a pulsating star on wavelength and pulsation parameters:

$$m(\lambda,t) = -1.086\epsilon Y_\ell^m(\theta_o,\phi_o)\{(T_1+T_2)\exp(i(\omega t+\Psi_T))+(T_3+T_4+T_5)\exp(i\omega t)\} \quad (3.2)$$

where $\epsilon \ll 1$ is an amplitude parameter and θ_o and ϕ_o are the inclination angles of the pulsation axis with respect to the observer. The terms $T_i\,(i=1,..5)$ are explained in Table 3.1, and the equation (3.2) is derived in the next section. The function P_ℓ is the Legendre polynomial of degree ℓ. A measure of the variation in the atmospheric gas pressure as surface gravity varies is given by $p^* = \left(\frac{\partial \log g}{\partial \log P_s}\right)_{\tau=1}$.

Table 3.1: Explanation of the terms in equation (3.2)

Term	Explicit Form	Description
T_1	$b_{\ell\lambda}\frac{\partial \log F_\lambda}{\partial \log T_{\rm eff}}B$	This is the temperature term for limb–darkening law $h_\lambda(\mu)$, $b_{\ell\lambda} = \int_0^1 h_\lambda \mu P_\ell d\mu$.
T_2	$\frac{\partial b_{\ell\lambda}}{\partial \log T_{\rm eff}}\frac{B}{2.3026}$	This accounts for limb- darkening variations due to surface temperature variations.
T_3	$b_{\ell\lambda}(2+\ell)(1-\ell)$	This term accounts for the variations in the actual geometry of the star. It includes surface normal variations and the projected surface area variations.
T_4	$-b_{\ell\lambda}p^*C\frac{\partial \log F_\lambda}{\partial \log g}$	This is the pressure term. $C = C(\ell,\sigma)$, σ is dimensionless frequency.
T_5	$-\frac{\partial b_{\ell\lambda}}{\partial \log g}\frac{p^*C}{2.3026}$	This term accounts for limb–darkening variations due surface gravity variations.

3.2 Applications and limitations

The five terms in Watson's formula are obtained from a model atmosphere grid covering given temperature and log g ranges. I used the ATLAS9 model atmosphere program (Kurucz 1993) to create such a grid with temperature and log g ranges of $(7000\,K, 8000\,K)$ and $(3, 5)$ respectively. The results for model atmospheres that represent α Cir abundances (Kupka *et al.* 1996) are shown in the following tables. The opacity distribution function specific to α Cir was kindly provided by Fritz Kupka of Vienna. Flux derivatives and weighted limb darkening functions based on model atmospheres for the α Cir–type stars are shown in Tables C.1, C.2 and D.1. A quadratic limb– darkening law with coefficients calculated as suggested by Wade & Rucinski (1985) was used to compute $b_{\ell\lambda}$. The $b_{\ell\lambda}$ for $\ell = 0$ are not tabulated since they are all unity ($b_{\ell=0\,\lambda} = 1.0$) in all colours. The monochromatic quantities were convolved with the filter response functions for the SAAO Modular Photometer and St Andrews Photometer (StAP) photometers shown in Fig 3.1.

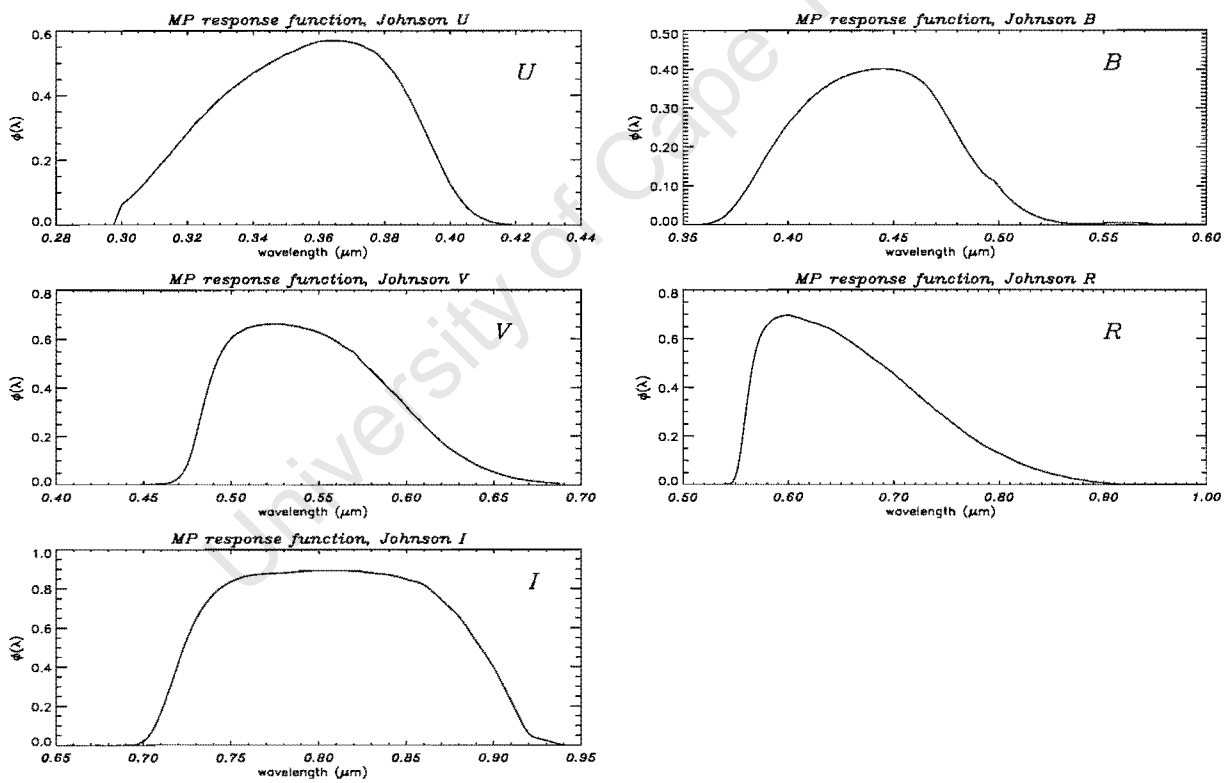

Figure 3.1: The Johnson filter response functions that were used to calculate flux derivatives and limb-darkening integrals in this chapter.

3.2.1 Determination of B

In order to determine the ratio of relative temperature to radius perturbations ($B = \frac{\delta T}{T}/\frac{\delta r(R)}{R}$), a relation between $\frac{\delta T}{T}$ and $\frac{\delta r(R)}{R}$ needs to be established. In the adiabatic case, the energy equation is

$$\frac{\delta T}{T} = \nabla_{ad}\frac{\delta P}{P} \tag{3.3}$$

The origin of this equation becomes clear in section (4.2). Dziembowski (1971) relates the non- radial pressure perturbation to radius perturbation at the stellar surface in the following way:

$$\frac{\delta P}{P} = C(\ell,\sigma)\,\frac{\delta r(R)}{R}\,\text{at the surface,} \tag{3.4}$$

where the perturbed gravitational potential is neglected, and C depends on ℓ and dimensionless frequency (σ) in the following way:

$$C(\ell,\sigma) = \frac{\ell\,(\ell+1)}{\sigma^2} - 4 - \sigma^2. \tag{3.5}$$

The meaning of C is explained in Buta & Smith (1979). It gives us a measure of whether the radial or the horizontal component of the oscillations dominates. It is clear that for pure radial oscillations C is negative, implying that pressure variations always act in opposition to the radius variations. Hence a star pulsating in pure radial mode is compressed at minimum radius, and rarefied at maximum radial perturbations. A situation for non-radial pulsator is different because here C can have a positive (horizontal motions dominate), zero, or negative sign where the radial motions dominate the horizontal ones.

Therefore adiabatic oscillations near the surface of a star relate $\frac{\delta T}{T}$ and $\frac{\delta r(R)}{R}$ as:

$$\frac{\delta T}{T} = \nabla_{ad}\,C(\ell,\sigma)\frac{\delta r(R)}{R}. \tag{3.6}$$

Hence Watson (1988) defines

$$B = \nabla_{ad}\,C(\ell,\sigma). \tag{3.7}$$

The energy equation for non-adiabatic oscillations is complex; it therefore results in a complex relation between $\frac{\delta T}{T}$ and $\frac{\delta P}{P}$ (see equation(4.49)). This introduces an amplitude parameter $R_{\rm ad}$ and the phase difference (Ψ_T) between the temperature and radius perturbations so that we obtain this relationship:

$$\frac{\delta T}{T} = R_{ad}\,\nabla_{ad}\,\exp(i\,\Psi_T)\,C(\ell,\sigma)\,\frac{\delta r(R)}{R}. \tag{3.8}$$

$R_{\rm ad}$ and Ψ_T can be considered free parameters that can be determined from a fit to multicolour photometric data as was done by Koen *et al.* (1999) on the δ Scuti star HD 95321, or from two– colour diagrams as was done by Medupe, Kurtz & Christensen-Dalsgaard (1998) in their study of α Cir (see Fig. 3.2), and Watson (1988). $R_{\rm ad} = 1$ for adiabatic oscillations and $R_{\rm ad} \longrightarrow 0$ for strongly non-adiabatic oscillations.

3.2.2 Implications for amplitudes

Watson (1988) used equation (3.2) to produce two colour amplitude ratio *vs* phase difference diagrams which he compared with photometric data in order to determine ℓ–values for β Cephei, δ Scuti, 53 Persei and ZZ Ceti variables with some measure of success. However, this technique did not work for roAp stars. Using the Tables C.1, C.2, D.1, D.2, D.3 and D.4 for α Cir, Medupe, Christensen-Dalsgaard & Kurtz (1998) also found that equation (3.2) does not fit roAp multi-colour ($U\,B\,V\,R\,I$) data when $R_{\rm ad} \approx 1$ (adiabatic case). However, values close to $R_{\rm ad} \approx 0$ (non-adiabatic case) described the wavelength dependence of the dipole mode amplitude well. This is demonstrated in Fig. 3.2 where in the top panel we show the locus of (R_{ad}, Ψ_T) on the $\frac{A_B}{A_V}$ $v.s$ $\phi_B - \phi_V$ plane. The values $(R_{\rm ad}, \Psi_T) = (0.01, 90^\circ)$ come the closest to the α Cir data. When these $(R_{\rm ad}, \Psi_T)$ are used in equation (3.2) the bottom plot in Fig. 3.2 results. It is noteworthy that $(R_{\rm ad}, \Psi_T)$ are obtained from two filters only, yet they fit data in all five filters well. For comparison the results for when $R_{ad} = 1.0$ and the results of Medupe & Kurtz's 1998 numerical models are included in the plot.

Medupe, Christensen-Dalsgaard & Kurtz (1998) also found that for $\ell < 4$, $R_{\rm ad} \approx 0$ makes the pressure term more dominant than the temperature and geometry terms, at least in Johnson U, B and V. To demonstrate this we use Watson's (1988) definition for a term $R_i = \frac{T_i}{\sum_{i=1}^{5} T_i}$ that describes the relative importance of each of the five pulsation terms. Histograms (in Johnson filters) showing R_i at different ℓ values in the non-adiabatic case are shown in Figs 3.3 and 3.4 for adiabatic case. It is therefore clear that for $\ell < 4$, T_4 dominates all terms in Johnson U, B and V, but things are different in R and I. However, T_4 is insensitive to $\ell < 4$ values in the $UBVRI$ region as shown in Fig. 3.5. In Fig. 3.6 we show the corresponding amplitudes *vs* wavelength at different ℓ values. It is clear from this diagram that even if $(R_{\rm ad}, \Psi_T) = (0.01, 90^\circ)$ fits the amplitude data well, it is not useful for mode identification.

3.2.3 Implications for phases

The amplitude of the Watson's equation is given as:

$$\Delta A_\lambda = \sqrt{A_r^2 + A_i^2}, \tag{3.9}$$

where A_r is the real part of the part of the Watson's formula that does not depend on time (t) and is given by:

$$A_r = (T_1 + T_2)\cos(\Psi_T + m\,\phi_0) + (T_3 + T_4 + T_5)\cos(m\,\phi_0), \tag{3.10}$$

and the imaginary part A_i is given by:

$$A_i = (T_1 + T_2)\sin(\Psi_T + m\,\phi_0) + (T_3 + T_4 + T_5)\sin(m\,\phi_0), \tag{3.11}$$

The pulsation phase (ϕ_λ) is given as:

$$\tan(\phi_\lambda) = \frac{\sin(\Psi_T + m\,\phi_0) + r\,\sin(m\,\phi_0)}{\cos(\Psi_T + m\,\phi_0) + r\,\cos(m\,\phi_0)}, \tag{3.12}$$

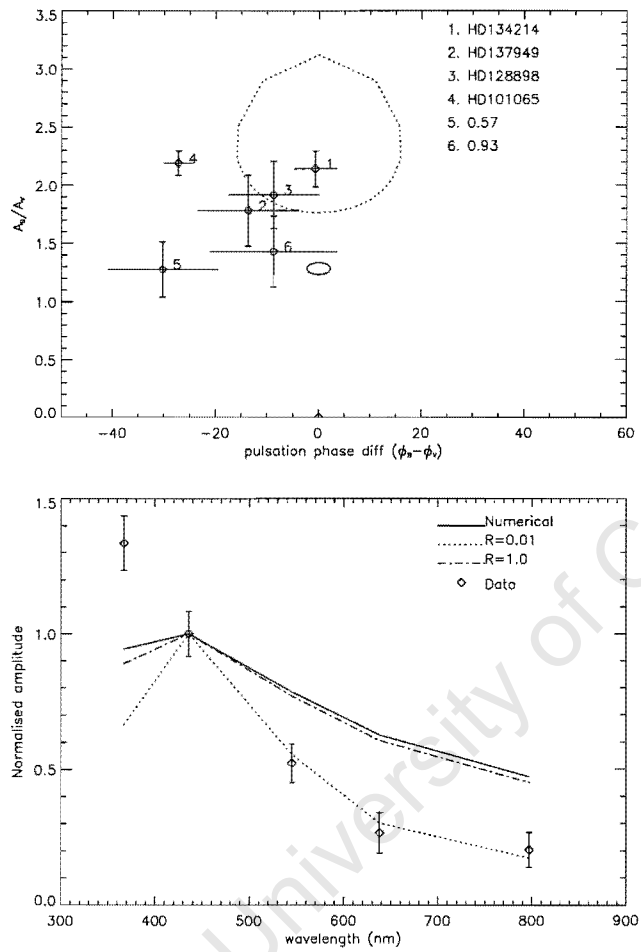

Figure 3.2: The top figure shows the $(R_{\rm ad}, \Psi_T)$ loci on the A_B/A_V vs $\phi_B - \phi_V$ plane for $\ell = 1$. The dotted line is a curve of constant $R_{\rm ad} = 0.01$, the solid line $R_{\rm ad} = 0.25$, (with Ψ_T varying from 0° to 360°). Also shown are the data points for five roAp stars. Star number 5 and 6 is HR 3831 at rotation phases 0.58 and 0.93. The bottom figure shows the amplitude *vs* wavelength data for α Cir. Also shown are predictions of Watson's formula for the fully adiabatic case ($R_{\rm ad} = 1.0$) and non-adiabatic case ($R_{\rm ad} = 0.01$). The $R_{\rm ad} = 0.01$, $\Psi_T = 90°$ values fit the B to I amplitude data quite well. The solid curve is the results of Medupe & Kurtz's (1998) numerical results.

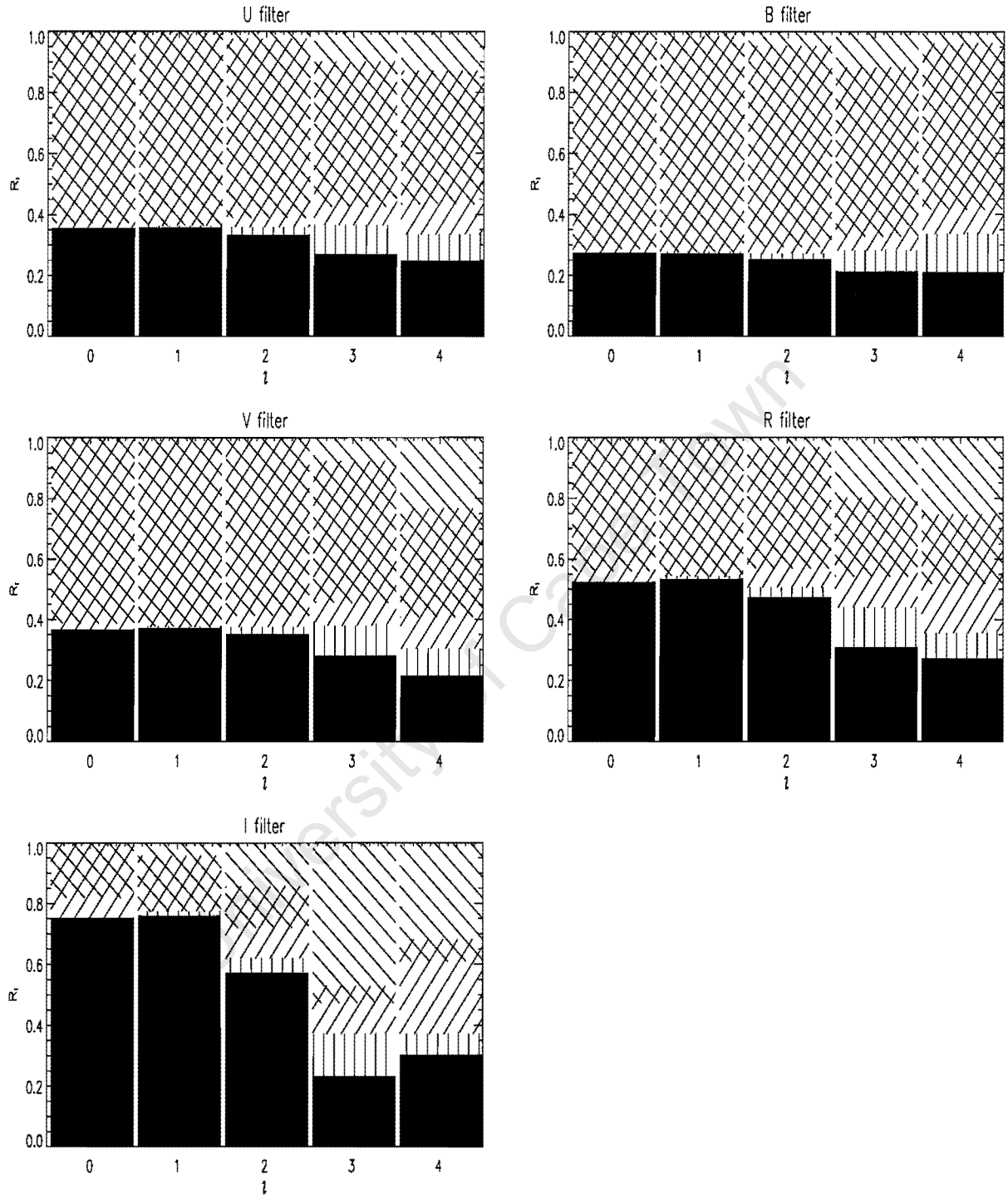

Figure 3.3: Histogram showing the fractional contribution of each term to light variations for $\ell = 0, 1, 2, 3, 4$ for $R_{ad} = 0.01$ and $\Psi_{\rm T} = 90°$, $T_{\rm eff} = 7900\,{\rm K}$, $\log\, g = 4.2$, α Cir abundance. The solid area is T_1, 45° hatching is T_3, the vertical hatching is T_2, the cross hatching the pressure term T_4 and 135° hatching is for T_5. For $\ell \leq 4$ the pressure term dominates in the Johnson U, B, V. In the Johnson R and I T_1 dominates for $\ell < 2$.

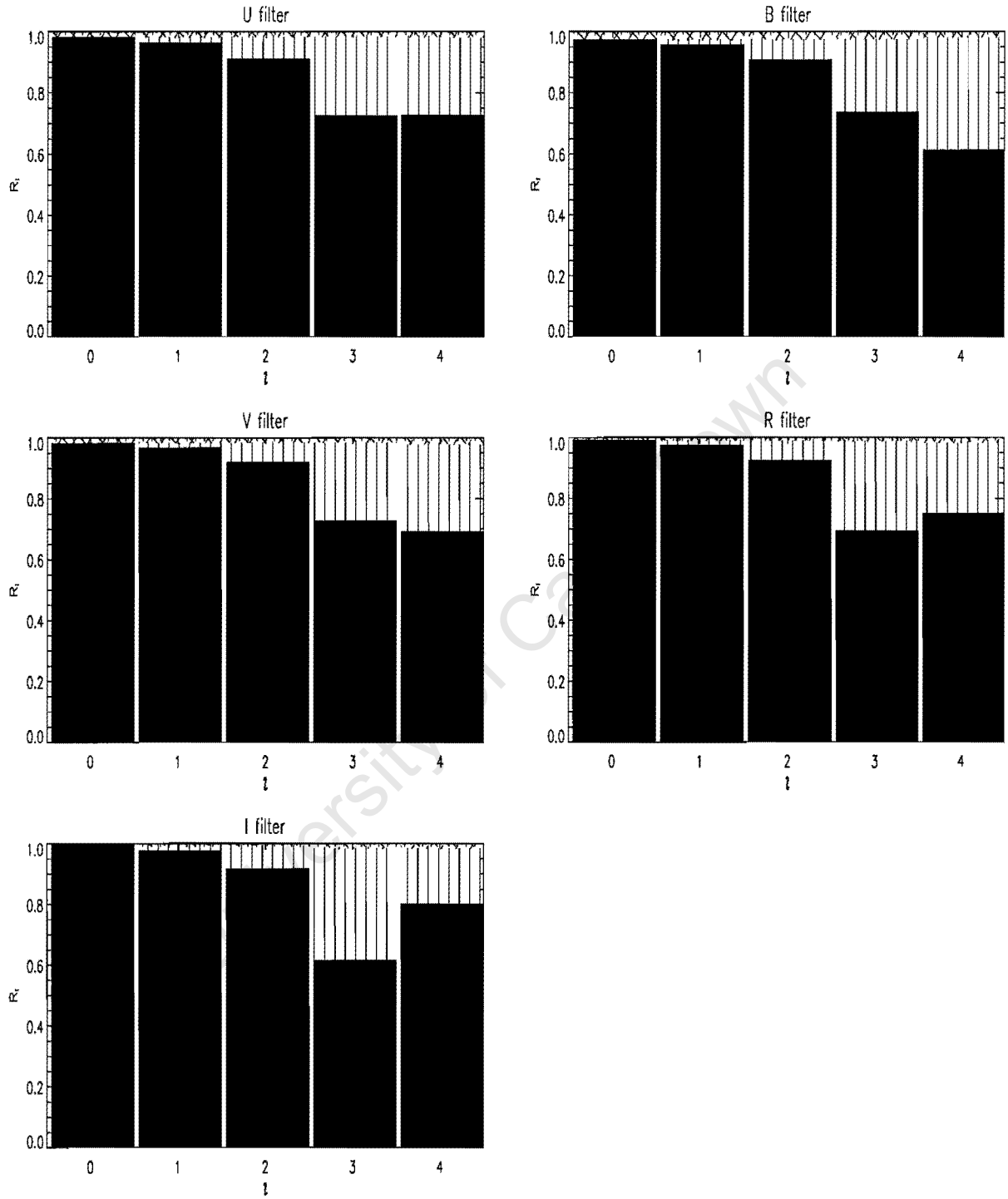

Figure 3.4: Histogram showing the fractional contribution of each of the five pulsation terms in the adiabatic case of $R_{\rm ad} = 1.0$ and $\Psi_{\rm T} = 90°$. In all filters the temperature term T_1 dominates. These are based on the same model grid as in Fig. 3.3. Although mode-identification using amplitudes is possible here, $R_{\rm ad} = 1.0$ does not fit the multi-colour data.

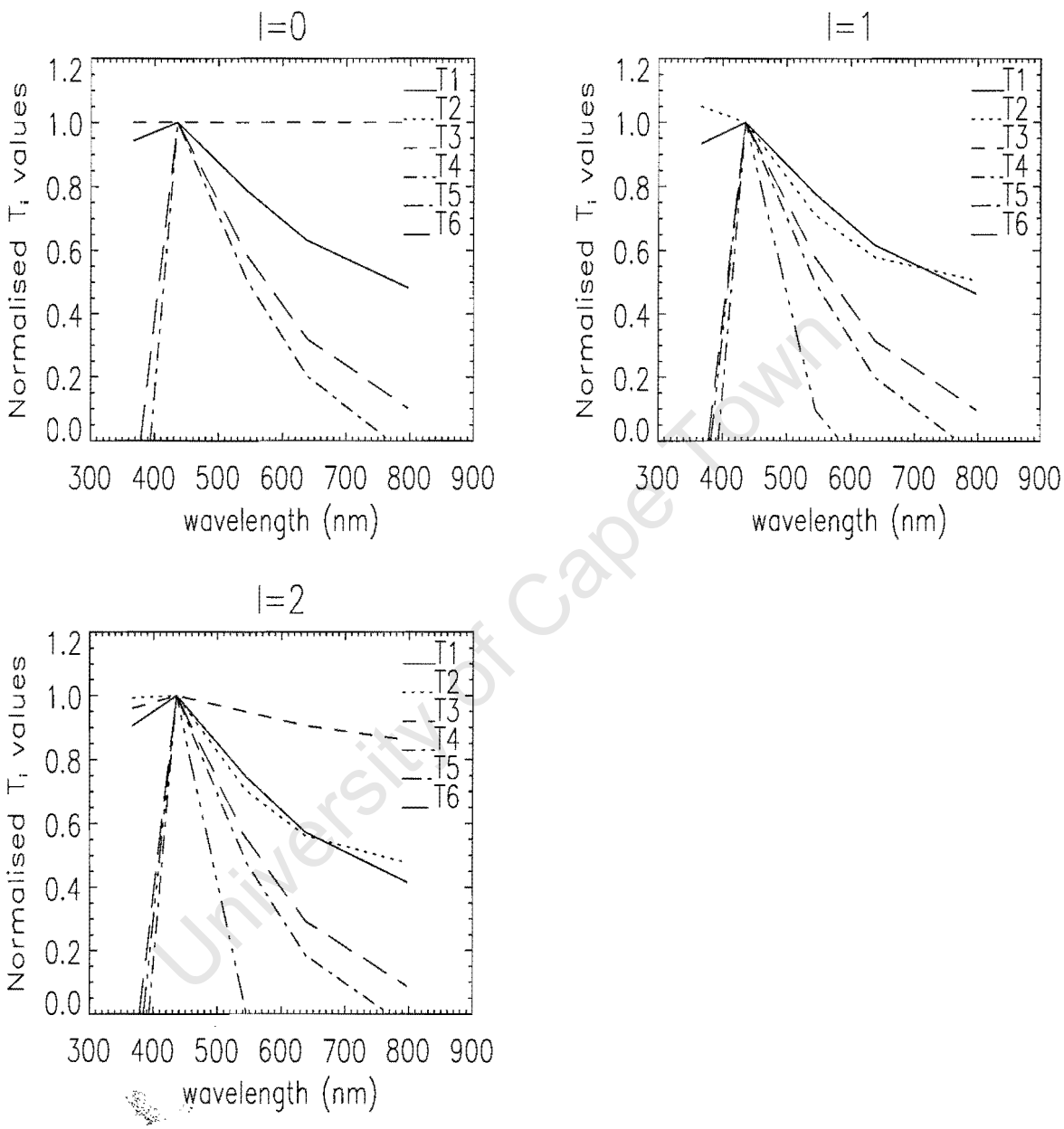

Figure 3.5: A plot of different terms T_1, T_2, T_3, T_4, T_5 normalised to 1 at Johnson B, as a function of wavelength at different ℓ values. From this plot a combination of T_4 and T_1 can explain the observed rapid decline of amplitude from B to I. The sharp drop in the U of T_4 is probably due to the strong lines and the Balmer jump, the U band "sits" across part of the Balmer discontinuity and some strong lines. Term T_6 is the sum of T_1 and T_4, *i.e.* $T_6 = T_1 + T_4$.

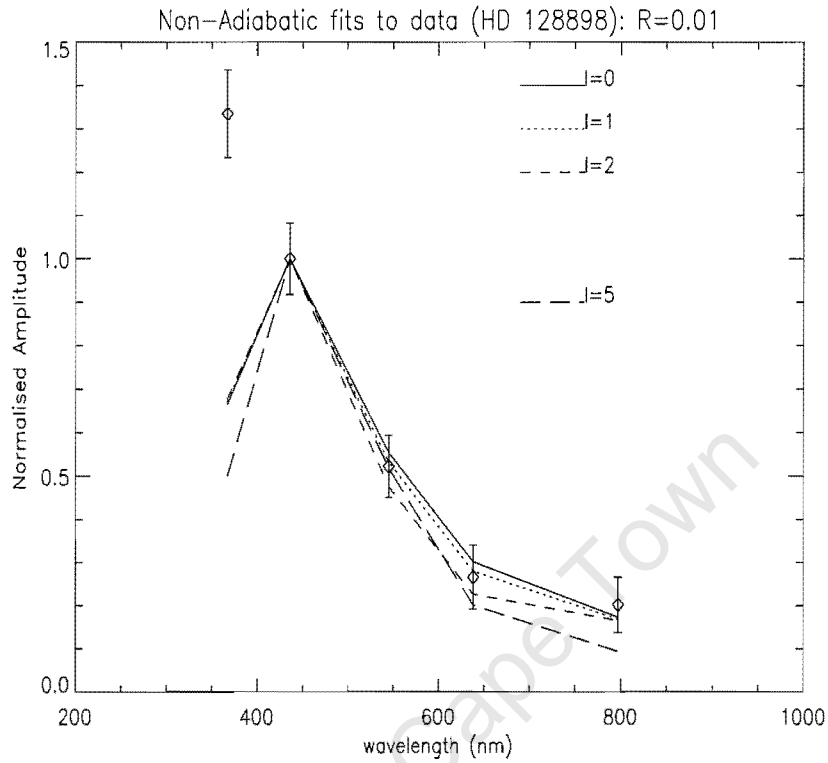

Figure 3.6: A plot showing the normalised amplitudes as a function of wavelength for the α Cir data. Also shown are the expected normalised values from Watson's equation for $\ell = 0, 1, 2$ and 5. Note that for small R_{ad} values (non-adiabatic) equation (3.2) is unable to discriminate between $\ell = 0, 1, 2$ and 5 values.

where r is the ratio of the geometry terms to the temperature terms and is given by:

$$r = \frac{T_3 + T_4 + T_5}{T_1 + T_2}, \tag{3.13}$$

and the dependence on $m\,\phi_0$ comes from the spherical harmonics relation:

$$Y_\ell^m(\theta_0, \phi_0) \propto P_\ell(\cos\,\theta_0)\,\exp(i\,m\,\phi_0). \tag{3.14}$$

The dependence of the pulsation phase on wavelength comes from the ratio of geometry to temperature effects and Ψ_T according to the above relation. If temperature terms $(T_1 + T_2)$ dominate the geometry terms $(T_3 + T_4 + T_5)$ as in Fig. 3.4, r is small and pulsation phase depends purely on Ψ_T. However, if the geometry effects dominate the temperature effects as seems to be the case in roAp stars (see Fig. 3.3), r cannot be ignored. A plot of $\phi\,(\lambda)$ at Johnson U, B V, R and I wavelengths based on equation (3.12) is shown in Fig. 3.7 for $R_{\rm ad} = 1.0, \Psi_T = 45°$. This plot shows that a constant phase difference between $\delta\,T_{\rm eff}/T_{\rm eff}$ and $\delta\,r(R)/R$ at various wavelengths leads to the almost constant $\phi\,(\lambda)$ for $R_{\rm ad} = 1$, compared to the markedly wavelength dependent phase observable in the α Cir data (see the last

chapter). $R_{\rm ad} = 0.01$ introduces a trend in the phase *vs* wavelength as shown in Fig. 3.8. An interesting thing is that at some values of Ψ_T this trend is different for different ℓ values suggesting that for roAp stars phase alone can be used for mode identification. According to Watson's formula, pulsation phase can change by up to 150° from Johnson B to I. There seems to be a range of r in which mode identification by phase alone is possible. For r much bigger than 0.01 and much smaller than 0.01 the curves for $\ell = 0$, 1 and 2 lie on top of each other. We show phase *vs* wavelength plots for $R_{ad} = 0.005$ in Fig. 3.10. If plots 3.8, 3.9 and 3.10 are to be believed, can phase alone be used to determine the ℓ value? Or can $R - I$ colour be used for ℓ determination? Johnson R and I phases often have larger errors because the R and I amplitudes are quite small, this would make mode discrimination difficult in those filters. We caution however, that Watson's formula has limitations that make its application to roAp stars questionable. This is discussed in section (3.2.4). Only with a modified Watson's formula (see section 3.4) can we investigate whether the phase data (ϕ_λ) alone can be used for mode identification.

3.2.4 Limitations

Watson's formula is based on intensities calculated from a boundary condition defined at the photosphere (*i.e.* $\tau = 2/3$). In other words the atmosphere is treated as a single layer with the assumption that the eigenfunctions are constant there. While this assumption is not bad for stars such as β Cephei stars, as shown by Cugier, Dziembowski & Pamyatnykh (1994), who showed that the eigenfunctions for β Cephei stars are indeed constant in their atmospheres, it does not apply for roAp stars where Medupe, Kurtz & Christensen-Dalsgaard (2000) show highly depth dependent temperature and displacement eigenfunctions. Even 'parameters' such as R_{ad} and Ψ_T are found not to be constant with depth. Proper and consistent treatment of the non-adiabatic pulsation equations, taking into consideration radiative transfer is necessary for such stars. This is the subject of section 4.

While the treatment of the adiabatic case is fine in Watson's formula, it is quite unsatisfactory when it comes to non-adiabatic oscillations. In chapter 4 it is shown that temperature perturbations are not simply related to pressure perturbations, the relations derived there could be used instead of equation (3.3). Another unsatisfactory relation is that between gravity perturbations and displacement. There is bound to be a complex relation between gravity and displacement eigenfunctions if the oscillations are non-adiabatic. If calculations are done properly, two more parameters (the amplitude and phase parameters) will be introduced!

It is exciting that Watson's formula indicates that phase alone can be used for mode-identification. However, the same formula shows no large phase changes between the Johnson U and V observed in HD 101065 and HR 3831. This indicates some missing information in the formula.

Suggestions on how to address some of the above–mentioned problems are discussed in section 3.4.

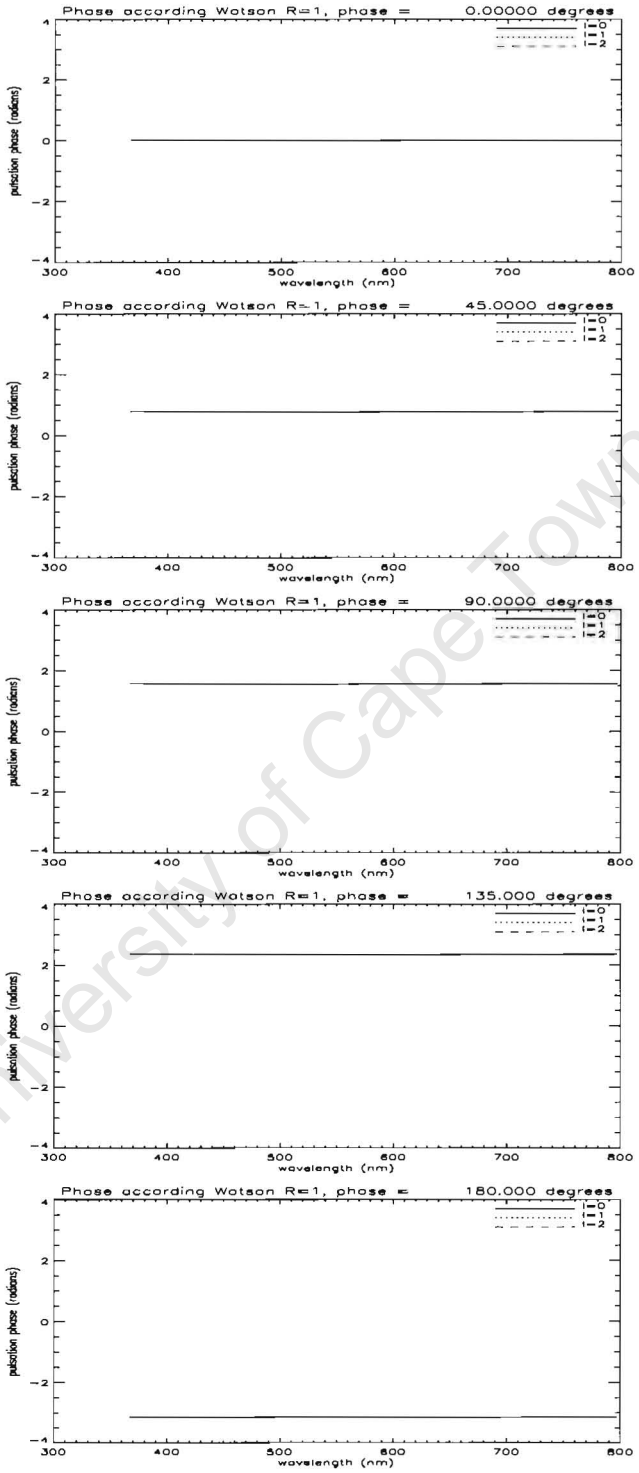

Figure 3.7: The expected variation of pulsation phases with wavelength for $R_{ad} = 1$ and several values of Ψ_T according to equation (3.12). It is clear that Watson's formula predicts a constant constant phase at various wavelength for adiabatic oscillations. The trend is the same for Ψ_T values 225°, 270°, 315° and 360°.

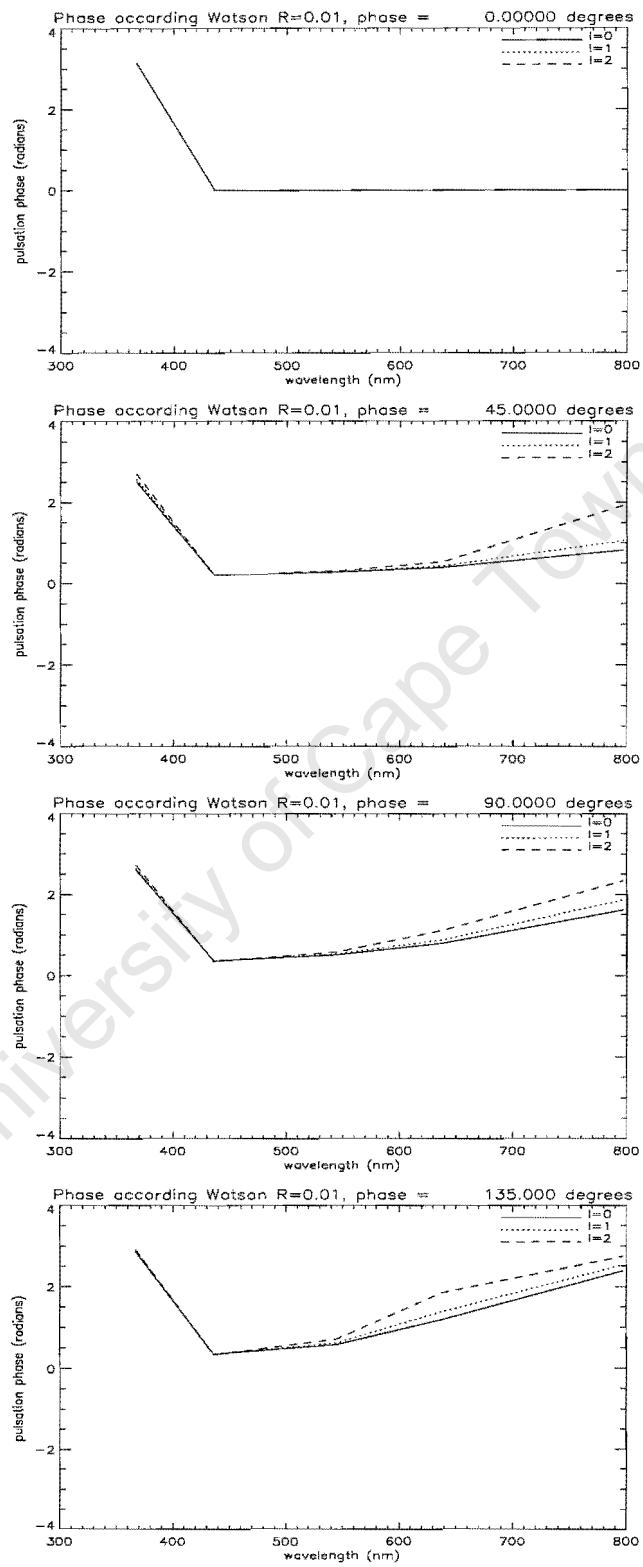

Figure 3.8: The expected variation of pulsation phases with wavelength for $R_{ad} = 0.01$ and several values of Ψ_T, according to equation (3.12). Here, for some values of Ψ_T, not only do we see a trend, it seems also that mode-identification is possible.

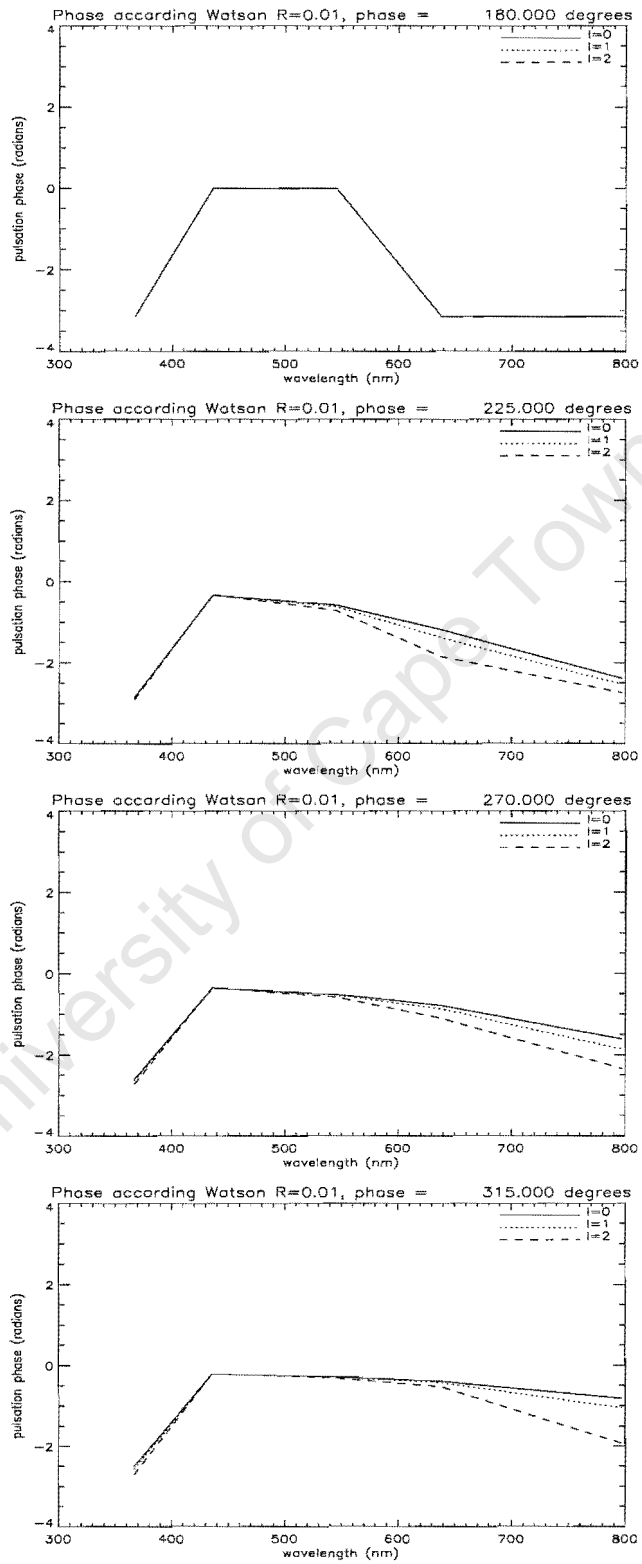

Figure 3.9: The expected variation of pulsation phases with wavelength for $R_{ad} = 0.01$, and $\Psi_{\rm T} = 180°, 225°, 270°$ and $315°$ according to equation (3.12). Can phase alone be used for mode identification? See the discussion in section 3.2.4.

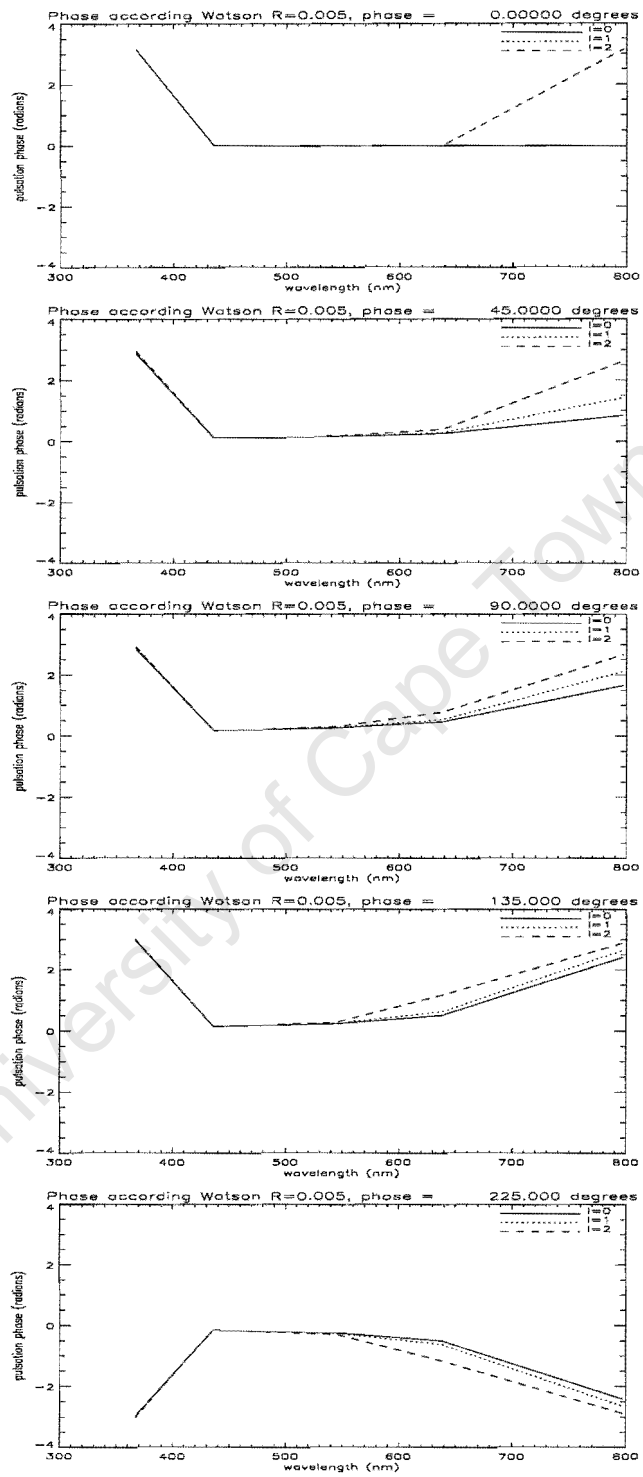

Figure 3.10: The expected variation of pulsation phases with wavelength $R_{ad} = 0.005$ and $\Psi_{\rm T} = 0°, 45°, 90°$ and 225° according to equation (3.12). Note that for $\Psi_T = 45°$ the separation in phase for different modes is quite large in the Johnson R and I. It seems that for $\Psi_T = 45°$ even the modest R and I data can be used to distinguish $\ell = 0$ and $\ell = 2$ modes.

3.3 Derivation of the formula

The basics of the formula are that the pulsations result in the perturbations of the surface temperature and gravity. However, since these two parameters define the observed flux of the star, the flux will also be perturbed. There are other effects, too. The radius of the star is also perturbed; this results in the radial and horizontal displacement. Consequently, the surface area and normal are perturbed. The latter results purely from the change in the direction of the surface normal from the radial direction during pulsations (see Buta & Smith 1979). The perturbation in the surface normal affects the limb-darkening. The limb-darkening also depends on surface temperature and gravity. All of these are taken into consideration in Watson's presentation of the formula. In this subsection we show how the formula as presented by Watson (1988) is derived. In section (3.2) it was shown that this formula is not suitable for application to roAp stars because of some of the assumptions used in the derivation of this formula. These and suggested modifications are part of a separate section 3.4. The derivations follow below:

Perturbation in the stellar flux results in:

$$F'_\lambda = F_{0\lambda} + \delta F_\lambda. \tag{3.15}$$

In terms of magnitudes:

$$\Delta m_\lambda = -2.5 \log\left(1 + \frac{\delta F_\lambda}{F_{0\lambda}}\right), \tag{3.16}$$

which is equivalent to:

$$\Delta m_\lambda = -1.086 \ln\left(1 + \frac{\delta F_\lambda}{F_{0\lambda}}\right), \tag{3.17}$$

note that $-2.5/\log 10 = -1.086$. Also note that for small x, $\ln(1+x) \approx x$, therefore, since $\delta F_\lambda / F_{0\lambda}$ is assumed small we get:

$$\Delta m_\lambda = -1.086 \frac{\delta F_\lambda}{F_{0\lambda}} \tag{3.18}$$

For a star in equilibrium, the flux is defined as:

$$F_\lambda = \int_S I_\lambda \frac{d a_0}{r_0^2}, \tag{3.19}$$

where $d a_0$ is the projected area of the surface element, r_0 is the radius of a star in equilibrium. The integration is done over the hemisphere visible to the observer, so that $0 < \theta < \frac{\pi}{2}$ and $0 < \phi < 2\pi$. One such surface element with its dimensions is shown in Fig. 3.11.
The surface area of such an element is therefore:

$$d A = r\, d\theta\, \vec{e}_\theta \times r \sin\theta\, d\phi\, \vec{e}_\phi. \tag{3.20}$$

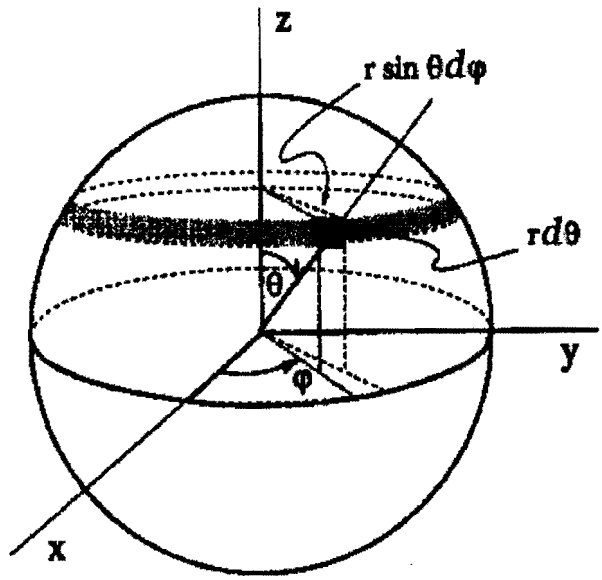

Figure 3.11: A sketch to show the surface element referred to in the derivation of Watson's formula.

Any textbook on vector calculus shows that when a position vector ($\vec{r}$) is transformed from cartesian ($\vec{e}_x$, $\vec{e}_y$, $\vec{e}_z$) to spherical ($\vec{e}_r$, $\vec{e}_\theta$, $\vec{e}_\phi$) coordinates, the unit vectors in the spherical coordinate system are given as:

$$\begin{aligned} \vec{e}_r &= \frac{1}{h_1}\frac{\partial \vec{r}}{\partial r}, \\ \vec{e}_\theta &= \frac{1}{h_2}\frac{\partial \vec{r}}{\partial \theta}, \\ \vec{e}_\phi &= \frac{1}{h_3}\frac{\partial \vec{r}}{\partial \phi}, \end{aligned} \tag{3.21}$$

where $h_1 = \left|\frac{\partial \vec{r}}{\partial r}\right|$, $h_2 = \left|\frac{\partial \vec{r}}{\partial \theta}\right|$ and $h_3 = \left|\frac{\partial \vec{r}}{\partial \phi}\right|$. It is easy to show that:

$$h_1 = 1, \tag{3.22}$$

$$h_2 = r, \tag{3.23}$$

and

$$h_3 = r\,\sin\theta. \tag{3.24}$$

Therefore,

$$\begin{aligned} \vec{e}_r &= \frac{\partial \vec{r}}{\partial r}, \\ \vec{e}_\theta &= \frac{1}{r}\frac{\partial \vec{r}}{\partial \theta}, \\ \vec{e}_\phi &= \frac{1}{r\,\sin\theta}\frac{\partial \vec{r}}{\partial \phi}. \end{aligned} \tag{3.25}$$

The properties of the position vector in spherical coordinates are:

$$\begin{aligned} \vec{r} &= r\sin\theta\cos\phi\,\vec{e_x} + r\sin\theta\sin\phi\,\vec{e_y} + r\cos\theta\,\vec{e_z} \\ \frac{\partial\vec{r}}{\partial r} &= \vec{e_r} \\ \frac{\partial\vec{r}}{\partial\theta} &= r\,\vec{e_\theta} \\ \frac{\partial\vec{r}}{\partial\phi} &= r\sin\theta\,\vec{e_\phi}, \end{aligned} \tag{3.26}$$

where $(\vec{e_r}, \vec{e_\theta}, \vec{e_\phi})$ are the unit vectors in spherical coordinates that have properties shown in Table 3.2.

Table 3.2: Properties of unit vectors in spherical coordinates.

Unit vectors	**Partial derivatives of unit vectors**
$\vec{e_r} = \vec{e_\theta} \times \vec{e_\phi}$	$\frac{\partial\vec{e_r}}{\partial\theta} = \vec{e_\theta}$
$\vec{e_\theta} = \vec{e_\phi} \times \vec{e_r}$	$\frac{\partial\vec{e_\theta}}{\partial\theta} = -\frac{\vec{r}}{r}$
$\vec{e_\phi} = \vec{e_r} \times \vec{e_\theta}$	$\frac{\partial\vec{e_\theta}}{\partial\phi} = \cos\theta\,\vec{e_\phi}$
	$\frac{\partial\vec{e_r}}{\partial\phi} = \sin\theta\,\vec{e_\phi}.$

Therefore, if in equation (3.20) we substitute the $\vec{e_\theta}$ and $\vec{e_\phi}$ by expressions in equation (3.25), the area of the surface element can also be written as:

$$d\vec{A} = \left(\frac{\partial\vec{r}}{\partial\theta} \times \frac{\partial\vec{r}}{\partial\phi}\right) d\theta\,d\phi, \tag{3.27}$$

where the magnitude of $d\vec{A}$ gives the actual area of the surface element and the direction of $d\vec{A}$ is that of the surface normal.

Stellar oscillations result in the perturbation of the equilibrium star, and perturbations in the flux arise from the perturbations in the intensity, area of the surface element and limb-darkening. The intensity is:

$$I_\lambda = I_{0\lambda}\,g_\lambda(\mu), \tag{3.28}$$

where g_λ is the limb-darkening function, $I_{0\lambda}$ is the intensity at the centre of the stellar disc and $\mu = \cos\theta$. Perturbations in the limb-darkening arise from the perturbations in the normal to the surface element, amongst other factors. Therefore, the angle $\Theta(t)$ between the local surface normal $(\vec{n}_s)$ and the unit vector in the direction of the observer $(\vec{n})$ will change as a result of the perturbations. The cosine of this angle is given as:

$$\cos\Theta(t) = \vec{n} \bullet \vec{n}_s = \mu', \tag{3.29}$$

where $\vec{n}_s$ is the perturbed surface normal.

Thus the perturbation of μ from the equilibrium is $\mu' - \mu$. Note that for a star in equilibrium $\vec{n}_s = \vec{e_r}$.

Since perturbations are assumed to be quite small, we can expand the limb-darkening function as a Taylor series around the equilibrium μ. If the perturbed μ is given as $\mu' = \mu + \delta\,\mu$, then $\mu' - \mu$ is very small. Therefore, by Taylor expansion we get:

$$g_\lambda(\mu') = g_\lambda(\mu) + (\mu' - \mu)\frac{\partial\, g_\lambda}{\partial\, \mu}. \tag{3.30}$$

Perturbing equation (3.19) and using equations (3.28) and (3.30) we get:

$$F'_\lambda = \int_S I_{0\,\lambda}\left(1 + \frac{\delta\, I_\lambda}{I_{0\,\lambda}}\right)\left(g_\lambda(\mu) + (\mu' - \mu)\frac{\partial\, g_\lambda}{\partial\, \mu}\right)\frac{(d\, a_0 + \delta\, d\, a)}{r_0^2}. \tag{3.31}$$

Let's denote the integrand in the above equation by A_λ, after linearizing the above equation we obtain:

$$A_\lambda = I_{0\,\lambda}\left([g_\lambda(\mu) + (\mu' - \mu)\frac{\partial\, g_\lambda}{\partial\, \mu}]\,\frac{d\, a_0}{r_0^2} + g_\lambda(\mu)\,\frac{\delta\, d\, a}{r_0^2} + \frac{\delta\, I_\lambda}{I_{0\,\lambda}}\, g_\lambda(\mu)\,\frac{d\, a_0}{r_0^2}\right). \tag{3.32}$$

Therefore:

$$F'_\lambda = \int_S I_{0\,\lambda} g_\lambda(\mu)\,\frac{d\, a_0}{r_0^2} + \int_S I_{0\,\lambda}\,(\mu' - \mu)\frac{\partial\, g_\lambda}{\partial\, \mu}\,\frac{d\, a_0}{r_0^2} + \int_S I_{0\,\lambda}\, g_\lambda(\mu)\,\frac{\delta\, d\, a}{r_0^2} + \int_S \frac{\delta\, I_\lambda}{I_{0\,\lambda}}\, g_\lambda(\mu)\,\frac{d\, a_0}{r_0^2} \tag{3.33}$$

Notice that $a_0/r_0^2 = \omega_0$ is the solid angle subtended by the surface element of area a_0, and $\delta\, a/r_0^2 = \delta\,\omega$ can be regarded as the perturbed solid angle. Equation (3.33) tells us that the perturbation in the flux is due to the perturbations in the **surface normal** (second term), **surface area** (3rd term) and the **surface brightness** (fourth term).

The spectrum of a star is defined primarily by two parameters, the surface temperature (T_{eff}) and gravity ($\log\, g$). Hence:

$$I_{0\,\lambda} = I_{0\,\lambda}\,(T_{\text{eff}},\, \log\, g), \tag{3.34}$$

and

$$g_\lambda = g_\lambda\,(T_{\text{eff}},\, \log\, g). \tag{3.35}$$

Note that g_λ is the un-normalised limb-darkening whereas g is gravity. It follows that small perturbations on T_{eff} and $\log\, g$ results in the perturbations in $I_{0\,\lambda}$ and g_λ given respectively as:

$$\frac{\delta\, I_\lambda}{I_{0\,\lambda}} = \alpha_T\,\frac{\delta\, T_{\text{eff}}}{T_{\text{eff}}} + \alpha_g\frac{\delta\, g}{g} \tag{3.36}$$

and

$$\frac{\delta\, g_\lambda}{g_\lambda} = \beta_T \frac{\delta\, T_{\rm eff}}{T_{\rm eff}} + \beta_g \frac{\delta\, g}{g}, \tag{3.37}$$

where:

$$\alpha_T = \frac{\partial \log\, F_\lambda}{\partial\, \log\, T_{\rm eff}}, \tag{3.38}$$

$$\alpha_g = \frac{\partial \log\, F_\lambda}{\partial\, \log\, g}, \tag{3.39}$$

$$\beta_T = \frac{1}{\ln\, 10} \frac{\partial \ln\, g_\lambda}{\partial\, \log\, T_{\rm eff}}, \tag{3.40}$$

and

$$\beta_g = \frac{1}{\ln\, 10} \frac{\partial \ln\, g_\lambda}{\partial\, \log\, g}. \tag{3.41}$$

If we introduce the perturbations in the limb-darkening law due to $T_{\rm eff}$ and $\log\, g$ in equation (3.33) and linearize we obtain:

$$\begin{aligned} F_{0\lambda} + \delta\, F_\lambda = F_{0\lambda} + \int_S I_{0\lambda}\, g_\lambda \left(\frac{\delta\, g_\lambda}{g_\lambda}\right) d\,\omega_0 + \int_S I_{0\lambda}\, (\mu' - \mu) \frac{\partial\, g_\lambda}{\partial\, \mu}\, d\,\omega_0 \\ + \int_S I_{0\lambda}\, g_\lambda\, \delta\, d\,\omega + I_{0\lambda} \int_S \frac{\delta\, I_\lambda}{I_{0\lambda}}\, g_\lambda\, d\,\omega_0 \end{aligned} \tag{3.42}$$

where:

$$F_{0\lambda} = \int_S I_{0\lambda}\, g_\lambda\, d\,\omega_0. \tag{3.43}$$

Applying equations (3.36) and (3.37) to equation (3.42) we get:

$$\begin{aligned} \delta\, F_\lambda = \frac{1}{2.3026} \int_S I_{0\lambda}\, \beta'_T \frac{\delta\, T_{\rm eff}}{T_{\rm eff}}\, d\,\omega_0 + \frac{1}{2.3026} \int_S I_{0\lambda}\, \beta'_g \frac{\delta\, g}{g}\, d\,\omega_0 \\ + \int_S I_{0\lambda}\, (\mu' - \mu) \frac{\partial\, g_\lambda}{\partial\, \mu}\, d\,\omega_0 + \int_S I_{0\lambda}\, g_\lambda\, \delta\, d\,\omega \\ + I_{0\lambda} \int_S \alpha_T \frac{\delta\, T_{\rm eff}}{T_{\rm eff}}\, g_\lambda\, d\,\omega_0 + I_{0\lambda} \int_S \alpha_g \frac{\delta\, g}{g}\, g_\lambda\, d\,\omega_0 \end{aligned} \tag{3.44}$$

where:

$$\beta'_T = \frac{\partial\, g_\lambda}{\partial\, \log\, T_{\rm eff}} \tag{3.45}$$

and

$$\beta'_g = \frac{\partial g_\lambda}{\partial \log g}. \tag{3.46}$$

We also notice that $\ln 10 = 2.3026$.

It is already becoming apparent in equation (3.44) that T_2 comes from the first term, T_5 from the second term, T_3 from the third and fourth terms, T_1 from the fifth term and T_4 from the last term.

We now divide equation (3.44) by equation (3.43) to get

$$\begin{aligned}\frac{\delta F_\lambda}{F_{0\lambda}} = \frac{1}{2.3026}\int_S \frac{\partial h_\lambda}{\partial \log T_{\text{eff}}}\frac{\delta T_{\text{eff}}}{T_{\text{eff}}}\,d\omega_0 + \frac{1}{2.3026}\int_S \frac{\partial h_\lambda}{\partial \log g}\frac{\delta g}{g}\,d\omega_0 \\ + \int_S (\mu' - \mu)\frac{\partial h_\lambda}{\partial \mu}\,d\omega_0 + \int_S h_\lambda\,\delta\,d\omega \\ + \int_S \alpha_T \frac{\delta T_{\text{eff}}}{T_{\text{eff}}} h_\lambda\,d\omega_0 + \int_S \alpha_g \frac{\delta g}{g} h_\lambda\,d\omega_0\end{aligned} \tag{3.47}$$

where $h_\lambda(\mu)$ is the limb-darkening law normalised in this way:

$$h_\lambda(\mu) = \frac{g_\lambda(\mu)}{\int_S g_\lambda(\mu)\,d\omega_0}. \tag{3.48}$$

Since $g_\lambda(\mu)$ does not depend on ϕ, we can express $h_\lambda(\mu)$ as:

$$h_\lambda(\mu) = \frac{1}{2\pi}\frac{g_\lambda(\mu)}{\int_0^{\frac{\pi}{2}} g_\lambda(\cos\theta)\,d\omega_0}. \tag{3.49}$$

In summary:

$$\begin{aligned}T_1 &= \int_S \alpha_T \frac{\delta T_{\text{eff}}}{T_{\text{eff}}} h_\lambda\,d\omega_0 \\ T_2 &= \frac{1}{2.3026}\int_S \frac{\partial h_\lambda}{\partial \log T_{\text{eff}}}\frac{\delta T_{\text{eff}}}{T_{\text{eff}}}\,d\omega_0 \\ T_3 &= \int_S (\mu' - \mu)\frac{\partial h_\lambda}{\partial \mu}\,d\omega_0 + \int_S h_\lambda\,\delta\,d\omega \\ T_4 &= \int_S \alpha_g \frac{\delta g}{g} h_\lambda\,d\omega_0 \\ T_5 &= \frac{1}{2.3026}\int_S \frac{\partial h_\lambda}{\partial \log g}\frac{\delta g}{g}\,d\omega_0.\end{aligned} \tag{3.50}$$

What is left now is to write, in explicit form, the expressions for $\mu' - \mu$, and $\delta\omega$. This we do by looking again at the definition of μ' and μ: In equilibrium, the cosine of the angle between the surface normal and the unit vector in the direction of the observer stays constant (assuming no rotation) and is given as:

$$\mu = \vec{n} \bullet \vec{e_r}, \tag{3.51}$$

where $\vec{n}$ is the unit vector in the direction of the observer. The cosine of the angle between the perturbed surface normal and the unit vector in the direction of the observer is given in equation (3.29). Therefore:

$$\mu' - \mu = \vec{n} \bullet (\vec{n_s} - \vec{e_r}). \tag{3.52}$$

It is easy to show that:

$$\vec{n} = \cos\theta\, \vec{e_r} - \sin\theta\, \vec{e_\theta}. \tag{3.53}$$

To determine $\vec{n_s}$ we need to work out the perturbed area of the surface element. We assume the perturbed radius of a pulsating star is given as:

$$\vec{r} = \vec{r_0} + \delta r \vec{e_r} + \delta \vec{h}, \tag{3.54}$$

where $\delta \vec{h}$ is the horizontal component which is not included in Watson's formulation. I also do not include it in the following derivations. Heynderickx, Waelkens & Smeyers (1994) did include this term, but the formula they derived turned out to be very similar to Watson's formula. Their V_1 is T_3 and V_2 is a sum of T_1, T_2, T_4 and T_5. Therefore, not including $\delta \vec{h}$ in equation (3.54) does not introduce significant errors.

Taking the partial derivative of equation (3.54) with respect to θ and neglecting $\delta \vec{h}$ results in:

$$\frac{\partial \vec{r}}{\partial \theta} = \frac{\partial \vec{r_0}}{\partial \theta} + \frac{\partial \delta\, ,r}{\partial \theta} \vec{e_r} + \delta r \frac{\partial \vec{e_r}}{\partial \theta}. \tag{3.55}$$

Using properties of the unit vectors in Table 3.2 we get:

$$\frac{\partial \vec{r}}{\partial \theta} = (r_0 + \delta r)\, \vec{e_\theta} + \frac{\partial \delta r}{\partial \theta} \vec{e_r}. \tag{3.56}$$

Similarly,

$$\frac{\partial \vec{r}}{\partial \phi} = \sin\theta\, (r_0 + \delta r)\, \vec{e_\phi} + \frac{\partial \delta r}{\partial \phi} \vec{e_r}. \tag{3.57}$$

Substituting equations (3.56) and (3.57) into equation (3.27) we get:

$$\frac{\partial \vec{r}}{\partial \theta} \times \frac{\partial \vec{r}}{\partial \phi} = r^2 \sin\theta\, \vec{e_\theta} \times \vec{e_\phi} + r \frac{\partial \delta r}{\partial \phi} \vec{e_\theta} \times \vec{e_r} + r \sin\theta \frac{\partial \delta r}{\partial \theta} \vec{e_r} \times \vec{e_\phi}. \tag{3.58}$$

Using properties in Table 3.2 we get:

$$d\vec{A} = r^2 \sin\theta\, d\theta\, d\phi \left(1, -\frac{1}{r_0} \frac{\partial \delta r}{\partial \theta}, -\frac{1}{r_0 \sin\theta} \frac{\partial \delta r}{\partial \phi}\right), \tag{3.59}$$

where $r = r_0 + \delta r$, therefore $r^2 = r_0^2 + 2 r_0^2\, \delta r$.

By definition,

$$\vec{n_s} = \left(1, -\frac{1}{r_0}\frac{\partial \delta r}{\partial \theta}, -\frac{1}{r_0 \sin\theta}\frac{\partial \delta r}{\partial \phi}\right) \tag{3.60}$$

is the perturbed surface normal; note that it meets the requirements $|\vec{n_s}| = 1$. The actual perturbation in $\vec{n_s}$ is $\delta\vec{n_s} = \vec{n_s} - \vec{e_r}$, and $\mu' - \mu = \vec{n} \bullet \delta\vec{n_s}$. Therefore, using equation (3.60) and (3.53) we get:

$$\mu' - \mu = \frac{sin\,\theta}{r_0}\frac{\partial \delta r}{\partial \theta}, \tag{3.61}$$

which in terms of μ is:

$$\mu' - \mu = -(1-\mu^2)\frac{\partial}{\partial \mu}\left(\frac{\delta r}{r_0}\right). \tag{3.62}$$

The projected surface area is:

$$\vec{n} \bullet d\vec{A} = r_0^2 \sin\theta\, d\theta\, d\phi \left\{\cos\theta + 2\frac{\delta r}{r_0}\cos\theta + \sin\theta\frac{\partial}{\partial \theta}\left(\frac{\delta r}{r_0}\right)\right\}. \tag{3.63}$$

In terms of μ,

$$\vec{n} \bullet d\vec{A} = -r_0^2\,\mu\, d\mu\, d\phi - r_0^2\, 2\frac{\delta r}{r_0}\mu\, d\mu\, d\phi + r_0^2(1-\mu^2)\frac{\partial}{\partial \mu}\left(\frac{\delta r}{r_0}\right) d\mu\, d\phi, \tag{3.64}$$

where the first term gives $d\,a_0$, and the second term gives $\delta\, da$. Hence the perturbed solid angle is:

$$\delta\omega = -2\frac{\delta r}{r_0}\mu\, d\mu\, d\phi + (1-\mu^2)\frac{\partial}{\partial \mu}\left(\frac{\delta r}{r_0}\right) d\mu\, d\phi. \tag{3.65}$$

In summary:

$$\begin{aligned} d\omega_0 &= -\mu\, d\mu\, d\phi, \\ \mu' - \mu &= -(1-\mu^2)\frac{\partial}{\partial \mu}\left(\frac{\delta r}{r_0}\right), \\ \delta\omega &= -2\frac{\delta r}{r_0}\mu\, d\mu\, d\phi + (1-\mu^2)\frac{\partial}{\partial \mu}\left(\frac{\delta r}{r_0}\right) d\mu\, d\phi. \end{aligned} \tag{3.66}$$

We revisit equations (3.50) and notice that they all involve surface integrals over the visible hemisphere of a pulsating star. The perturbation in the radius is of the form:

$$\frac{\delta r}{r} = \epsilon\, Y_\ell^m(\theta, \phi)\, \exp(i\omega t). \tag{3.67}$$

where ϵ is the amplitude parameter much smaller than unity. Watson and other authors sought to express $\frac{\delta T_{\rm eff}}{T_{\rm eff}}$, $\frac{\delta g}{g}$ and $\mu' - \mu$ in terms of $\frac{\delta r}{r}$ at the upper boundaries of the stellar

envelope (often taken to be at $\tau = 2/3$). Therefore the atmosphere was not treated in full, just a single boundary layer. The various coefficients and factors are explained in full in section 3.2. $\frac{\delta T_{\rm eff}}{T_{\rm eff}}$ and $\frac{\delta r}{r}$ are related as:

$$\frac{\delta T_{\rm eff}}{T_{\rm eff}} = B \frac{\delta r}{r}. \tag{3.68}$$

To relate $\frac{\delta g}{g}$ and $\frac{\delta r}{r}$ a relation between perturbation in the gravity and local gas pressure of the form:

$$\frac{\delta g}{g} = \frac{\partial \log g}{\partial \log P}\Big|_{\tau=1} \frac{\delta P}{P} \tag{3.69}$$

is used. A relation between pressure perturbations and displacement was derived by Baker & Kippenhahn (1965) for radial pulsations, and Dziembowski (1971) for non-radial pulsations. We show this relation only as:

$$\frac{\delta P}{P} = -C \frac{\delta r}{r}; \tag{3.70}$$

again the coefficient is described in full in the next section.

Hence the terms become:

$$\begin{aligned}
T_1 &= \epsilon \int_0^{2\pi} \int_0^1 \alpha_T B h_\lambda Y_\ell^m(\mu, \phi)\, \mu\, d\mu\, d\phi \\
T_2 &= \frac{\epsilon}{2.3026} \int_0^{2\pi} \int_0^1 \frac{\partial h_\lambda}{\partial \log T_{\rm eff}} B Y_\ell^m(\mu, \phi)\, \mu\, d\mu\, d\phi \\
T_3 &= -\epsilon \int_0^{2\pi} \int_0^1 (1-\mu^2) \frac{\partial Y_\ell^m}{\partial \mu} \frac{\partial h_\lambda}{\partial \mu}\, \mu\, d\mu\, d\phi \\
&\quad + \epsilon \int_0^{2\pi} \int_0^1 h_\lambda \left(2 Y_\ell^m(\mu, \phi)\, \mu + (1-\mu^2) \frac{\partial Y_\ell^m(\mu, \phi)}{\partial \mu} \right) d\mu\, d\phi \\
T_4 &= -\epsilon p^* C \int_0^{2\pi} \int_0^1 \alpha_g h_\lambda Y_\ell^m(\mu, \phi)\, \mu\, d\mu\, d\phi \\
T_5 &= -\frac{\epsilon p^* C}{2.3026} \int_0^{2\pi} \int_0^1 \frac{\partial h_\lambda}{\partial \log g} Y_\ell^m(\mu, \phi)\, \mu\, d\mu\, d\phi.
\end{aligned} \tag{3.71}$$

If we rotate our coordinate axes (θ, ϕ) so that the polar axis points towards the observer, then the spherical harmonics in the old system (before rotation) can be expressed as a linear combination of spherical harmonics of the same ℓ in the new coordinate system (θ', ϕ') (Matthews & Walker 1970; Buta & Smith 1979), *i.e.*

$$Y_\ell^m(\theta, \phi) = \sum_{m'=-\ell}^{\ell} C_{m\,m'}^{\ell}\, Y_\ell^{m'}(\theta', \phi'). \tag{3.72}$$

The coefficients $C_{m\,m'}^{\ell}$ are obtained from:

$$C_{m\,m'}^{\ell} = \int_S Y_\ell^{m'\,*}(\theta', \phi')\, Y_\ell^m(\theta, \phi)\, \sin\theta'\, d\theta'\, d\phi' \tag{3.73}$$

Upon integration over the surface of a star, the only non-zero term in equation (3.72) is the one with coefficient $C^{\ell}_{m\,0}$, given by:

$$C^{\ell}_{m\,0} = \left(\frac{4\pi}{2\ell+1}\right)^{\frac{1}{2}} Y^m_\ell(\theta_0, \phi_0), \tag{3.74}$$

where $(\theta_0,\, \phi_0)$ are the angular coordinates of the observer in the $(\theta,\, \phi)$ system. Therefore equation (3.72) becomes:

$$\begin{aligned} Y^m_\ell(\theta,\, \phi) &= \left(\frac{4\pi}{2\ell+1}\right)^{\frac{1}{2}} Y^m_\ell(\theta_0, \phi_0)\, Y^0_\ell(\theta',\, \phi'), \\ &= Y^m_\ell(\theta_0, \phi_0)\, p_\ell(\mu'), \end{aligned} \tag{3.75}$$

where P_ℓ is the Legendre polynomial.

Let's consider T_3:

$$\begin{aligned} T_3 &= \epsilon\, Y^m_\ell(\theta_0,\, \phi_0) \left\{ \int_0^1 h_\lambda \left(2\, p_\ell\, \mu - (1-\mu^2)\, \frac{\partial\, p_\ell}{\partial\, \mu} \right) d\,\mu - \int_0^1 (1-\mu^2)\, \frac{\partial\, p_\ell}{\partial\, \mu}\, \frac{\partial\, h_\lambda}{\partial\, \mu} \right\} \mu\, d\,\mu \\ &= 2\, b_{\ell\lambda} - \int_0^1 (1-\mu^2)\, \frac{\partial\, p_\ell}{\partial\, \mu}\, h_\lambda\, d\,\mu - \int_0^1 (1-\mu^2)\, \frac{\partial\, p_\ell}{\partial\, \mu}\, \frac{\partial\, h_\lambda}{\partial\, \mu}\, \mu\, d\,\mu, \end{aligned} \tag{3.76}$$

where $b_{\ell\lambda} = \int_0^1 h_\lambda\, \mu\, p_\ell\, d\mu$. We evaluate the integral in the third term by parts to get:

$$\begin{aligned} \int_0^1 (1-\mu^2)\, \frac{\partial\, p_\ell}{\partial\, \mu}\, \frac{\partial\, h_\lambda}{\partial\, \mu}\, \mu\, d\mu &= -\int_0^1 h_\lambda\, (1-\mu^2)\, \frac{\partial\, p_\ell}{\partial\, \mu}\, d\,\mu \\ &\quad - \int_0^1 h_\lambda \left((1-\mu^2)\, \frac{\partial^2\, p_\ell}{\partial\, \mu^2} - 2\,\mu\, \frac{\partial\, p_\ell}{\partial\, \mu} \right) \mu\, d\,\mu. \end{aligned} \tag{3.77}$$

The Legendre differential equation is:

$$(1-\mu^2)\, \frac{\partial^2\, p_\ell}{\partial\, \mu^2} - 2\,\mu\, \frac{\partial\, p_\ell}{\partial\, \mu} + \ell\,(\ell+1)\, p_\ell = 0. \tag{3.78}$$

Therefore, substituting equation (3.78) into equation (3.77) we get:

$$\int_0^1 (1-\mu^2)\, \frac{\partial\, p_\ell}{\partial\, \mu}\, \frac{\partial\, h_\lambda}{\partial\, \mu}\, \mu\, d\,\mu = -\int_0^1 h_\lambda\, (1-\mu^2)\, \frac{\partial\, p_\ell}{\partial\, \mu}\, d\,\mu + \ell\,(\ell+1)\, b_{\ell\lambda}. \tag{3.79}$$

Finally, substituting equation (3.79) into equation (3.76) we obtain

$$\begin{aligned} T_3 &= \{2 - \ell\,(\ell+1)\}\, b_{\ell\lambda} \\ &= (2+\ell)\,(1-\ell)\, b_{\ell\lambda}. \end{aligned} \tag{3.80}$$

By substituting $Y^m_\ell\,(\theta,\, \phi)$ in equation (3.71) by equation (3.75) it is easy to show that:

$$\begin{aligned} T_1 &= \epsilon\, Y^m_\ell\,(\theta_0,\, \phi_0)\, \alpha_T\, B\, b_{\ell\lambda} \\ T_2 &= \frac{\epsilon}{2.3026}\, Y^m_\ell\,(\theta_0,\, \phi_0)\, B\, \frac{\partial\, b_{\ell\lambda}}{\partial\, log\, T_{\rm eff}} \\ T_3 &= \epsilon\, Y^m_\ell\,(\theta_0,\, \phi_0)\, (2+\ell)\,(1-\ell)\, b_{\ell\lambda} \\ T_4 &= -\epsilon\, Y^m_\ell\,(\theta_0,\, \phi_0)\, \alpha_g\, p^*\, C\, b_{\ell\lambda} \\ T_5 &= -\frac{\epsilon}{2.3026}\, Y^m_\ell\,(\theta_0,\, \phi_0)\, p^*\, C\, \frac{\partial\, b_{\ell\lambda}}{\partial\, \log\, g}. \end{aligned} \tag{3.81}$$

In this case:

$$B = R\,\nabla_{ad}\,\exp(i\,\Psi_T)\,C(\ell,\sigma). \tag{3.82}$$

3.4 Suggested improvements to the formula

.

Given the limitations of Watson's formula discussed in section 3.2.4 we propose some modifications to the formula in this section. Before we even consider modifying the formula to include the variation of eigenfunctions with depth in the stellar atmosphere, we consider the fact that the relation between $\frac{\delta g}{g}$ and $\frac{\delta r}{r}$ is complex. This introduces the amplitude parameter p' and the phase difference Ψ_g between $\frac{\delta g}{g}$ and $\frac{\delta r}{r}$. When these are introduced into Watson's formula we obtain:

$$\begin{aligned}\Delta m(\lambda,t) &= -1.086\epsilon Y_\ell^m(\theta_o,\phi_o)\{(T_1'+T_2')\exp(i\,\Psi_T)+ \\ &\quad T_3'+(T_4'+T_5')\,p'\,\exp(i\,\Psi_g)\}\exp(i\,\omega\,t), \qquad (3.83)\\ &\qquad (3.84)\end{aligned}$$

where:

$$\begin{aligned}T_1' &= \alpha_T\,\nabla_{ad}\,C\,b_{\ell\lambda}\\ T_2' &= \nabla_{ad}\,C\,\frac{1}{2.3026}\,\frac{\partial\,b_{\ell\lambda}}{\partial\,\log T_{\rm eff}}\\ T_3' &= (2+\ell)\,(1-\ell)\,b_{\ell\lambda} \qquad (3.85)\\ T_4' &= \alpha_g\,b_{\ell\lambda}\\ T_5' &= \frac{1}{2.3026}\,\frac{\partial\,b_{\ell\lambda}}{\partial\,\log g}.\end{aligned}$$

Therefore, parameters to be determined empirically are R_{ad}, Ψ_T, p' and Ψ_g. In chapter 4 we show that none of these parameters is constant with depth in the atmospheres of the roAp stars.

The pulsation phase is therefore given as:

$$\tan\,\phi_\lambda = \frac{\sin(\Psi_T+m\,\phi_0)+r_1\sin(m\,\phi_0)+r_2\sin(\Psi_T+m\,\phi_0)}{cos(\Psi_T+m\,\phi_0)+r_1\cos(m\,\phi_0)+r_2\cos(\Psi_g+m\,\phi_0)}, \tag{3.86}$$

where

$$r_1 = \frac{T_3}{T_1+T_2} \tag{3.87}$$

and

$$r_2 = \frac{T_4+T_5}{T_1+T_2}. \tag{3.88}$$

The parameter r_1 is the ratio of geometry to temperature variations, and r_2 gives the ratio of perturbations in gravity to that in temperature, so it depends on the ratio p'/R_{ad}. It would be interesting to see how this ratio varies for different pulsating stars.

An even better approach is to calculate different terms from the solutions of the non-adiabatic pulsation equations in the atmospheres of stars. We do this in the following manner: Consider the following equation:

$$\frac{\delta F_\lambda}{F_{0\lambda}} = \int_S h_\lambda \left(\frac{\delta h_\lambda}{h_\lambda}\right) d\omega_0 + \int_S (\mu' - \mu) \frac{\partial h_\lambda}{\partial \mu} d\omega_0 + \int_S h_\lambda \delta d\omega + \int_S \frac{\delta I_\lambda}{I_{0\lambda}} h_\lambda d\omega_0, \tag{3.89}$$

which comes from equation (3.42). The second and third terms are the T_3 which is purely analytical. $\frac{\delta I_\lambda}{I_{0\lambda}}$ and $\frac{\delta I_\lambda}{I_\lambda}$ and are obtainable from the solution of the non-adiabatic equations as described in chapter 4. We then obtain $\frac{\delta h_\lambda}{h_\lambda}$ from

$$\frac{\delta h_\lambda}{h_\lambda} = \frac{\delta I_\lambda}{I_\lambda} - \frac{\delta I_{0\lambda}}{I_{0\lambda}}. \tag{3.90}$$

Chapter 4

Non–adiabatic studies

In this chapter we solve non-adiabatic radial pulsation equations in the interior of a star. We do this by dividing the star into two regions, the atmosphere and the envelope. The treatment of oscillations in the atmosphere as implemented in our code is discussed in detail in sections 4.2. The inclusion of the envelope in our code is discussed in section 4.3. The two regions are put together in section 4.4 where various tests on the code are discussed.

4.1 Equilibrium Model

For the radial studies of the oscillations of the roAp stars, the equilibrium models were calculated using the ATLAS9 model atmosphere program (Kurucz 1993). Our code calculates the intensities using the Feautrier method (Mihalas & Mihalas 1984, and Rutten *http : //www.astro.uu.nl/ ~ rutten*), which was quicker and easier to handle than solving the transfer equation as is done in the ATLAS9 program. The details of the Feautrier method are given in the next subsection.

4.1.1 The Feautrier method for solving the transfer equation

Here the transfer equation is cast as a second order boundary value problem. The condition we impose at the top boundary is that of zero incoming radiation, at the bottom of the atmosphere we impose the diffusion approximation. The Feautrier method is demonstrated for the transfer equation with Rosseland opacity. The general results that include scattering are straightforward and will be given without derivations at the end of next subsection.

Equations

If the outgoing intensity is denoted as $I^+(+\mu)$ and inward-going as $I^-(-\mu)$ we define a mean- intensity-like variable:

$$j = \frac{1}{2}\left(I^+(+\mu) + I^-(-\mu)\right), \tag{4.1}$$

and the flux-like variable:

$$h = \frac{1}{2}\left(I^{+}(+\mu) - I^{-}(-\mu)\right). \tag{4.2}$$

Both cases apply for $0 \leq \mu \leq 1$.

We apply the radiative transfer equation $\mu\frac{dI}{d\tau} = I - S$ to both $I^{+}(+\mu)$ and $I^{-}(-\mu)$, thus:

$$+\mu\frac{d\,I^{+}}{d\,\tau} = I^{+} - S \tag{4.3}$$

and

$$-\mu\frac{d\,I^{-}}{d\,\tau} = I^{-} - S. \tag{4.4}$$

Add equations (4.3) and (4.4) to get:

$$\mu\frac{d\,(I^{+} - I^{+})}{d\,\tau} = (I^{+} + I^{-}) - 2S, \tag{4.5}$$

which is

$$\mu\frac{d\,h}{d\,\tau} = j - S. \tag{4.6}$$

Subtracting equation (4.4) from (4.3) we get:

$$\mu\frac{d\,j}{d\,\tau} = h. \tag{4.7}$$

Combining equations (4.6) and (4.7) we get:

$$\mu^{2}\frac{d^{2}\,j}{d\,\tau^{2}} = j - S. \tag{4.8}$$

Note that

$$I^{+} = h + j. \tag{4.9}$$

The three intensity moments are defined as the mean intensity, given as:

$$J(\tau) = \int I(\theta,\,\phi)\,d\Omega, \tag{4.10}$$

the Eddington flux, given as:

$$H(\tau) = \int I(\theta,\,\phi)\cos\theta\,d\Omega, \tag{4.11}$$

and the second moment which is proportional to radiation pressure is given as:

$$K(\tau) = \int I(\theta,\,\phi)\cos^{2}\theta\,d\Omega, \tag{4.12}$$

where Ω is the solid angle and the integrals are over the whole visible stellar surface.

For large optical depths, there is a near cancellation of j with S, resulting in instabilities in the calculations. To avoid these we realise that at large τ, the intensity assumes a simple form, and the radiation flux is given by the temperature gradient, in much the same way that diffusion processes involve flow of material as a result of gradients (concentration gradient for gas diffusion, or temperature gradient in the case of heat diffusion, *etc.*). Mihalas (1978) shows that under these conditions the solution of the transfer equation results in:

$$I(\tau,\mu) = B(\tau) + \mu\frac{dB}{d\tau} + \mu^2\frac{d^2B}{d\tau^2} + ... \tag{4.13}$$

The Eddington flux becomes:

$$H(\tau) = \frac{1}{3}\frac{dB}{d\tau} + ..., \tag{4.14}$$

the mean intensity becomes:

$$J(\tau) = B(\tau) + \frac{1}{3}\frac{d^2B}{d\tau^2} + ... \tag{4.15}$$

and the second order moment ($K(\tau)$) which is related to radiation pressure becomes:

$$K(\tau) = \frac{1}{3}B(\tau) + \frac{1}{5}\frac{d^2B}{d\tau^2} \tag{4.16}$$

We used equations (4.15) and (4.9) to calculate the Feautrier h at large τ with the following equation:

$$h = B(\tau) + \mu\frac{dB}{d\tau} + \mu^2\frac{d^2B}{d\tau^2} - j. \tag{4.17}$$

Moments of the transfer equation

With the moments of the transfer equation expressed in terms of the Feautrier variables, the derivations follow. The mean intensity J (also called zeroth moment) is given as:

$$J(\tau) = \frac{1}{2}\int_{-1}^{0} I^-(-\mu)\,d(-\mu) + \frac{1}{2}\int_{0}^{+1} I^+(\mu)\,d\mu \tag{4.18}$$

and can be expressed as:

$$J(\tau) = \frac{1}{2}\int_{0}^{+1} I^-(-\mu)\,d\mu + \frac{1}{2}\int_{0}^{+1} I^+(\mu)\,d\mu. \tag{4.19}$$

Thus in terms of j (from 4.1) we get

$$J(\tau) = \int_{0}^{1} j(\mu)\,d\mu. \tag{4.20}$$

The Eddington Flux (H) (first moment) is given as:

$$H(\tau) = \frac{1}{2}\int_{-1}^{0} I^{-}(-\mu)\,(-\mu)\,d\,(-\mu) + \frac{1}{2}\int_{0}^{+1} I^{+}(\mu)\,\mu\,d\,\mu. \tag{4.21}$$

In terms of h we get:

$$H(\tau) = \int_{0}^{1} h(\mu)\,\mu\,d\,\mu. \tag{4.22}$$

And the second moment K is:

$$K(\tau) = \frac{1}{2}\int_{-1}^{0} I^{-}(-\mu)\,\mu^2\,d\,(-\mu) + \frac{1}{2}\int_{0}^{+1} I^{+}(\mu)\,\mu^2\,d\,\mu, \tag{4.23}$$

which results in:

$$K(\tau) = \int_{0}^{1} j(\mu)\,\mu^2\,d\,\mu. \tag{4.24}$$

4.1.2 Boundary conditions

At the surface of a star we expect to have no radiation from the outside, *i.e.* $I^{-}(-\mu) = 0$. In terms of the Feautrier variables (h and j) we get $h(\tau = 0) = \frac{1}{2}I^{+}$ and $j(\tau = 0) = \frac{1}{2}I^{+}$, so from (4.7) we get, at the upper boundary:

$$\mu\frac{d\,j(0)}{d\,\tau} = j(0). \tag{4.25}$$

We assume a semi-infinite atmosphere, and require radiative transfer to take the form of diffusion approximation: $I(\tau_{max}) = B(\tau_{max}) + \mu\frac{dB}{d\tau}\,|_{\tau=\tau_{max}}$, with $j = B(\tau_{max})$. Therefore we get

$$\frac{d\,j}{d\,\tau}\,|_{\tau=\tau_{max}} = \frac{d\,B}{d\,\tau}\,|_{\tau=\tau_{max}} \tag{4.26}$$

as the boundary condition at the bottom of the atmosphere.

4.1.3 Results

Equation (4.8) was solved using twenty limb-darkening angles (μ values) to calculate the radiation moments. Fig. 4.1 plots the τ dependence of $J(\tau)$ compared to $B(\tau)$. As is expected, $J(\tau)$ approaches $B(\tau)$ at greater τ values. $H(\tau)$ is plotted in Fig. 4.2. In Fig. 4.3 we plot the run of Eddington factor $f_{osc}(\tau) = \frac{K(\tau)}{J(\tau)}$, we notice that $f_{osc} \rightarrow \frac{1}{3}$ at greater depths as is expected from the diffusion approximation.

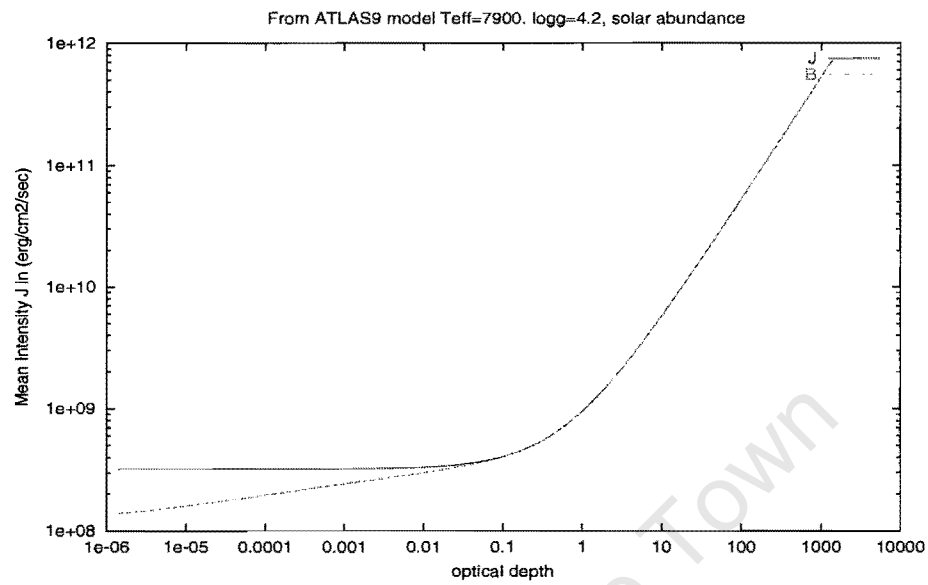

Figure 4.1: The depth dependence of the equilibrium grey mean intensity J and the frequency-integrated Planck function B for model parameters $T_{\rm eff} = 7900\,{\rm K}$, $\log {\rm g} = 4.2$. Note that already at $\tau = \frac{2}{3}$ the condition $J = B$ is satisfied. For lower optical depth J departs from B.

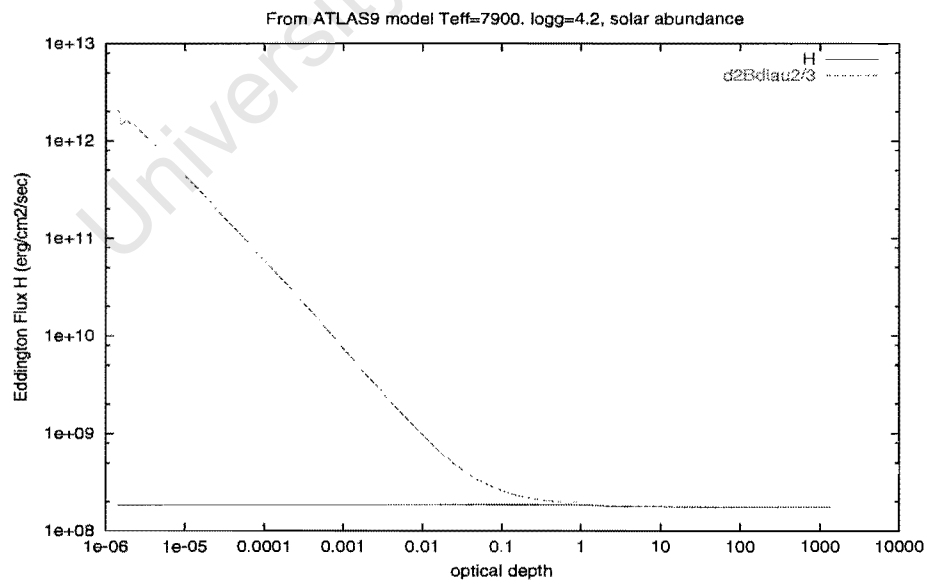

Figure 4.2: The depth dependence of equilibrium grey Eddington flux H for the same model atmosphere as in Fig. 4.1. H approaches $\frac{1}{3}\frac{dB}{d\tau}$ at large τ as expected from the diffusion approximation, equation (4.14).

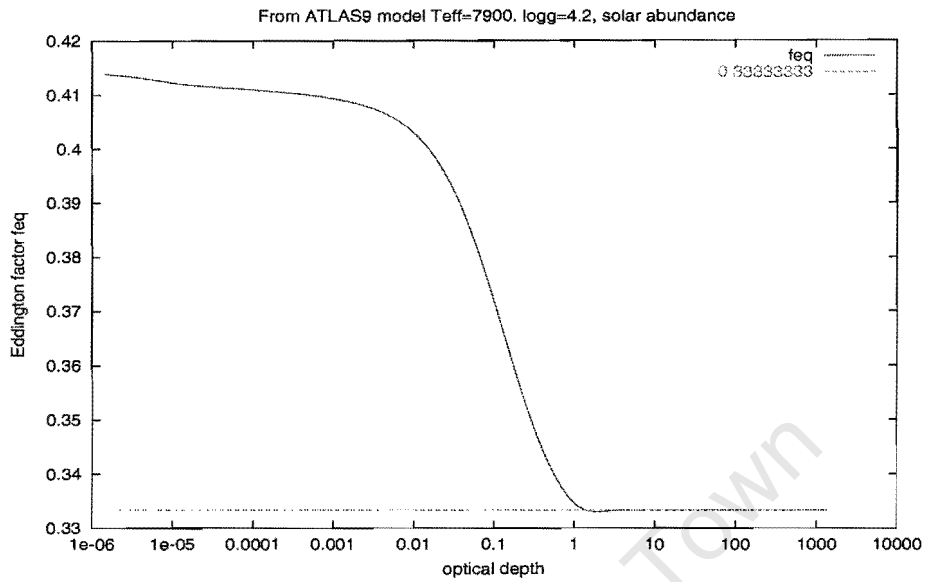

Figure 4.3: The depth dependence of equilibrium grey $f_{eq} = \frac{K}{J}$ for the same model atmosphere as in Fig. 4.1. Note that at large τ the condition $f_{eq} = \frac{1}{3}$ as is expected from the diffusion approximation. Near the surface the diffusion approximation does not apply, and consequently f_{eq} departs from $\frac{1}{3}$. Here the improved Eddington approximation (*cf.* Mihalas 1978, p.63) show that $f_{eq}(\tau = 0) = 0.405$ compared to our 0.404768.

4.2 Radial pulsation equations in the atmosphere

Since we are not concerned with pulsations in the deeper layers of the stars, we do not need to treat the equilibrium star as a complete sphere. In fact in cool main sequence A stars the atmospheres are so thin compared to the total stellar radius that they can be considered plane-parallel. Moreover, since we are only concerned with radial perturbations, the horizontal components will be completely ignored in the following formulation. In other words we use the following assumptions:

1. plane parallel atmospheres,
2. purely radial motions.

The consequence of items 1 and 2 is that the expressions for gradient (∇V) and divergence ($\nabla \cdot F$) simplify to

$$\nabla V = \frac{\partial V}{\partial r} \tag{4.27}$$

and

$$\nabla \cdot \vec{F} = \frac{\partial \vec{F}_r}{\partial r}. \tag{4.28}$$

We derive the pulsation equations below:

The continuity equation in plane parallel atmosphere

The unperturbed continuity equation becomes:

$$\frac{d\rho}{dt} + \rho\frac{dv}{dr} = 0. \tag{4.29}$$

Applying perturbations in a straightforward manner results in:

$$\frac{d\delta\rho}{dt} + \rho\frac{\partial\delta\vec{v}}{\partial r} = 0, \tag{4.30}$$

where d/dt is the Lagrangian time derivative explained in the subsection 1.4. Integrating with respect to time and remembering that $\delta v = \frac{d\delta r}{dt}$ we get:

$$\frac{d\delta r}{dr} = -\frac{\delta\rho}{\rho}. \tag{4.31}$$

The equation of motion in plane parallel atmosphere

Firstly, we use the convention that the magnitude of any vector pointing inwards is negative, and that pointing radially outwards positive, so that, for example, the gravity vector $\vec{g} = -g\,\vec{e_r}$. Therefore, the equation of motion becomes:

$$\rho\frac{dv}{dt} = -\frac{dP}{dr} - \rho g + f_{turb}\rho, \tag{4.32}$$

where f_{turb} is the force per unit mass due to turbulence. We will use the mass variable $dm = \rho dr$ in the plane-parallel case, since the Lagrangian perturbation commutes with d/dm and not with d/dr. Upon perturbing the above equation and taking $\delta f_{turb} = 0$ we get:

$$\frac{dv_o}{dt} + \frac{d\delta v}{dt} = -\frac{dP}{dm} - \frac{d\delta P}{dm} - \tilde{g} - \delta g. \tag{4.33}$$

We expect an infinitely slow uniform vertical displacement to be part of the solution if we assume $\delta f_{turb} = 0$. One of the assumptions we made in section 1.4 is that the equilibrium star is static, therefore all time derivatives of equilibrium quantities vanish. We also assume the time dependence of perturbed quantities to be of the form $\exp(-i\omega t)$, therefore equation (4.33) becomes:

$$\omega^2\delta r = \left(\frac{dP}{dm} + \frac{d\delta P}{dm}\right) + \tilde{g} + \delta g, \tag{4.34}$$

where δg is the Lagrangian perturbation in gravity. For radial oscillations Christensen-Dalsgaard (1998) shows that the perturbations in the gravitational potential is related to the displacement in the following manner:

$$\frac{d\Phi'}{dr} = g' = 4\pi G\rho\delta r \tag{4.35}$$

where Φ' is the Eulerian perturbation in gravitational potential and G is the gravitational constant. Transforming the above equation to Lagrangian form we obtain:

$$\delta g = (dg/dr + 4\pi G\rho)\,\delta r \tag{4.36}$$

Using the following relation

$$\frac{d}{dm}\left(\frac{\delta P}{P}\right) = \frac{1}{P}\frac{d\delta P}{dm} - \frac{\delta P}{P^2}\frac{dP}{dm}, \tag{4.37}$$

and the hydrostatic support equation $\frac{dP}{dm} = -g$ we end up with this equation:

$$\frac{[(\omega^2 - dg/dr - 4\pi G\rho)\,\delta r - \tilde{g}]}{P} = \frac{d}{dm}\left(\frac{\delta P}{P}\right) - \frac{\tilde{g}}{P}\left(\frac{\delta P}{P} + 1\right) \tag{4.38}$$

which can be rearranged to

$$\frac{d}{dr}\left(\frac{\delta P}{P}\right) = \frac{\rho}{P}\left[\tilde{g}\frac{\delta P}{P} + (\omega^2 - dg/dr - 4\pi G\rho)\,\delta r\right]. \tag{4.39}$$

The sum of the dg/dr and $4\pi G\rho$ ranges from about 10^{-7} s^{-2} in the A stellar atmospheres to 10^{-4} s^{-2} in the envelope. Therefore, this sum can be ignored in the atmosphere and the equation of motion becomes similar to equation (2.5) of Christensen-Dalsgaard & Frandsen (1983). In the atmosphere, we will therefore not include the gravitational perturbations terms, but will include them in the envelope.

The energy equation in plane parallel atmosphere

The energy equation becomes:

$$i\omega\left(\frac{\delta T}{T} - \nabla_{ad}\frac{\delta P}{P}\right) = \frac{1}{\rho c_p T}\delta\left(\frac{dF_R}{dr}\right). \tag{4.40}$$

In order to determine $\delta\left(\frac{dF_R}{dr}\right)$ we first obtain $\frac{dF_R}{dr}$ from the radiative transfer equation, then perturb the results. The following derivations are a review of those presented in Christensen-Dalsgaard & Frandsen (1983). The transfer equation in the plane parallel case, with isotropic scattering terms is of this form:

$$\mu\frac{dI_\nu}{dr} = \rho\kappa_{a\nu}B_\nu + \rho\kappa_{s\nu}J_\nu - \rho\left(\kappa_{a\nu} + \kappa_{s\nu}\right)I_\nu, \tag{4.41}$$

where $\kappa_{a\nu}$ is the cross-section for all the absorption processes, and that for the scattering processes is denoted by $\kappa_{s\nu}$. The difficulty in solving equation (4.41) can be appreciated by noting that it includes $J_\nu = \frac{1}{2}\int_{-1}^{1} I_\nu(\mu)\,d\mu$, it is therefore an integro-differential equation. We define flux in the radial direction as

$$F_R = 4\pi\int_0^\infty H_\nu\,d\nu\,\vec{e_r}, \tag{4.42}$$

where H_ν is the Eddington flux defined in equation (4.21). Equation (4.41) is then integrated over $\mu \epsilon [-1, +1]$ to obtain this expression of H_ν:

$$\frac{d\,H_\nu}{d\,r} = \rho\,\kappa_{a\,\nu}\,(B_\nu - J_\nu). \tag{4.43}$$

Note that the scattering terms cancel, and B_ν, J_ν do not depend on μ. Upon integrating over ν and applying our definition of F_R we get:

$$\frac{d\,F_R}{d\,r} = 4\pi\rho \int_0^\infty \kappa_{a\,\nu}\,(B_\nu - J_\nu)\,d\,\nu. \tag{4.44}$$

Since we are going to neglect effects on the spectral lines such as Doppler shifts *etc.*, we can perturb and linearise equation (4.44) in a straightforward manner to obtain:

$$\frac{d\,\delta\,F_R}{d\,r} = \frac{\delta\rho}{\rho}\frac{d\,F_R}{d\,r} + 4\pi\rho \int_0^\infty \{\delta\kappa_{a\,\nu}(B_\nu - J_\nu) + \kappa_{a\,\nu}(\delta B_\nu - \delta J_\nu)\}\,d\,\nu. \tag{4.45}$$

When equation (4.45) is substituted into equation (4.40) we obtain a relationship between $\frac{\delta T}{T}$, $\frac{\delta\rho}{\rho}$ and $\frac{\delta P}{P}$. We reduce the number of dependent variables by expressing $\frac{\delta T}{T}$ in terms of $\frac{\delta P}{P}$ only. This can be done by realising that $\rho = \rho(T, P)$ and $\kappa_{a\,\nu} = \kappa_{a\,\nu}(T, P)$. Therefore perturbations in ρ and $\kappa_{a\,\nu}$ can be written respectively as:

$$\frac{\delta\rho}{\rho} = \rho_T\frac{\delta\,T}{T} + \rho_P\frac{\delta\,P}{P}, \tag{4.46}$$

where $\rho_T = \frac{\partial \ln\rho}{\partial \ln T}\,|_P$ and $\rho_P = \frac{\partial \ln\rho}{\partial \ln P}\,|_T$, and

$$\frac{\delta\kappa_{a\,\nu}}{\kappa_{a\,\nu}} = \kappa_{a\,\nu\,T}\frac{\delta\,T}{T} + \kappa_{a\,\nu\,P}\frac{\delta\,P}{P}, \tag{4.47}$$

where $\kappa_{a\,\nu\,T} = \frac{\partial \ln\kappa_{a\,\nu}}{\partial \ln T}\,|_P$ and $\kappa_{a\,\nu\,P} = \frac{\partial \ln\kappa_{a\,\nu}}{\partial \ln P}\,|_T$.

Another relation worth noting is that the Planck function depends on temperature only (it also depends on wavelength of observation, but since we do not consider perturbation in wavelength, this statement is true), *i.e.* $B_\nu = B_\nu(T)$. Therefore:

$$\delta\,B_\nu = \left(T\frac{d\,B_\nu}{d\,T}\right)\frac{\delta\,T}{T}. \tag{4.48}$$

Substituting equations (4.46), (4.47) and (4.48) into equation (4.45), and putting the result into equation (4.40) we get the following equation:

$$\frac{\delta\,T}{T}\left\{i\omega - \frac{4\pi}{c_p\,T}\int_0^\infty \left(\kappa_{a\,\nu}(B_\nu - J_\nu)(\rho_T + \kappa_{a\,\nu\,T}) + \kappa_{a\,\nu}T\frac{d\,B_\nu}{d\,T}\right)\,d\,\nu\right\} =$$
$$\frac{\delta\,P}{P}\left\{\frac{4\pi}{c_p\,T}\int_0^\infty \kappa_{a\,\nu}(\kappa_{a\,\nu\,P} + \rho_P)(B_\nu - J_\nu)\,d\,\nu + i\omega\nabla_{ad}\right\} - \frac{4\pi}{c_p\,T}\int_0^\infty \kappa_{a\,\nu}\delta\,J_\nu\,d\,\nu. \tag{4.49}$$

We therefore still need to determine δJ_ν in order to obtain $\frac{\delta T}{T}$. For this we perturb the transfer equation (equation (4.41)). We use the mass variable (for the same reason as in equation (4.33) $dm = \rho dr$, then in a straightforward manner we obtain:

$$\mu \frac{d\delta I}{dm} = \kappa_{s\nu}\delta J_\nu + \delta\kappa_{s\nu} J_\nu + \kappa_{a\nu}\delta B_\nu + \delta\kappa_{a\nu} B_\nu - (\kappa_{s\nu} + \kappa_{a\nu})\delta I_\nu - (\delta\kappa_{s\nu} + \delta\kappa_{a\nu}) I_\nu. \quad (4.50)$$

To obtain the perturbed transfer equation with no scattering we set all $\kappa_{s\nu}$ and $\delta\kappa_{s\nu}$ to zero. This can also be verified by perturbing $\mu\frac{dI_\nu}{dm} = \kappa_{a\nu}(B_\nu - I_\nu)$.

The moments of the perturbed transfer equation become:

$$\delta J_\nu(r) = \frac{1}{2}\int_{-1}^{+1} \delta I_\nu(\mu, r)\, d\mu \quad (4.51)$$

$$\delta H_\nu(r) = \frac{1}{2}\int_{-1}^{+1} \delta I_\nu(\mu, r)\mu\, d\mu \quad (4.52)$$

$$\delta K_\nu(r) = \frac{1}{2}\int_{-1}^{+1} \delta I_\nu(\mu, r)\mu^2\, d\mu. \quad (4.53)$$

If equation (4.50) is integrated over μ on both sides, one obtains:

$$\frac{d\delta H_\nu}{dr} = \rho\left\{\delta\kappa_{a\nu}(B_\nu - J_\nu) + \kappa_{a\nu}(\delta B_\nu - \delta J_\nu)\right\}. \quad (4.54)$$

Multiplying equation (4.50) by μ and integrating over $\mu\epsilon[-1, 1]$ results in:

$$\frac{d\delta K_\nu}{dr} = -\rho\left(\delta\kappa_\nu H_\nu + \kappa_\nu\delta H_\nu\right), \quad (4.55)$$

where $\kappa_\nu = \kappa_{s\nu} + \kappa_{a\nu}$ and $\delta\kappa_\nu = \delta\kappa_{s\nu} + \delta\kappa_{a\nu}$.

Equations (4.31), (4.39), (4.54) and (4.55) form a system of 4 equations with five dependent variables (δr, $\frac{\delta P}{P}$, δJ_ν, δH_ν and δK_ν). To close the system we need to relate two of those variables. δJ_ν and δK_ν can be related by a variable Eddington factor $f_{osc} = \frac{\delta K_\nu}{\delta J_\nu}$. However, since f_{osc} is not known beforehand, the system of equations will have to be solved by making initial guess of f_{osc}, then improving that value by iteration.

Christensen-Dalsgaard & Frandsen (1983) suggested the following procedure for solving this system of equations:

1. Make an initial estimate of $f_{osc} = f_{eq}$, where $f_{eq} = \frac{K_\nu}{J_\nu}$ is the equilibrium Eddington factor.
2. Solve the system of equations (4.31), (4.39), (4.54) and (4.55) replacing $\delta J_\nu = \frac{\delta K_\nu}{f_{osc}}$.
3. Obtain $\delta\kappa_\nu$ from $\frac{\delta T}{T}$ and $\frac{\delta P}{P}$ calculated in (2) above using equations (4.49) and (4.47), then integrate equation (4.50) to obtain δI_ν.
4. Obtain δJ_ν and δK_ν from equations (4.51), and (4.53) respectively, and determine f_{osc}.
5. If f_{osc} has not converged, go to item number 2.

The perturbed transfer equation

Since the Feautrier method was used to solve the transfer equation (*cf.* section 4.1) numerically, our formulation will be based on Feautrier variables j_ν and h_ν. Note that Christensen-Dalsgaard & Frandsen (1983) do not use the Feautrier formulation, therefore, the formulation in this and the next subsection is entirely mine. Equations (4.6) and (4.7) can be expressed in terms of the mass variable in the following way:

$$\mu \frac{d\, h_\nu}{d\, m} = \kappa_{a\,\nu}(S_\nu - j_\nu), \tag{4.56}$$

and

$$\mu \frac{d\, j_\nu}{d\, m} = -\kappa_{a\,\nu}\, h_\nu. \tag{4.57}$$

For the case of no-scattering $S_\nu = B_\nu$. When equations (4.56) and (4.57) are perturbed the following respective equations are the results:

$$\mu \frac{d\, \delta\, h_\nu}{d\, \tau_\nu} = \frac{\delta \kappa_{a\,\nu}}{\kappa_{a\,\nu}} (j_\nu - B_\nu) + (\delta\, j_\nu - \delta\, B_\nu)\,, \tag{4.58}$$

$$\mu \frac{d\, \delta\, j_\nu}{d\, \tau_\nu} = \delta\, h_\nu + \frac{\delta \kappa_{a\,\nu}}{\kappa_{a\,\nu}}\, h_\nu. \tag{4.59}$$

Taking the derivative of equation (4.59), the above two equations can be put together to form a second order ordinary differential equation:

$$\mu^2 \frac{d^2\, \delta\, j_\nu}{d\, \tau_\nu^2} = \delta\, j_\nu - \delta\, B_\nu + \frac{\delta \kappa_{a\,\nu}}{\kappa_{a\,\nu}} (j_\nu - B_\nu) + \mu \frac{d}{d\, \tau_\nu} \left(\frac{\delta \kappa_{a\,\nu}}{\kappa_{a\,\nu}}\, h_\nu\right). \tag{4.60}$$

Moments of the perturbed transfer equation

Moments of the perturbed radiative transfer equation can be derived in a manner similar to that in section 4.1. I will only present them here:

$$\delta\, J_\nu = \int_0^1 \delta\, j_\nu(\mu)\, d\, \mu. \tag{4.61}$$

$$\delta\, H_\nu = \int_0^1 \delta\, h_\nu(\mu)\, \mu\, d\, \mu. \tag{4.62}$$

$$\delta\, K_\nu = \int_0^1 \delta\, j_\nu(\mu)\, \mu^2\, d\, \mu. \tag{4.63}$$

4.2.1 The non-grey case

Here we take into consideration the dependence on frequency of opacity in the stars that we want to model. Therefore the pulsation equations depend on depth and frequency of observations. We discretize the frequencies so that frequency varies from $\nu_{j=1}$ to $\nu_{j=Nf}$, where N_f is the number of discrete frequency points. Therefore optical depth is given as:

$$\tau_j = -\int_x^0 \kappa_j \, \rho \, x \, dx \tag{4.64}$$

where x is the physical depth in the star. Integrals over frequencies are evaluated as sums, so that for example,

$$\int_0^\infty f(\nu)\, d\nu \approx \sum_{i=1}^{N_f} f(\nu_i)\, w_i \tag{4.65}$$

where w_i is the integration coefficient obtained so as to minimize the error obtained in performing the above approximation. We use the w_i in ATLAS9 and obtained by fitting a quadratic to the function f by least squares method (Kurucz 1970).
If we collect the non-grey equations together we obtain:

$$\begin{aligned}
\frac{d\,\delta r}{d\,r} &= -\rho_T \frac{\delta T}{T} - \rho_P \frac{\delta P}{P} \\
\frac{d}{d\,r}\left(\frac{\delta P}{P}\right) &= \frac{\rho}{P}\left[\tilde{g}\frac{\delta P}{P} + \omega^2\, \delta r\right] \\
\frac{d\,\delta H_\nu}{d\,r} &= \rho\,\kappa_\nu \left[\frac{\delta \kappa_\nu}{\kappa_\nu}(B_\nu - J_\nu) + T\frac{d\,B_\nu}{d\,T}\frac{\delta T}{T} - \frac{\delta K_\nu}{f_{osc\,\nu}}\right] \\
\frac{d\,\delta K_\nu}{d\,r} &= -\rho\,\kappa_\nu \left[\frac{\delta \kappa_\nu}{\kappa_\nu} H_\nu + \delta H_\nu\right]
\end{aligned} \tag{4.66}$$

where in the third equation of the above system I substituted equation (4.48) and replaced δJ_ν using the variable Eddington factor. Applying equation (4.47) in the above system of pulsation equations we get:

$$\begin{aligned}
\frac{d\,\delta r}{d\,r} &= -\rho_T \frac{\delta T}{T} - \rho_P \frac{\delta P}{P} \\
\frac{d}{d\,r}\left(\frac{\delta P}{P}\right) &= \frac{\rho}{P}\left[\tilde{g}\frac{\delta P}{P} + \omega^2\, \delta r\right] \\
\frac{d\,\delta H_\nu}{d\,r} &= \rho\,\kappa_\nu \left[\{\kappa_{\nu T}(B_\nu - J_\nu) + T\frac{d\,B_\nu}{d\,T}\}\frac{\delta T}{T} + \kappa_{\nu P}(B_\nu - J_\nu)\frac{\delta P}{P} - \frac{\delta K_\nu}{f_{osc\,\nu}}\right] \\
\frac{d\,\delta K_\nu}{d\,r} &= -\rho\,\kappa_\nu \left[\kappa_{\nu T} H_\nu \frac{\delta T}{T} + \kappa_{\nu P} H_\nu \frac{\delta P}{P} + \delta H_\nu\right]
\end{aligned} \tag{4.67}$$

The above system of equations is not closed; there are five variables and four equations. If we substitute equation (4.49) into equations (4.67), they become coupled because equation (4.49) involves the integral of δJ_ν which is not known prior to solving the system. We approximate the integrals by the summation discussed above so that the temperature and pressure perturbations are related in this manner:

$$\frac{\delta T}{T} \approx \frac{c_2}{c_1}\frac{\delta P}{P} - \frac{4\pi}{c_p T}\frac{1}{c_1}\sum_i \frac{\kappa_i w_i \delta K_i}{f_{osci}}, \tag{4.68}$$

where c_1 is

$$c_1 = i\omega - \frac{4\pi}{c_p T}\int_0^\infty \left(\kappa_{a\nu}(B_\nu - J_\nu)(\rho_T + \kappa_{a\nu T}) + \kappa_{a\nu} T\frac{dB_\nu}{dT}\right) d\nu, \tag{4.69}$$

and c_2 is given thus:

$$c_2 = \frac{4\pi}{c_p T}\int_0^\infty \kappa_{a\nu}(\kappa_{a\nu P} + \rho_P)(B_\nu - J_\nu)\, d\nu + i\omega\nabla_{ad}. \tag{4.70}$$

We now substitute equation (4.68) into equations (4.67) to get

$$\begin{aligned}
\frac{d\delta r}{dr} &= -\left(\rho_T\frac{c_2}{c_1} + \rho_P\right)\frac{\delta P}{P} + \frac{4\pi\rho_T}{c_P T}\frac{1}{c_1}\sum_i q_i \delta K_i \\
\frac{d}{dr}\left(\frac{\delta P}{P}\right) &= \frac{\rho}{P}\left[\tilde{g}\frac{\delta P}{P} + \omega^2 \delta r\right] \\
\frac{d\delta H_j}{dr} &= \rho\kappa_j\left[\left\{\left(\kappa_{jT}(B_j - J_j) + T\frac{dB_j}{dT}\right)\frac{c_2}{c_1} + \kappa_{jP}(B_j - J_j)\right\}\frac{\delta P}{P}\right. \\
&\quad \left. -\frac{\delta K_j}{f_{oscj}} - \left(\kappa_{jT}(B_j - J_j) + T\frac{dB_j}{dT}\right)\frac{4\pi}{c_P T}\frac{1}{c_1}\sum_i q_i\delta K_i\right] \\
\frac{d\delta K_j}{dr} &= -\rho\kappa_j\left[H_j\left(\kappa_{jT}\frac{c_2}{c_1} + \kappa_{jP}\right)\frac{\delta P}{P} - \frac{4\pi\kappa_{jT}H_j}{c_P T}\frac{1}{c_1}\sum_i q_i\delta K_i + \delta H_j\right]
\end{aligned} \tag{4.71}$$

where

$$q_i = \frac{\kappa_i w_i}{f_{osci}} \tag{4.72}$$

If we use the Rosseland optical depth as the independent variable (in place of the radial distance), we obtain the following system:

$$\begin{aligned}
\frac{d\delta r}{d\tau_R} &= \frac{1}{\kappa_R\rho}\left(\rho_T\frac{c_2}{c_1} + \rho_P\right)\frac{\delta P}{P} - \frac{4\pi\rho_T}{c_P T}\frac{1}{c_1}\frac{1}{\kappa_R\rho}\sum_i q_i\delta K_i \\
\frac{d}{d\tau_R}\left(\frac{\delta P}{P}\right) &= -\frac{1}{\kappa_R P}\left[\tilde{g}\frac{\delta P}{P} + \omega^2\delta r\right] \\
\frac{d\delta H_j}{d\tau_R} &= -\frac{\kappa_j}{\kappa_R}\left[\left\{\left(\kappa_{jT}(B_j - J_j) + T\frac{dB_j}{dT}\right)\frac{c_2}{c_1} + \kappa_{jP}(B_j - J_j)\right\}\frac{\delta P}{P}\right.
\end{aligned}$$

$$-\frac{\delta K_j}{f_{osc\,j}} - \left(\kappa_{jT}(B_j - J_j) + T\frac{dB_j}{dT}\right)\frac{4\pi}{c_P T}\frac{1}{c_1}\sum_i q_i \delta K_i\Bigg] \tag{4.73}$$

$$\frac{d\delta K_j}{d\tau_R} = \frac{\kappa_j}{\kappa_R}\left[H_j\left(\kappa_{jT}\frac{c_2}{c_1} + \kappa_{jP}\right)\frac{\delta P}{P} - \frac{4\pi\kappa_{jT}H_j}{c_P T}\frac{1}{c_1}\sum_i q_i \delta K_i + \delta H_j\right]$$

We then introduce the following scaling in the dependent variables:

$$\delta r = H_P \delta\tilde{r}, \quad \delta H_j = H_{0j}\delta\tilde{H}_j, \quad \delta K_j = K_{0j}\delta\tilde{K}_j, \tag{4.74}$$

where H_P is the pressure scale height, H_{0j} and K_{0j} are the monochromatic equilibrium values of the Eddington flux and the second moment of the radiative transfer equation all evaluated at $\tau_R = 2/3$.

Applying the above scalings to the system (4.73) leads to

$$\begin{aligned}
\frac{d\delta\tilde{r}}{d\tau_R} &= \frac{1}{\kappa_R\rho}\left(\rho_T\frac{c_2}{c_1} + \rho_P\right)\frac{\delta P}{P} - \frac{4\pi\rho_T}{c_P T}\frac{1}{c_1}\frac{1}{\kappa_R\rho}\sum_i \tilde{q}_i\delta\tilde{K}_i \\
\frac{d}{d\tau_R}\left(\frac{\delta P}{P}\right) &= -\frac{1}{\kappa_R P}\left[\tilde{g}\frac{\delta P}{P} + \omega^2 H_P\delta\tilde{r}\right] \\
\frac{d\delta\tilde{H}_j}{d\tau_R} &= -\frac{\kappa_j}{\kappa_R}\frac{1}{H_{0j}}\Bigg[\left\{\left(\kappa_{jT}(B_j - J_j) + T\frac{dB_j}{dT}\right)\frac{c_2}{c_1} + \kappa_{jP}(B_j - J_j)\right\}\frac{\delta P}{P} \\
&\quad -\frac{K_{0j}\delta\tilde{K}_j}{f_{osc\,j}} - \left(\kappa_{jT}(B_j - J_j) + T\frac{dB_j}{dT}\right)\frac{4\pi}{c_P T}\frac{1}{c_1}\sum_i \tilde{q}_i\delta\tilde{K}_i\Bigg] \qquad (4.75) \\
\frac{d\delta\tilde{K}_j}{d\tau_R} &= \frac{\kappa_j}{\kappa_R}\frac{1}{K_{0j}}\left[H_j\left(\kappa_{jT}\frac{c_2}{c_1} + \kappa_{jP}\right)\frac{\delta P}{P} - \frac{4\pi\kappa_{jT}H_j}{c_P T}\frac{1}{c_1}\sum_i \tilde{q}_i\delta\tilde{K}_i + \delta H_j\right]
\end{aligned}$$

where

$$\tilde{q}_i = \frac{\kappa_i w_i K_{0i}}{f_{osc\,i}}. \tag{4.76}$$

Therefore, if we let

$$y_1 = \delta\tilde{r}, \quad y_2 = \frac{\delta P}{P}, \quad y_k = \delta\tilde{H}_j \quad \text{and} \quad y_{k+1} = \delta\tilde{K}_j \tag{4.77}$$

for $k = 2j + 1$, the system we solve for is of the form

$$\begin{aligned}
\frac{dy_1}{d\tau_R} &= p_1 y_2 - p_2\sum_i \tilde{q}_i y_{2i+2} \\
\frac{dy_2}{d\tau_R} &= -p_3 y_2 - p_4 y_1 \qquad (4.78) \\
\frac{dy_k}{d\tau_R} &= -p_{5,j}\,y_2 + p_{6,j}\sum_i \tilde{q}_i y_{2i+2} + p_{7,y_{k+1}} \\
\frac{dy_{k+1}}{d\tau_R} &= p_{8,j}\,y_2 - p_{9,j}\sum_i \tilde{q}_i y_{2i+2} + p_{10,j}\,y_k
\end{aligned}$$

(4.79)

The coefficients are given below:

$$
\begin{aligned}
p_1 &= \frac{1}{\kappa_R \rho}\left(\rho_T \frac{c_2}{c_1} + \rho_P\right) \\
p_2 &= \frac{4\pi \rho_T}{c_P T}\frac{1}{c_1}\frac{1}{\kappa_R \rho} \\
p_3 &= \frac{\tilde{g}}{\kappa_R P} \\
p_4 &= \frac{\omega^2 H_P}{\kappa_R P} \\
p_{5,j} &= \frac{\kappa_j}{\kappa_R}\frac{1}{H_{0j}}\left\{\left(\kappa_{jT}\left(B_j - J_j\right) + T\frac{dB_j}{dT}\right)\frac{c_2}{c_1} + \kappa_{jP}\left(B_j - J_j\right)\right\} \\
p_{6,j} &= \left\{\kappa_{jT}\left(B_j - J_j\right) + T\frac{dB_j}{dT}\right\}\frac{4\pi}{c_P T}\frac{1}{c_1}\frac{\kappa_j}{\kappa_R}\frac{1}{H_{0j}} \\
p_{7,j} &= \frac{\kappa_j}{\kappa_R}\frac{K_{0j}}{H_{0j}}\frac{1}{f_{oscj}} \\
p_{8,j} &= \frac{\kappa_j}{\kappa_R}\frac{H_j}{K_{0j}}\left(\kappa_{jT}\frac{c_2}{c_1} + \kappa_{jP}\right) \\
p_{9,j} &= \frac{4\pi \kappa_{jT} H_j}{c_P T K_{0j}}\frac{1}{c_1}\frac{\kappa_j}{\kappa_R} \\
p_{10,j} &= \frac{H_{0j}\kappa_j}{K_{0j}\kappa_R}
\end{aligned}
\tag{4.80}
$$

4.2.2 The grey case

In the grey atmosphere the opacity is independent of the frequency of radiation. This will of course not change the form of equations (4.31) and (4.39). It is easy to show that after the perturbed transfer equation (4.50) and equation (4.55) are integrated over ν, they will not change form. However, equation (4.49) simplifies to:

$$
\begin{aligned}
&\left\{i\omega - \omega_R\left(4 - \Delta_c\left(\kappa_{aT} + \rho_T\right)\right)\right\}\frac{\delta T}{T} = \\
&\left\{i\omega\nabla_{ad} - \omega_R\Delta_c(\kappa_{aP} + \rho_P)\right\}\frac{\delta P}{P} - \omega_R\frac{\delta J}{B},
\end{aligned}
\tag{4.81}
$$

where $\omega_R = \frac{4\pi B \kappa_a}{c_p T}$ is the characteristic radiative relaxation rate in the optically thin limit, B is the frequency–integrated Planck function, $\delta J = \int_0^\infty \delta J_\nu \, d\nu$ and $\Delta_c = J/B - 1 = -\frac{divF_R}{4\pi\rho\kappa_a B}$ is a measure of the departure from radiative equilibrium.

Equation (4.81) can be rewritten as:

$$
\left\{i - \frac{\omega_R}{\omega}\left(4 - \Delta_c\left(\kappa_{aT} + \rho_T\right)\right)\right\}\frac{\delta T}{T} =
$$

$$\left\{ i\,\nabla_{ad} - \frac{\omega_R}{\omega}\Delta_c(\kappa_a{}_P + \rho_P) \right\} \frac{\delta P}{P} - \frac{\omega_R}{\omega}\frac{\delta J}{B}, \tag{4.82}$$

Therefore, areas where $\frac{\omega_R}{\omega}$ is much smaller than one oscillate adiabatically since then the second term on the left-hand side of the above equation can be ignored. The second and third terms on the right-hand side can also be ignored leaving us with

$$\frac{\delta T}{T} - \nabla_{ad}\frac{\delta P}{P} = 0. \tag{4.83}$$

Another simple relation can be derived if one notices that in the stellar interior $\Delta_c \longrightarrow 0$, then equation (4.81) becomes:

$$\left(i\frac{\omega}{\omega_R} - 4 \right) \frac{\delta T}{T} = i\frac{\omega}{\omega_R}\frac{\delta P}{P} - \frac{\delta J}{J}. \tag{4.84}$$

Since ω_R increases with depth, the areas where $\frac{\omega}{\omega_R}$ is so small as to be ignored will have $\frac{\delta T}{T}$ and $\frac{\delta J}{J}$ related as:

$$\frac{\delta J}{J} = 4\frac{\delta T}{T} \tag{4.85}$$

Hence, at large depths where radiative equilibrium is also a valid assumption, the above relation is expected to hold true. When equation (4.54) is integrated over ν it takes this form:

$$\frac{d\,\delta H}{d\,r} = \rho\,\kappa\,B\left[\frac{\delta\kappa}{\kappa}(1 - \frac{J}{B}) + \frac{T}{B}\frac{dB}{dT}\frac{\delta T}{T} - \frac{\delta J}{B} \right] \tag{4.86}$$

Noting that

$$\frac{T}{B}\frac{dB}{dT} = 4 \tag{4.87}$$

for grey Planck function B, and substituting equation (4.81) into the equation (4.86) we obtain the following:

$$\frac{d\,\delta H}{d\,r} = \rho\,\kappa\,B\left[-\frac{\delta\kappa}{\kappa}\Delta_c + 4\frac{c_2}{c_1}\frac{\delta P}{P} - \frac{\delta J}{B}\frac{1}{c_1}(4\,\omega_R + c_1) \right] \tag{4.88}$$

where

$$c_1 = i\,\omega - \omega_R\left(4 - \Delta_c(\kappa_a{}_T + \rho_T)\right), \tag{4.89}$$

and

$$c_2 = i\,\omega\nabla_{ad} - \omega_R\Delta_c\left(\kappa_a{}_P + \rho_P\right). \tag{4.90}$$

Therefore,

$$4\,\omega_R + c_1 = i\,\omega + \Delta_c\,\omega_R\left(\kappa_T + \rho_T\right) \tag{4.91}$$

Finally equation (4.88) becomes:

$$\frac{d\,\delta H}{d\,r} = \rho B\kappa_a \left[\frac{4\{i\,\omega\nabla_{ad} - \omega_R\Delta_c\,(\kappa_{a\,P} + \rho_P)\}}{i\,\omega - \omega_R\,(4 - \Delta_c\,(\kappa_{a\,T} + \rho_T))}\frac{\delta\,P}{P}\right. \\ \left. -\frac{i\,\omega + \omega_R\Delta_c\,(\kappa_{a\,T} + \rho_T)}{i\,\omega - \omega_R\,(4 - \Delta_c\,(\kappa_{a\,T} + \rho_T))}\frac{\delta\,J}{B} - \Delta_c\frac{\delta\,\kappa}{\kappa}\right]. \tag{4.92}$$

4.2.3 Boundary conditions for pulsation equations

The system of equations that we want to solve has been reduced effectively to four equations with four independent variables that require four boundary conditions. We impose three boundary conditions at the upper boundary, and one at the bottom boundary. The boundary conditions derived here may also be applied to the non-grey equations.

A closer inspection of equation (4.81) shows that the solution becomes adiabatic when $\omega < \omega_R$. A plot of ω and ω_R is shown in Fig. 4.4, where it can be seen that for the model we use, the condition $\omega < \omega_R$ does not quite apply near the surface, above the photosphere. We shall nonetheless impose boundary conditions at the upper surface point based on the results of adiabatic calculations. Also near $\tau = 0$, the atmosphere is nearly isothermal (see Cox & Giuli vol 2, p. 602). Given these two points, we will derive the boundary condition on $\frac{\delta P}{P}$ as follows:

The energy equation simplifies to:

$$\frac{\delta\,P}{P} = \Gamma_1\frac{\delta\,\rho}{\rho}, \tag{4.93}$$

in the adiabatic case. Using the continuity, energy and momentum equations (4.31), (4.93) and (4.39), we end up with the following first order ordinary differential equations:

$$\frac{d\,\delta\,r}{d\,r} = -\frac{1}{\Gamma_1}\frac{\delta\,P}{P}, \tag{4.94}$$

and

$$\frac{d}{d\,r}\left(\frac{\delta\,P}{P}\right) = \frac{\rho\,g}{P}\frac{\delta\,P}{P} + \frac{\rho\,\omega^2}{P}\delta\,r. \tag{4.95}$$

Substituting equation (4.94) into equation (4.95), and setting $\delta\,r = H_P\,\delta\tilde{r}$ we obtain:

$$\frac{d^2\,\delta\tilde{r}}{d\,r^2} - \frac{\rho\,g}{P}\frac{d\,\delta\tilde{r}}{d\,r} + \frac{\omega^2}{\Gamma_1}\frac{\rho}{P}\delta\tilde{r} = 0, \tag{4.96}$$

where H_P is the pressure scale height evaluated at $\tau = 2/3$. Notice that $\frac{1}{c_s^2} = \frac{\rho}{\Gamma_1 P}$, since the speed of sound $c_s^2 = \Gamma_1\frac{P}{\rho}$. Therefore $\frac{1}{\omega_{ac}^2} = \frac{4\,H_P^2}{c_s^2}$, where ω_{ac} is the acoustical cut-off frequency. Equation (4.96) can be written as:

$$\frac{d^2\,\delta\tilde{r}}{d\,r^2} + \frac{1}{P}\frac{d\,P}{d\,r}\frac{d\,\delta\tilde{r}}{d\,r} + \frac{\omega^2}{\omega_{ac}^2}\frac{1}{4\,H_P^2}\delta\tilde{r} = 0. \tag{4.97}$$

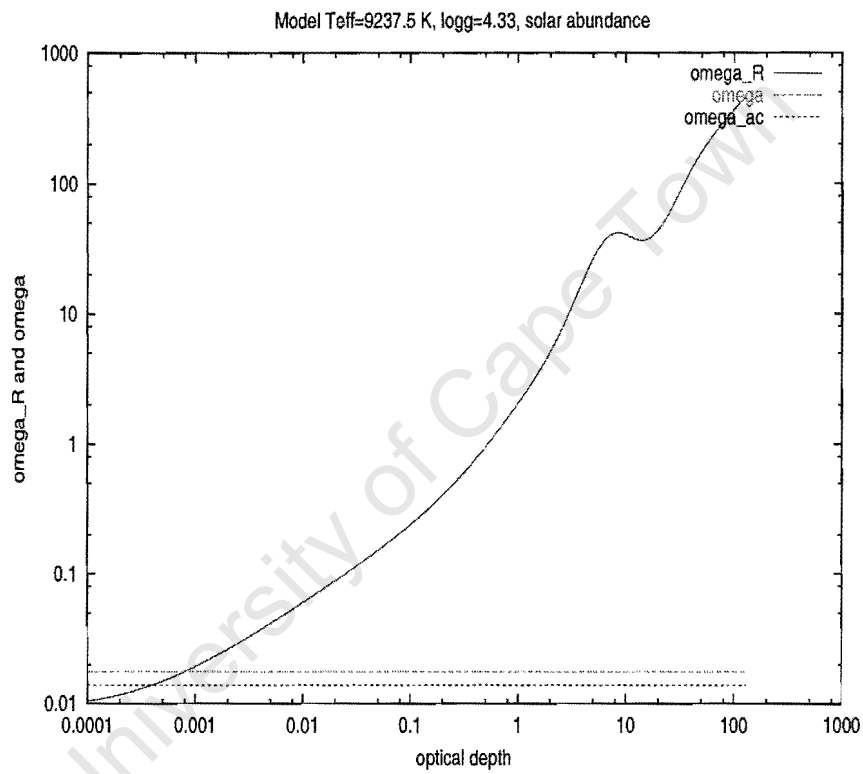

Figure 4.4: A plot of the radiation relaxation time ω_R as a function of depth in the atmosphere of an A star. The pulsation frequency ω chosen to correspond to that of α Cir is also indicated. Notice that although near the surface the ratio $\frac{\omega_R}{\omega}$ is smaller than one, it is not small enough to make the solution adiabatic. Also shown is the acoustic cut-off frequency (ω_{ac}), α Cir oscillates at frequency above ω_{ac}.

To have an idea of the variation of pressure and density with h in an isothermal atmosphere we consider the equation of hydrostatic support:

$$\frac{dP}{dr} = -\frac{P}{H_P}. \tag{4.98}$$

Here we assume the equation of state of the form:

$$P = \frac{k_B \rho T}{\mu m_u}. \tag{4.99}$$

The solution of equation (4.98) for a constant pressure scale height is:

$$P = P_0 \exp\left(-\frac{h}{H_P}\right) \tag{4.100}$$

where P_0 is the pressure at $\tau = 0$, $h = r - R$ is the height above the photosphere, R is the photospheric radius. The density (ρ) has the same form as equation (4.100). Finally, equation (4.97) becomes

$$\frac{d^2\delta\tilde{r}}{dh^2} - \frac{1}{H_P}\frac{d\delta\tilde{r}}{dh} + \frac{\omega^2}{\omega_{ac}^2}\frac{1}{4H_P^2}\delta\tilde{r} = 0. \tag{4.101}$$

The solution to equation (4.101) is:

$$\delta\tilde{r} = a_+ \exp\left(\lambda_+ \frac{h}{H_P}\right) + a_- \exp\left(\lambda_- \frac{h}{H_P}\right) \tag{4.102}$$

where

$$\lambda_\pm = \frac{1}{2} \pm \frac{1}{2}\left(1 - \frac{\omega^2}{\omega_{ac}^2}\right)^{\frac{1}{2}}. \tag{4.103}$$

Equation (4.102) has two constants a_+ and a_-. To fix one of the constants we consider the energy density in the atmosphere. For a semi-infinite atmosphere, we expect the energy density to approach zero at large h values. The energy density is proportional to $\rho\delta r^2$. Therefore the pulsation energy density has the form:

$$\text{energy density} \propto \exp\left(\pm\left(1 - \frac{\omega^2}{\omega_{ac}^2}\right)^{\frac{1}{2}} \frac{h}{H_P}\right). \tag{4.104}$$

It is clear that for $\omega < \omega_{ac}$, the solution with λ_- is the desired one since it keeps the energy density from blowing up at large h. We therefore set $a_+ = 0$, and the solution is:

$$\delta\tilde{r} = a_- \exp\left(\lambda_- \frac{h}{H_P}\right). \tag{4.105}$$

And, using equation (4.94) the pressure perturbations are given as

$$\frac{\delta P}{P} = -\Gamma_1 \lambda_- \delta\tilde{r}. \tag{4.106}$$

This is our pressure perturbation boundary condition at the surface. Note that this condition takes into account that possibility that waves can propagate out. Baker & Kippenhahn (1965) derived a perfectly reflective boundary condition:

$$\frac{\delta P}{P} = -\left(4+\sigma^2\right)\frac{\delta r}{r} \tag{4.107}$$

for radial pulsations (see section 3 for the non-radial case). Equation (4.107) was derived using the same assumptions as equation (4.106). However, since Baker & Kippenhahn (1965) wanted to apply this condition to the atmospheres of Cepheids they had to use pulsation equations in spherical coordinates. Thus, the 4 in equation (4.107) comes from the momentum equation in spherical coordinates.

At low pulsation frequencies we can use the binomial theorem to show that:

$$\lambda_- = \frac{1}{2}\left(1-\left(1-\frac{1}{2}\frac{\omega^2}{\omega_{ac}^2}\right)\right) \tag{4.108}$$

which equals:

$$\lambda_- = \frac{\omega^2}{\Gamma_1}\frac{H_P}{g}, \tag{4.109}$$

where g is the acceleration due to gravity. Substituting equation (4.109) into equation (4.106) leads to

$$\frac{\delta P}{P} = -\sigma^2\frac{\delta r}{r}. \tag{4.110}$$

where it can be shown that $\sigma^2 = R\omega^2/g$. This shows that equation (4.106) becomes equation (4.107) at low frequencies.

The condition for $\omega > \omega_{ac}$ requires that the solution matches to an outwardly propagating wave hence, in this case, λ_+ provides the desired solution. Therefore, the upper boundary condition between $\delta P/P$ and $\delta\tilde{r}$ is

$$\frac{\delta P}{P} = -\Gamma_1\lambda_+\delta\tilde{r}, \tag{4.111}$$

where

$$\lambda_+ = \frac{1}{2}+\frac{1}{2}i\left(\frac{\omega^2}{\omega_{ac}^2}-1\right)^{1/2}. \tag{4.112}$$

We also apply the normalisation condition on $\delta\tilde{r}$:

$$\delta\tilde{r} = 1, \tag{4.113}$$

at $\tau_\nu = \tau_{s\nu}$, where $\tau_{s\nu}$. is the surface value of τ_ν.

An isolated single star will have no source of radiation from outside, and therefore another condition we impose at the upper boundary is that of no incoming radiation. This, in terms of another variable Eddington factor $g_{osc\nu}$ takes the form:

$$\delta H_\nu(\tau_{s\nu}) = g_{osc\nu}\frac{\delta K_\nu(\tau_{s\nu})}{f_{osc\nu}(\tau_{s\nu})}, \tag{4.114}$$

where $g_{osc\nu}$ is determined from the iteration for $f_{osc\nu}$, with initial estimate of $g_{osc\nu} = g_{eq\nu} = H_\nu/J_\nu$.

The solution is expected to become increasingly adiabatic near the bottom boundary of a semi-infinite atmosphere, and from equation (4.40) we obtain this boundary condition at the bottom of the atmosphere:

$$\frac{\delta T}{T} = \nabla_{ad}\frac{\delta P}{P}. \tag{4.115}$$

Boundary conditions for the perturbed transfer equation

For an isolated star, we do not expect any radiation to come from outside at its surface, therefore $I^-(\tau_{s\nu}, -\mu) = 0$. The subscript s denotes τ_ν at the upper boundary of the atmosphere. Therefore at $\tau_\nu = \tau_{s\nu}$, Feautrier variables become:

$$\delta h_\nu(\tau_{s\nu}) = \delta j_\nu(\tau_{s\nu}). \tag{4.116}$$

Then, using equation (4.59) we have, as the boundary condition of the perturbed transfer equation in the Feautrier formulation:

$$\mu\frac{d\,\delta j_\nu(\tau_{s\nu})}{d\tau_\nu} = \delta j(\tau_{s\nu}) + \frac{\delta\kappa_{a\,,\nu}(\tau_{s\nu})}{\kappa_{a\nu}} h_\nu(\tau_{s\nu}). \tag{4.117}$$

The second boundary condition is obtained by applying the diffusion approximation at the base of a semi–infinite atmosphere (which is what we assume to be the case). We are thus able to express the intensity as

$$I^+_\nu(\tau_{max\,\nu}) = B_\nu(\tau_{max\,\nu}) + \mu\frac{dB_\nu}{d\tau_\nu}. \tag{4.118}$$

Note also that $I^+_\nu = j_\nu + h_\nu$, by definition, so that using equation (4.7) we get:

$$I^+_\nu = j_\nu + \mu\frac{dj_\nu}{d\tau_\nu}. \tag{4.119}$$

This equation is perturbed to produce

$$\delta I^+_\nu = \delta j_\nu + \frac{\delta\kappa_{a\nu}}{\kappa_{a\nu}}\left(j_\nu - I^+_\nu\right) + \mu\frac{d\,\delta j_\nu}{d\tau_\nu}. \tag{4.120}$$

Equation (4.118) can similarly be shown to be of this form when perturbed:

$$\delta I^+_\nu = \delta B_\nu + \frac{\delta\kappa_{a\nu}}{\kappa_{a\nu}}\left(B_\nu - I^+_\nu\right) + \mu\frac{d\,\delta B_\nu}{d\tau_\nu}. \tag{4.121}$$

Comparison of equations (4.120) and (4.121) leads to the following boundary conditions at the bottom of the atmosphere:

$$\delta j_\nu + \mu \frac{d\,\delta j_\nu}{d\,\tau_\nu} - \delta B_\nu + \frac{\delta \kappa_{a\nu}}{\kappa_{a\nu}} (j_\nu - B_\nu) - \mu \frac{d\,\delta B_\nu}{d\,\tau_\nu} = 0. \tag{4.122}$$

4.2.4 Eigenfrequencies

The problem as defined in section 4.2 allows for the solution for any value of ω to be determined. To look for a standing wave solution we impose another boundary condition in addition to the four discussed in the previous subsection on the system. This turns the problem into an eigenvalue problem. This can be achieved in two ways; one by imposing a displacement node at the base of the atmosphere, *i.e.*

$$\delta \tilde{r}(\tau_{max,\nu}) = 0, \tag{4.123}$$

at $\tau_\nu = \tau_{max,\nu}$. To obtain the value of ω that satisfies equation (4.123) we notice that:

$$\delta \tilde{r}(\omega, \tau_{max,\nu}) = 0, \tag{4.124}$$

becomes a root-finding problem. Therefore initial estimates of ω are made, they are then refined by secant or Newton-Raphson methods. However, since ω is a complex variable, we found that Muller's method is faster and more suitable for finding complex roots. Muller's method involves fitting a quadratic to three points, and looking for roots near those three points see Press *et al.* (1992) for more details.

Another condition that can be imposed at the bottom of the atmosphere is the requirement that the part of the model interior to base point of the atmosphere perform no work on the part above the base point. Mathematically it takes the form:

$$\text{Im}\ (\delta r^*\, \delta P) = 0, \tag{4.125}$$

where a star (*) denotes a complex conjugate. The way to implement this is to select the real part of ω and keep it constant, regarding the imaginary part as the real eigenvalue. So we look for the imaginary part of ω that makes condition (4.125) true. This becomes a root finding problem which can be solved by the secant method.

4.2.5 Implementation of the grey equations in our code

In our code, the dependent variable is the optical depth τ, and so the equations derived in subsection 4.2.2 will be re-written and non-dimensionalised in this section. We will start with expressing $\frac{\delta T}{T}$ in terms of $\frac{\delta P}{P}$ and δK. In order to do that we define the following coefficients:

$$c_3 = i\,\omega + \omega_R \Delta_c\ (\kappa_{aT} + \rho_T)\,. \tag{4.126}$$

We then replace δJ by $\frac{\delta K}{f_{osc}}$ to get:

$$\frac{\delta T}{T} = \frac{c_2}{c_1}\frac{\delta P}{P} - \frac{\omega_R}{c_1}\frac{\delta K}{f_{osc} B}. \tag{4.127}$$

We then substitute equation (4.127) into equation (4.46) and the result into the continuity equation (4.31) to get:

$$\frac{d\delta r}{d\tau} = \frac{1}{\kappa_a \rho}\left(\rho_P + \rho_T \frac{c_2}{c_1}\right)\frac{\delta P}{P} - \left(\frac{\rho_T}{\kappa_a \rho}\frac{\omega_R}{c_1}\frac{1}{B f_{osc}}\right)\delta K. \tag{4.128}$$

The equation of motion becomes:

$$\frac{d}{d\tau}\left(\frac{\delta P}{P}\right) = -\frac{1}{\kappa_a P}\left(\tilde{g}\frac{\delta P}{P} + \omega^2 \delta r\right). \tag{4.129}$$

Equation (4.93) becomes:

$$\frac{d\delta H}{d\tau} = -\left\{\left(4\frac{c_2}{c_1} - \Delta_c \kappa_{aT}(\kappa_{aP} + \frac{c_2}{c_1})\right) B\frac{\delta P}{P} + \left(\Delta_c \kappa_{aT}\frac{\omega_R}{c_1} - \frac{c_3}{c_1}\right)\frac{\delta K}{f_{osc}}\right\}. \tag{4.130}$$

The perturbed second moment (equation (4.55)) is:

$$\frac{\delta K}{d\tau} = \left(\kappa_{aP} + \kappa_{aT}\frac{c_2}{c_1}\right) H\frac{\delta P}{P} - \kappa_{aT}\frac{\omega_R}{c_1}\frac{1}{f_{osc}} H\frac{\delta K}{B} + \delta H. \tag{4.131}$$

Dimensionless form

Equations (4.128), (4.129), (4.130) and (4.131) are now put into dimensionless form. Here we note that $\frac{\delta P}{P}$, c_1/c_2, ρ_T, ρ_P, κ_{aT}, κ_{aP} and τ are dimensionless. So we only need to consider variables δr, δH and δK. We scale these in the following manner:

$$\delta \tilde{r} = \frac{\delta r}{H_P}, \tag{4.132}$$

$$\delta \tilde{H} = \frac{\delta H}{H_o}, \tag{4.133}$$

$$\delta \tilde{K} = \frac{\delta K}{K_o}, \tag{4.134}$$

where H_o and K_o are first and second moments respectively, at $\tau = 2/3$.

The whole system of equations becomes:

$$\begin{aligned}
\frac{d\,\delta\tilde{r}}{d\,\tau} &= p_1(\tau)\,\frac{\delta\,P}{P} - p_2(\tau)\,\delta\tilde{K} \\
\frac{d}{d\,\tau}\left(\frac{\delta\,P}{P}\right) &= -p_3(\tau)\,\frac{\delta\,P}{P} - p_4(\tau)\,\delta\tilde{r} \\
\frac{d\,\delta\,\tilde{H}}{d\,\tau} &= p_5(\tau)\,\frac{\delta\,P}{P} + p_6(\tau)\,\delta\tilde{K} \\
\frac{d\,\delta\,\tilde{K}}{d\,\tau} &= p_7(\tau)\,\frac{\delta\,P}{P} - p_8(\tau)\,\delta\tilde{K} + p_9(\tau)\,\delta\,\tilde{H},
\end{aligned} \tag{4.135}$$

where coefficients $p_i, i = 1, 9$ are functions of depth and their explicit form is given below:

$$\begin{aligned}
p_1(\tau) &= \left(\rho_P + \rho_T\frac{c_2}{c_1}\right)\frac{1}{H_P\,\kappa_a\rho} \\
p_2(\tau) &= \left(\frac{\rho_T}{\kappa_a\rho}\frac{\omega_R}{c_1}\frac{1}{B\,f_{osc}}\right)\frac{K_o}{H_P} \\
p_3(\tau) &= \frac{g}{\kappa_a\,P} \\
p_4(\tau) &= \frac{\omega^2\,H_P}{\kappa_a\,P} \\
p_5(\tau) &= \left(\Delta_c(\kappa_{a\,P} + \kappa_{a\,T}\frac{c_2}{c_1}) - 4\frac{c_2}{c_1}\right)\frac{B}{H_o} \\
p_6(\tau) &= \left(\frac{c_3}{c_1} - \Delta_c\kappa_{a\,T}\frac{\omega_R}{c_1}\right)\frac{1}{f_{osc}}\frac{K_o}{H_o} \\
p_7(\tau) &= \left(\kappa_{a\,P} + \kappa_{a\,T}\frac{c_2}{c_1}\right)\frac{H}{K_o} \\
p_8(\tau) &= \kappa_{a\,T}\frac{\omega_R}{c_1}\frac{1}{f_{osc}}\frac{H}{B} \\
p_9(\tau) &= \frac{H_o}{K_o}.
\end{aligned} \tag{4.136}$$

For demonstration purposes, we used the equilibrium model atmosphere that is representative of A stars with $T_{\rm eff} = 9237.5\,{\rm K}$, $\log g = 4.33$ and solar abundance. The model was calculated from Christensen-Dalsgaard 's envelope program. In the introduction of this thesis, we discussed that some roAp stars which are what we hope to apply our code to, have highly non-solar abundance. The increased line opacity in the UV spectra of these stars, due to abundance peculiarities affect their temperature structure. Increased line opacity blocks radiation in the optically thick regions of a star. The star compensates for this by increasing temperature in deeper layers in order to maintain constant energy flow. In optically thin regions the star radiates more easily, here the star adjusts by lowering the temperature.

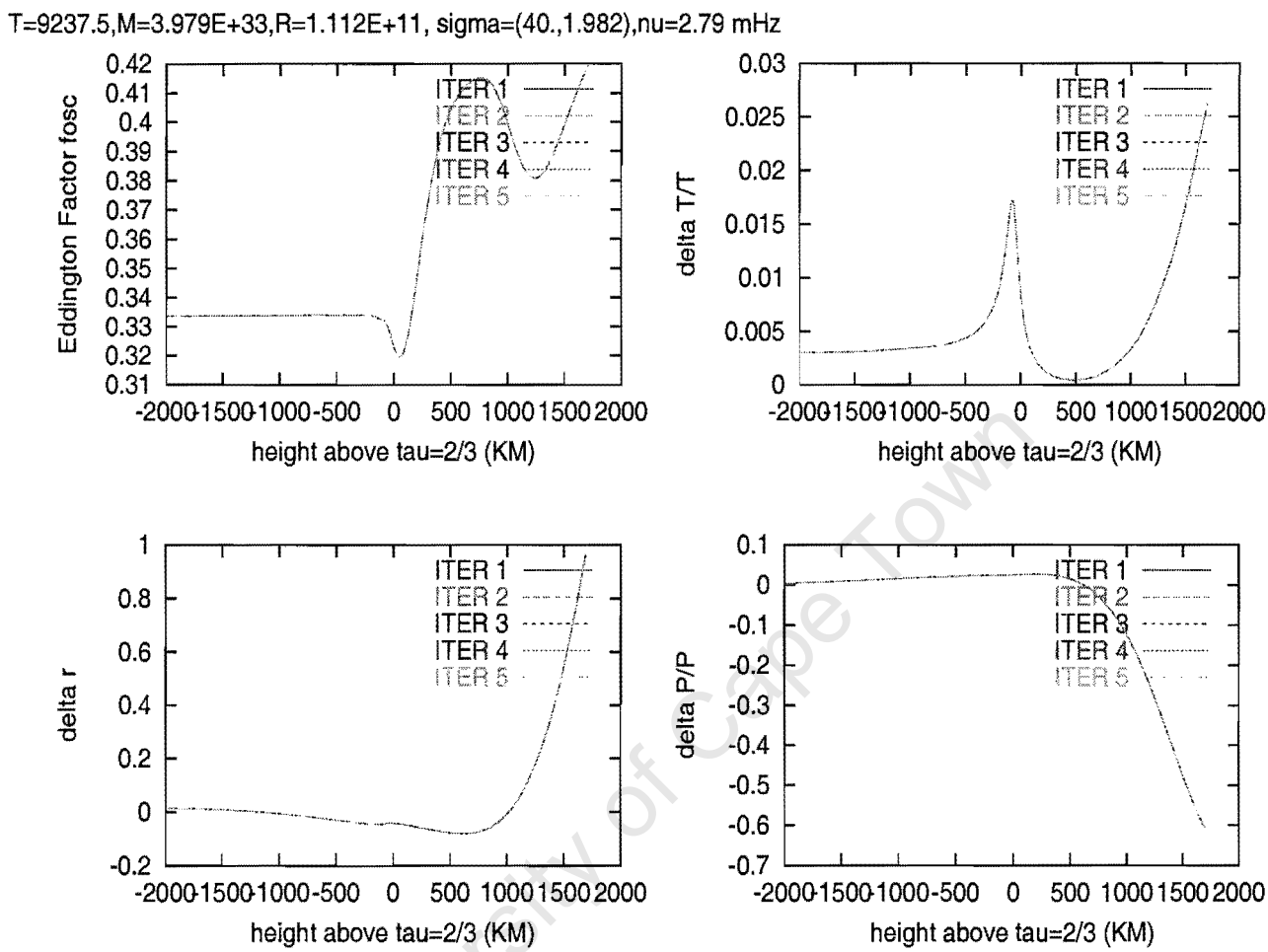

Figure 4.5: A plot of the result of our grey code for $\sigma = (40, 1.9)$; the top-left shows $f_{osc}(\tau)$, bottom-left $\delta\tilde{r}(\tau)$, top-right $\frac{\delta T}{T}(\tau)$, and bottom right is $\frac{\delta P}{P}(\tau)$. The convergence is evidently very fast, plots for all the 5 iterations lie on top of each other.

Hence a steeper temperature structure is expected for star with increased line opacity such as HD 101065. The effects are lesser for mild Ap stars like α Cir (see section 1.2.7). A steeper temperature structure affects the determined acoustic cut-off frequency and possibly damping rates. The eigenfrequencies were then determined from the no work boundary condition (equation 4.125 in section 4.2.4). To show the rate of convergence of the solutions we show the results of running our code for the oscillation frequency $\nu = 2.79\,\mathrm{mHz}$ in Fig. 4.5 with five iterations. The solution converges almost after the first iteration.
Fig. 4.6 compares f_{eq} and f_{osc}. They differ mainly in the atmosphere. They both tend to $\frac{1}{3}$ at large depths.

Next we investigate whether it was worth our while to undertake these studies; in other words, are the parts of the star where oscillation amplitudes are large adiabatic or not? This we do by plotting $\delta T/T - \nabla_{ad}\,\delta P/P$ as a function of depth in the star in Fig. 4.7.

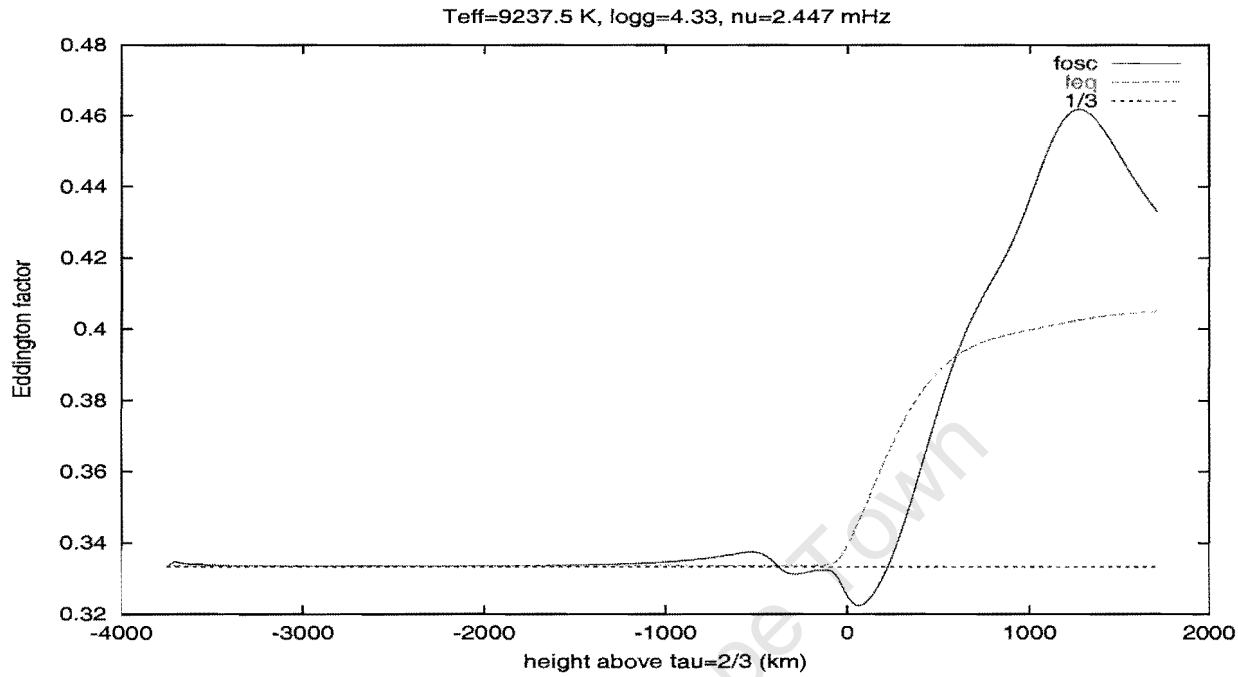

Figure 4.6: The depth dependence of equilibrium Eddington factor (f_{eq}, dashed line), and $f_{osc} = \frac{\delta K}{\delta J}$. f_{osc} shows marked difference from f_{eq} near the surface, but tends to the same asymptotic value as f_{eq} of $\frac{1}{3}$.

Equation (4.40) shows that this expression should equal zero for the adiabatic case (no perturbed flux or energy generation rate).

The plot in Fig. 4.7 shows that the oscillations are nearly adiabatic below the photosphere. At smaller optical depths the response of the atmosphere to small perturbations in temperature is to dampen them over time scales of $1/\omega_R$ (Mihalas & Mihalas 1984). However, if in these regions the pulsation frequencies are much larger than ω_R, the rate of heat losses are smaller than oscillation periods, this is one way to achieve adiabatic conditions. However, in section 4.2.3 it is shown that for roAp stars, the pulsation frequencies are not so large compared to ω_R for this to happen. Therefore, here the oscillations are not adiabatic. Mathematically this is demonstrated in section 4.2.2 (see equation 4.81 and discussions below it).

4.2.6 The work integral

In the derivation of the work integral, I regard non-adiabatic effects as small perturbations to the adiabatic pulsation equations. Therefore if the equation of motion can be written in the form:

$$\omega^2 \delta r = \mathcal{F}(\delta r) \tag{4.137}$$

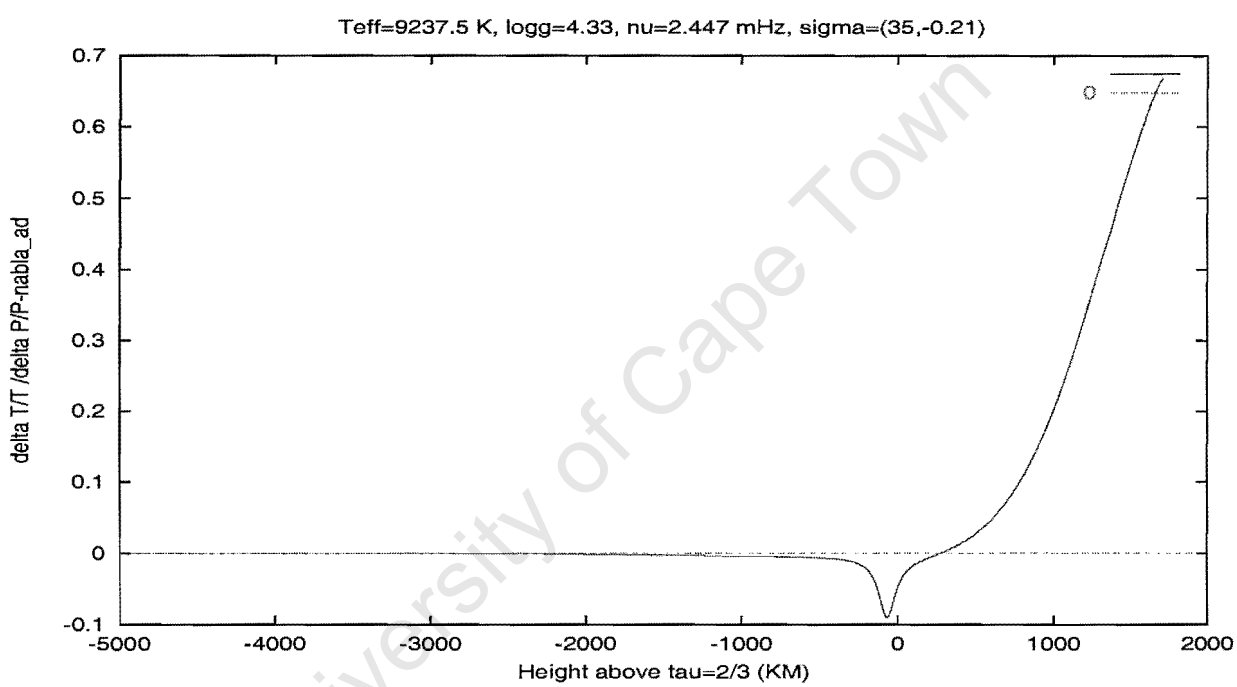

Figure 4.7: In the adiabatic case a simple relation of the form $\delta T/T - \nabla_{\rm ad}\,\delta P/P = 0$ exists between temperature and pressure perturbations; thus in this plot, departures from zero means the oscillations in that part of the star are non-adiabatic. The relation $\delta T/T - \nabla_{ad}\,\delta P/P$ is plotted as a function of depth in the star. It is clear that below the atmosphere the solution is adiabatic. Thus in the part of the atmosphere we are interested in, non-adiabaticity cannot be ignored.

where $\mathcal{F}$ is linear functional of δr which for our system of equations is given as:

$$\mathcal{F}(\delta r) = \frac{P}{\rho}\frac{d}{dr}\left(\frac{\delta P}{P}\right) - \tilde{g}\frac{\delta P}{P}, \tag{4.138}$$

a perturbation in $\mathcal{F}$ due to non-adiabatic effects leads to:

$$\mathcal{F}(\delta r) = \mathcal{F}_a(\delta r) + \delta\mathcal{F}(\delta r). \tag{4.139}$$

where $\mathcal{F}_a(\delta r)$ is the operator for adiabatic oscillations and $\delta\mathcal{F}(\delta r)$ is the perturbation in $\mathcal{F}(\delta r)$ due to non-adiabatic effects. The perturbations in frequency can be shown to be:

$$\delta\omega^2 = \frac{< \delta r, \delta\mathcal{F}(\delta r) >}{< \delta r, \delta r >}, \tag{4.140}$$

(see Schiff (1949) for example) where $<,>$ is the inner product defined in the Hilbert space. A Hilbert space is defined as the space of two component vectors ζ and η such that

$$< \zeta, \eta >= \int_V \zeta^* \eta \rho\, dV, \tag{4.141}$$

where ζ and η are complex functions and "*" denotes complex conjugate (see also Christensen-Dalsgaard 1981;1998).

Equation (4.140) therefore becomes

$$\delta\omega^2 = \frac{\int_V \rho\,\delta r^*\,\delta\mathcal{F}(\delta r)\,dV}{\int_V \rho\,|\delta r|^2\,dV}. \tag{4.142}$$

Since $\delta\omega^2 \simeq 2\omega_r\,\delta\omega$, equation (4.142) becomes:

$$\delta\omega = \frac{1}{2\,\omega_r}\frac{\int_V \rho\,\delta r^*\,\delta\mathcal{F}(\delta r)\,dV}{\int_V \rho\,|\delta r|^2\,dV} \tag{4.143}$$

where ω_r is the real part of ω. The complete perturbed energy equation can be written so that:

$$\frac{\delta P}{P} = \frac{\delta P}{P}_{ad} + \frac{\delta P}{P}_{non}, \tag{4.144}$$

where

$$\frac{\delta P}{P}_{ad} = \frac{1}{\nabla_{ad}}\frac{\delta T}{T}, \tag{4.145}$$

and

$$\frac{\delta P}{P}_{non} = -\frac{i}{\omega\,\nabla_{ad}\,\rho\,C_p\,T}\,\delta\left(\rho\epsilon - div\,F\right). \tag{4.146}$$

Substituting equation (4.144) into the perturbed equation of motion (4.39) and re- arranging we obtain:

$$\omega^2 \delta r = \left[\frac{P}{\rho}\nabla\left(\frac{\delta P}{P}_{ad}\right) - g\frac{\delta P}{P}_{ad}\right] + \frac{P}{\rho}\nabla\left(\frac{\delta P}{P}_{non}\right) - g\frac{\delta P}{P}_{non}, \tag{4.147}$$

i.e. we have separated the above equation into the adiabatic and non-adiabatic parts. Therefore, comparing with equation (4.139) and substituting equation (4.146) we find that:

$$\delta\mathcal{F}(\delta r) = -\frac{i}{\omega}\frac{P}{\rho}\nabla\left[\frac{\delta(\rho\epsilon - div\,F)}{\rho\nabla_{ad}c_pT}\right] + g\frac{i}{\omega}\frac{\delta(\rho\epsilon - div\,F)}{\rho\nabla_{ad}c_pT}. \tag{4.148}$$

If we substitute the above equation into equation (4.143) we obtain:

$$\begin{aligned}\delta\omega &= -\frac{1}{2\omega_r}\frac{i}{\omega}\frac{\int_V P\,\delta r^*\nabla\left[\frac{\delta(\rho\epsilon - div\,F)}{\rho\nabla_{ad}c_pT}\right]dV}{\int_V \rho\,|\delta r|^2\,dV} \\ &\quad + g\frac{1}{2\omega_r}\frac{i}{\omega}\frac{\int_V \delta r^*\frac{\delta(\rho\epsilon - div\,F)}{\nabla_{ad}c_pT}\,dV}{\int_V \rho\,|\delta r|^2\,dV}\end{aligned} \tag{4.149}$$

The integral in the numerator of the first term of the above equation can be written as:

$$\begin{aligned}\int_V P\,\delta r^*\nabla\left[\frac{\delta(\rho\epsilon - div\,F)}{\rho\nabla_{ad}c_pT}\right]dV &= \int_V \nabla\left[P\,\delta r^*\frac{\delta(\rho\epsilon - div\,F)}{\rho\nabla_{ad}c_pT}\right]dV \\ &\quad - \int_V div\,(P\,\delta r^*)\,\frac{\delta(\rho\epsilon - div\,F)}{\rho\nabla_{ad}c_pT}\,dV\end{aligned} \tag{4.150}$$

The first term on the right of the above equation can be transformed by Gauss's theorem into an integral over the surface and equals to zero. Therefore,

$$\int_V P\,\delta r^*\nabla\left[\frac{\delta(\rho\epsilon - div\,F)}{\rho\nabla_{ad}c_pT}\right]dV = -\int_V div\,(P\,\delta r^*)\,\frac{\delta(\rho\epsilon - div\,F)}{\rho\nabla_{ad}c_pT}\,dV. \tag{4.151}$$

If we expand the right-hand-side and substitute the continuity equation we obtain:

$$\begin{aligned}\int_V P\,\delta r^*\nabla\left[\frac{\delta(\rho\epsilon - div\,F)}{\rho\nabla_{ad}c_pT}\right]dV &= -\int_V \nabla\,(P)\,\delta r^*\frac{\delta(\rho\epsilon - div\,F)}{\rho\nabla_{ad}c_pT}\,dV \\ &\quad + \int_V \frac{P}{\rho}\frac{\delta\rho^*}{\rho}\frac{\delta(\rho\epsilon - div\,F)}{\nabla_{ad}c_pT}\,dV\end{aligned} \tag{4.152}$$

Using the equation of hydrostatic equilibrium we end up with:

$$\begin{aligned}\int_V P\,\delta r^*\nabla\left[\frac{\delta(\rho\epsilon - div\,F)}{\rho\nabla_{ad}c_pT}\right]dV &= \int_V g\,\delta r^*\frac{\delta(\rho\epsilon - div\,F)}{\rho\nabla_{ad}c_pT}\,dV \\ &\quad + \int_V \frac{P}{\rho}\frac{\delta\rho^*}{\rho}\frac{\delta(\rho\epsilon - div\,F)}{\nabla_{ad}c_pT}\,dV.\end{aligned} \tag{4.153}$$

Therefore, when we substitute equation (4.153) into equation (4.150) we get:

$$\delta\omega = -\frac{i}{2\,\omega_r}\frac{1}{\omega}\frac{\int_V \frac{P}{\rho}\frac{\delta\rho^*}{\rho}\frac{\delta(\rho\epsilon - div\,F)}{\nabla_{ad}\,c_p\,T}\,dV}{\int_V \rho\,|\delta r|^2\,dV}. \tag{4.154}$$

The damping rates are therefore:

$$\omega_i = -\frac{1}{2\,\omega_r}\,Re\,\{\frac{1}{\omega}\frac{\int_V \frac{P}{\rho}\frac{\delta\rho^*}{\rho}\frac{\delta(\rho\epsilon - div\,F)}{\nabla_{ad}\,c_p\,T}\,dV}{\int_V \rho\,|\delta r|^2\,dV}\}, \tag{4.155}$$

where Re denotes the real part of the expression in curly brackets.

The work integral, which is the internal positive or negative energy dissipation due to non-adiabatic effects is therefore:

$$W(V) = -\frac{i}{2\,\omega_r^2}\,Re\,\{\frac{1}{\omega}\frac{\int_V \frac{P}{\rho}\frac{\delta\rho^*}{\rho}\frac{\delta(\rho\epsilon - div\,F)}{\nabla_{ad}\,c_p\,T}\,dV}{\int_V \rho\,|\delta r|^2\,dV}\}. \tag{4.156}$$

For radial oscillations it is easy to show that:

$$W(r_b) = -\frac{1}{2\,\omega_r^2}\,Re\,\{\frac{1}{\omega}\frac{\int_{r_b}^{r_s} \frac{P}{\rho}\frac{\delta\rho^*}{\rho}\frac{\delta(\rho\epsilon - div\,F)}{\nabla_{ad}\,c_p\,T}\,r^2\,dr}{\int_{r_b}^{r_s} \rho\,|\delta r|^2\,r^2\,dr}\}, \tag{4.157}$$

where r_s and r_b are the values of the radial distance r at the surface and base of the atmosphere respectively.

However, modes that are not reflected back in (at the surface) lose energy, and that energy loss is given by Christensen-Dalsgaard & Frandsen (1983) as:

$$\eta_s = \frac{Im\,(r^2\,\delta r^*\,\delta P)}{2\,\omega_r^2\,E}, \tag{4.158}$$

where all the factors are evaluated at the surface boundary point and Im denotes the imaginary part, η is a relative term, it gives the ratio of contributions of oscillation energy losses to the imaginary part of the frequency (ω_i) to the real part of the frequency (ω_r), and E is related to the kinetic energy of the oscillations and is given as

$$E = \int_V \rho\,|\delta r|^2\,dV. \tag{4.159}$$

Therefore, for the whole star (atmosphere and envelope), the ratio of the imaginary part of the frequency to the real part η is given as:

$$\eta = \eta_s + W\,(r) \tag{4.160}$$

We used our code to calculate damping rates using the condition in equation (4.125) that the layers of the star beneath the bottom boundary layer perform no work on those above it. The solutions were used in equations (4.157) and (4.158) in order to determine η from equation (4.160). The results are compared with the ratio of the imaginary to real part of the frequency obtained from the code at several pulsation frequencies in Fig. 4.8.

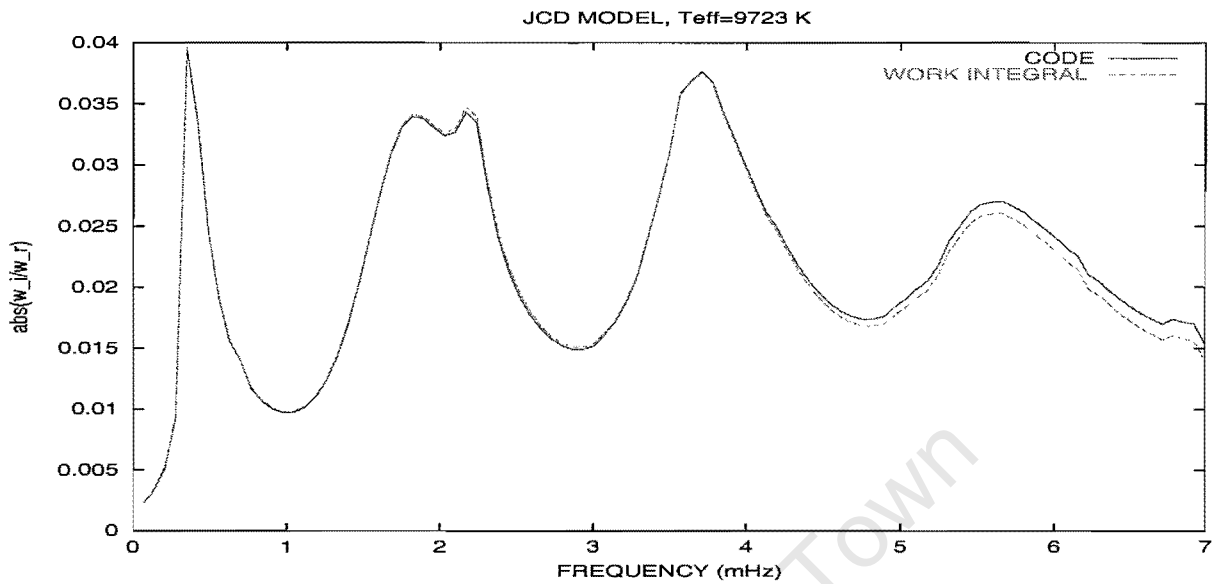

Figure 4.8: The ratio ω_i/ω_r for the various values of the ω_r and the corresponding damping rates obtained from the boundary condition equations (4.106) and (4.111). This is compared to the ratio obtained from the work integral, for τ between 10^{-4} and 128. The solid curve is the ratio obtained from the code by imposing an extra boundary condition, the dotted line is obtained from the work-integral.

4.3 Pulsation equations in the stellar envelope

While the radiative transfer simplifies to the diffusion approximation in the envelope of the star, the plane- parallel approximation breaks down and the complete spherical equations need to be used. Our approach here takes advantage of the diffusion approximation since spherical radiative transfer is more complicated (as shown in the appendix of Christensen-Dalsgaard & Frandsen 1983). In spherical coordinates the continuity equation becomes:

$$\frac{1}{r^2}\frac{d(r^2\,\delta r)}{dr} = -\frac{\delta\rho}{\rho}. \tag{4.161}$$

The equation of motion becomes:

$$\frac{d}{dr}\left(\frac{\delta P}{P}\right) = \frac{\rho\tilde{g}}{P}\frac{\delta P}{P} + \frac{\rho}{P}\left(\omega^2 + \frac{2}{r}g(1+\lambda) - d\,g/dr - 4\pi G\rho\right)\delta r, \tag{4.162}$$

where $\lambda = \tilde{g}/g$. The version of this equation shown here includes the perturbation in gravitational potential discussed in section 4.2. In the diffusion approximation for a star in equilibrium, the Eddington flux can be written as:

$$H = -\frac{a\tilde{c}T^3}{3\pi\kappa\rho}\frac{dT}{dr} \tag{4.163}$$

where a is the radiation density constant, and $\tilde{c}$ is the speed of light.

The mass variable in spherical coordinates is:

$$\frac{\partial m}{\partial r} = 4\pi\rho r^2. \tag{4.164}$$

Therefore, expressing the Eddington flux in terms of the mass variable we obtain

$$H = -\frac{4\,a\,\tilde{c}}{3}\frac{r^2 T^3}{\kappa}\frac{dT}{dm}. \tag{4.165}$$

Upon perturbing and linearising equation (4.165) we get:

$$\frac{d}{dm}\left(\frac{\delta T}{T}\right) = \frac{d\ln T}{dm}\{\frac{\delta H}{H} + \frac{\delta T}{T}(\kappa_T - 4) + \kappa_P\frac{\delta P}{P} - 2\frac{\delta r}{r}\}. \tag{4.166}$$

Therefore in terms of optical depth τ equation (4.166) becomes:

$$\frac{d}{d\tau}\left(\frac{\delta T}{T}\right) = \frac{d\ln T}{d\tau}\{\frac{\delta H}{H} + \frac{\delta T}{T}(\kappa_T - 4) + \kappa_P\frac{\delta P}{P} - 2\frac{\delta r}{r}\}. \tag{4.167}$$

The energy equation we use only contains radiative flux, again we do not include convection and conduction. We do not go near enough to the core that we will need nuclear energy generation rate in our energy equation, so it stays as:

$$\delta(div\,F) = i\omega\rho C_P T\left(\frac{\delta T}{T} - \nabla_{ad}\frac{\delta P}{P}\right). \tag{4.168}$$

In terms of H and τ the perturbed energy equation becomes:

$$\frac{d\delta H}{d\tau} = 2\frac{\delta H}{\kappa\rho r} - \frac{i\omega C_P T}{4\pi\kappa}\left(\frac{\delta T}{T} - \nabla_{ad}\frac{\delta P}{P}\right). \tag{4.169}$$

Substituting $\frac{\delta\rho}{\rho} = \rho_T\frac{\delta T}{T} + \rho_P\frac{\delta P}{P}$ in equation (4.161) we obtain:

$$\frac{d\delta r}{d\tau} = \frac{1}{\kappa\rho}\left(\rho_T\frac{\delta T}{T} + \rho_P\frac{\delta\,,P}{P} + 2\frac{\delta r}{r}\right). \tag{4.170}$$

We then scale the equations using $\delta r = H_P\,\delta\tilde{r}$ and $\delta H = H_o\,\delta\tilde{H}$ to obtain the following dimensionless system of equations for the envelope of the star:

$$\begin{aligned}
\frac{d\delta\tilde{r}}{d\tau} &= \frac{1}{H_P\kappa\rho}\left(\rho_T\frac{\delta T}{T} + \rho_P\frac{\delta P}{P} + 2\,H_P\frac{\delta\tilde{r}}{r}\right)\\
\frac{d}{d\tau}\left(\frac{\delta P}{P}\right) &= -\frac{\tilde{g}}{\kappa P}\frac{\delta P}{P} - \frac{H_P}{\kappa P}\left(\omega^2 + \frac{2}{r}g\,(1+\lambda) - \frac{dg}{dr} - 4\pi G\rho\right)\delta\tilde{r}\\
\frac{d}{d\tau}\left(\frac{\delta T}{T}\right) &= \frac{d\ln T}{d\tau}\{(\kappa_T - 4)\frac{\delta T}{T} + \kappa_P\frac{\delta P}{P} + \left(\frac{H_o}{H}\right)\delta\tilde{H} - 2\,H_P\frac{\delta\tilde{r}}{r}\}\\
\frac{d\delta\tilde{H}}{d\tau} &= 2\frac{\delta\tilde{H}}{\kappa\rho r} - \frac{i\omega C_P T}{4\pi\,H_o\kappa}\left(\frac{\delta T}{T} - \nabla_{ad}\frac{\delta P}{P}\right).
\end{aligned} \tag{4.171}$$

4.4 Matching atmosphere to the envelope

We have seen that the equations governing pulsations in the stellar atmosphere are different from those for the envelope. While there is a need to take into consideration the detailed radiative transfer in the atmosphere, things are simplified as one gets deeper into the star, radiative transfer assumes a simpler diffusion approximation. This simplifies the envelope pulsation equations. For example, while the pulsation equations in the atmosphere form an unclosed system (and have to be iterated to get at the solution), those for the envelope form a closed fourth order system that do not require iteration. Therefore these different-looking equations in different regions need to be matched at the boundary between the two regions (*i.e.* the atmosphere and envelope). This is the subject of this section.

The system of equations (4.136) are matched to equations (4.171) using a second-order boundary-value-problem package (Baker, Moore & Spiegel 1971), originally written by D. Gough and modified by J. Christensen-Dalsgaard. The following surface boundary conditions for the matched atmosphere and envelope were used:

$$\begin{aligned} \delta\tilde{r} &= 1 \\ \frac{\delta P}{P} &= \lambda_{-}\,\Gamma_1\,\delta\tilde{r} \\ \delta H &= g_{osc}\frac{\delta K}{f_{osc}} \end{aligned} \tag{4.172}$$

and are explained in section 4.2.3. The following conditions were used at the matching point:

$$\begin{aligned} \delta\tilde{r}^{II} &= \delta\tilde{r}^{I} \\ \frac{\delta P^{II}}{P} &= \frac{\delta P^{I}}{P} \\ \delta\tilde{H}^{II} &= \delta\tilde{H}^{I} \\ \frac{\delta T^{II}}{T} &= \frac{\delta T^{I}}{T} \end{aligned} \tag{4.173}$$

where the superscripts II and I denote the different regions, region I is the atmosphere and II is the envelope.

At the base of the envelope we require that the oscillations be adiabatic:

$$\frac{\delta T}{T} - \nabla_{ad}\frac{\delta P}{P} = 0. \tag{4.174}$$

The whole matched systems of equations are iterated until the atmospheric pulsation equations converge. Before we present the results (in the next chapter), we discuss the tests to show that the code gives reasonable results.

4.4.1 Tests on the code

The first obvious test is to verify that the f_{osc} calculated by the code approaches 1/3 at large optical depths. We found that a plot of f_{osc} at various depth points is similar to that in Fig. 4.6 and that $f_{osc} \longrightarrow 1/3$ as $\tau \longrightarrow \infty$.

The next test, is to verify if the solution becomes adiabatic with depth below the atmosphere. The very upper part of the atmosphere might or might not be adiabatic depending on the ratio ω_R/ω as discussed in section 4.2.3. A comparison of the real part of $\delta T/T$ and $\delta P/P$ at different depth points in and below the atmosphere shows that the solution is not adiabatic in the atmosphere, but becomes adiabatic in the interior of the star. This is similar to what is shown in Fig. 4.7. The fact that the expression $\delta T/T - \nabla_{ad}\delta P/P$ deviates from zero in the upper part of the atmosphere demonstrates that the solution does not become adiabatic there.

Based on the discussions in section (4.2.2) we expect that at great depths ω/ω_R approaches zero, hence the solution should show:

$$\frac{\delta J}{J} = 4\frac{\delta T}{T}. \tag{4.175}$$

A plot of $\delta J/J$ and $4\,\delta T/T$ in Fig. 4.9 shows that this is the case.

Finally, for high overtone pulsators such as the roAp stars, their pulsations can be described by asymptotic theory. This is because for high overtone pulsations, the perturbation in the gravitational potential can be neglected and this reduces the system to second order. Asymptotic theory has to do with obtaining asymptotic expressions for the eigenfunctions and eigenvalues for such a second order pulsation equation. One such expression is given by Christensen-Dalsgaard (1998) as:

$$\delta r(r) = A\,\rho(r)^{-\frac{1}{2}}\,c(r)^{-\frac{1}{2}}\,r^{-1}\,\cos\left(\omega\int_r^R \frac{dr'}{c(r)} - (\frac{1}{4}+\alpha)\,\pi\right), \tag{4.176}$$

where A is the constant obtainable from a boundary condition far from the turning points, $c(r)$ is the sound speed and α is the phase constant. It should be noted that equation (4.176) breaks down near the surface and the lower turning points for trapped modes.

Since equation (4.176) was derived for adiabatic oscillations, and the oscillations become adiabatic in the envelope, we can compare the displacement eigenfunction from our code with equation (4.176). We expect agreement in the envelope (far away from the inner turning point). Equation (4.176) implies that $\rho^{\frac{1}{2}}\,c^{\frac{1}{2}}\,r\,\delta r$ should have a constant amplitude with depth in a star for purely adiabatic oscillations with zero damping.

We calculated $\rho^{\frac{1}{2}}\,c^{\frac{1}{2}}\,r\,\delta r$ using our code and compared it with $A\,\cos\left(\omega\int_r^R \frac{dr}{c(r)} - (\frac{1}{4}+\alpha)\pi\right)$. A was made to match the numerical solution at some point in the envelope, and α was adjusted for various frequencies and damping. We show the results in Fig. 4.10. Indeed for zero damping both asymptotic theory and the code give constant amplitude throughout

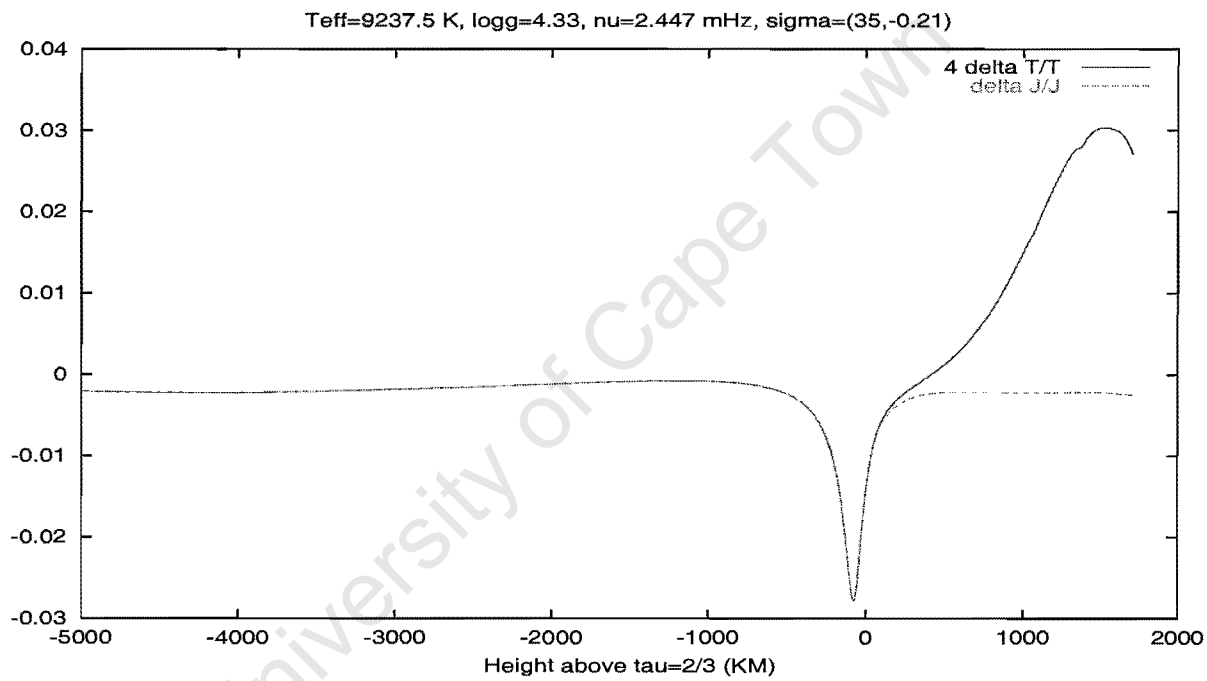

Figure 4.9: A comparison of $4\,\delta T/T$ and $\delta J/J$ as a function of depth in the atmosphere. In the upper part of the atmosphere $4\,\delta T/T$ deviates from $\delta J/J$, indicating departures from radiative equilibrium. Below $\tau = 2/3$ the two curves lie on top of each other, indicating adiabaticity there. Therefore, this plot is consistent with that in Fig. 4.7.

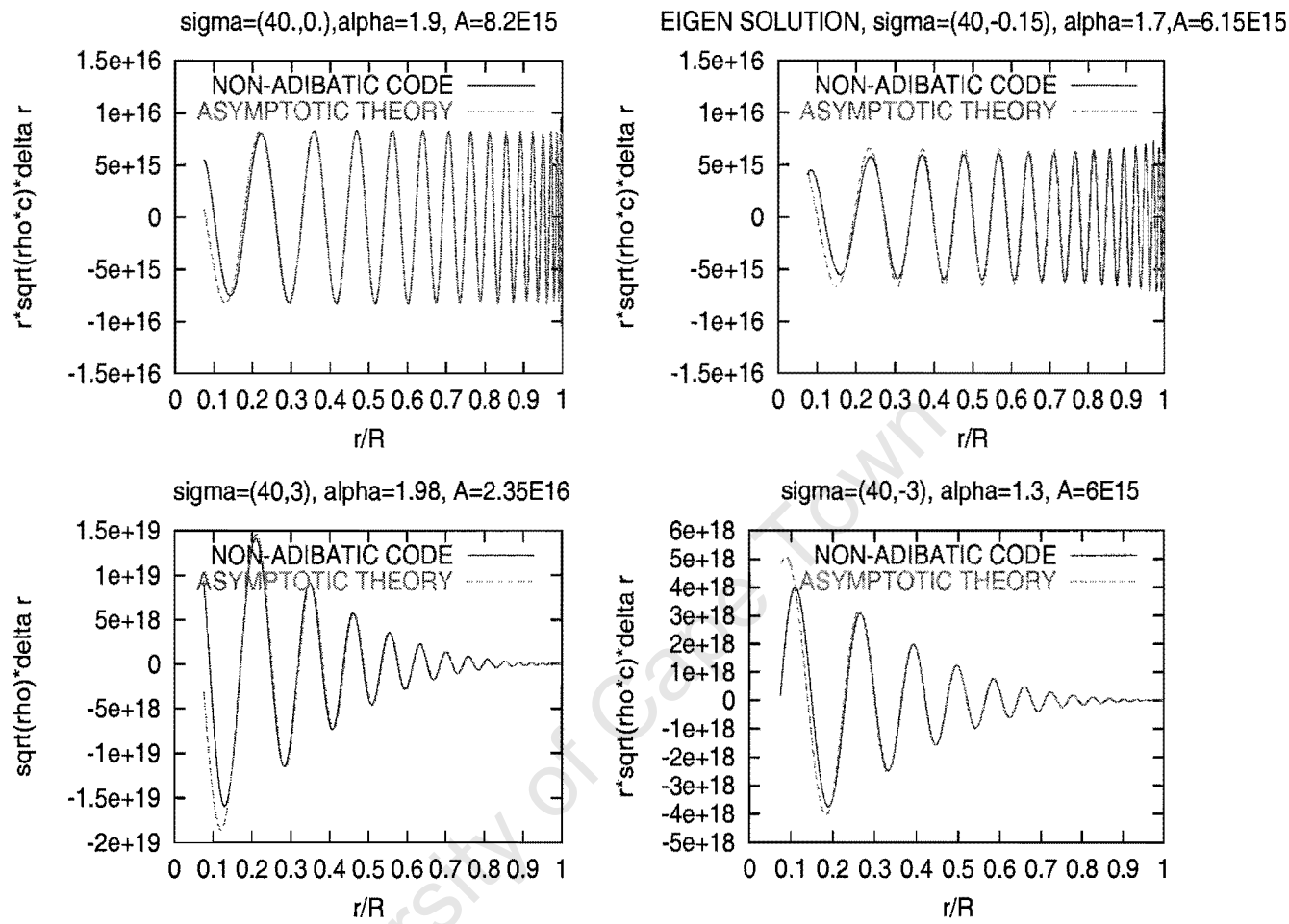

Figure 4.10: A plot of $\rho^{\frac{1}{2}} c^{\frac{1}{2}} r\,\delta r$ calculated from our code compared with equation (4.176) for for $\nu = 2.79\,\mathrm{mHz}$ at various damping rates. The values of α and the amplitude A are shown on each panel.

much of the envelope except near the base of the envelope, perhaps here we are close to the inner turning point. However, for non-zero damping (or excitation) the amplitude is varying but the two approaches are still in agreement.

It should be noted that although equation (4.176) was derived for adiabatic pulsations, it agrees with non-adiabatic equations that we used in our envelope model. Damping or excitation introduces imaginary part of the frequency, so that $\omega = \omega_r + i\,\omega_i$. In this case

$$A\,\cos\left(\omega \int_r^R d\,r'/c(r') - (1/4+\alpha)\,\pi\right) =$$

$$A\,\{\cos\left(\omega_r \int_r^R d\,r'/c(r') - (1/4+\alpha)\pi\right)\cos\, i\omega_i + \qquad (4.177)$$

$$A\left\{\sin\left(\omega_r\int_r^R dr'/c(r') - (1/4+\alpha)\pi\right)\sin\, i\omega_i\right\}$$

The real part of the above is:

$$y(r)\,\rho(r)^{\frac{1}{2}}\,c(r)^{\frac{1}{2}}\,r = \frac{A}{2}\left(e^{\omega_i\int_r^R dr'/c(r')} + e^{-\omega_i\int_r^R dr'/c(r')}\right)cos\left(\omega_r\int_r^R dr'/c(r') - (1/4+\alpha)\right.$$

$$= A\cosh\left(\omega_i\int_r^R dr'/c(r')\right)\cos\left(\omega_r\int_r^R dr'/c(r') - (1/4+\alpha)\,\pi\right) \quad (4.1$$

It therefore appears that the solution of non-adiabatic oscillations in the envelope goes as the product of the hyperbolic cosine and trigonometric cosine as in the above equation.

Figs 4.9 and 4.10 indicate that our code has passed the tests well, and this gives us confidence to use it to investigate non-adiabaticity in the atmospheres of roAp stars. We do this in the next chapter.

Yet another test of our code is to compare the damping rates calculated using the work integral equation (4.157) with those from imposing an additional boundary condition (such as that the part of the star interior to the boundary point exerts no work on the part above the boundary point). This comparison is discussed in the next chapter.

Chapter 5

Results

In this chapter we present the results obtained using the code that solves equations described and presented in chapter 4. In section 5.1 we present the results of the calculations of the eigenfunctions and eigenfrequencies using the code described in section 4.

5.1 Results of the theoretical calculations

The equilibrium model atmospheres were calculated using a program by Christensen-Dalsgaard that fits Hopf function to the ATLAS9 model atmospheres (Kurucz 1993). Such models were matched to the envelope models calculated.

5.1.1 Results of the grey calculations

The results presented in this section are based on the computer code discussed in section 4.4 that matches the solutions in the atmosphere with those in the envelope. The results of the non-grey code are discussed in section 5.7.

The behaviour of eigenfunctions for the equilibrium model $T_{\rm eff} = 9237.5\,{\rm K}$, $\log g = 4.33$ for frequency $\nu = 2.79\,{\rm mHz}$ in the atmosphere and envelope respectively are presented in Fig. 5.1. The damping rates were obtained by imposing an additional condition that the parts inner to the base of the envelope exert no work on those above it. This condition takes care of the fact that our equilibrium model is truncated and does not include regions near the core of the star. After the second iteration the solutions lie on top of each other indicating a fast convergence. However, there is a marked difference between the first and second iterations. Therefore, at least three iterations are required in order to obtain a reasonably well converged solution. It is clear from Fig. 5.1 that the amplitudes of the perturbed Eddington flux are different for the first iteration than for subsequent iterations.

For the mode depicted in Fig. 5.1 of overtone $n = 32$, there is evidence of a temperature node in the atmosphere and the temperature perturbations are highly variable there. There is also a displacement node in the atmosphere, this is discussed in detail in section 5.2.

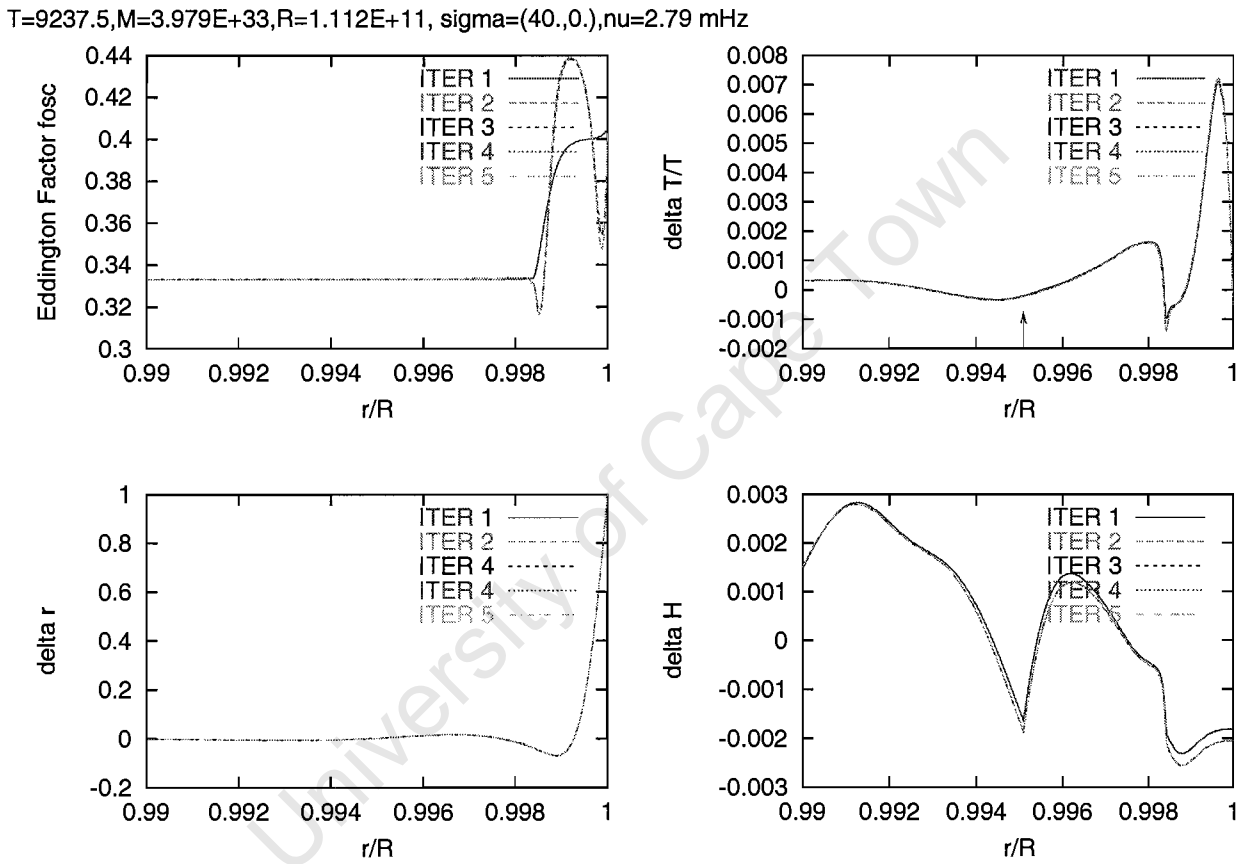

Figure 5.1: A plot of the real part of the eigenfunctions in the atmosphere for $\nu = 2.79$ mHz after five iterations. It is clear that the solutions converge fast, and that only three iterations are needed to arrive at a good solution. However, it is certain that a single iteration is not good enough; it affects the calculated perturbed Eddington flux. The arrow on the $\delta T/T$ plot shows the point at which the solutions were matched.

This is just a continuation of Fig. 5.1 to cover the rest of the envelope. Again here the solution converges fast.

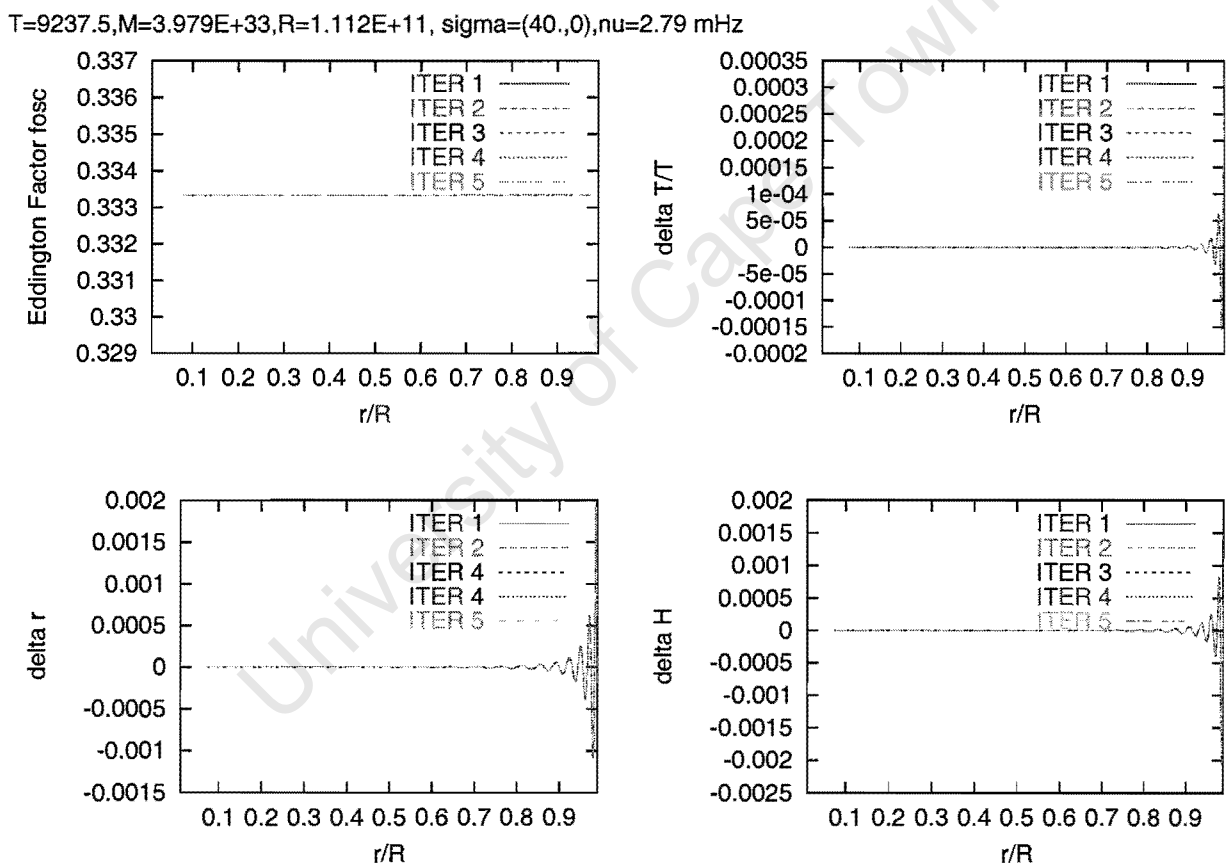

5.1.2 Damping rates

We calculated the damping rates for mode frequencies ranging from 0.01 to 7 mHz by imposing the condition that the part of the star below the base of the stellar envelope does no work on the part above the base. The damping rates determined in this way and those calculated from the work integral equation (4.157) are shown in Fig. 5.2 for the surface boundary condition (equations 4.106 and 4.111) and Fig. 5.3 for the boundary condition equation (4.107). In both plots there is a good agreement between the damping rates, this gives us further confidence that our code works well. An arrow indicates the acoustic cut-off frequency.

For the equilibrium model with homogeneous abundance we used, no radial modes in the roAp frequency region $1.0 < \nu < 3.0\,\mathrm{mHz}$ are excited. This is consistent with the Balmforth *et al.*'s (2001) analysis of the equatorial region of their composite model. In fact we found no excitation in all the frequencies up to 7 mHz. At the cut-off frequency there is increased damping due to waves being lost as they propagate through the stellar surface. This is the result of the boundary condition we used because, if all the modes are trapped, as shown in Fig. 5.3, no increased damping shows near the cut-off frequency.

The increased damping near 1 mHz is explained by studying the un-normalised work-integral and the pulsational kinetic energy (given in equation 4.159) separately. The un-normalised work-integral at various pulsation frequencies as a function of depth is shown in Fig. 5.4. It increases with increasing pulsation frequencies (at least in the atmosphere. This is opposite to the behaviour of the kinetic energy (as shown in Fig. 5.5). Throughout the star the pulsational kinetic energy decreases with increasing pulsation frequency. A ratio of these two quantities is directly related to the damping rates, this therefore, explains the low damping rates at low frequencies. However, the kinetic energy is unaffected for the pulsation frequency near 1 mHz, whereas the work integral shows a maximum in the 'jump' associated with the hydrogen ionization zone. The maximum in the 'jump' (near 1 mhz and 3 mHz) is also seen in the relative mean intensity perturbations ($\frac{\delta J}{J}$) (see Fig. 5.6). The relative mean intensity perturbations are in actual fact perturbations in the radiative energy density $\delta u/u$. It therefore appears that the perturbations to the radiative energy density due to pulsations peaks near 1 mHz, *ie.* the radiative energy density resonates near that frequency. This also explains why the the 'bump' seen in the temperature perturbations reaches the maximum near 1 mHz shown in Fig. 5.10 (bearing in mind that $\frac{\delta T}{T}$ is directly related to $\frac{\delta J}{B}$).

In Fig. 5.7 we show the contribution to the damping by the leaking of wave energy for a purely reflective boundary condition. It is clear that in this case the internal damping processes dominate the leakage of all frequencies in the range we have considered. A very interesting result are the peaks seen near $\nu = 2.5$ mHz, 3.7 mHz, 4.6 mHz and $\nu = 5.7$ mHz. The fact that these four peaks correspond to minima in pulsation energy implies that those peaks could be due to chromospheric modes. Simon & Landsman (1997) show evidence for chromospheres in the UV spectra of three A stars, α Aql, α Cep and τ^3 Eri. They still have not published the results of analysis the UV spectra of α Cir which they also observed.

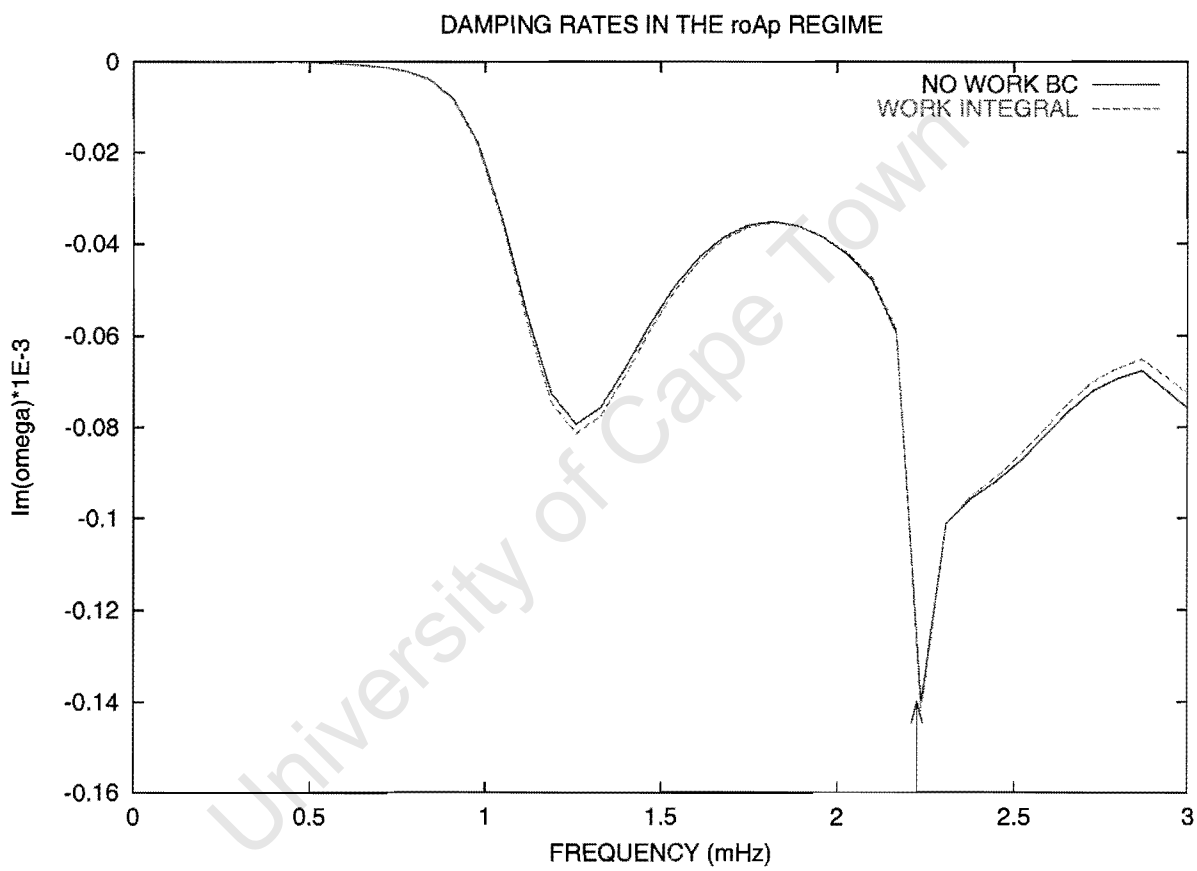

Figure 5.2: The damping rates obtained from using the upper boundary condition that takes into consideration the fact that modes with $\omega > \omega_{ac}$ are not reflected but dissipate out through the atmosphere equation (4.111). The solid line shows the results of the code, the dashed line is from the work integral calculations.

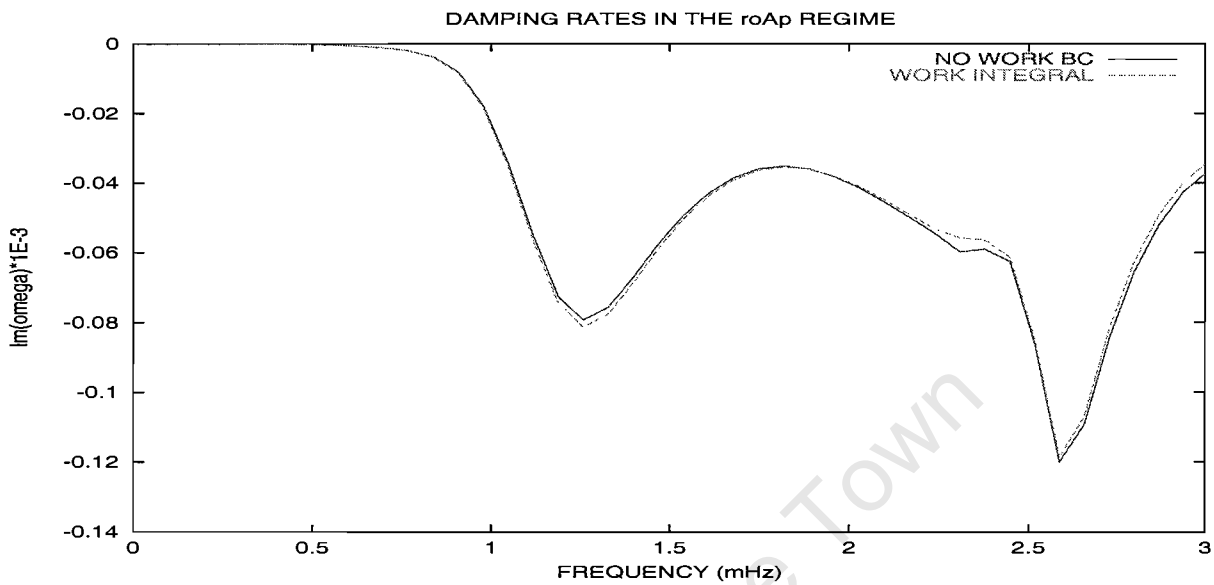

Figure 5.3: The damping rates obtained by using the boundary condition that is purely reflective equation (4.107). This boundary condition does not allow for waves to propagate across the surface boundary.

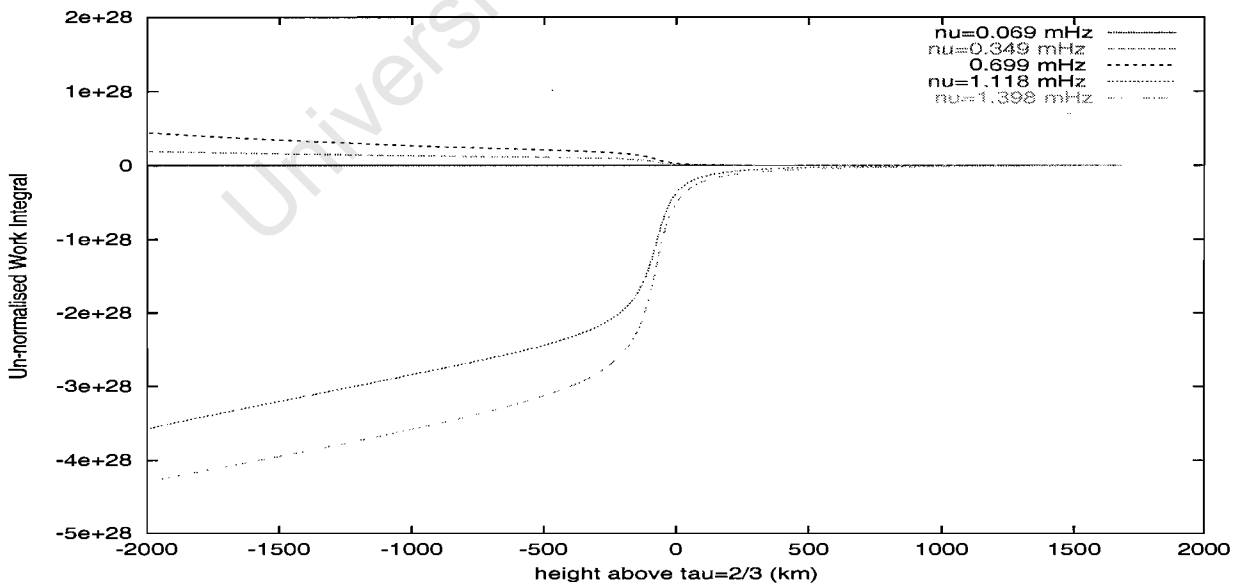

Figure 5.4: The variation of un-normalised work integral as a function of depth at various pulsation frequencies.

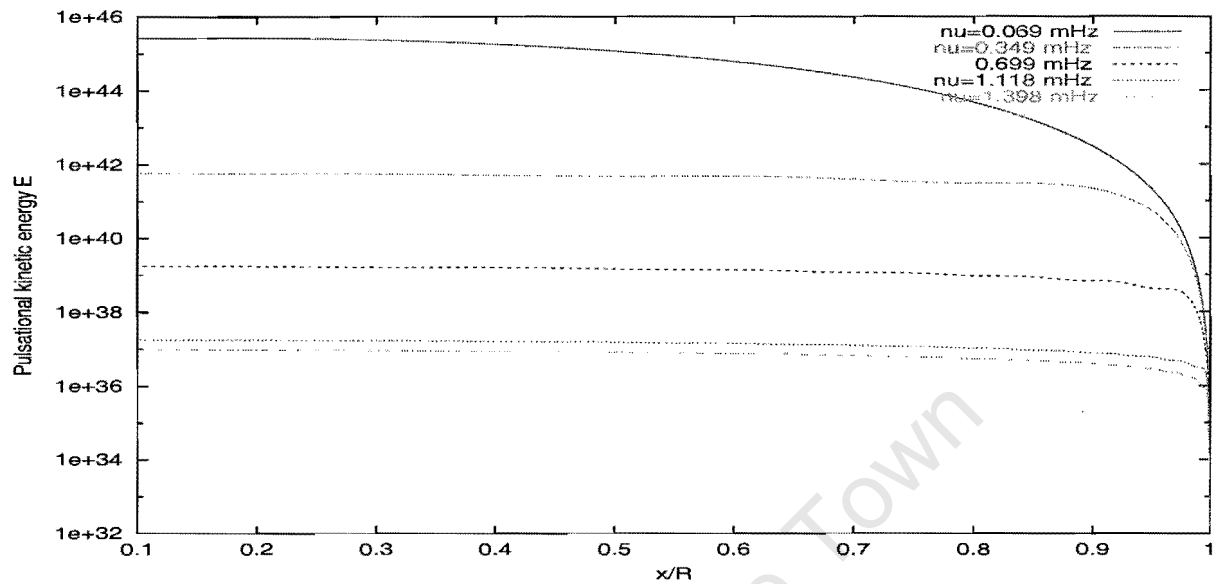

Figure 5.5: The variation of pulsational kinetic energy as a function of depth below the surface at various pulsation frequencies. Throughout the star, lower frequencies have higher energy than than the higher ones.

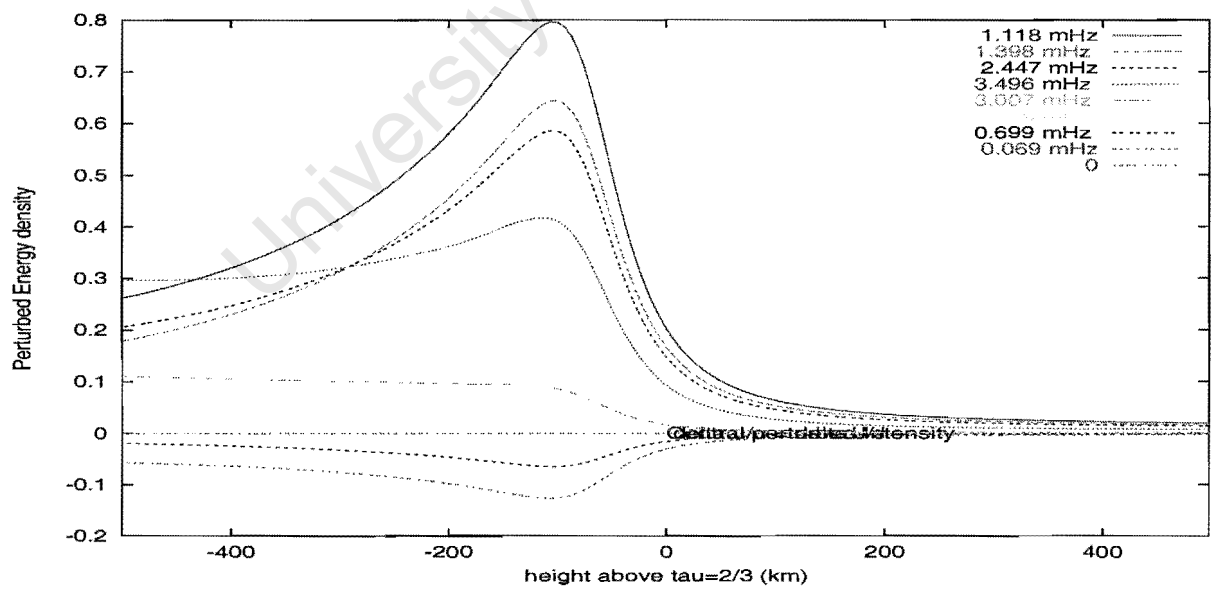

Figure 5.6: The variation of radiative energy density with depth below the atmosphere at various pulsation pulsation frequencies. Note that $\delta u/u = \delta J/J$ hence this plot is really a plot of $\delta J/J$. The curves corresponding to $\nu = 1.118\,\mathrm{mHz}$ and $\nu = 3.496\,\mathrm{mHz}$ are at the Hydrogen ionization zone resonances.

Their analysis is based on the spectra obtained from the HST/Goddard High Resolution Spectrograph. They were able to see Lyα and Si III emission lines which are indicative of a chromosphere. Latest results based on UV studies of and A5 V star, β pictoris, using FUSE (Far Ultra-violet Spectroscopic explorer) indicate that this star has chromospheric emission lines (Deleuil *et al. 2001*). The FUSE homepage (http://fuse.pha.jhu.edu/) has a comprehensive list of all the papers produced based on FUSE data. I look at the whole and found not publication on attempts to detect chromospheric emissions in Ap stars. Clearly such study is necessary.

The case for when we use the boundary condition equation (4.106 and 4.111) is shown in Fig. 5.8. Here the energy losses due to surface leakage become almost comparable to the internal losses for frequencies $\omega > \omega_{ac}$. There are no surface losses for frequencies $\omega < \omega_{ac}$, *i.e.* all frequencies are reflected back at the surface. There is a minimum in the pulsation energy at the cut-off frequency. This is due to increased losses due to the waves propagating out of the stellar surface (and dissipating as they do so).

5.1.3 Excitation mechanism

Here we investigate the possible damping and excitation regions in the homogeneous equilibrium models we use. I need to emphasise that Balmforth *et al.* (2001) have a much better treatment of the physics of the equilibrium model. They use composite models that include the effects of magnetic fields in the polar regions (see section 1.2.10 for more details).

We use our calculations of the work integral to discuss the possible excitation or damping of the modes within the roAp star frequency range. First, to locate the damping or excitation zones in the star we plot the derivative of the work integral as a function of depth in the upper part of the star in Fig. 5.9. Damping regions have negative dW/dr, and excitation zones have positive dW/dr. Therefore, the mode shown is damped in much of the atmosphere, except in small regions near the hydrogen ionisation and another one around 2000 km below the photosphere. In the same figure, a comparison is made between the work integral calculated using the exact case, Ando & Osaki and the Eddington approximations. The Ando & Osaki approach is the Eddington approximation with the assumption of radiative equilibrium (see appendix A). In all these cases, the excitation regions are found deeper in the star.

Cunha (2002) uses the models used by Balmforth *et al.* (2001) to discuss predictions with regard to theoretical edges of the instability strip relevant to roAp stars. Unfortunately because we do not find any excited modes in our models(largely because of the inadequacies in the physics of our models), we are unable to comment on her predictions and discussions.

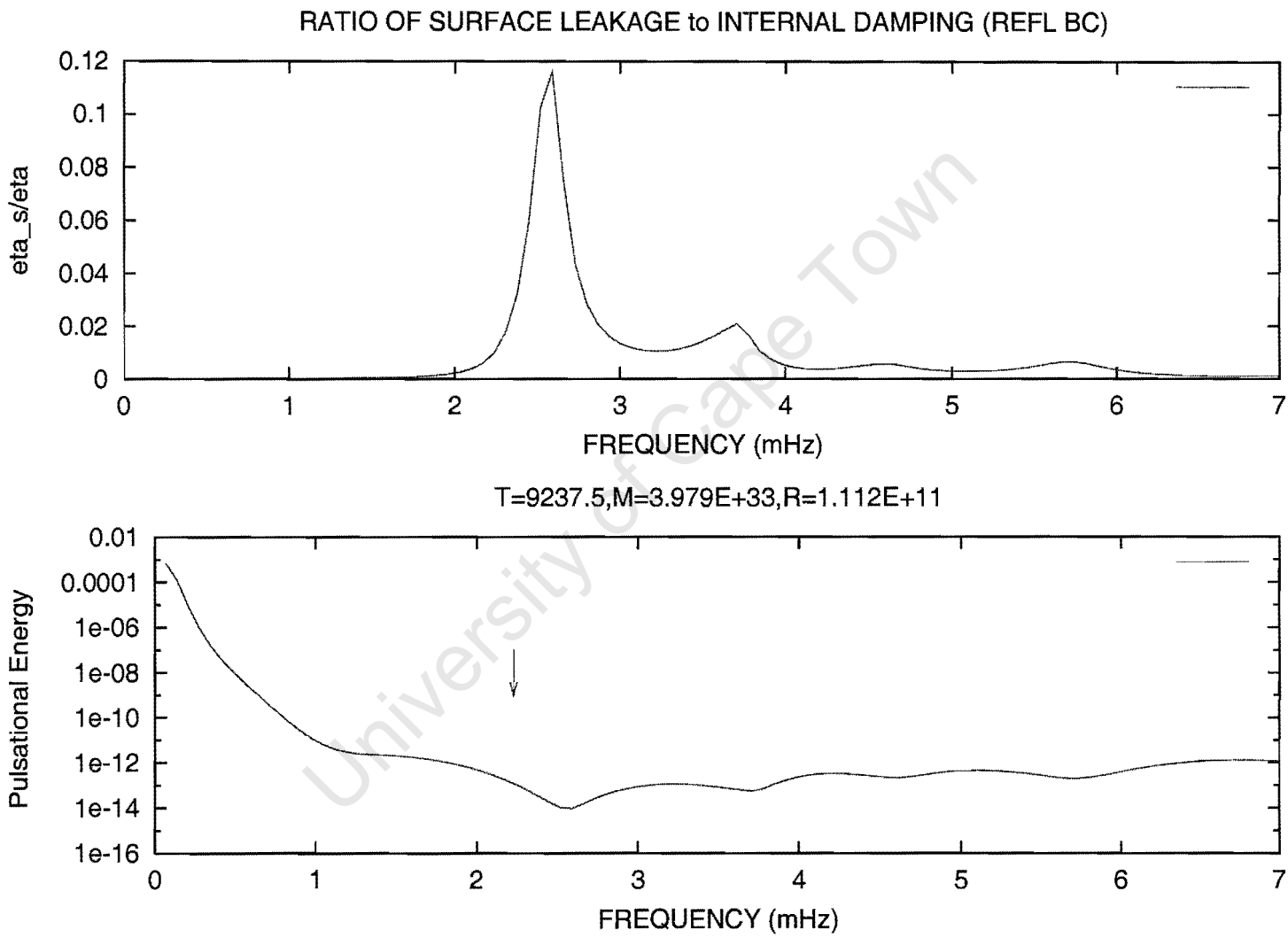

Figure 5.7: The contribution to total damping (or excitation) of surface losses when reflective boundary condition is used. There is an increased surface losses near $\nu = 2.5$ mHz, 3.7 mHz, 4.6 mHz and 5.7 mHz.

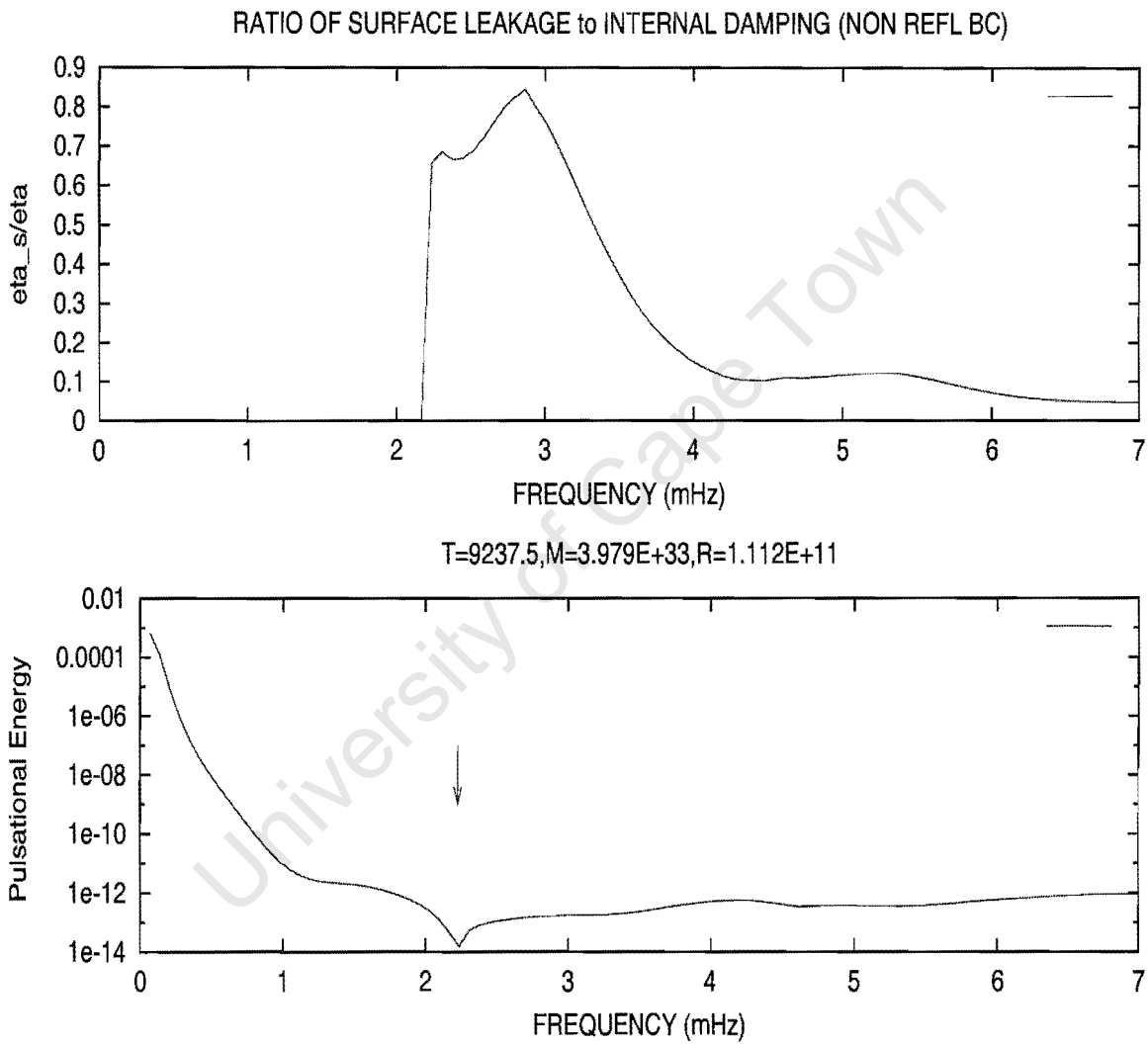

Figure 5.8: The contribution of surface losses to total damping. This is based on the surface boundary condition that allows waves to propagate through the boundary. The arrow indicate the cut-off frequency. There is energy minimum at the cut-off frequency.

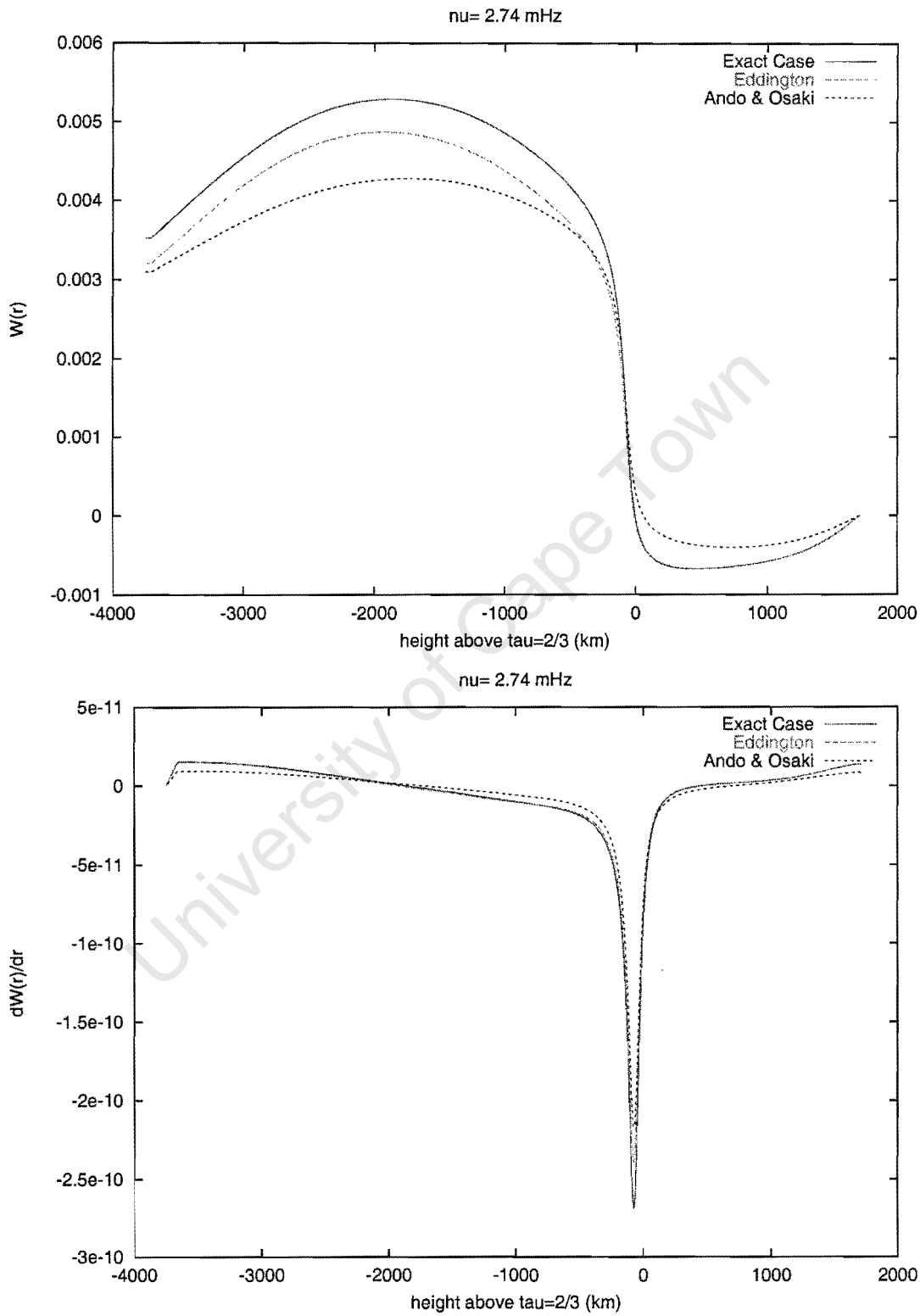

Figure 5.9: The top panel shows a plot of the work integral (equation 4.157) as a function of depth in the stellar atmosphere. The bottom panel shows the derivative of the work integral with respect to depth for an eigenmode with $\nu = 2.74$ mHz.

Table 5.1: A listing of the frequencies and their corresponding damping rates used in Figs 5.10 to 5.23

σ	ω	ν **(mHz)**	n
(1.0,-1.9E-8)	(4.394E-4,-8.6E-12)	0.069	1
(5.0,-4.1E-5)	(2.197E-3,-1.8E-08)	0.349	3
(10.0,-2.6E-3)	(4.393E-3,-1.1E-06)	0.669	7
(15.0,-7.8E-2)	(6.590E-3,-3.4E-05)	1.048	11
(20.0,-0.2)	(8.787E-3,-6.6E-5)	1.398	16
(25.0,-8.1E-2)	(0.0109,-3.5E-5)	1.748	19
(30.0,-0.10)	(0.01318,-4.4E-5)	2.097	23
(35.0,-0.21)	(1.537E-2,-9.2E-05)	2.447	28
(40.0,-0.16)	(0.0170,-6.9E-5)	2.797	32
(45.0,-0.21)	(0.0190,-9.227E-5)	3.146	36
(50.0,-0.31)	(0.0220,-1.3E-4)	3.496	40
(55.0,-0.36)	(0.0241,-1.5E-4)	3.846	43

5.2 Nodes in the atmospheres of the roAp stars

The discussions in the next two subsections are based on the solutions calculated for the frequencies shown in Table 5.1. The damping rates shown in that table were determined by imposing the condition that the layers of the star above the base of the envelope do no work in those below the base of the envelope (*cf.* 5.1.2).

5.2.1 Temperature nodes

The real and imaginary parts of the temperature perturbations are shown in Fig. 5.10 calculated for the frequencies shown in Table 5.1.

Visual inspections of the real part of $\delta T/T$ in Fig. 5.10 show that with exception of $\nu =$ 0.349 mHz (where a node is visible in the atmosphere) the position of the first temperature node seems to shift towards the stellar surface with increasing pulsation frequency. For pulsation frequencies larger than 2.097 mHz the temperature nodes lie in and above the

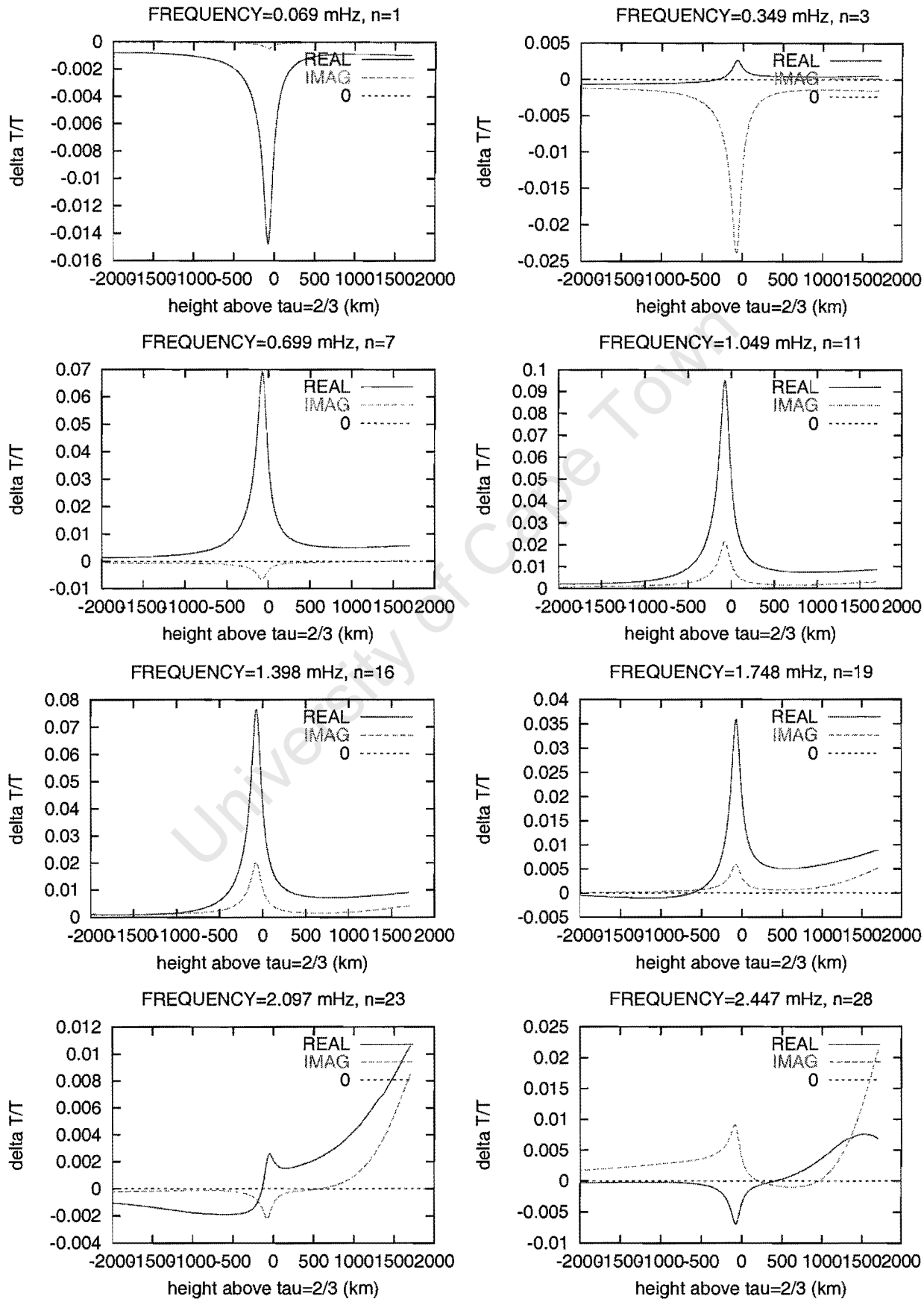

Figure 5.10: The real part of the temperature eigenfunctions in the atmosphere calculated for various eigenfrequencies displayed in Table 5.1.

... continues from Fig. 5.10.

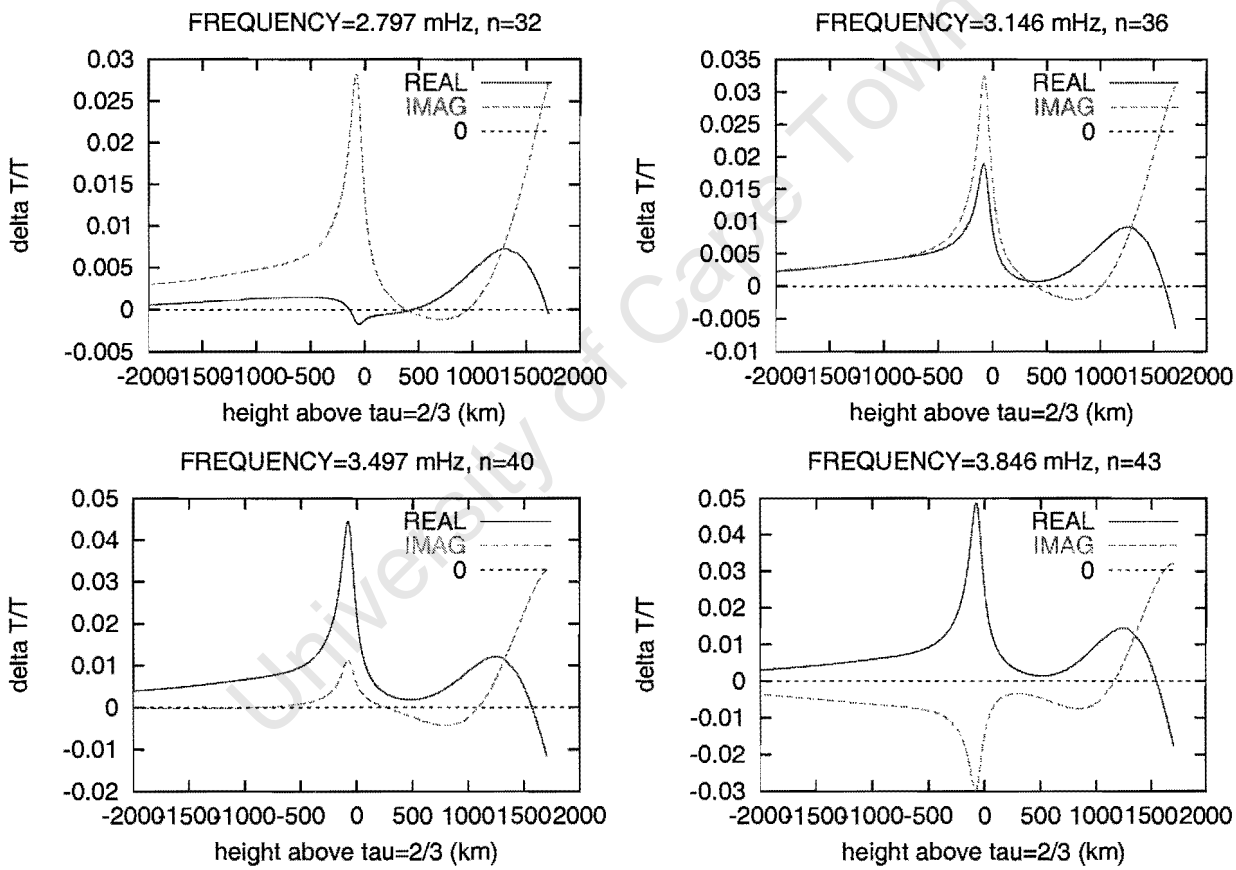

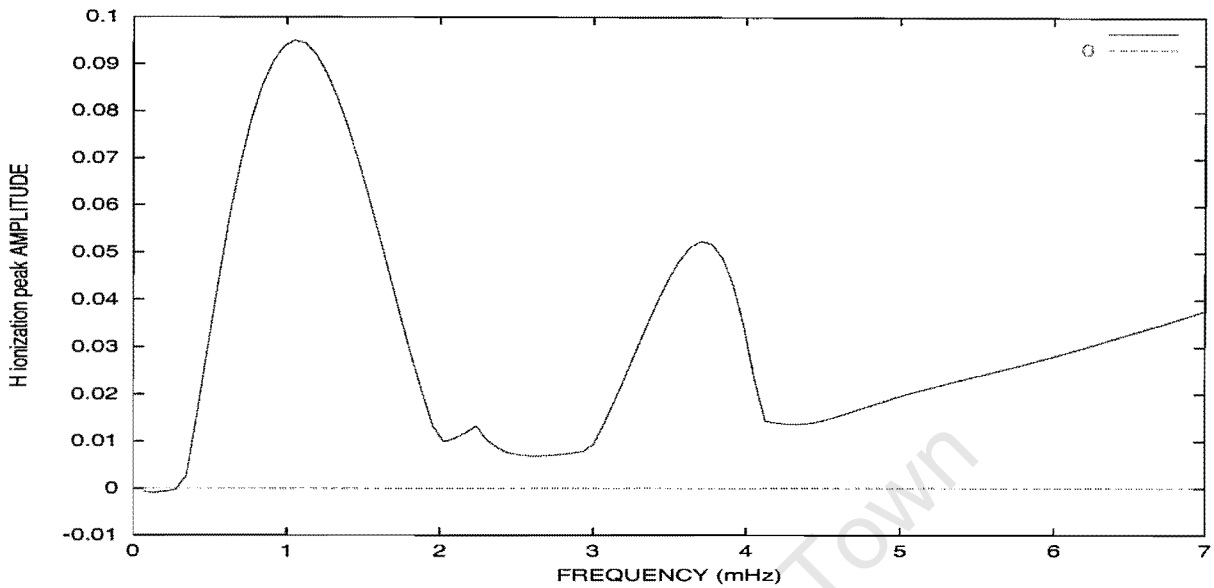

Figure 5.11: The amplitude of the hydrogen ionisation peak (seen in the real part of the temperature eigenfunction) as a function of pulsation frequency. This curve has a zero near $\nu = 0.3$ mHz. This zero is responsible for the temperature node at low pulsation frequencies.

photosphere.

To investigate why a temperature node would be visible in the atmosphere at such low overtones (as seen for $\nu = 0.349$ mHz) we plotted the amplitude of the hydrogen ionisation peak seen in the temperature perturbation plot as a function of pulsation frequency. This came out of a belief that the presence of the hydrogen ionisation zone near the photosphere of our equilibrium model has something to do with this behaviour since it is only seen in the temperature perturbations and not in displacement or pressure perturbations. A plot of the amplitude of the temperature peak as a function of pulsation frequency is shown in Fig. 5.11. The curve in Fig. 5.11 has a zero near $\nu = 0.3$ mHz which causes a zero in the temperature perturbations. This figure really gives the response of the H-ionization zone to small radial acoustic waves. There is a specific frequency where the ionization zone does not respond to the waves (near 0.3 mHz). This results in a node in the temperature perturbations in the atmosphere of A stars. There are also resonant frequencies that result in increased damping (or possibly, excitation) near 1 mHz and 3.5 mHz. For the equilibrium model we used, this falls within the roAp regime. The increased damping near 1 mHz therefore corresponds to one of these resonance frequencies. The perturbed radiative energy density peaks at these two resonance frequencies (as discussed in section 5.1.2.

The mode with $\nu = 0.3$ mHz lies in the δ Scuti frequency regime. Our calculations indicate, therefore, that it is possible for δ Scuti pulsators to have temperature nodes in their photospheres. According to Medupe & Kurtz (1998) multi-colour photometry of such stars ought to reveal pulsation amplitude that decreases with increasing wavelength in a manner

similar to what has been found in roAp stars (see section 2). Martinez & Medupe (1998) report a 30 minute period for the star HD 75425 which has insecure Ap classification. If this star is indeed an Ap star with δ Scuti pulsations, it would be interesting to study its amplitude in various wavelengths to find any consistencies with the above predictions. As far as we know, no such studies on HD 75425 have been published. We do however, have multi-colour photometric data on this star which we will publish soon.

5.2.2 Displacement nodes

The real and imaginary parts of the displacement are shown in Fig. 5.12 calculated for the frequencies shown in Table 5.1.

Inspection of Fig. 5.12 show that there is very little variation of the displacement with depth in the atmosphere at low frequencies ($n \leq 3$). At $n = 7$ the displacement decreases down to half its surface value at the base of the atmosphere. By the time we reach the roAp pulsation frequency regime, the displacement decreases very rapidly within 4000 km of the stellar surface. The first displacement node starts appearing within 3000 km below the surface when $n = 23$. The position of the first displacement node moves progressively closer to the stellar surface after this.

Analytical investigation

We consider the conditions under which displacement node will appear in the photosphere of a pulsator. We follow the treatment for an isothermal atmosphere given in Christensen-Dalsgaard (1998) and presented in section 4.2.3 of this thesis. It is clear from equation (4.105) that the displacement will not have a node in the atmosphere at frequencies lower than the acoustic cut-off frequency, since in this case, the displacement is an exponential function. In the case where the pulsation frequency is larger than the cut-off frequency, the real part of the displacement will have a zero under the following condition:
If we substitute equation (4.112) into equation (4.105) we end up with

$$\exp(\frac{h}{2\,H_P}) \exp\left[i\left(\frac{\omega^2}{\omega_{ac}^2} - 1\right)^{1/2} \frac{h}{2\,H_P}\right] = 0. \tag{5.1}$$

Taking the real part we obtain

$$\cos\left[\left(\frac{\omega^2}{\omega_{ac}^2} - 1\right)^{1/2} \frac{h}{2\,H_P}\right] = 0, \tag{5.2}$$

which leads to this condition for a displacement node when $\omega > \omega_{ac}$:

$$\frac{1}{2}\left(\frac{\omega^2}{\omega_{ac}^2} - 1\right)^{1/2} \frac{h}{H_P} = \frac{\pi}{2}\,j, \tag{5.3}$$

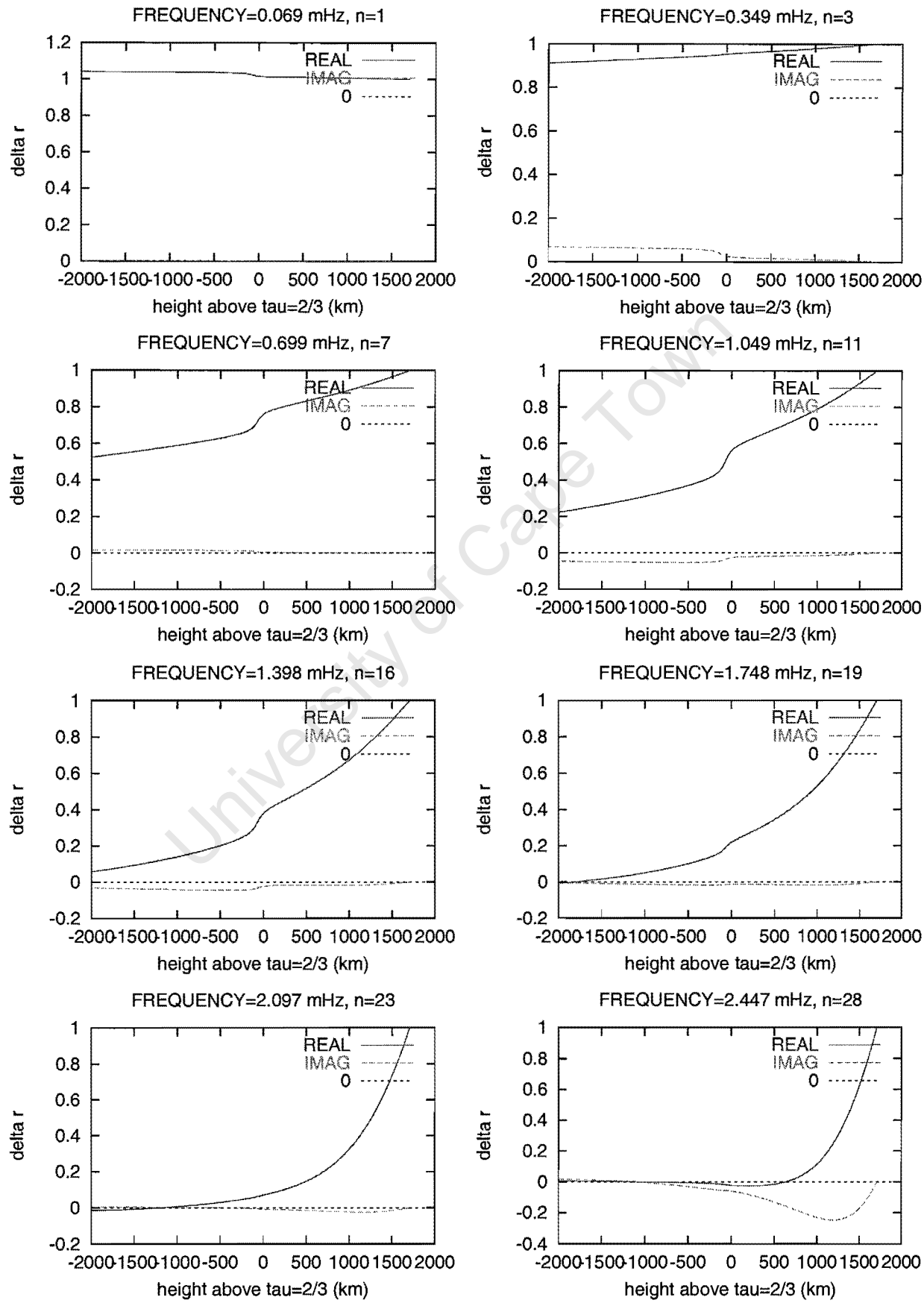

Figure 5.12: The real and imaginary parts of the displacement eigenfunctions calculated using the eigenfrequencies in Table 5.1.

... continues from Fig. 5.12.

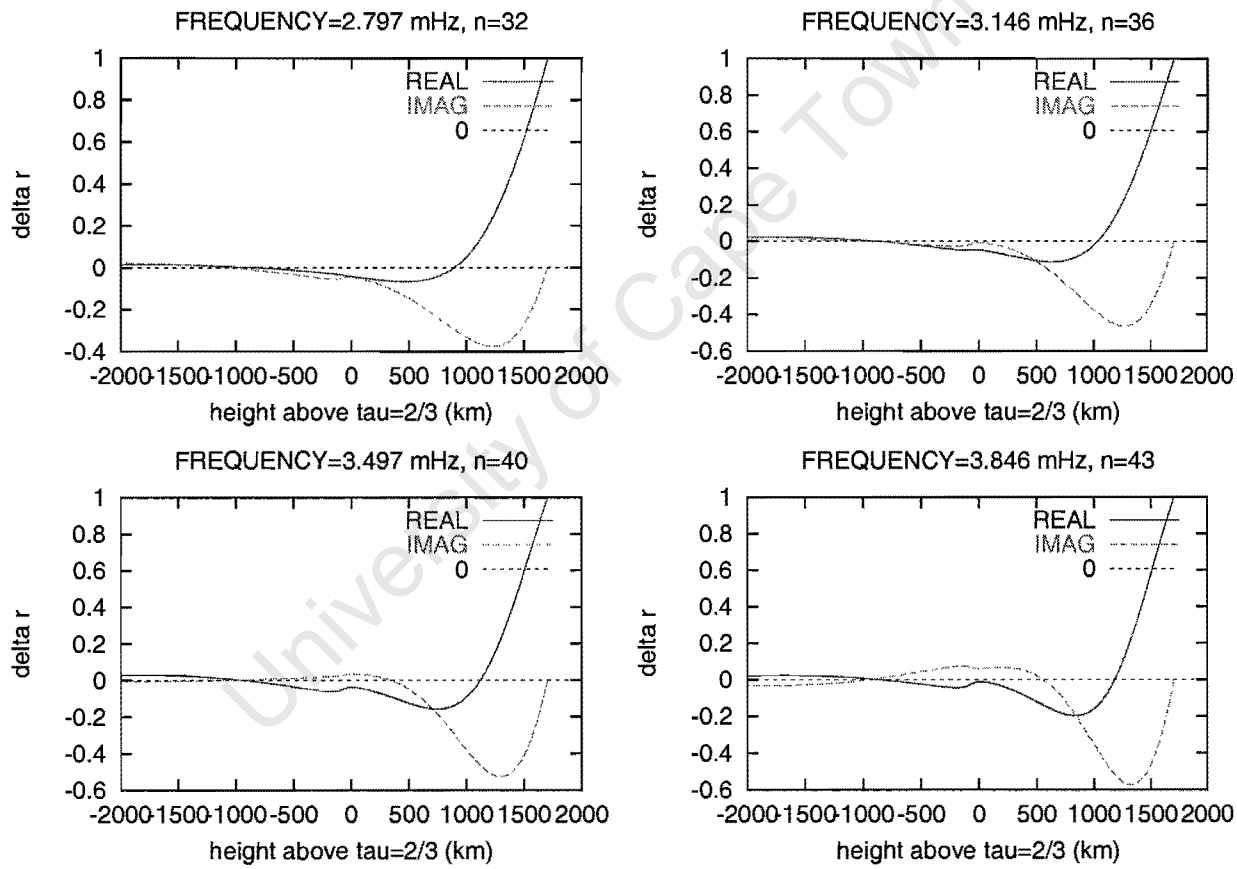

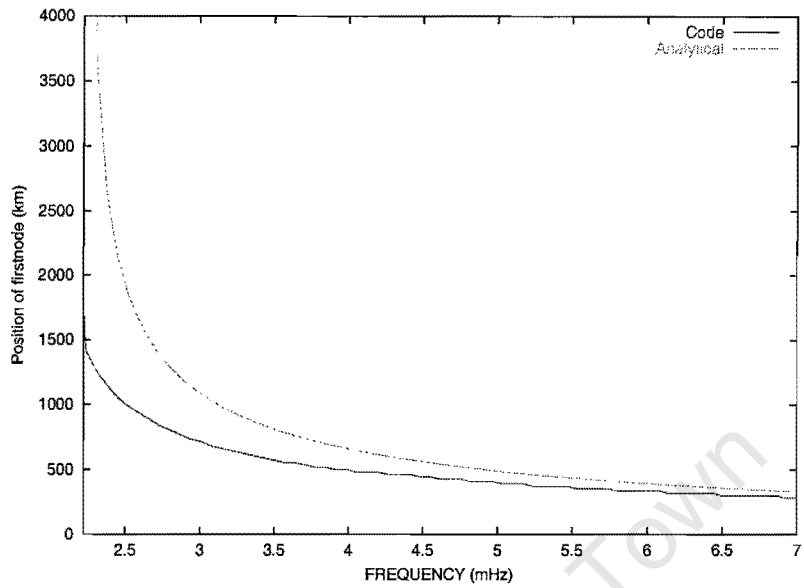

Figure 5.13: The position of the first node from our code is compared with equation (5.13) at several frequencies above the acoustic cut-off frequency.

where $j = 1, 3, 5, \ldots$ such that $j = 1$ denotes the first node, $j = 2$ the second node *etc.* Therefore the height at which a real part of the displacement node will appear is given as

$$h = \frac{\pi\, j\, H_P}{\left(\frac{\omega^2}{\omega_{ac}^2} - 1\right)^{1/2}}. \tag{5.4}$$

In Fig. 5.13 we compare the height at which a displacement node occurs obtained from our code with equation (5.6). Although in the roAp frequency regime the differences between equation (5.6) and our code can be large, the differences become smaller at higher frequencies.

Similarly, for the imaginary part of the displacement to have a node the following condition must be met:

$$\sin\left[\left(\frac{\omega^2}{\omega_{ac}^2} - 1\right)^{1/2} \frac{h}{2\, H_P}\right] = 0, \tag{5.5}$$

Therefore, the height of the node for the imaginary part of the displacement is given as

$$h = \frac{2\,\pi\, k\, H_P}{\left(\frac{\omega^2}{\omega_{ac}^2} - 1\right)^{1/2}}. \tag{5.6}$$

where $k = 0, 1, 2, \ldots$ It is clear from this that the position of the displacement node does not change much for $\omega \gg \omega_{ac}$.

For $\omega > \omega_{ac}$ the pressure perturbations are given as

$$\frac{\delta P}{P} = -\frac{\Gamma_1 a_- e^{-\frac{h}{2H_P}}}{2H_P} \left\{1 + i\left(\frac{\omega^2}{\omega_{ac}^2} - 1\right)^{1/2}\right\} \exp\left[-\frac{i}{2}\left(\frac{\omega^2}{\omega_{ac}^2} - 1\right)\frac{h}{H_P}\right], \tag{5.7}$$

which can be re-written as

$$\frac{\delta P}{P} = -\frac{\Gamma_1 a_- e^{-\frac{h}{2H_P}}}{2H_P} \frac{\omega}{\omega_{ac}} \exp\left[i\left\{\Psi - \frac{1}{2}\left(\frac{\omega^2}{\omega_{ac}^2} - 1\right)\frac{h}{H_P}\right\}\right] \tag{5.8}$$

where

$$\tan\Psi = \left(\frac{\omega^2}{\omega_{ac}^2} - 1\right)^{1/2}. \tag{5.9}$$

Therefore, the condition for a node in the real part of the pressure perturbation is

$$h = \frac{2\left(\Psi - \frac{\pi}{2}m'\right)H_P}{\left(\frac{\omega^2}{\omega_{ac}^2} - 1\right)^{1/2}} \tag{5.10}$$

where $m' = 1, 3, 5, \ldots$. It is easy to show that the position of a node in the imaginary part of the pressure perturbation is given as

$$h = \frac{2\left(\Psi - \pi n'\right)H_P}{\left(\frac{\omega^2}{\omega_{ac}^2} - 1\right)^{1/2}} \tag{5.11}$$

where $n' = 0, 1, 2, \ldots$
In the adiabatic case the position of the temperature node will also follow this trend.

5.2.3 Comparison of displacement and temperature nodes

In this subsection we aim to determine critical pulsation frequency (or overtone number) for which a temperature and displacement node becomes visible in the stellar atmosphere. To do this, we determined the frequencies and damping rates using the condition that the layers of the star above the base of the envelope do no work on those below the base. We then plotted the location of the first temperature, displacement and pressure node as a function of pulsation frequencies. The plot that resulted from this is shown in Fig. 5.14.

It is clear from Fig. 5.14 that for low overtones (low frequencies) the temperature, pressure and displacement nodes lie very deep into the envelope of a star. The curve shows that the first temperature node for modes with frequencies near 0.3 mHz lies in the photosphere. We have suggested in subsection 5.2.1 that this is due to the hydrogen ionisation effects on the temperature perturbations. Modes with $n > 7$ lie within 4000 km below the stellar surface. However, the node for modes with $14 < n < 18$ lies much deeper (down to 25000 km). It is clear that this abnormal behaviour is not a result of the hydrogen ionisation zone since this does not show in Fig. 5.11. From Fig. 5.14 we deduce that the critical frequency for which the real part of temperature, pressure perturbations and displacement have a node visible in the atmosphere is around $\nu_{crit} = 2.7$ mHz. This corresponds to $n_{crit} = 25$.

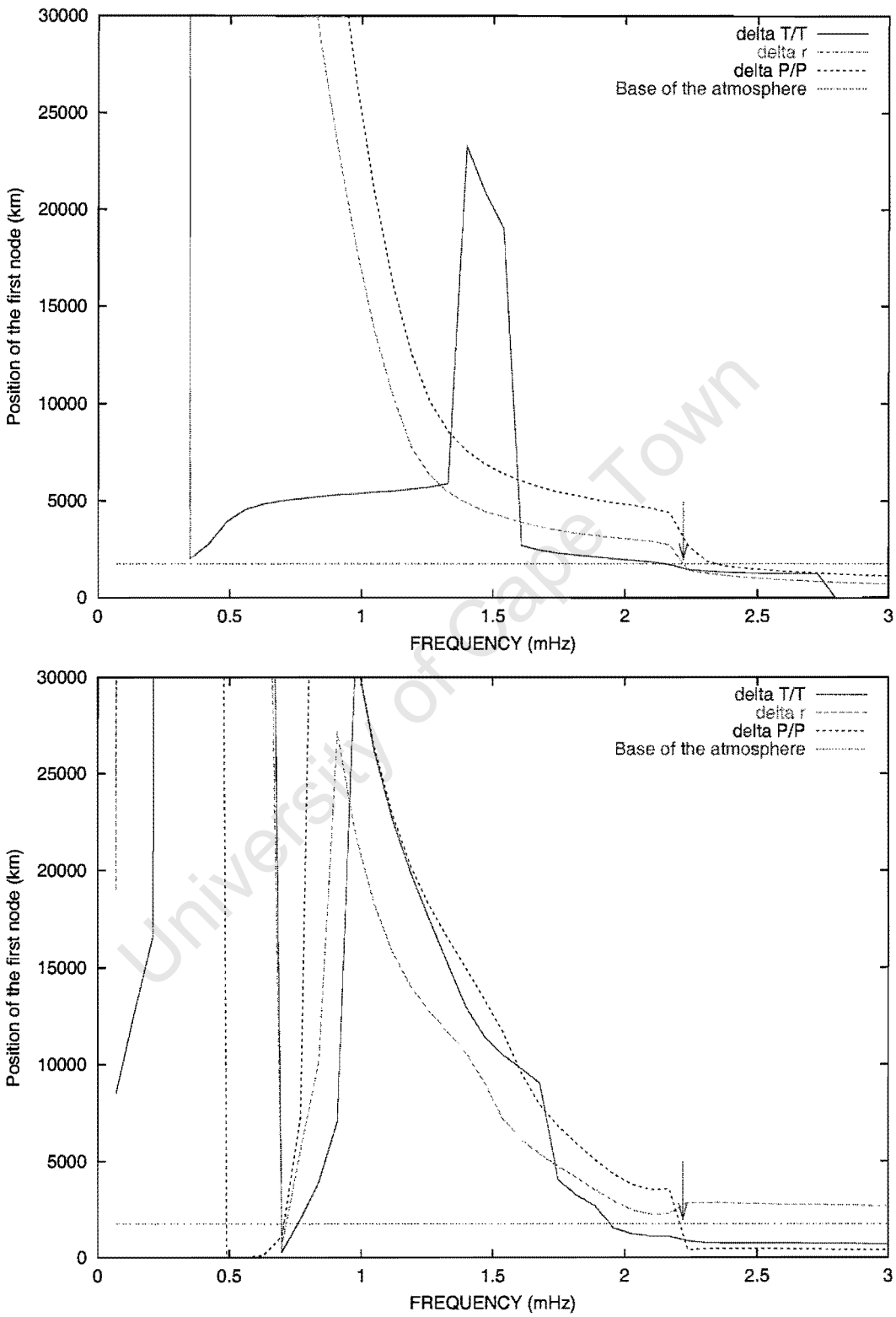

Figure 5.14: The location of the first temperature, pressure and displacement nodes as a function of pulsation frequency. The top panel is for the real part of the solution, the bottom for the imaginary part. The arrow indicates the acoustic cut-off frequency.

5.2.4 Node separation

Baldry *et al.* (1998) found variations in bisector velocity along the depth of the Hα line in α Cir such that the velocity amplitudes from the core of the line decreased to a zero mid-way and increased again towards the line wings. They interpreted this as a variation of the pulsation velocities as a function of physical depth inside the star. On similar studies of HR 3831, Baldry & Bedding (2000) also found variation of bisector velocities with depth in HR 3831, but surprisingly with the same pattern as in α Cir. HR 3831 has a longer pulsation period than α Cir, and thus it was expected that the velocity pattern in these two stars would be quite different. In particular, the node separation in HR 3831 is expected to be larger than for α Cir. Baldry & Bedding (2000) offered two possible explanations that either the bisector velocity variations are due to surface effects or that HR 3831 and α Cir have different atmospheric structure.

To investigate this phenomenon, we calculated the distance between the first and second node at several pulsation frequencies. This is plotted in Fig. 5.15. The first arrow marks the pulsation frequency of HR 3831 and the higher frequency arrow indicate α Cir 's frequency. It is clear that indeed provided that both HR 3831 and α Cir have similar atmospheric structures, the node separation for HR 3831 would be much larger than that of α Cir. Another thing to note is that for stars with pulsation frequencies larger than their acoustic cut-off frequencies, their node separation will be significantly smaller. Therefore, if the atmospheric structure of HR 3831 is different from that of α Cir such that HR 3831 also pulsates with a frequency larger than its acoustic cut-off frequency, then it could have similar node spacing as α Cir. This can also be achieved if all roAp stars oscillate with frequencies larger than their acoustic cut-off frequencies. A cautionary note is that the comparison of α Cir and HR 3831 only makes sense if their first nodes occur in their photospheres. According to Fig. 5.14 the first temperature node for a star pulsating with HR 3831 frequency occurs very deep below the photosphere so that a node (or node separation) will have no observable effect on the radial velocities or photometry of a star. Fig. 5.15 is based on equilibrium model of higher surface temperature than the surface temperatures for both stars. We should also investigate the node structure of stars with varying surface temperatures.

5.3 Effects of non-adiabaticity on phases

We investigate the phases defined as

$$\tan \Psi_y = Im\{y\}/Re\{y\}, \tag{5.12}$$

where y is any eigenfunction under consideration in order to see how non-adiabaticity affects them throughout the atmosphere and envelope of the star. The plots for displacement, perturbed pressure, temperature and flux phases are shown in Figs 5.16, 5.17, 5.18 and 5.19 respectively.

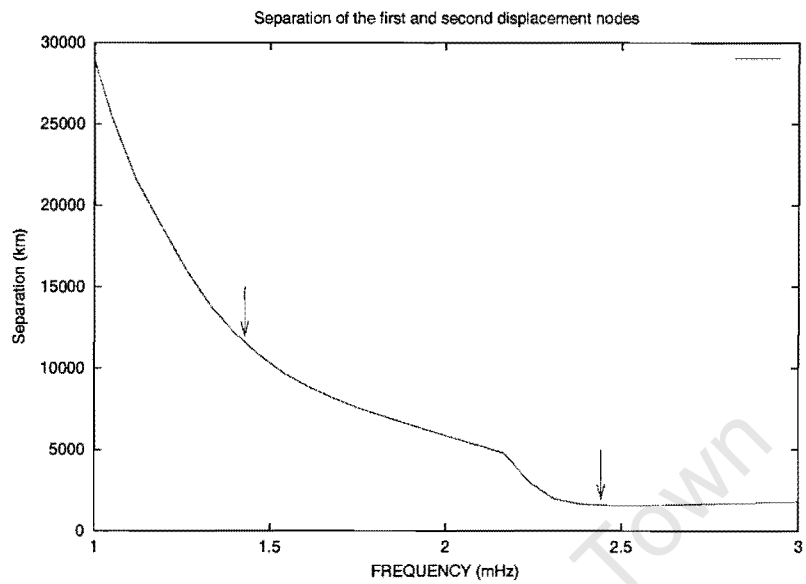

Figure 5.15: The distance between the first and second nodes in kilometres at different pulsation frequencies. The arrow on the left indicate the position of HR 3831 and that on the right α Cir.

5.4 The f and Ψ_T values.

Here we present the calculations of the ratios of relative temperature perturbations to displacement (f), *i.e.*

$$f = \left| \frac{\delta T/T}{\delta r/r} \right| ,$$

and the phase difference between temperature perturbations and displacement Ψ_T. The f value is plotted as a function of depth in a star at several frequencies shown in Table 5.1 in Fig. 5.20. The peak at zero height is due to the hydrogen ionisation zone effects on the opacity and opacity derivatives. It is visible at all frequencies shown there. The phase difference Ψ_T as a function of depth is shown in Figs 5.21. If we consider the amount by which Ψ_T changes from the surface to the photosphere (zero height) $\Delta\,\Psi_T$, we see that $\Delta\,\Psi_T$ is small for $n < 7$. In the frequency range $1.049 < \nu < 2.097$ mHz $\Delta\,\Psi_T$ is under 57° but for higher frequencies $\Delta\,\Psi_T$ is much larger.

In chapter 3 we indicate that the ratio of relative pressure perturbations to displacement C needs to be included in Watson's formula. Here C is:

$$C = \left| \frac{\delta P/P}{\delta r/r} \right| .$$

The variation of C with depth in the atmosphere is shown in Fig. 5.22. C also feels the effects of the hydrogen ionisation zone at all frequencies. There is also the phase difference

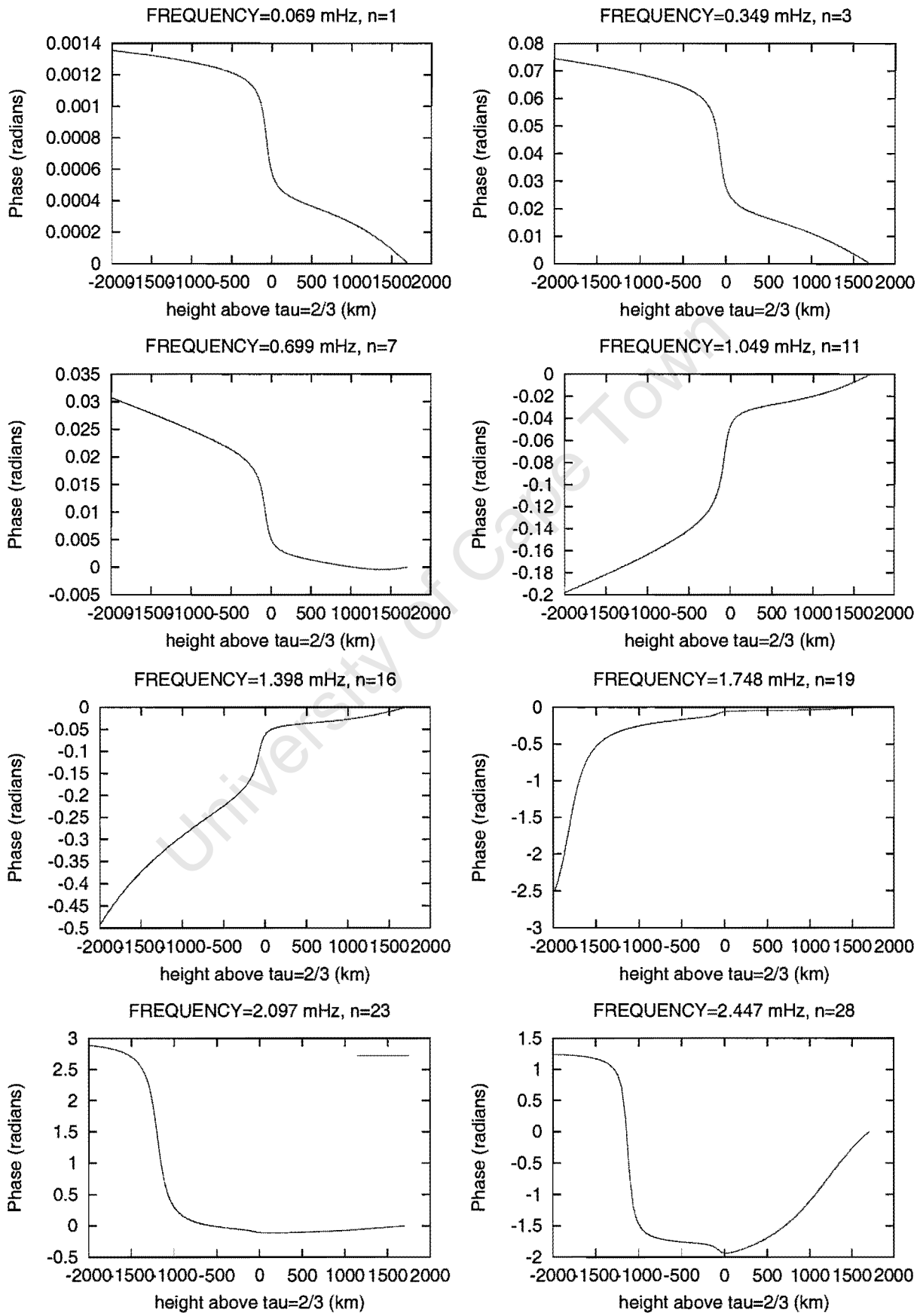

Figure 5.16: A plot of Ψ_y as a function of height above the photosphere, where $y = \delta\tilde{r}$ for various pulsation frequencies.

... continues from Fig. 5.16.

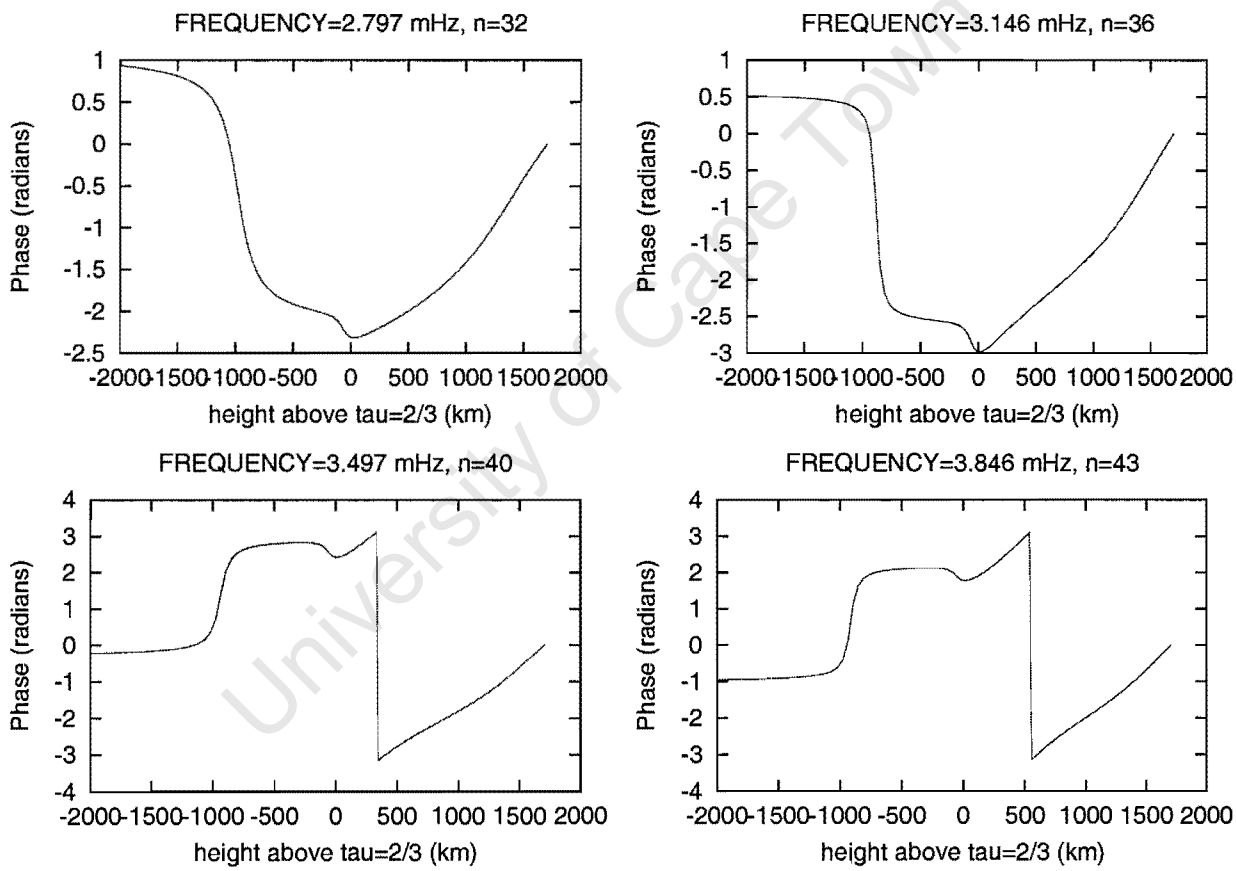

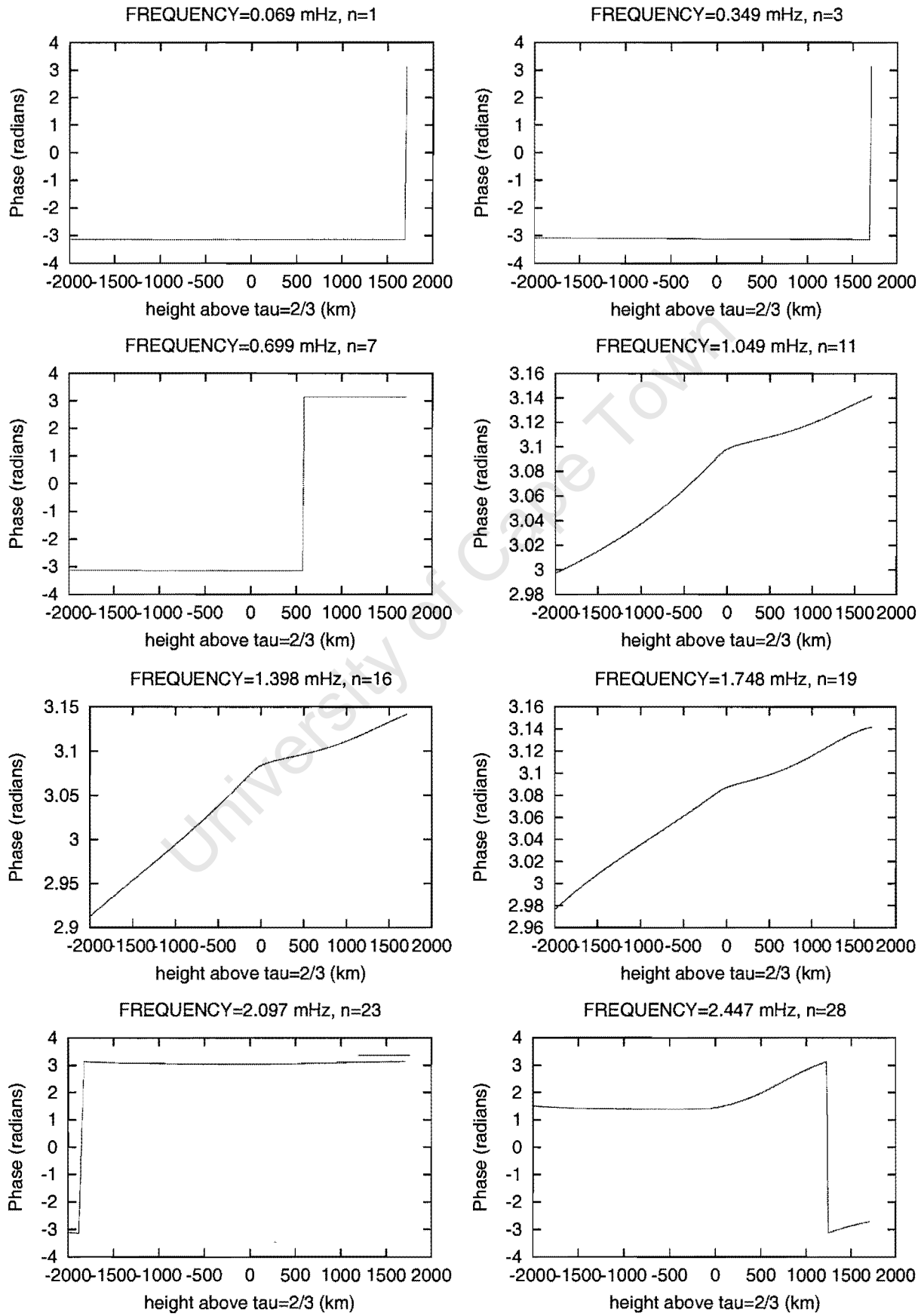

Figure 5.17: A plot of Ψ_y as a function of height above the photosphere, where $y = \delta P/P$ for various pulsation frequencies.

... continues from Fig. 5.17.

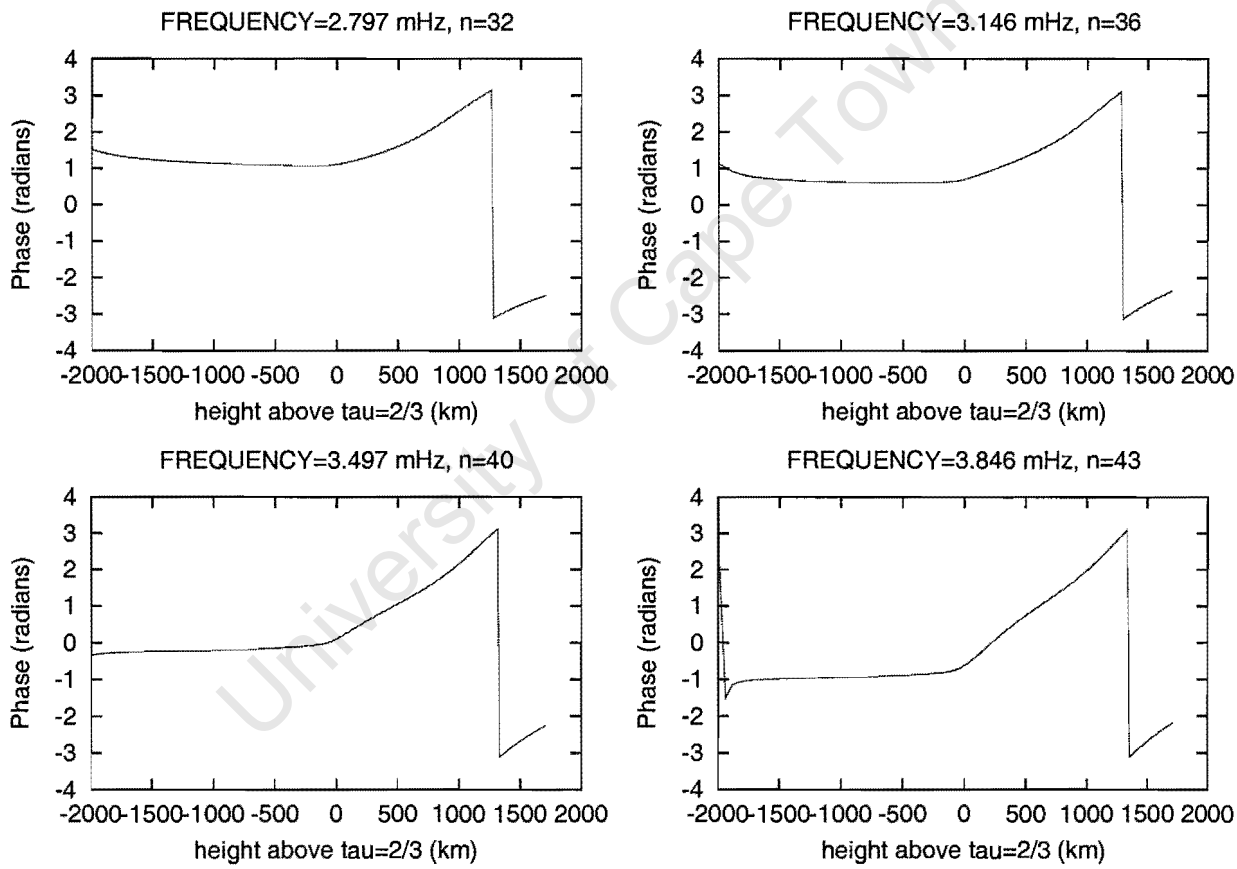

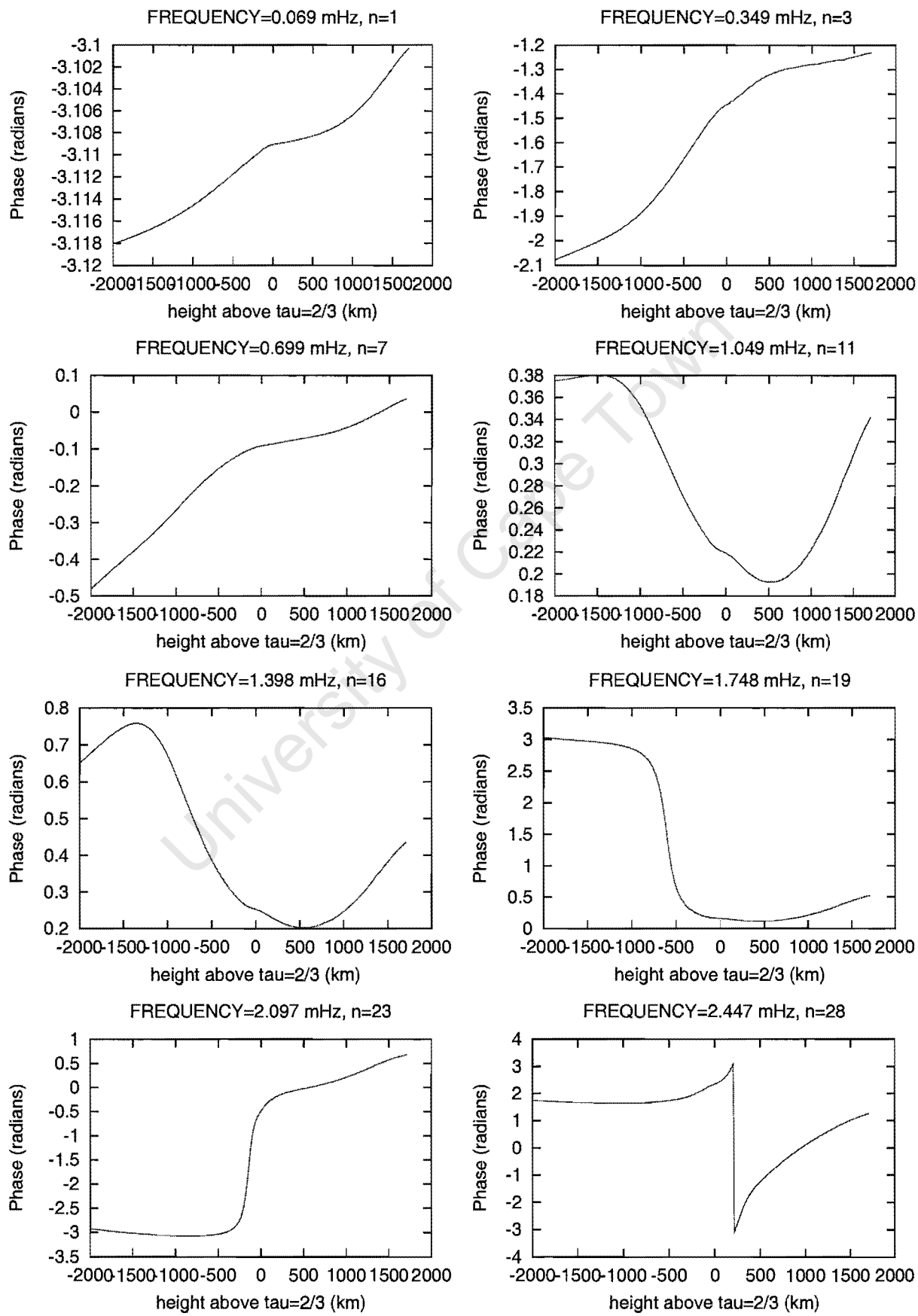

Figure 5.18: A plot of Ψ_y as a function of height above the photosphere, where $y = \delta T/T$ for various pulsation frequencies.

... continues from Fig. 5.18.

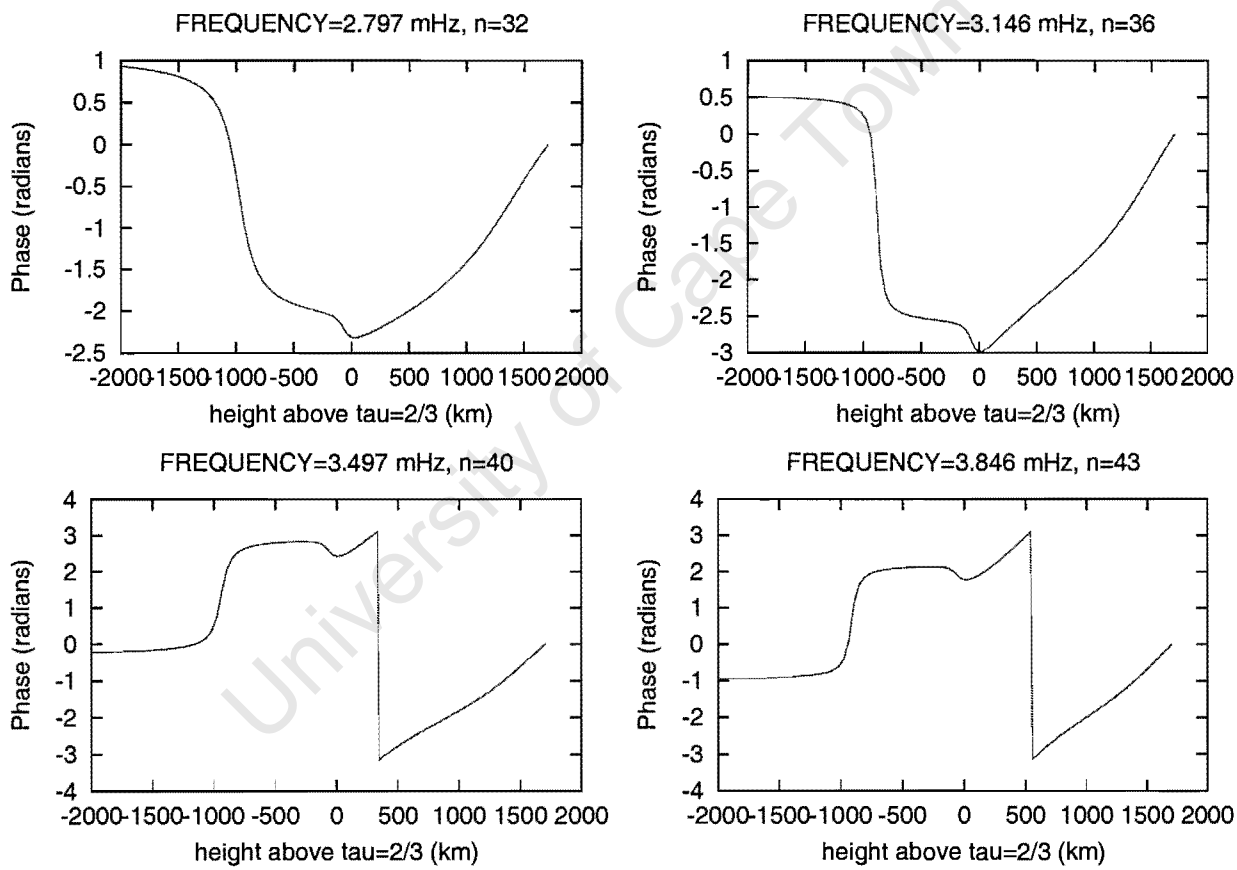

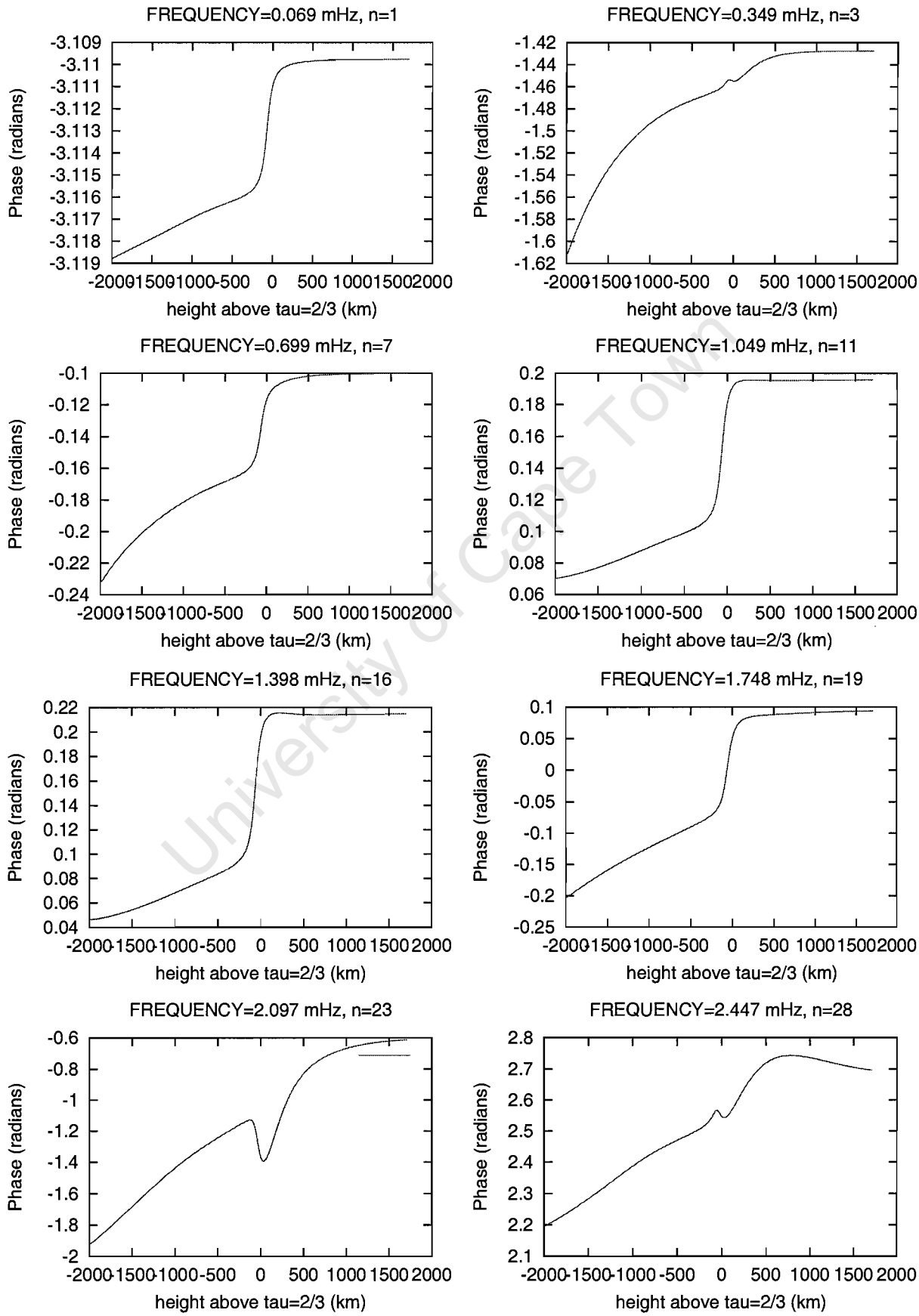

Figure 5.19: A plot of Ψ_y as a function of height above the photosphere, where $y = \delta H/H$ for various pulsation frequencies.

... continues from Fig. 5.19.

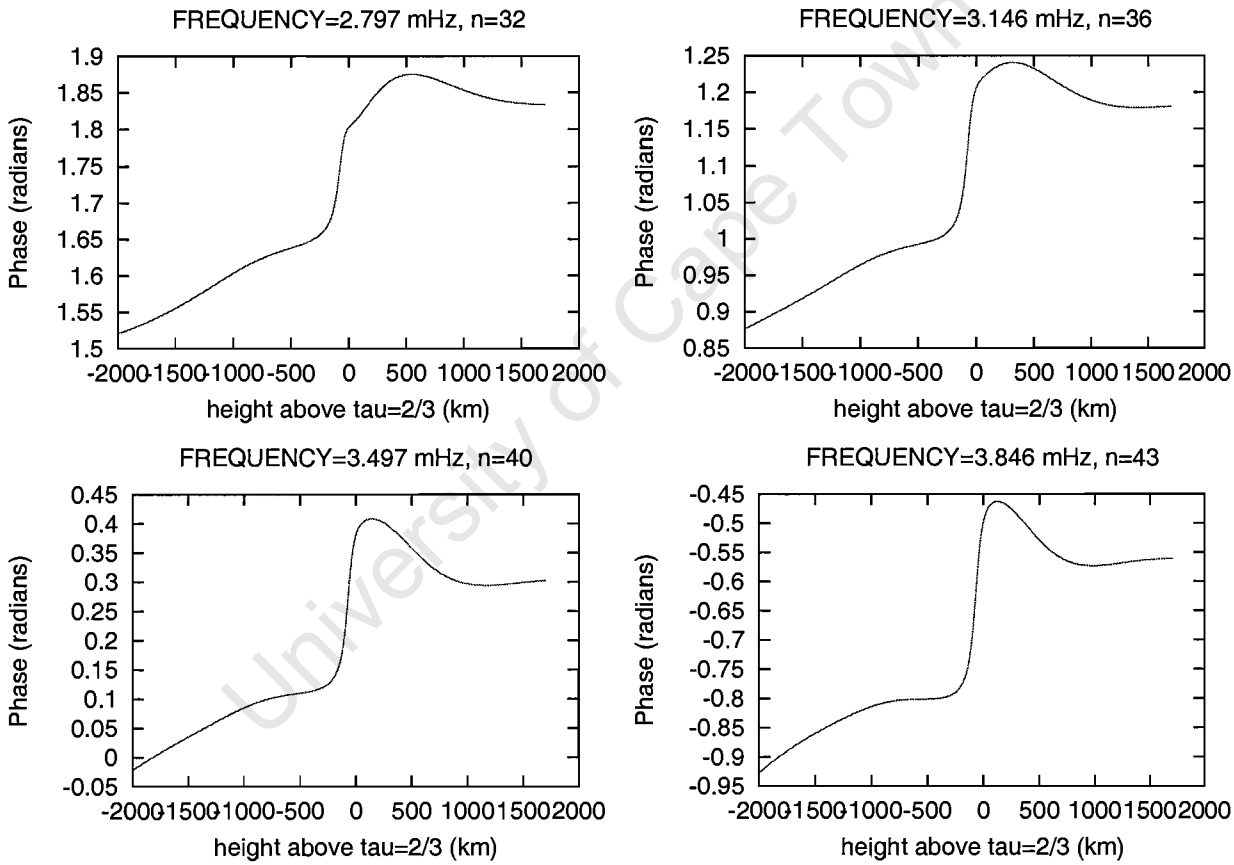

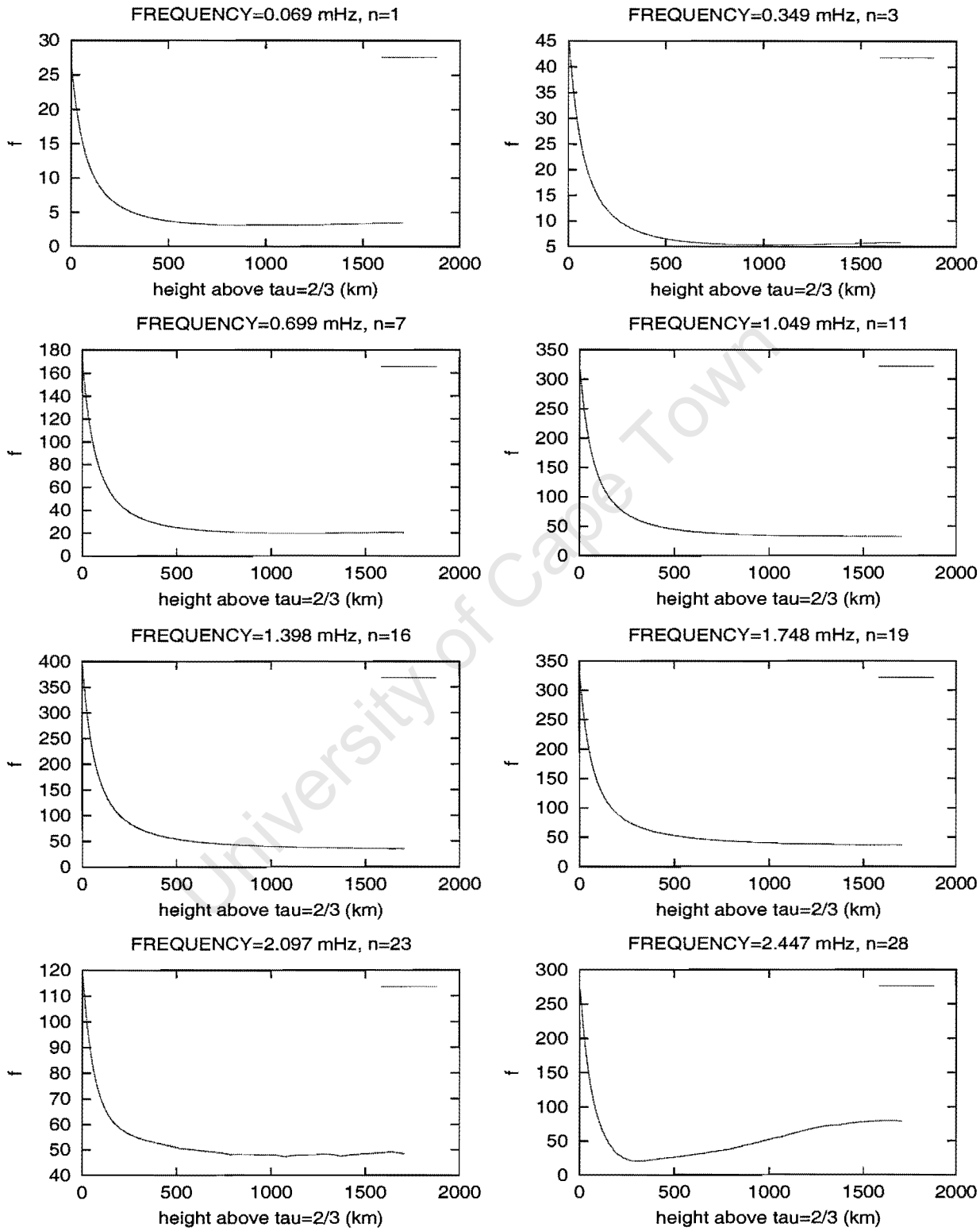

Figure 5.20: The ratio of $\delta T/T$ to $\delta r/r$ is plotted as a function of height above the photosphere in the atmosphere for several eigenfrequencies depicted in Table 5.1.

... continues from Fig. 5.20.

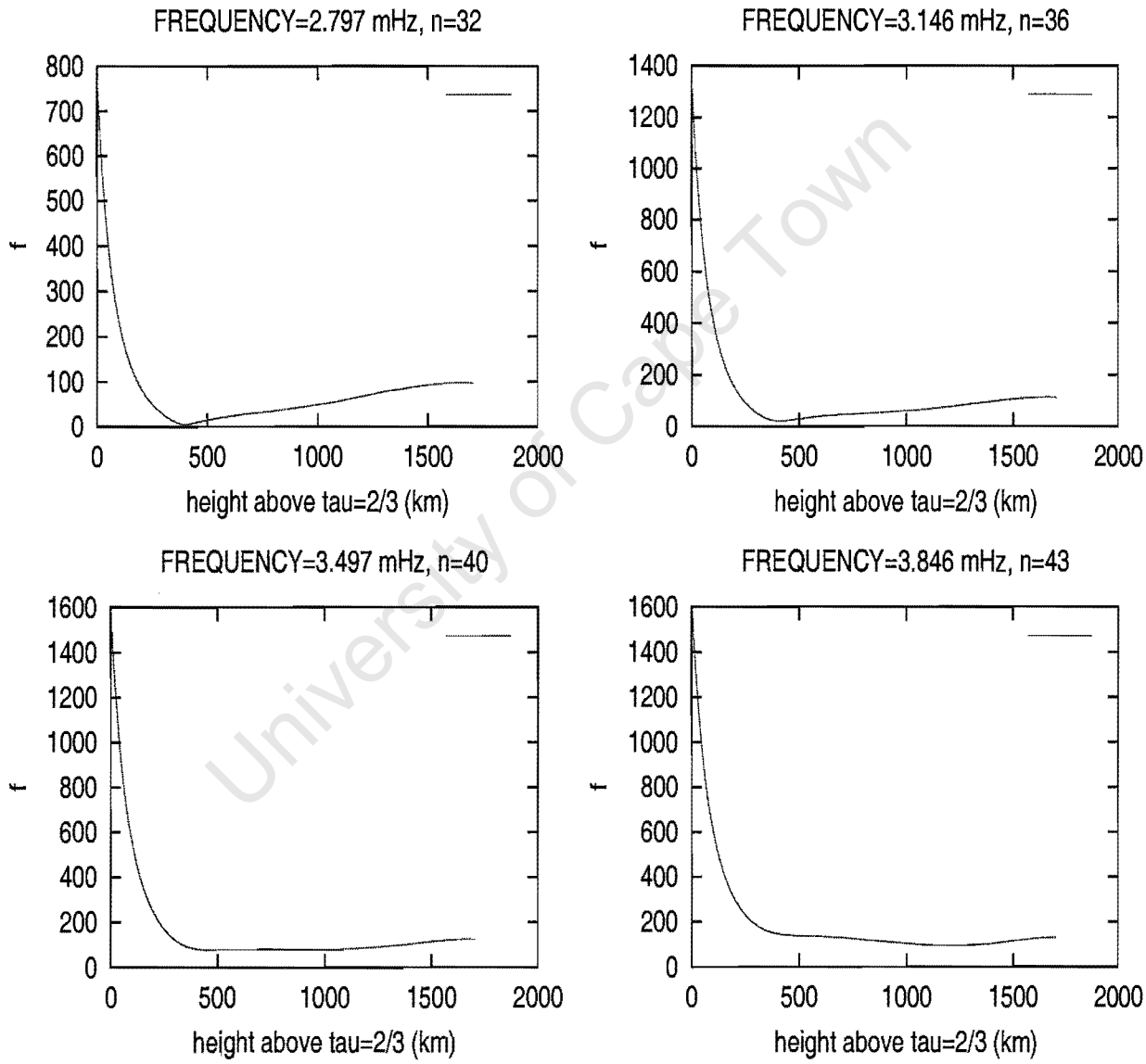

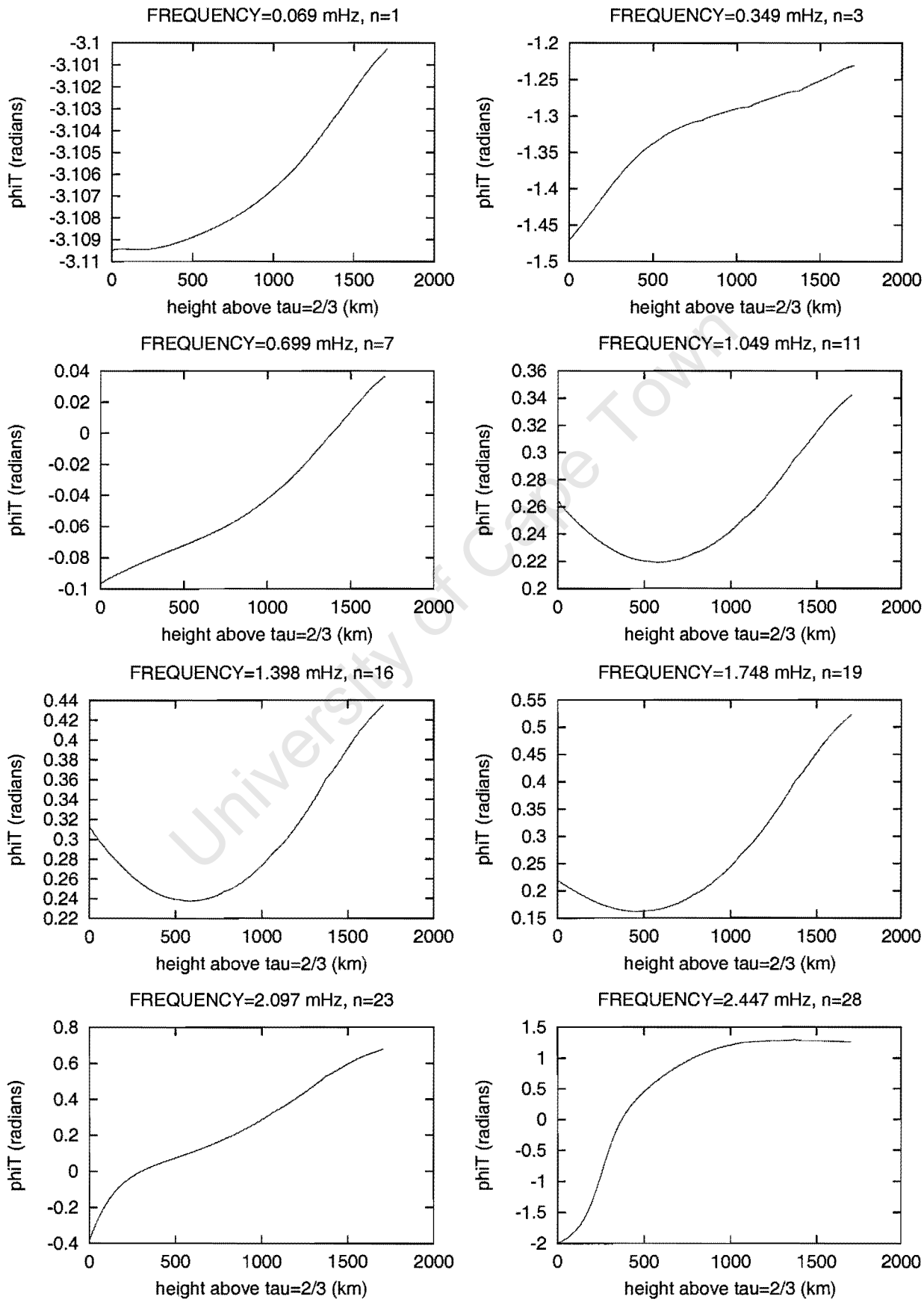

Figure 5.21: The phase difference between $\delta T/T$ and $\delta r/r$ is plotted as a function of height above the photosphere at several eigenfrequencies.

... continues from Fig. 5.21.

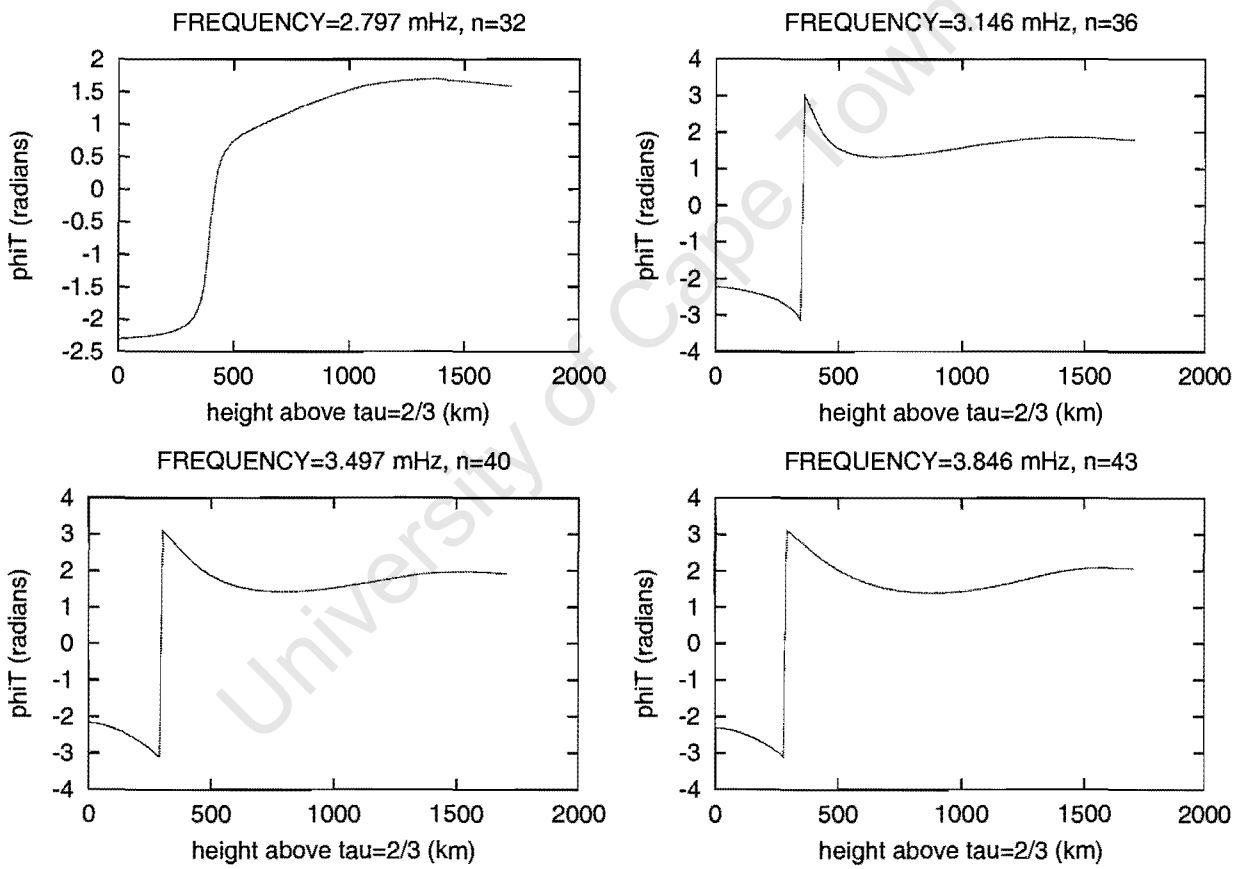

Ψ_P between pressure perturbations and displacement. Plots for Ψ_P are shown in Figs. 5.23. For $\nu < 2.097$ mHz Ψ_P does not change much in the photosphere. At higher frequencies the change in Ψ_P can be larger but is always under 57°.

5.5 Comparison of grey results with photometry

Here we compare our results with Watson's formula presented in chapter 3. Watson's formula is monochromatic whereas we have grey results. Therefore, to compare our results with Watson's formula we need to convert it to bolometric amplitudes. This we do by simply integrating the formula (numerically) over all the available wavelengths. The resulting bolometric amplitude is compared with the surface perturbed flux from our code in Fig. 5.24 at various frequencies. The corresponding pulsation phases are shown in Fig. 5.25. The value of B (see chapter 3) was determined from the boundary condition in equation (4.106) and (4.111). It is clear from Fig 5.24 that for low frequencies there is some agreement between the bolometric amplitudes obtained from the two aproaches. However, in the roAp frequency regime there is no agreement at all. Whereas Watson's formula predicts a monotonic increase of amplitude with pulsation frequency, our code predicts an increase followed by a decrease. The dependence on pulsation frequency of the amplitude in Watson's formula is purely a consequence of the boundary condition we used (equations 4.106 and 4.111), whereas our code is based on consistent treatment of radiative transfer.

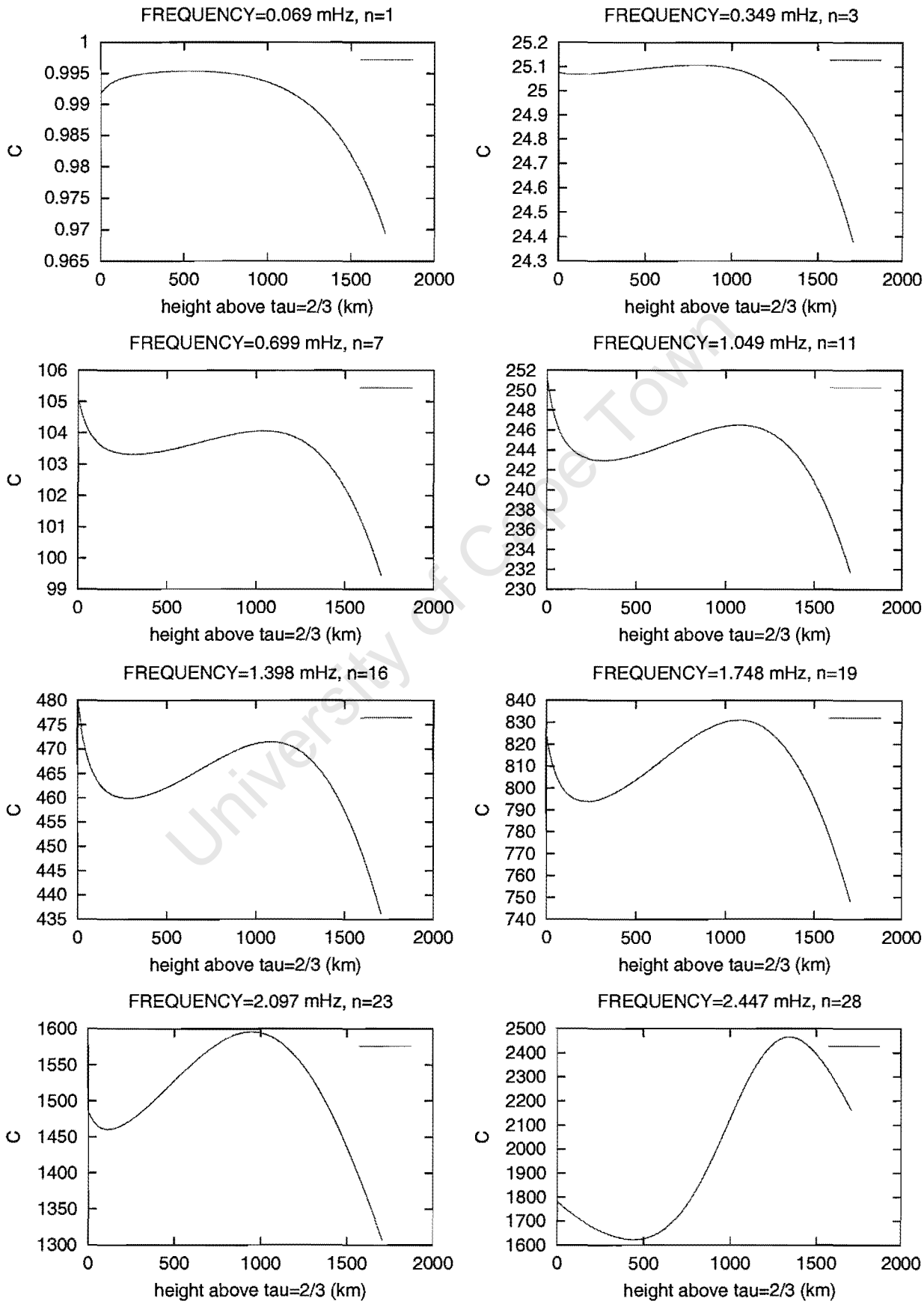

Figure 5.22: The ratio of $\delta P/P$ to $\delta r/r$ is plotted as a function of height above the photosphere in the atmosphere for several eigenfrequencies depicted in Table 5.1.

... continues from Fig. 5.22.

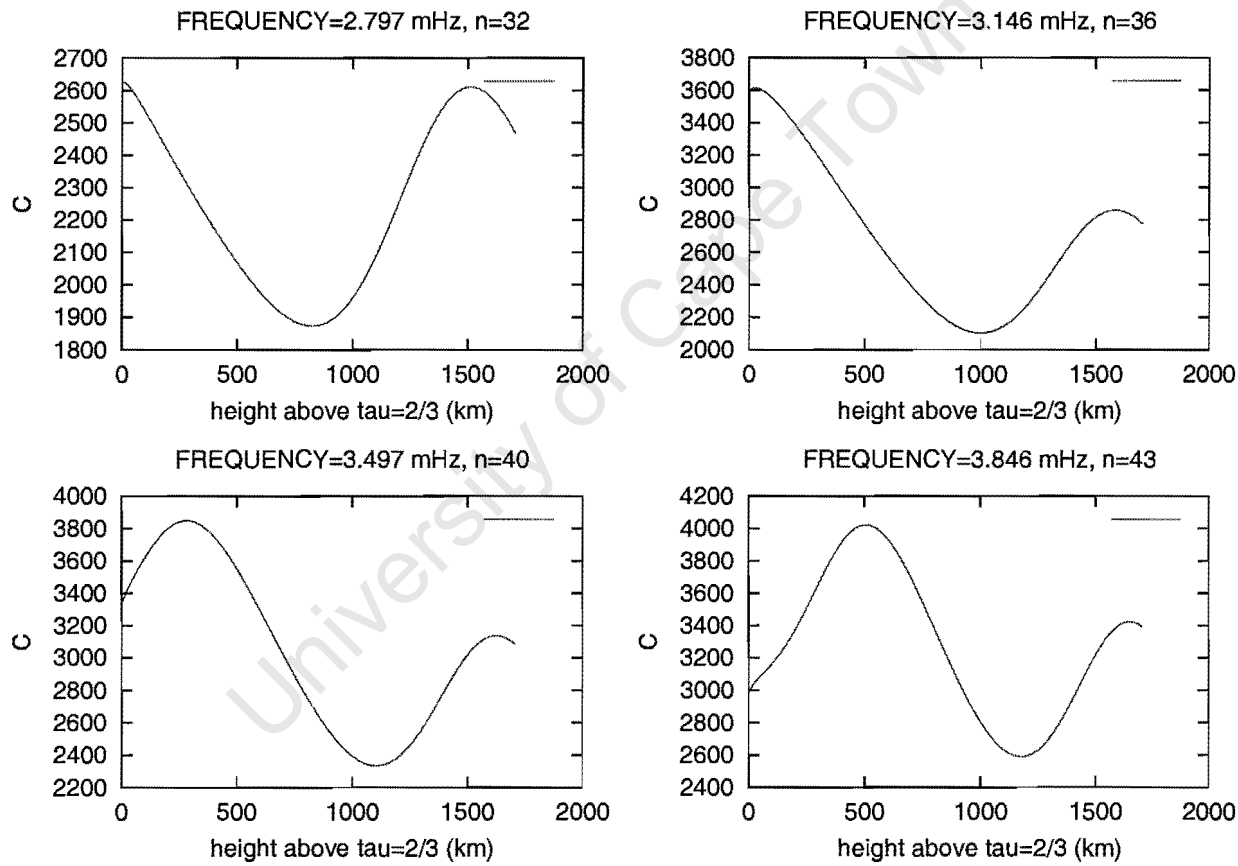

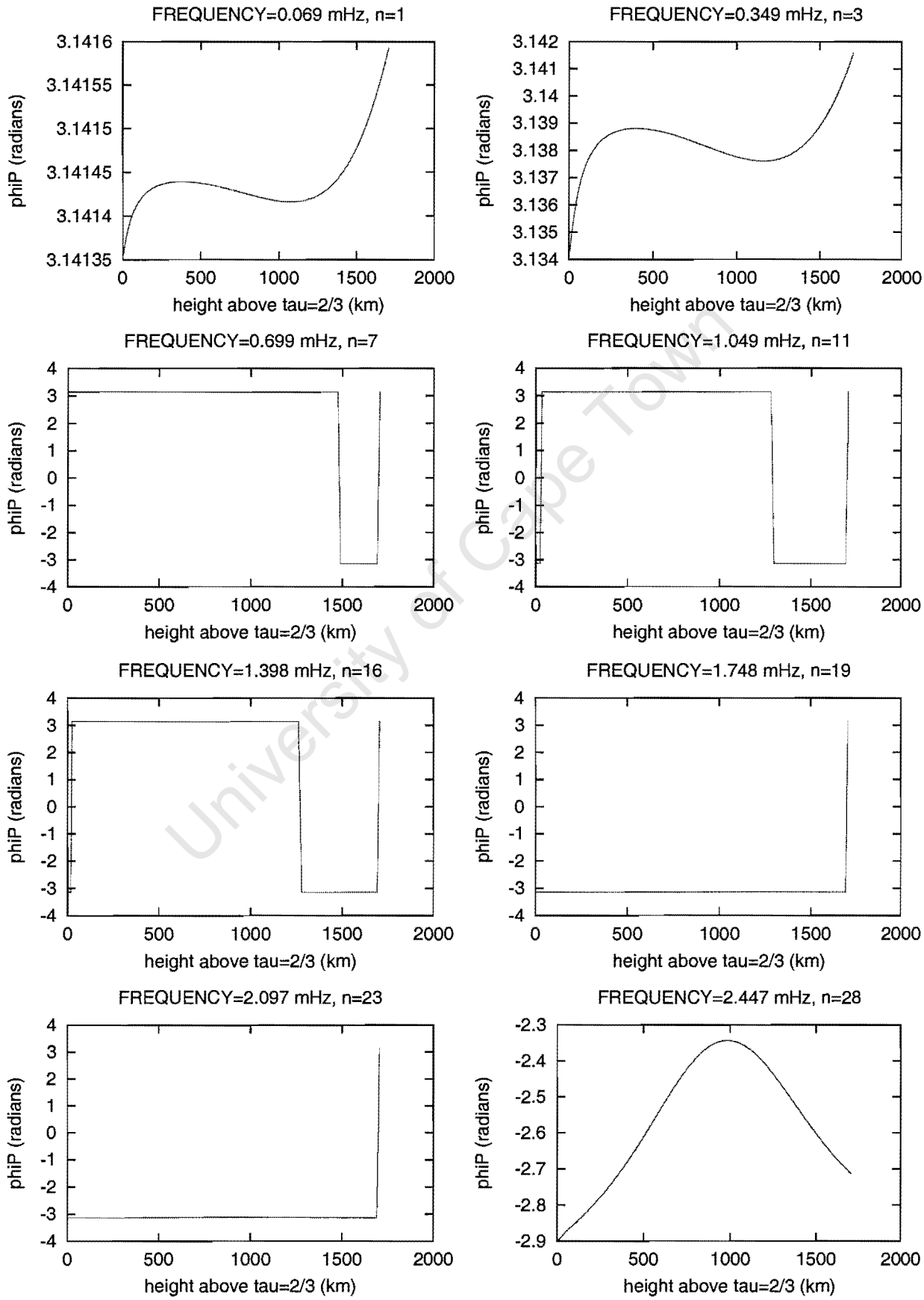

Figure 5.23: The phase difference between $\delta P/P$ and $\delta r/r$ is plotted as a function of height above the photosphere at several eigenfrequencies.

... continues from Fig. 5.23.

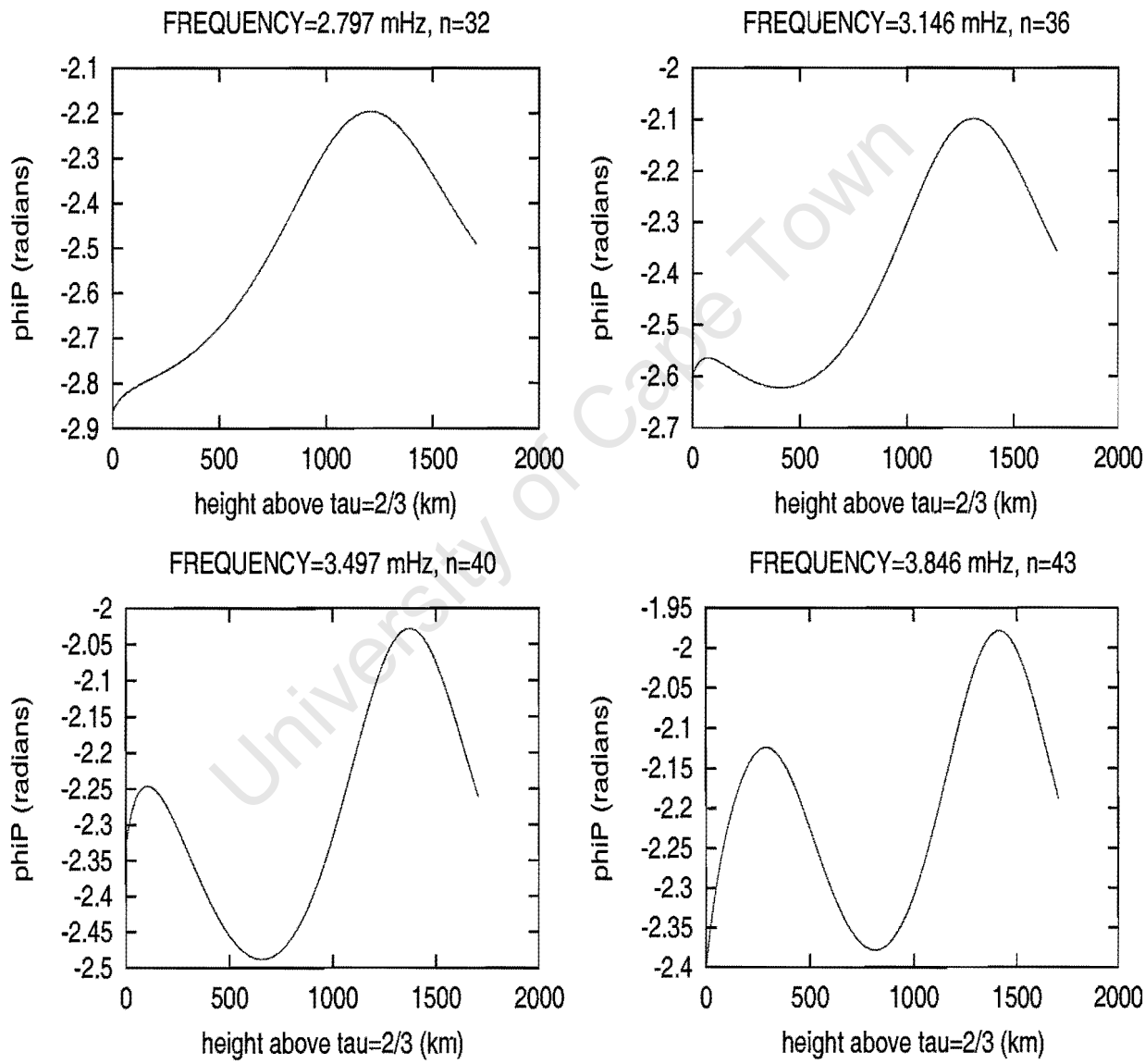

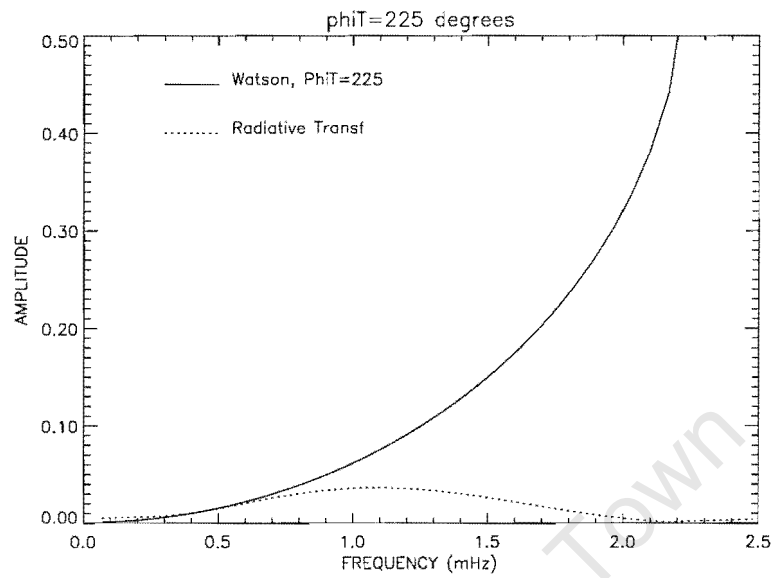

Figure 5.24: A comparison of the bolometric amplitudes obtained from Watson's formula to the surface value of the real part of $\delta H/H$ at various pulsation frequencies. The value of the relative ratio of temperature perturbation to the displacement (B) is calculated from the boundary condition equations (4.106) and (4.111).

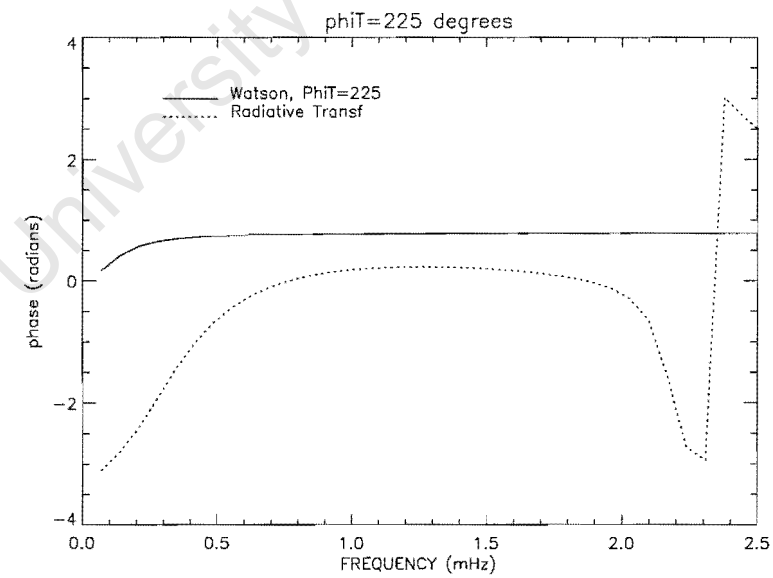

Figure 5.25: A comparison of the bolometric pulsation phases obtained from Watson's formula to the surface value of the real part of $\delta H/H$ at various pulsation frequencies. The value of the relative ratio of temperature perturbation to the displacement (B) is calculated from the boundary condition equations (4.106) and (4.111).

5.6 Comparison of radiative transfer and Eddington approximation

In this subsection we compare the results of using the Eddington approximation, diffusion approximation and radiative transfer in the energy equation of the pulsation equations. We also consider the approximations used by Ando & Osaki (1975) where they assumed radiative equilibrium in addition to the Eddington approximation. We present the effect of using these four approaches on the eigenfrequencies, damping rates and temperature nodes. All of the results presented in this subsection are based on the upper boundary condition that allows modes with frequencies larger than the acoustic cut-off frequency to dissipate.

The effects on the eigenfrequencies

We determined the eigenfrequencies by requiring that there be a displacement node at the base of the envelope and solving for ω (real and imaginary parts). The results are shown in Table 5.2 for the Ando & Osaki, diffusion approximations and the exact case. The first thing to notice is that the damping rates calculated using the Ando & Osaki and diffusion approximations are consistently lower than those from the complete radiative transfer treatment. Using the Ando & Osaki and diffusion approximations leads to higher eigenfrequencies in the roAp regime than in the exact case. These observations are clearly shown in Fig. 5.26. It is clear that the Eddington approximation without Ando & Osaki approximation is virtually indistinguishable from the exact case. However, the exact case has an eigenfrequency near the acoustic cut-off frequency unlike when the Eddington approximation is used.

The effects on the damping rates

Here the damping rates determined by requiring that the layers of the star beneath the base of the envelope perform no work on those above the base for the four approaches are compared. The results are shown in Fig. 5.27. As in Fig. 5.26, the Ando & Osaki and Diffusion approximations have systematically small damping rates compared to the radiative transfer case. Another noticeable result is that the diffusion approximation is not responsive to the upper boundary condition that allows modes with $\omega > \omega_a$ to dampen.

The effects on the temperature nodes

In Fig. 5.28 we compare the position of the first temperature node as a function of pulsation frequency obtained using the consistent treatment of radiative transfer with those using diffusion and the Eddington approximations. Generally the first temperature node occurs deeper when the Eddington and diffusion approximations are used in the atmosphere than when the more exact method is used. It is only in frequencies between 1.5 mHz and 2.2 mHz that nodes occur close to the stellar surface. The diffusion and Ando & Osaki approximations are in agreement at low pulsation frequencies up to about $\nu = 1.5$ mHz, but they are both in disagreement with the exact case.

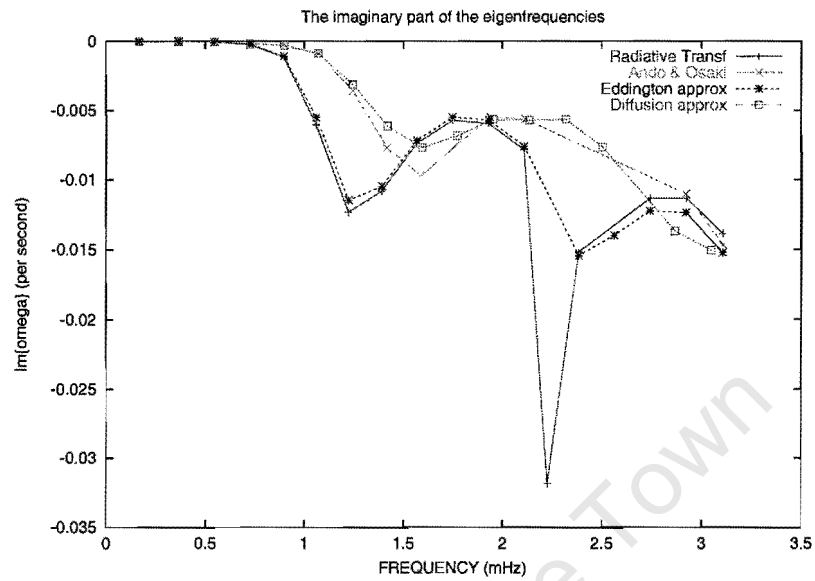

Figure 5.26: A plot of the imaginary parts of the eigenfrequencies determined from using different approaches, Ando & Osaki, diffusion and radiative transfer, also shown in Table 5.2. The curve labelled 'Eddington' was obtained by setting $f_{osc} = 1/3$ in the system of equation (4.136).

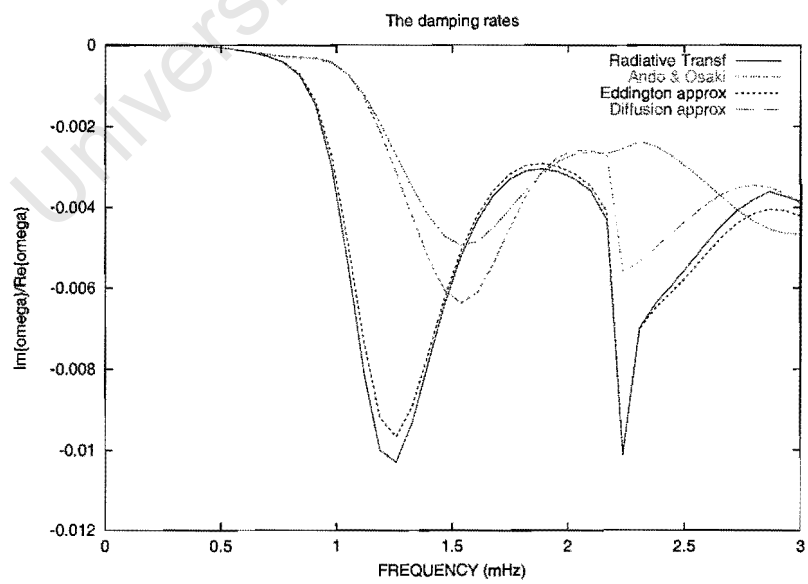

Figure 5.27: The damping rates calculated using radiative transfer, Ando & Osaki, Eddington and diffusion approximations.

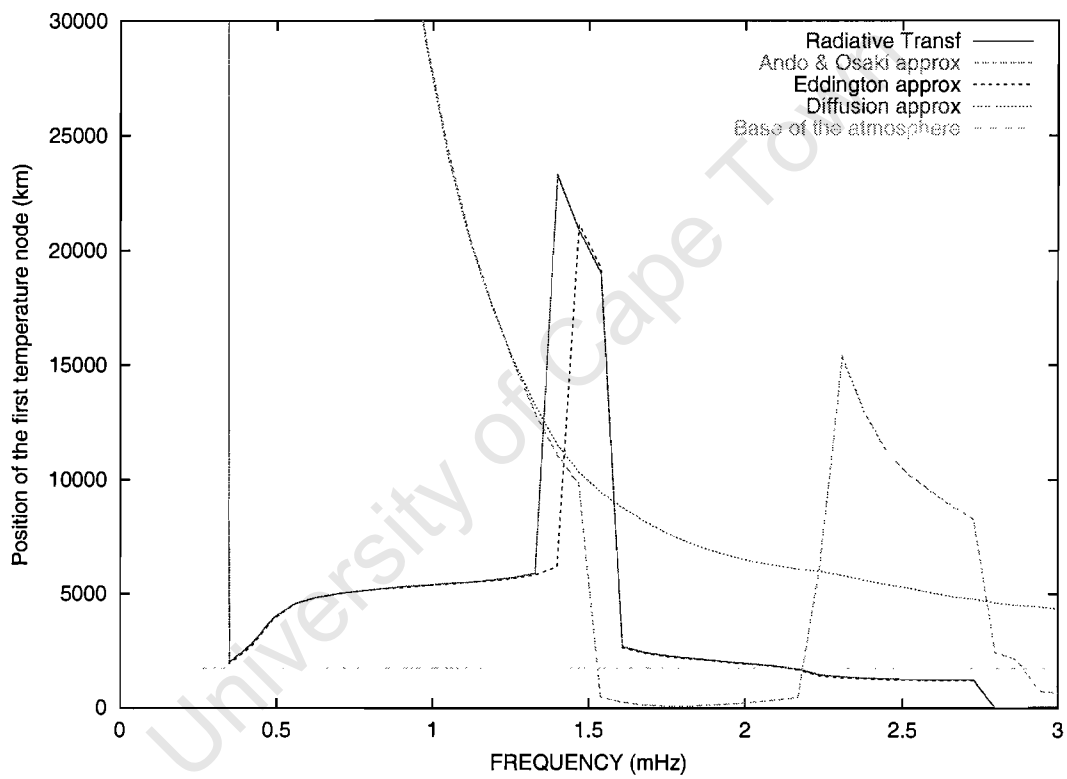

Figure 5.28: The distance of the first temperature node from the stellar surface calculated using radiative transfer, Eddington, Ando & Osaki and diffusion approximations.

Table 5.2: A listing of the eigenfrequencies determined from Eddington, diffusion approximation and consistent treatment of radiative transfer. Columns with no entries are frequencies where no eigenfrequencies were not found.

Radiative transf		**Ando & Osaki approx**		**Diffusion approx**	
ν (mHz)	η	ν (mHz)	η	ν (mHz)	η
0.16	-6.38×10^{-8}	0.16	-6.39×10^{-8}	0.16	-6.48×10^{-8}
0.36	-1.1×10^{-5}	0.36	-1.07×10^{-5}	0.36	-1.07×10^{-5}
0.54	-9.35×10^{-5}	0.54	-9.16×10^{-5}	0.55	-9.19×10^{-5}
0.73	-3.14×10^{-4}	0.73	-2.43×10^{-4}	0.73	-2.50×10^{-4}
0.89	-1.28×10^{-3}	0.90	-3.08×10^{-4}	0.90	-3.33×10^{-4}
1.06	-5.69×10^{-3}	1.07	-8.58×10^{-4}	1.07	-8.42×10^{-4}
1.22	-1.00×10^{-2}	1.25	-2.88×10^{-3}	1.25	-2.50×10^{-3}
1.39	-7.77×10^{-3}	1.42	-5.42×10^{-3}	1.42	-4.32×10^{-3}
1.57	-4.71×10^{-3}	1.59	-6.11×10^{-3}	1.59	-4.82×10^{-3}
1.75	-3.27×10^{-3}	1.76	-4.29×10^{-3}	1.77	-3.85×10^{-3}
1.93	-3.07×10^{-3}	1.94	-2.83×10^{-3}	1.95	-2.89×10^{-3}
2.11	-3.71×10^{-3}	2.12	-2.66×10^{-3}	2.14	-2.66×10^{-3}
2.23	-1.42×10^{-2}			2.32	-2.44×10^{-3}
2.39	-6.36×10^{-3}			2.50	-3.06×10^{-3}
2.74	-4.13×10^{-3}			2.87	-4.76×10^{-3}
2.92	-3.87×10^{-3}	2.92	-3.77×10^{-3}	2.87	-3.14×10^{-3}
3.11	-4.46×10^{-3}	3.11	-4.72×10^{-3}	3.05	-4.94×10^{-3}

5.7 Results of the non-grey calculations

In this final subsection of this chapter we do not include the results of solving the complete non-grey pulsation equations described in section 4.2.1. This is work in progress, the results of which will be published soon. Instead we use the $\delta T/T$ and $\delta P/P$ calculated from the grey equations to solve the perturbed monochromatic transfer equation.

The $\delta T/T$ and $\delta P/P$ were calculated as in section 4.4 with the atmosphere matched to the envelope. They were then substituted into equation (4.60). This equation is then solved to obtain δH_ν, δJ_ν and δK_ν. The results of doing this using the absorption processes only are shown in Fig. 5.29 at several pulsation frequencies. It is clear that in the wavelength range 400 to 700 nm the surface value of $\delta H_\nu/H_\nu$ decreases with increasing wavelength. This is to be expected from Watson's formula. It is also clear that this dependence of $\delta H_\nu/H_\nu$ on wavelength becomes steeper with increasing pulsation frequencies. In the wavelength region $750-810$ nm the amplitude actually increases with wavelength. If this phenomenon is real, it would be difficult to detect with current detectors in roAp stars because of the very low signal-to-noise ratio at those wavelengths. However, this phenomenon can be investigated on large amplitude δ Scuti stars since it is there even at low pulsation frequencies in our models. As a test on our results we show a plot of $f_{osc\nu} = \delta K_\nu/\delta J_\nu$ determined from this method in Fig. 5.31. Indeed $f_{osc\nu}$ approaches 1/3 deeper in the atmosphere at all the

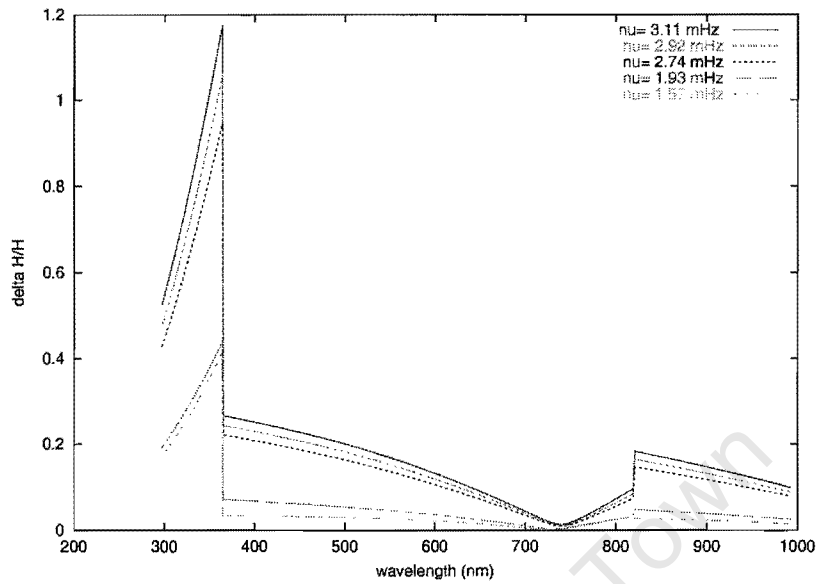

Figure 5.29: A plot of the surface value of $\delta H_\nu/H_\nu$ at different pulsation frequencies. The opacities used were calculated using ATLAS9 opacity subroutines (Kurucz 1993b). Scattering processes and line opacities are not included in the calculations.

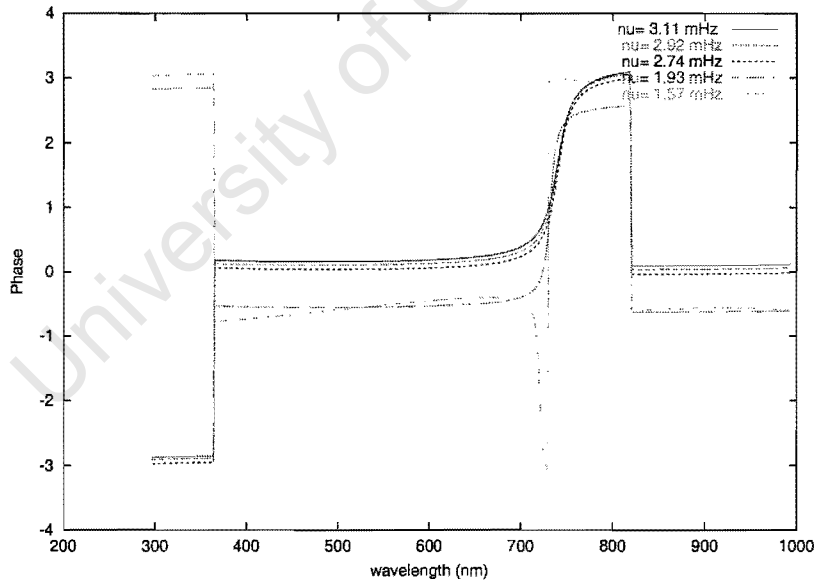

Figure 5.30: A plot of the phase corresponding to the $\delta H_\nu/H_\nu$ shown in Fig. 5.29.

wavelengths shown.

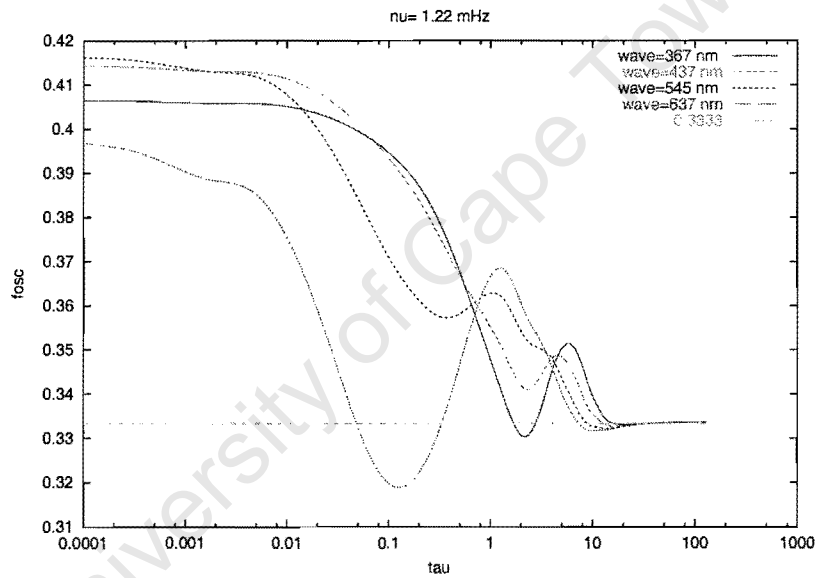

Figure 5.31: A plot of $f_{osc\nu}$ as a function of Rosseland mean optical depth for various wavelengths of observations.

Chapter 6

Conclusions

6.1 A summary of conclusions

In this chapter I review all the findings of this thesis. I caution that the theoretical results are based on radiative processes only. My models do not include convective, rotational and magnetic effects. Balmforth *et al.* (2001) show how important magnetic fields can be in the excitation of the roAp stars oscillations. In addition, Cunha & Gough (2000) show that the coupling of acoustic and Alfvenic waves lead to losses in the pulsation energy. Furthermore, Bigot *et al.* (2000) find that the imaginary part of the pulsation frequencies introduced by magnetic processes can be of the same order as the one due to non-adiabatic processes. All of these have to be borne in mind when considering the results that are presented here. It is clear that future improvements of our theory will have to include convection and magnetic fields.

From this thesis we draw the following conclusions

- Photometric pulsation phases for some roAp stars vary from Johnson U to V by up to 80°.
- No significant night-to-night variations in the amplitude *vs* wavelength and phase *vs* wavelength relations were detected in HR 3831.
- Watson's formula fails to describe the roAp photometric amplitudes and phases.
- The effect of the hydrogen ionisation zone on the pulsations of A stars is to create a peak in the temperature perturbations. The amplitude of this peak has a zero (a root) near $\nu = 0.3$ mHz. This introduces a temperature node in the atmosphere (if the hydrogen ionisation zone is near the photosphere) of the A stars that pulsate with frequencies near $\nu = 0.3$ mHz. An Ap star HD 75425 has been found to oscillate with pulsation period of around 30 minutes (Martinez & Medupe 1998). It would be interesting to see if multi-colour photometry of this star reveal a steeply decreasing pulsation amplitude with wavelength similar to that of roAp stars. If the steep decrease of pulsation amplitude with wavelength is a consequence of temperature pulsation node

in the atmosphere then HD 75425 ought to show photometry similar to that of roAp stars.

- Radial modes for which temperature, pressure and displacement nodes are visible within 5000 km below the surface of A stars must have overtones $n = 20$ or more. However, for nodes to be visible in the photosphere and above, the condition that $n > 20$ must be satisfied.

- All the modes from 0.06 mHz to 7 mHz are damped, although in roAp stars there are a number of excited modes.

- The phase difference between temperature perturbations and displacement Ψ_T in the roAp frequency regime shows a marked variation in the atmosphere. It changes by about 9° at 1 mHz to 285° at 2.7 mHz. This is based on looking at the changes that occur from the surface to the photosphere (zero height). In chapter 3 we showed that for dipole modes the photometric pulsation phase depends directly on Ψ_T. Therefore these variations in Ψ_T over the atmospheres could explain the large pulsation phase variations seen in HR 3831 and HD 101065.

- The oscillations in roAp stars are not adiabatic at the surface as is often assumed in frequency calculations. Therefore using boundary conditions that assume adiabatic conditions at the surface is questionable.

- There is evidence for chromospheric mode at $\nu = 2.5$ mHz, 3.7 mHz, 4.6 mHz and 5.7 mHz. Evidence for the presence of chromospheres in A stars has been observed in α Aql, α Cep and τ^3 Eri by Simon & Landsman (1997). Their analysis is based on ultraviolet spectra obtained from the HST/Goddard High Resolution Spectrograph. They were able to see Lα and Si III emission lines which are indicative of a chromosphere.

- Comparison of our approach with the Ando & Osaki approximation shows that damping rates determined from their approximation are systematically lower than our approach. The eigenfrequencies determined by the Ando & Osaki approximation are systematically higher than those determined by our approach in the roAp frequency regime. However, one must note that the Ando & Osaki approximation assumes radiative equilibrium in the atmosphere. We have shown that this is not the case in realistic stellar atmospheres. The two approaches are in agreement at low frequencies. This may be a result of the fact that low frequency modes reside in the interior of the star where the Eddington approximation tends to diffusion approximation (our interior equations use diffusion approximation). Comparison of our approach with the Ando & Osaki approximation must bear in mind the errors in both our equilibrium model and pulsation equations due to the assumptions we made. Temperature nodes appear deeper in the star when diffusion and Ando & Osaki approximations are used compared to when consistent treatment of radiative transfer is used.

- Comparison of our code with bolometric Watson's formula indicates an agreement between the two approaches at lower frequencies. However, at higher frequencies,

the amplitudes determined from Watson's formula increase monotonically with pulsation frequencies whereas amplitudes determined from our code show an increase with pulsation frequencies, followed by a decrease at higher frequencies.

- Investigation of the node separation at various pulsation frequencies reveal that for stars that pulsate with frequencies below their acoustic cut-off frequencies, node separation decreases with increasing pulsation frequency. HR 3831 pulsate with frequency below acoustic cut-off frequency and α Cir with frequency above the acoustic cut-off frequency. Hence, according to the equilibrium model we use, the node separation for HR 3831 should be much larger that in α Cir. This contradicts the results of Baldry & Bedding (2000) (as they correctly pointed out). They find similar velocity patterns in the two stars. Our analysis also indicate that for stars that pulsate with frequencies larger than their acoustic cut-off frequencies, their node separation does not change significantly with increasing frequency. We caution that according to our models, HR 3831 should not have displacement or temperature nodes visible in the photosphere, therefore these nodes cannot not have observable effect on its measured radial velocities or photometry. Again things will become clearer when the node structure is investigated as a function of surface temperature.

- Preliminary non-grey results indicate that the amplitude *vs.* wavelength relationship becomes steeper with increasing pulsation frequency. The fact that the amplitude *vs.* wavelength relation for δ Scuti stars is less steep compared to that of the roAp stars (see chapter 2) seems to concur with these results.

Chapter 7

Thoromo ya dinaledi ka boripana (Setswana)

Mefuta ya dinaledi tse ke di ithutang di bidiwa di Ap, mo go rayang gore mogote wa loapi lwa tsone o magareng ga digarata di le dikete tse supa le dikete tse lesome. Dinaledi di nale megote e e farologaneng mme seno ke lebaka le ereng maitsiboa fa o leba godimo, o fitlhele dinaledi di nale mebala e e farologaneng. Dingwe di bo-pududu, dingwe di-tshweu fa tse dingwe di le khibidu kgotsa bo-serolwana. Mebala e, e bontsha megote. O a tle o bone fa o ka fisa tshipi gore e simolola e le khibidu, e nne tshweu e re fa o dirisa mogote o o tseneletseng e nne pududu. Fela jalo, naledi e e pududu ke e e naleng mogote o o tseneletseng, e tshweu e mogote o o lekanetseng fa e e khibidu e le mogote o o tlase. Kana mme megote e re buang ka yone fa e sa ntse e le ko godimo fa re e lekanya le megote e re e tlwaetseng. Fa go le digarata dile some-a-mararo mo Mafikeng ra re go a fisa. Fa di le some a mararo tlhano ra re go mogote o o ntshang tlhapi metsing. Jaanong, nagana fela re re naledi e e mogote wa digarata dile dikete tse tharo e tsididi? Jaanong dinaledi di rulagantswe ka mogote le phatshimo ya tsone. Fa o ka lekantsha mogote le phatsimo ya bontsi jwa dinaledi o tla fitlhela gore dinaledi tse di mogote di phatshimo-kgolo, mme tse di seng mogote thata di phatshimo-potlana.Tsamaelano eno e bidiwa **main sequence**. Bontsi jwa dinaledi di wela mo 'main sequence'. Fela, go na le dinaledi tse di leng mogote-potlana mme di le phatsimo-kgolo, tse di bidiwa di 'red giants' bodimo ba ba hibidu. Seno se diragala ka gore phatsimo e tlisiwa ke maatla a a naledi e a ntshang le bogolo jwa naledi eo. Naledi e e kgolo e kgona go nna le phatsimo-kgolo le fa e ntsha maatla a le mannye, mme e e seng kgolo mo go kalo e kgona go nna phatsimo-kgolo fa e kgona go ntsha kelo e kgolo ya maatla. Gape go nale dinaledi tse di leng mogote-mogolo mme di le phatsimo-tlase, tse di bidiwa di 'white dwarf'. Letsatsi le lone ke naledi, lebaka le le dirang gore letsatsi le phatshime go gaisa dinaledi tse dingwe ke gore le gaufi go di feta. Go tshwana fela le fa go le bosigo o bona koloi e tla ntlheng ya gago. Fa e le kgakala dipone tsa yone di bonala fela jaaka tlhase ya lesedi, fa e go atumetse dipone di bonala bogolo. Letsatsi lone le serolwana, ka mogote wa digarata tse dikete tse thataro.

Ka popego dinaledi di kgolokwe fela jaaka kgwele ya maoto. Gape di nale loapi fela jaaka

lefatshe le nale loapi. Loapi lwa naledi ke karolo e e mo godimo ga yone e lesedi le re le bonang le tswang mo go yone. Bontsi jwa naledi ga bo letlelele lesedi go feta mo go yone. Lesedi le tsaya nako e e telele go tswa go mpeng ya naledi go fitlha ko go dimo (loaping).

Mo ngwageng tse somepedi tse di fetileng motlhatlheledi wa me eleng Don Kurtz o ne a lemoga fa lesedi le le tswang go tsona di lemosa di nale thoromo. Thoromo ya tsone ke ya makhubu a a makhutshwane mme a batlile a tshwana le thoromo ya lefatshe e re tleng re utlwele ka yone, e reneng ra e bona ngwagola mo Mafikeng mo. Pharologanyo ke gore lefatshe le dirilwe ka mmu, matlapa jalo jalo, dilo tse di tiileng, e bile mogote wa lefatshe o ko tlase thata fa le tshwantshanywa le dinaledi. E bile lefatshe jaaka ngwedi ga le itirele maatla a lone ka gore mogote wa lone o ko tlase. Kana mogote wa botengteng jwa letsatsi (go fa sekai) o fitlhelela digarata di le dimilione dile some tlhano! Ka jalo, fa letsatsi le ka bo le dirilwe ka mmu, metsi le matlapa jaaka lefatse, dilo tse di ka be di bidile tsa be tsa fetogela go nna gase jaaka mowa o re o hemang wa loapi.

Tironyana e ke go batlisisa ka dinaledi tse di roromang fela jaaka lefatshe le tle le rorome. Le fa lebaka la thoromo la dinaledi tse ke di ithutang le ise le itsewe sentle, re kgona go ithuta go le go ntsi ka mateng a tsona fela jaaka borra-maranyane a lefatshe ba kgona go itse popego ya lefatshe ka go ithuta thoromo ya lone. Re kgona go itse gore a mogote wa naledi o oketsega fa o tsena mo teng ga yone jalo jalo. Re kgona go itse mefuta ya digase tse di mo teng ga dinaledi tse di roromang le tsamao ya digase tseo. Re kgona le go itse go dikologa ga dinaledi ka go ithuta ka thoromo ya tsone. Ke gore tiro e, e tshwana fela le go fa o ka tsaya sefofu o be o se raya ore se tlhotlhomise gore katara e dirilwe ka logong lofe ka go reetsa mmino wa katara eo. Fa sefofu seo se itse 'acoustics' kgotsa 'seismology' a ka kgona go rarabolola bothata jo le fa ise a bona katara eo ka matlho!

Jaanong, Batswana le ma-aforika a re rateng dipuo tsa rona, re di tlhabololeng gore mo isagong bana ba rona ba kgone go di dirisa go kwala sengwe le sengwe ka tsona jaaka ke lekile fa. Le tla lemoga gore ga ke a kgona go tlhalosa tsotlhe ka diphitlhelelo tsa dipatlisiso tsa me ka ntlha ya gore puo ya rona ga e a godisiwa. Puo ngwe le ngwe e kgona go gola e be e lekana le dipuo tse di maatla jaaka sekgoa fela fa beng ba puo eo ba batla. Ke kgwetlho go ma-aforika otlhe gore a re kwaleng di 'theses' tsa rona le dilo tsotlhe fela ka diteme tsa rona.

Appendix A

The Ando & Osaki Approximation

Here we show that the Eddington approximation pulsation equations as presented by Ando & Osaki (1975) can be derived from the more general non-adiabatic pulsation equations as presented in chapter 4 of this thesis.

Hydrodynamic equations in the plane parallel atmosphere where energy transport is described by the Eddington approximation (see Ando & Osaki 1975) are

$$\begin{aligned} \frac{d\rho}{dt} + \rho\, div\, v &= 0 \\ \rho \frac{dv}{dt} &= -\nabla P + \rho f \\ \frac{dF_R}{dr} &= \rho C_p \left(\frac{dT}{dt} - \nabla_{ad} \frac{T}{P} \frac{dP}{dt} \right) \\ \frac{dJ}{dr} &= -\frac{3\kappa}{4\pi} F_R \end{aligned} \tag{A.1}$$

and

$$J = B + \frac{\rho C_p}{4\pi} \left(\frac{dT}{dt} - \nabla_{ad} \frac{T}{P} \frac{dP}{dt} \right) \tag{A.2}$$

where $\frac{d}{dt}$ is the material derivative and F_R is the radiative flux. Perturbing and linearising the first two equations of the above system result in equations (4.31) and (4.39). When the third and fourth equations are perturbed the results are

$$\frac{d\delta F_R}{dr} = i\omega \rho C_P T \left[\frac{\delta T}{T} - \nabla_{ad} \frac{\delta P}{P} \right], \tag{A.3}$$

and

$$\frac{d\delta J}{dr} = -3\rho\kappa \left[\delta H + \frac{\delta \kappa}{\kappa} H \right]. \tag{A.4}$$

One of the major assumptions in the Eddington approximation is that $J(\tau) = 3K(\tau)$. Therefore, equation (A.4) becomes

$$\frac{d\delta K}{dr} = -\rho\kappa\left[\delta H + \frac{\delta\kappa}{\kappa}H\right]. \tag{A.5}$$

Equation (A.5) looks similar to the fourth equation in the system of equations (4.66) derived from the radiative transfer equation. If we perturb equation (A.2) the result is

$$\frac{\delta J}{B} = 4\frac{\delta T}{T} + \frac{i\omega C_P T}{4\pi B\kappa}\left[\frac{\delta T}{T} - \nabla_{ad}\frac{\delta P}{P}\right] \tag{A.6}$$

We recall equation (4.86) determined from radiative transfer equation:

$$\frac{d\delta H}{dr} = \rho\kappa B\left\{4\frac{\delta T}{T} - \frac{\delta J}{B} - \frac{\delta\kappa}{\kappa}\Delta_c\right\} \tag{A.7}$$

Substitute equation (A.6) into equation (A.7) and set $\Delta_c = 0$ we get

$$\frac{d\delta H}{dr} = -\rho\kappa B\left\{\frac{i\omega C_P T}{4\pi B\kappa}\left(\frac{\delta T}{T} - \nabla_{ad}\frac{\delta P}{P}\right)\right\}. \tag{A.8}$$

It is clear that if Δ_c is set to zero then equation (A.7) becomes equation (A.3). Hence I have shown that the radial pulsation equations with consistent treatment of radiative transfer reduce to pulsation equations with Eddington approximation in radiative equilibrium.

For completeness, under the Ando & Osaki approximation, the radial pulsation equations in plane parallel atmosphere become

$$\begin{aligned}
\frac{d\delta r}{dr} &= -\frac{\delta\rho}{\rho} \\
\frac{d}{dr}\left(\frac{\delta P}{P}\right) &= \frac{\rho}{P}\left[\tilde{g}\frac{\delta P}{P} + (\omega^2 - dg/dr - 4\pi G\rho)\delta r\right] \\
\frac{d\delta H}{dr} &= \frac{i\omega\rho C_P T}{4\pi}\left[\frac{\delta T}{T} - \nabla_{ad}\frac{\delta P}{P}\right] \\
\frac{d\delta K}{dr} &= -\rho\kappa\left[\delta H + \frac{\delta\kappa}{\kappa}H\right]
\end{aligned} \tag{A.9}$$

Appendix B

Further comparisons of Eddington approximations and exact methods

In this chapter we include plots to show how the Eddington approximations affects the eigenfunctions. The plots in Figs B.1 to B.4 were calculated using damping rates determined by requiring that layers beneath the base of the envelope perform no work to those above it.

Fig. B.5 shows the effects of the Eddington approximations on the position of the first displacement and pressure nodes.

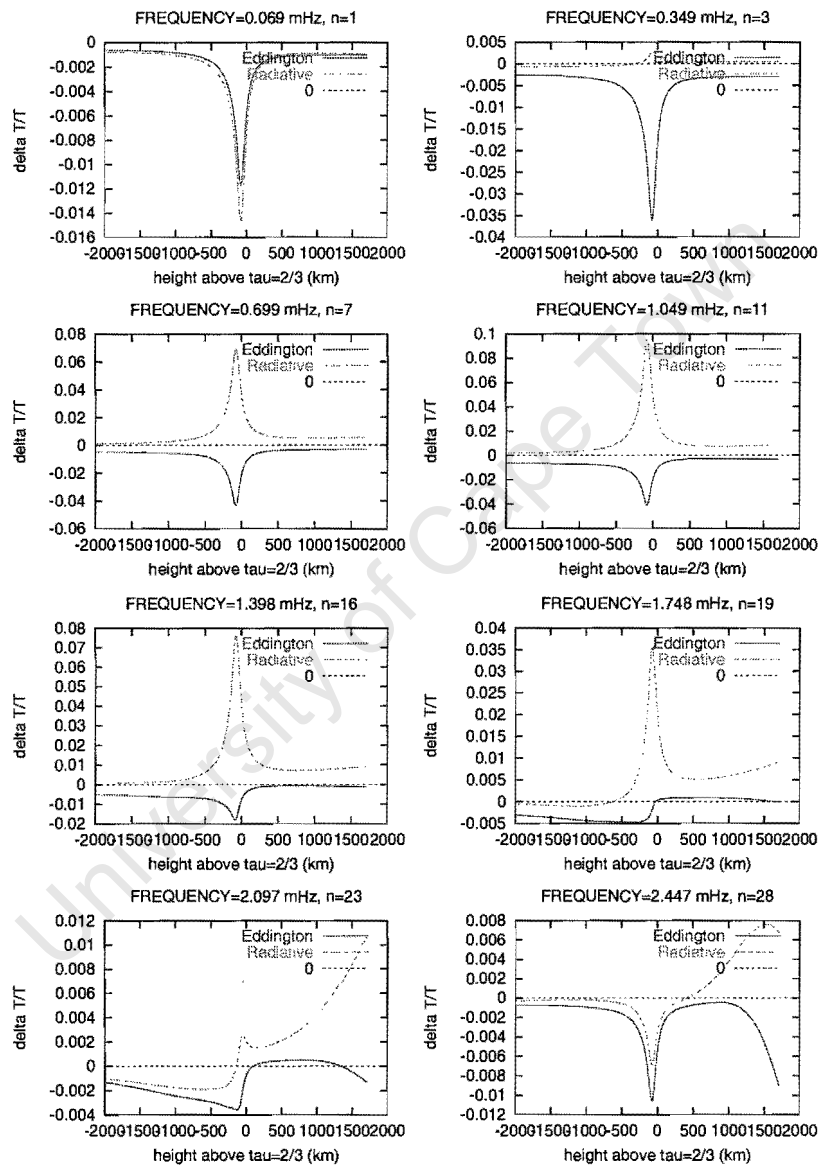

Figure B.1: A comparison of the real parts of the temperature perturbations computed using the Eddington approximation and the exact case at various pulsation frequencies.

... continues from Fig. B.1.

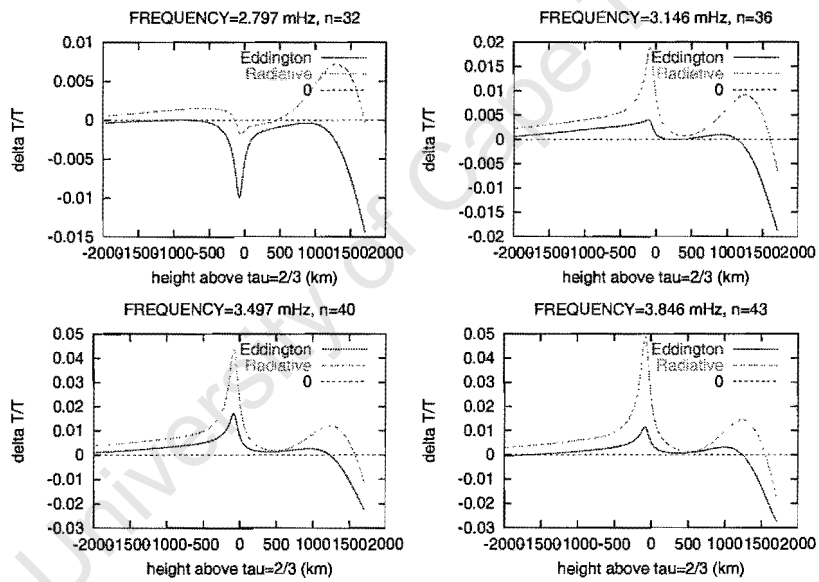

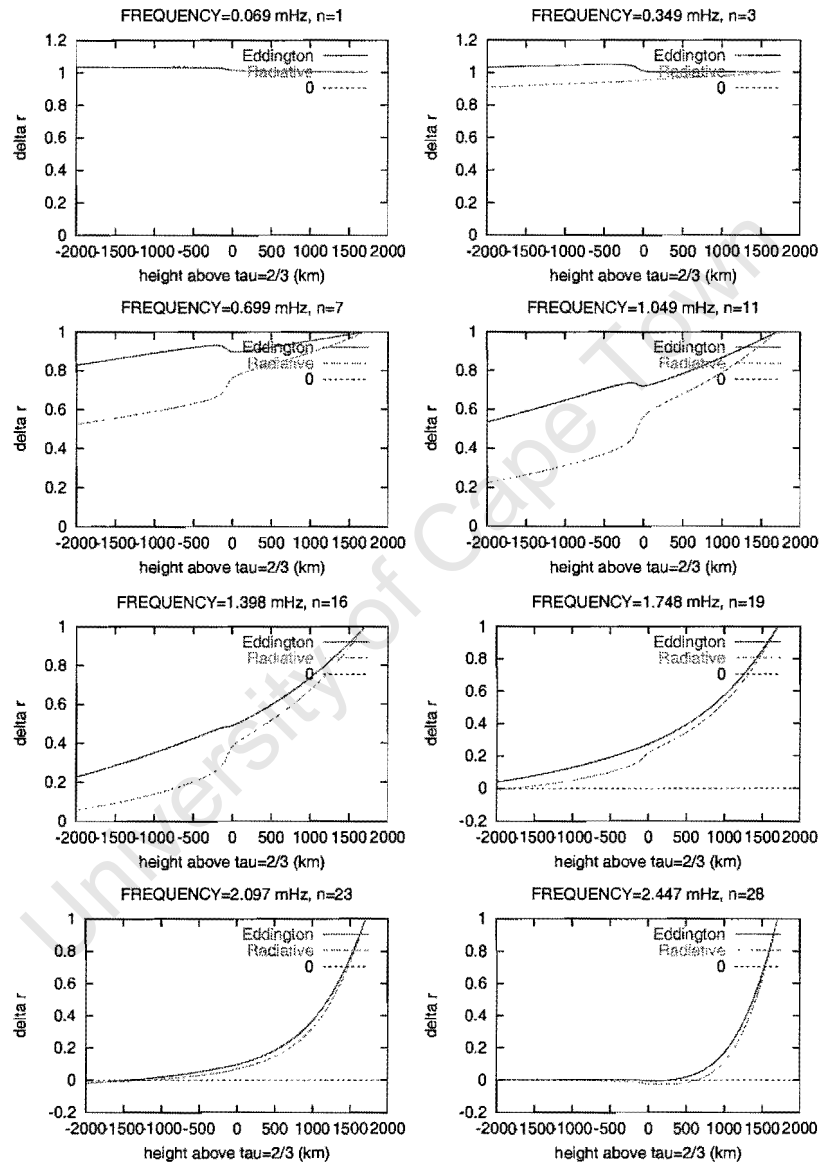

Figure B.2: A comparison of the real parts of the displacement computed using the Eddington approximation and the exact case at various pulsation frequencies.

... continues from Fig. B.2.

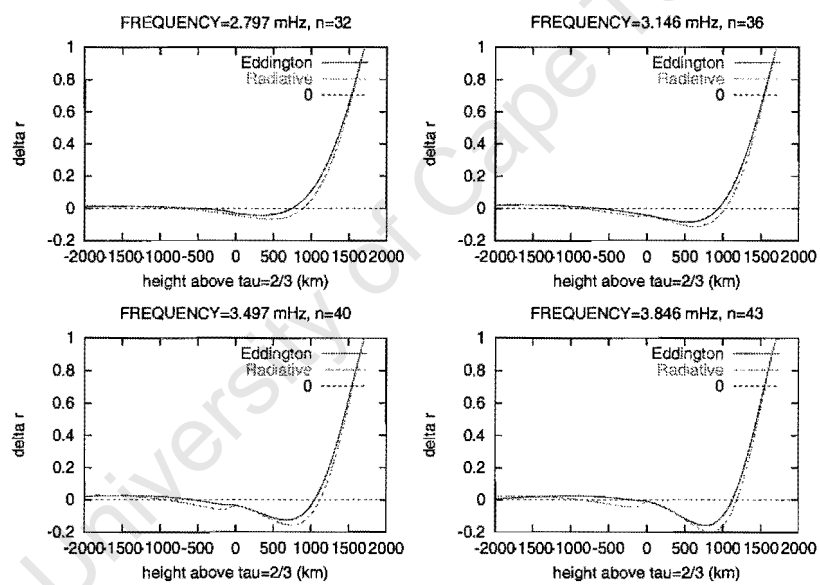

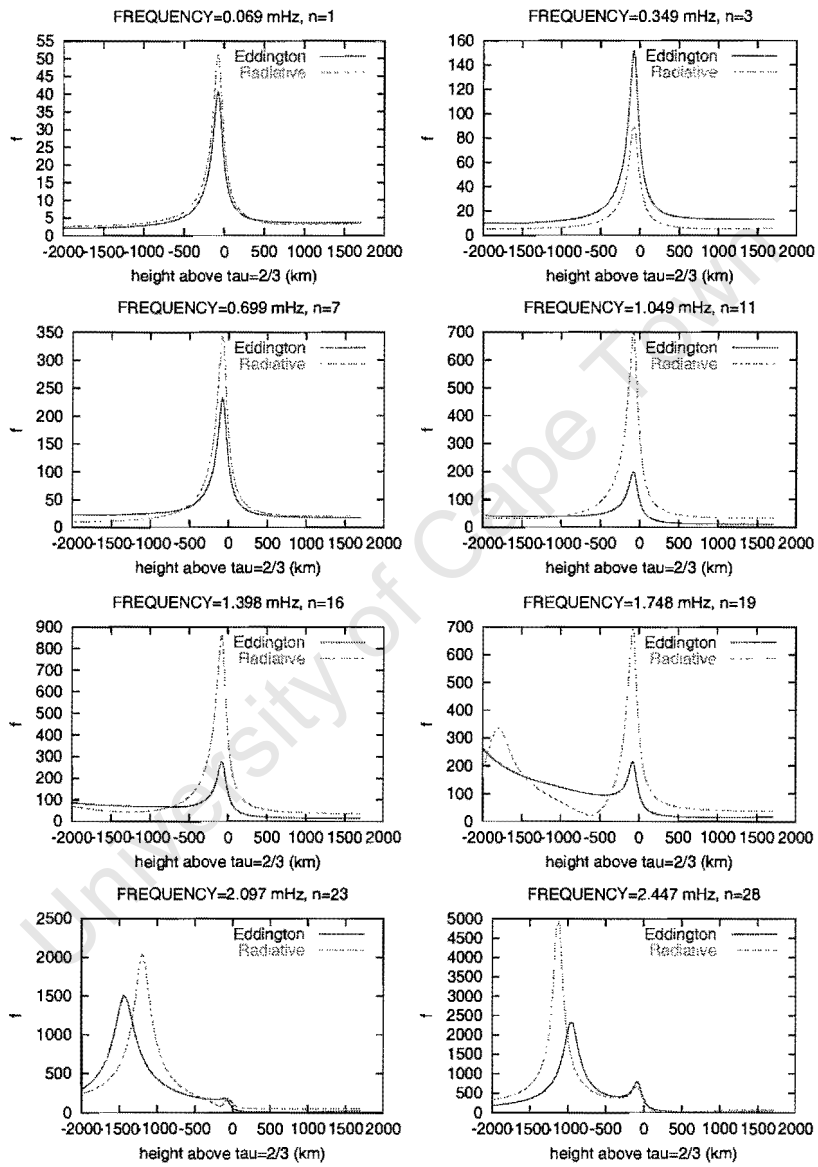

Figure B.3: A comparison of $f = \left|\frac{\delta T/T}{\delta r/r}\right|$ computed using the Eddington approximation and the exact case at various pulsation frequencies.

... continues from Fig. B.3.

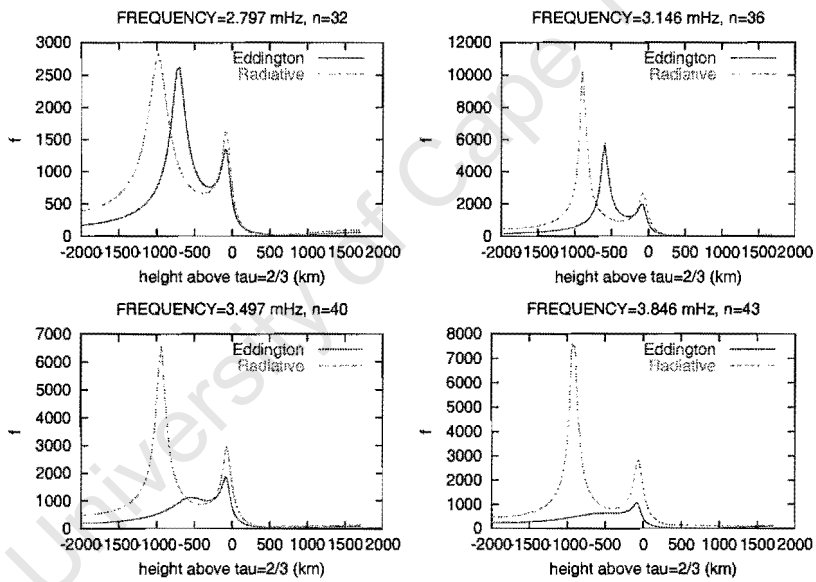

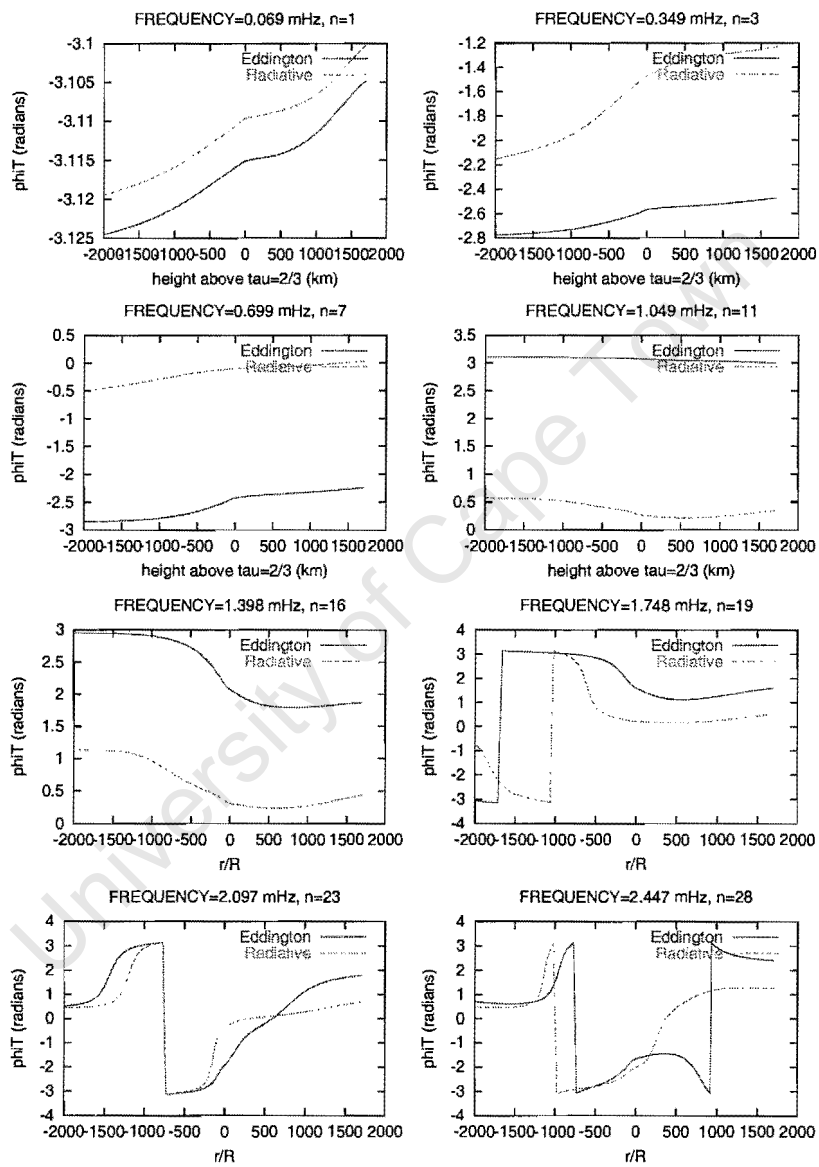

Figure B.4: A comparison of Ψ_T computed using the Eddington approximation and the exact case at various pulsation frequencies.

... continues from Fig. B.4.

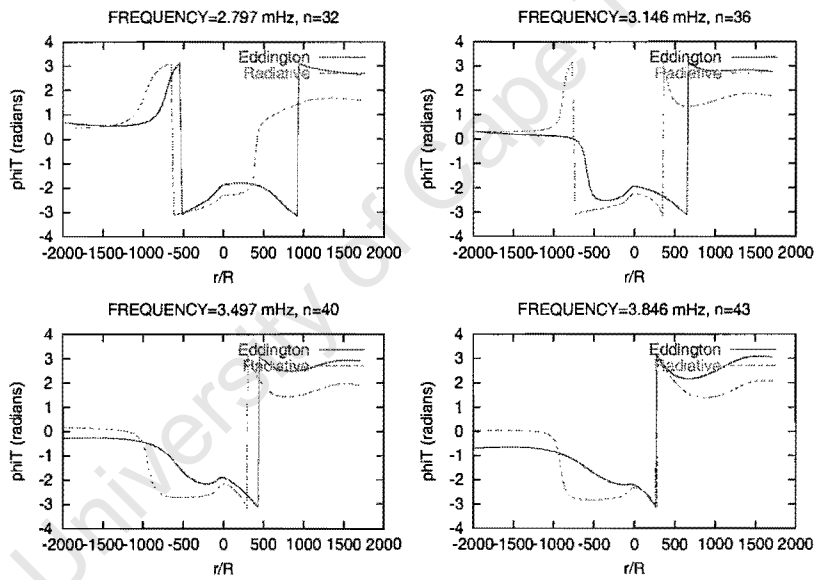

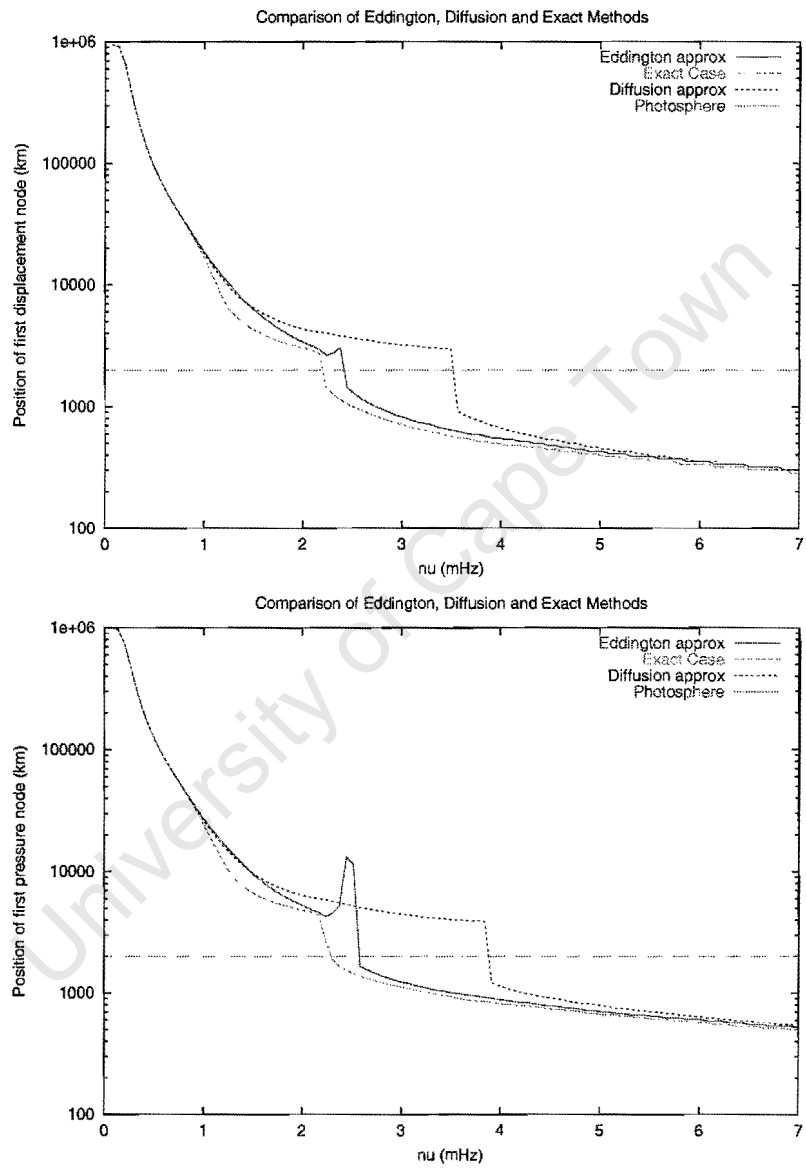

Figure B.5: The top panel shows the distance of the first displacement node from the stellar surface calculated using radiative transfer, Eddington and diffusion approximations. The bottom panel shows the same for pressure node.

Appendix C

Flux derivatives for α Cir

Table C.1: Flux derivatives in the Strömgren and Johnson bands, the α Cir case. The surface gravity is kept at $\log g = 4.2$

$T_{\rm eff}$ (K)	$\frac{\partial \log F_\lambda}{\partial \log T}$								
	u	v	b	y	U	B	V	R	I
7000.0	4.7434	5.7621	5.0337	4.2645	5.1286	5.3900	4.3058	3.5076	2.7382
7050.0	4.6928	5.7957	5.0685	4.2352	5.0788	5.4212	4.2794	3.4740	2.7125
7100.0	4.6114	5.8187	5.1001	4.2009	4.9952	5.4431	4.2470	3.4336	2.6785
7150.0	4.5554	5.7815	5.0809	4.1828	4.9369	5.4144	4.2290	3.4154	2.6604
7200.0	4.5041	5.7445	5.0495	4.1580	4.8943	5.3820	4.2053	3.3928	2.6379
7250.0	4.4475	5.7230	5.0242	4.1371	4.8505	5.3580	4.1850	3.3720	2.6133
7300.0	4.4103	5.6970	4.9979	4.1177	4.8187	5.3313	4.1664	3.3552	2.5928
7350.0	4.3777	5.6658	4.9662	4.0978	4.7875	5.2989	4.1463	3.3375	2.5726
7400.0	4.3534	5.6289	4.9333	4.0751	4.7582	5.2648	4.1220	3.3143	2.5538
7450.0	4.3910	5.5573	4.8698	4.0450	4.7735	5.2016	4.0918	3.3036	2.5590
7500.0	4.4045	5.4906	4.8103	4.0202	4.7721	5.1415	4.0667	3.2980	2.5606
7550.0	4.3510	5.4640	4.7795	4.0038	4.7295	5.1126	4.0500	3.2792	2.5312
7600.0	4.3067	5.4480	4.7508	3.9757	4.6964	5.0902	4.0232	3.2493	2.4969
7650.0	4.2718	5.4296	4.7238	3.9432	4.6672	5.0675	3.9919	3.2155	2.4637
7700.0	4.2583	5.3968	4.6987	3.9183	4.6412	5.0371	3.9673	3.1895	2.4430
7750.0	4.2632	5.3615	4.6709	3.8951	4.6277	5.0054	3.9439	3.1699	2.4300
7800.0	4.2517	5.3196	4.6195	3.8598	4.6154	4.9613	3.9089	3.1421	2.4031
7850.0	4.2437	5.2814	4.5683	3.8194	4.6037	4.9182	3.8698	3.1087	2.3734
7900.0	4.2575	5.2420	4.5261	3.7868	4.5994	4.8776	3.8372	3.0833	2.3545
7950.0	4.2481	5.3764	4.5875	3.8349	4.6859	4.9786	3.8900	3.1361	2.4050

... continues from Table C.1.

8000.0	4.2639	5.3266	4.5380	3.8057	4.6925	4.9320	3.8602	3.1145	2.3961
8050.0	4.3011	5.1095	4.3872	3.6928	4.6096	4.7488	3.7438	3.0136	2.3140
8100.0	4.3058	5.0726	4.3442	3.6534	4.6029	4.7105	3.7066	2.9814	2.2858
8150.0	4.3249	5.0155	4.2872	3.6108	4.5984	4.6552	3.6626	2.9475	2.2648
8200.0	4.3562	4.9714	4.2153	3.5588	4.6173	4.6009	3.6112	2.9126	2.2475
8250.0	4.3785	4.9329	4.1350	3.4997	4.6411	4.5469	3.5567	2.8755	2.2296
8300.0	4.3958	4.8780	4.0690	3.4477	4.6501	4.4904	3.5072	2.8378	2.2112
8350.0	4.4303	4.8282	4.0155	3.4047	4.6631	4.4419	3.4645	2.8048	2.1943
8400.0	4.4883	4.7354	3.9180	3.3473	4.6852	4.3530	3.4061	2.7765	2.1855
8450.0	4.4998	4.6657	3.8392	3.2991	4.6850	4.2837	3.3577	2.7459	2.1599
8500.0	4.4769	4.6348	3.7979	3.2540	4.6611	4.2488	3.3128	2.6976	2.1174
8550.0	4.4811	4.5638	3.7278	3.1887	4.6415	4.1811	3.2471	2.6421	2.0813
8600.0	4.4838	4.5251	3.6882	3.1553	4.6329	4.1440	3.2146	2.6168	2.0630

Table C.2: Flux derivatives in the Strömgren and Johnson bands - the α Cir case. The effective temperature is kept at $T_{\rm eff} = 7900$ K.

$\log g$	$\frac{\partial F_\lambda}{\partial \log g}$								
	u	v	b	y	U	B	V	R	I
3.0	0.0633	-0.0431	-0.0183	-0.0081	-0.0024	-0.0313	-0.0106	-0.0004	0.0039
3.1	0.0643	-0.0438	-0.0186	-0.0084	-0.0012	-0.0317	-0.0109	-0.0006	0.0039
3.2	0.0659	-0.0453	-0.0196	-0.0091	0.0010	-0.0328	-0.0116	-0.0011	0.0037
3.3	0.0668	-0.0456	-0.0210	-0.0101	0.0041	-0.0334	-0.0126	-0.0019	0.0034
3.4	0.0674	-0.0452	-0.0223	-0.0112	0.0076	-0.0336	-0.0135	-0.0027	0.0033
3.5	0.0682	-0.0459	-0.0232	-0.0120	0.0099	-0.0342	-0.0143	-0.0034	0.0033
3.6	0.0692	-0.0469	-0.0241	-0.0126	0.0119	-0.0350	-0.0150	-0.0040	0.0031
3.7	0.0701	-0.0480	-0.0249	-0.0133	0.0138	-0.0359	-0.0156	-0.0045	0.0029
3.8	0.0709	-0.0489	-0.0256	-0.0139	0.0157	-0.0365	-0.0162	-0.0051	0.0026
3.9	0.0712	-0.0493	-0.0265	-0.0146	0.0176	-0.0370	-0.0169	-0.0057	0.0022
4.0	0.0711	-0.0487	-0.0277	-0.0157	0.0199	-0.0372	-0.0179	-0.0066	0.0018
4.1	0.0712	-0.0482	-0.0285	-0.0165	0.0222	-0.0372	-0.0186	-0.0073	0.0017
4.2	0.0717	-0.0486	-0.0291	-0.0169	0.0240	-0.0376	-0.0190	-0.0077	0.0017
4.3	0.0721	-0.0490	-0.0298	-0.0174	0.0257	-0.0381	-0.0195	-0.0081	0.0015
4.4	0.0721	-0.0493	-0.0305	-0.0180	0.0271	-0.0385	-0.0200	-0.0087	0.0011
4.5	0.0719	-0.0494	-0.0310	-0.0185	0.0283	-0.0387	-0.0204	-0.0092	0.0007
4.6	0.0716	-0.0485	-0.0316	-0.0189	0.0297	-0.0385	-0.0209	-0.0097	0.0003
4.7	0.0711	-0.0473	-0.0323	-0.0195	0.0313	-0.0382	-0.0213	-0.0102	0.0000
4.8	0.0707	-0.0466	-0.0323	-0.0202	0.0326	-0.0378	-0.0218	-0.0109	-0.0002
4.9	0.0704	-0.0462	-0.0325	-0.0205	0.0337	-0.0377	-0.0221	-0.0112	-0.0005
5.0	0.0702	-0.0461	-0.0329	-0.0203	0.0342	-0.0379	-0.0219	-0.0111	-0.0005

Appendix D

Weighted limb-darkening functions for α Cir

Table D.1: The weighted limb-darkening function ($b_{\ell=1,\lambda}$) for the Strömgren and Johnson bands - the α Cir case. The surface gravity is kept at $\log g = 4.2$.

$T_{\rm eff}$ (K)	$b_{1\lambda}$								
	u	v	b	y	U	B	V	R	I
7000.0	0.7181	0.7272	0.7225	0.7123	0.7195	0.7242	0.7128	0.7040	0.6953
7050.0	0.7175	0.7267	0.7221	0.7121	0.7189	0.7237	0.7126	0.7039	0.6952
7100.0	0.7169	0.7264	0.7219	0.7119	0.7184	0.7235	0.7124	0.7037	0.6950
7150.0	0.7163	0.7261	0.7218	0.7118	0.7179	0.7233	0.7122	0.7035	0.6948
7200.0	0.7158	0.7259	0.7216	0.7116	0.7174	0.7231	0.7121	0.7034	0.6946
7250.0	0.7152	0.7256	0.7215	0.7115	0.7168	0.7229	0.7119	0.7032	0.6945
7300.0	0.7147	0.7253	0.7213	0.7113	0.7163	0.7227	0.7118	0.7031	0.6943
7350.0	0.7142	0.7250	0.7211	0.7111	0.7159	0.7224	0.7116	0.7029	0.6941
7400.0	0.7137	0.7247	0.7209	0.7110	0.7154	0.7222	0.7114	0.7027	0.6939
7450.0	0.7132	0.7244	0.7206	0.7108	0.7149	0.7219	0.7112	0.7025	0.6937
7500.0	0.7127	0.7240	0.7203	0.7105	0.7144	0.7215	0.7110	0.7023	0.6935
7550.0	0.7123	0.7236	0.7200	0.7103	0.7140	0.7212	0.7107	0.7021	0.6933
7600.0	0.7118	0.7232	0.7196	0.7100	0.7135	0.7208	0.7104	0.7019	0.6932
7650.0	0.7114	0.7228	0.7193	0.7098	0.7131	0.7204	0.7102	0.7017	0.6930
7700.0	0.7110	0.7224	0.7189	0.7095	0.7126	0.7200	0.7099	0.7015	0.6928
7750.0	0.7105	0.7220	0.7186	0.7093	0.7122	0.7197	0.7097	0.7013	0.6926
7800.0	0.7101	0.7216	0.7183	0.7090	0.7118	0.7193	0.7094	0.7011	0.6924
7850.0	0.7097	0.7212	0.7179	0.7087	0.7114	0.7189	0.7092	0.7009	0.6922
7900.0	0.7093	0.7208	0.7175	0.7085	0.7110	0.7185	0.7089	0.7006	0.6920
7950.0	0.7089	0.7204	0.7172	0.7082	0.7106	0.7182	0.7086	0.7004	0.6918

... continues from Table D.1.

8000.0	0.7087	0.7200	0.7168	0.7080	0.7104	0.7179	0.7084	0.7003	0.6917
8050.0	0.7084	0.7196	0.7164	0.7077	0.7100	0.7174	0.7081	0.7000	0.6915
8100.0	0.7080	0.7192	0.7160	0.7074	0.7096	0.7170	0.7078	0.6998	0.6914
8150.0	0.7077	0.7187	0.7156	0.7071	0.7092	0.7166	0.7075	0.6996	0.6912
8200.0	0.7073	0.7183	0.7152	0.7068	0.7088	0.7162	0.7072	0.6993	0.6910
8250.0	0.7070	0.7178	0.7148	0.7065	0.7085	0.7157	0.7069	0.6991	0.6908
8300.0	0.7066	0.7174	0.7143	0.7062	0.7081	0.7153	0.7066	0.6988	0.6906
8350.0	0.7063	0.7169	0.7139	0.7058	0.7078	0.7149	0.7062	0.6986	0.6904
8400.0	0.7060	0.7165	0.7135	0.7055	0.7074	0.7144	0.7059	0.6983	0.6902
8450.0	0.7057	0.7160	0.7130	0.7051	0.7071	0.7140	0.7055	0.6980	0.6900
8500.0	0.7053	0.7155	0.7125	0.7048	0.7068	0.7135	0.7051	0.6978	0.6898
8550.0	0.7050	0.7151	0.7120	0.7044	0.7064	0.7131	0.7048	0.6975	0.6895
8600.0	0.7046	0.7147	0.7116	0.7041	0.7061	0.7126	0.7045	0.6972	0.6894

Table D.2: The weighted limb-darkening function ($b_{\ell=2,\lambda}$) for the Strömgren and Johnson bands - the α Cir case. The surface gravity is kept at $\log g = 4.2$.

$T_{\rm eff}$ (K)	$b_{2\lambda}$								
	u	v	b	y	U	B	V	R	I
7000.0	0.3416	0.3585	0.3500	0.3313	0.3441	0.3531	0.3321	0.3162	0.3005
7050.0	0.3405	0.3575	0.3492	0.3309	0.3431	0.3522	0.3317	0.3159	0.3002
7100.0	0.3395	0.3569	0.3489	0.3306	0.3421	0.3518	0.3314	0.3156	0.2999
7150.0	0.3384	0.3564	0.3486	0.3303	0.3411	0.3514	0.3311	0.3153	0.2996
7200.0	0.3374	0.3559	0.3483	0.3300	0.3401	0.3509	0.3308	0.3150	0.2992
7250.0	0.3364	0.3554	0.3480	0.3297	0.3392	0.3505	0.3305	0.3147	0.2989
7300.0	0.3355	0.3548	0.3476	0.3294	0.3383	0.3501	0.3302	0.3144	0.2986
7350.0	0.3346	0.3542	0.3472	0.3291	0.3374	0.3495	0.3299	0.3141	0.2982
7400.0	0.3337	0.3536	0.3468	0.3287	0.3365	0.3490	0.3295	0.3138	0.2979
7450.0	0.3327	0.3530	0.3463	0.3283	0.3356	0.3485	0.3291	0.3134	0.2976
7500.0	0.3319	0.3522	0.3456	0.3278	0.3347	0.3478	0.3286	0.3130	0.2972
7550.0	0.3311	0.3514	0.3450	0.3273	0.3339	0.3470	0.3281	0.3126	0.2968
7600.0	0.3303	0.3505	0.3443	0.3269	0.3331	0.3463	0.3276	0.3122	0.2965
7650.0	0.3295	0.3498	0.3436	0.3264	0.3323	0.3456	0.3271	0.3118	0.2962
7700.0	0.3287	0.3490	0.3429	0.3259	0.3315	0.3448	0.3266	0.3114	0.2958
7750.0	0.3280	0.3483	0.3423	0.3254	0.3307	0.3441	0.3261	0.3110	0.2955
7800.0	0.3272	0.3475	0.3416	0.3249	0.3299	0.3434	0.3256	0.3106	0.2951
7850.0	0.3265	0.3467	0.3409	0.3244	0.3292	0.3427	0.3251	0.3102	0.2948
7900.0	0.3258	0.3459	0.3402	0.3239	0.3284	0.3419	0.3246	0.3098	0.2944
7950.0	0.3251	0.3451	0.3395	0.3234	0.3277	0.3412	0.3241	0.3094	0.2941
8000.0	0.3247	0.3445	0.3388	0.3230	0.3273	0.3406	0.3237	0.3091	0.2939
8050.0	0.3241	0.3436	0.3381	0.3224	0.3266	0.3398	0.3231	0.3087	0.2935
8100.0	0.3234	0.3428	0.3373	0.3218	0.3259	0.3390	0.3225	0.3082	0.2932
8150.0	0.3228	0.3420	0.3365	0.3213	0.3252	0.3382	0.3220	0.3078	0.2929
8200.0	0.3222	0.3411	0.3357	0.3207	0.3245	0.3374	0.3214	0.3074	0.2925
8250.0	0.3216	0.3403	0.3349	0.3201	0.3239	0.3365	0.3208	0.3069	0.2921
8300.0	0.3210	0.3395	0.3341	0.3195	0.3233	0.3357	0.3201	0.3064	0.2918
8350.0	0.3204	0.3386	0.3332	0.3189	0.3226	0.3349	0.3195	0.3059	0.2914
8400.0	0.3198	0.3378	0.3324	0.3182	0.3220	0.3341	0.3189	0.3055	0.2911
8450.0	0.3192	0.3369	0.3315	0.3175	0.3214	0.3332	0.3182	0.3049	0.2907
8500.0	0.3186	0.3360	0.3306	0.3169	0.3207	0.3323	0.3176	0.3045	0.2903
8550.0	0.3180	0.3351	0.3298	0.3163	0.3201	0.3315	0.3169	0.3040	0.2900
8600.0	0.3173	0.3344	0.3290	0.3157	0.3195	0.3308	0.3163	0.3035	0.2896

Table D.3: The weighted limb-darkening function ($b_{\ell=1,\lambda}$) for the Strömgren and Johnson bands, the α Cir case. The effective temperature is kept at $T_{\rm eff} = 7900$ K.

$\log g$	$b_{1\lambda}$								
	u	v	b	y	U	B	V	R	I
3.0	0.7058	0.7226	0.7169	0.7080	0.7121	0.7195	0.7087	0.7003	0.6916
3.1	0.7061	0.7226	0.7170	0.7081	0.7119	0.7195	0.7087	0.7004	0.6916
3.2	0.7063	0.7225	0.7171	0.7081	0.7117	0.7194	0.7087	0.7004	0.6916
3.3	0.7066	0.7224	0.7171	0.7082	0.7115	0.7194	0.7088	0.7004	0.6916
3.4	0.7069	0.7222	0.7172	0.7082	0.7114	0.7193	0.7088	0.7004	0.6916
3.5	0.7071	0.7221	0.7173	0.7083	0.7113	0.7193	0.7088	0.7005	0.6917
3.6	0.7074	0.7220	0.7173	0.7083	0.7112	0.7192	0.7089	0.7005	0.6917
3.7	0.7077	0.7218	0.7174	0.7083	0.7111	0.7191	0.7089	0.7005	0.6918
3.8	0.7080	0.7216	0.7174	0.7084	0.7110	0.7190	0.7089	0.7006	0.6918
3.9	0.7083	0.7214	0.7175	0.7084	0.7110	0.7189	0.7089	0.7006	0.6919
4.0	0.7087	0.7212	0.7175	0.7084	0.7109	0.7188	0.7089	0.7006	0.6919
4.1	0.7090	0.7210	0.7175	0.7085	0.7109	0.7187	0.7089	0.7006	0.6920
4.2	0.7093	0.7208	0.7175	0.7085	0.7110	0.7185	0.7089	0.7006	0.6920
4.3	0.7097	0.7206	0.7175	0.7085	0.7110	0.7184	0.7089	0.7006	0.6921
4.4	0.7100	0.7203	0.7175	0.7085	0.7111	0.7183	0.7089	0.7007	0.6921
4.5	0.7103	0.7200	0.7175	0.7085	0.7111	0.7181	0.7088	0.7007	0.6922
4.6	0.7107	0.7197	0.7174	0.7085	0.7112	0.7179	0.7088	0.7007	0.6923
4.7	0.7110	0.7194	0.7174	0.7085	0.7113	0.7177	0.7087	0.7007	0.6923
4.8	0.7114	0.7191	0.7173	0.7084	0.7115	0.7175	0.7087	0.7007	0.6924
4.9	0.7117	0.7189	0.7173	0.7084	0.7116	0.7174	0.7086	0.7007	0.6924
5.0	0.7121	0.7186	0.7171	0.7084	0.7118	0.7172	0.7086	0.7007	0.6925

Table D.4: The weighted limb-darkening function ($b_{\ell=2,\lambda}$) for the Strömgren and Johnson bands - the α Cir case. The effective temperature is kept at $T_{\rm eff} = 7900$ K.

$\log g$	$b_{2\lambda}$								
	u	v	b	y	U	B	V	R	I
3.0	0.3195	0.3491	0.3386	0.3228	0.3304	0.3435	0.3240	0.3091	0.2935
3.1	0.3199	0.3490	0.3388	0.3229	0.3301	0.3434	0.3241	0.3092	0.2935
3.2	0.3204	0.3488	0.3390	0.3230	0.3297	0.3433	0.3241	0.3092	0.2936
3.3	0.3208	0.3486	0.3392	0.3232	0.3293	0.3432	0.3242	0.3093	0.2936
3.4	0.3213	0.3484	0.3394	0.3232	0.3291	0.3432	0.3243	0.3093	0.2937
3.5	0.3218	0.3483	0.3395	0.3234	0.3289	0.3431	0.3244	0.3094	0.2938
3.6	0.3224	0.3481	0.3396	0.3235	0.3288	0.3430	0.3244	0.3095	0.2938
3.7	0.3229	0.3477	0.3398	0.3235	0.3286	0.3428	0.3245	0.3095	0.2939
3.8	0.3235	0.3474	0.3399	0.3236	0.3285	0.3427	0.3245	0.3096	0.2940
3.9	0.3240	0.3470	0.3400	0.3237	0.3284	0.3425	0.3245	0.3096	0.2941
4.0	0.3246	0.3466	0.3400	0.3238	0.3283	0.3423	0.3246	0.3097	0.2942
4.1	0.3252	0.3463	0.3401	0.3239	0.3284	0.3421	0.3246	0.3097	0.2943
4.2	0.3258	0.3459	0.3402	0.3239	0.3284	0.3419	0.3246	0.3098	0.2944
4.3	0.3264	0.3455	0.3402	0.3239	0.3285	0.3417	0.3246	0.3098	0.2945
4.4	0.3270	0.3450	0.3402	0.3239	0.3286	0.3415	0.3246	0.3099	0.2947
4.5	0.3276	0.3445	0.3402	0.3240	0.3287	0.3412	0.3245	0.3099	0.2948
4.6	0.3282	0.3440	0.3401	0.3240	0.3289	0.3409	0.3245	0.3099	0.2949
4.7	0.3288	0.3435	0.3401	0.3240	0.3291	0.3406	0.3244	0.3099	0.2950
4.8	0.3295	0.3430	0.3399	0.3239	0.3293	0.3402	0.3243	0.3099	0.2951
4.9	0.3301	0.3426	0.3399	0.3239	0.3296	0.3400	0.3243	0.3099	0.2952
5.0	0.3307	0.3420	0.3397	0.3239	0.3299	0.3396	0.3242	0.3099	0.2954

Bibliography

[1] Abraham, Z., Iben, I., 1971, ApJ, **170**, 157.

[2] Ando, H., Osaki, Y., 1975, PASJ, **27**, 581.

[3] Alecian, G., 1986, In *Upper Main Sequence Stars with Anomalous Abundances.* Proc. IAU Colloq. No. 90, p. 381, Dordrecht: Reidl, eds. C.R. Cowley, M.M. Dworetsky, C. Megessier.

[4] Allen, C.W., 1963, Astrophysical Quantities, 2nd edition, The Athlone Press, University of London, 2 Gower Street, London, W.C.1.

[5] Babcock, H.W., 1947, PASP, **59**, 260.

[6] Babcock, H.W., 1958, ApJS, **3**, 141.

[7] Bachmann, K.T., Brown, T.M., 1993, ApJ, **411**, L45.

[8] Bagnulo, S., Landolfi, M., Mathys, G., Landi Degl'Innocenti, M., 2000, A&A, **358**, 929.

[9] Bagnulo, S., Landi Degl'Innocenti, E., Landolfi, M., Leroy, J.L., 1995, A&A, **295**, 459.

[10] Bahcall, J.N., 1989, *Neutrino Astrophysics*, Cambridge university Press, Cambridge.

[11] Bahcall, J.N., Ulrich, R.K., 1971, ApJ, **170**, 593.

[12] Bahcall, J.N., Pinsonneault, M.H., 1992,

[13] Bahcall, J.N., Pinsonneault, M.H., Basu, S., 2001, ApJ, **555**, 990.

[14] Baker, N. H. & Kippenhahn, R., 1965, ApJ, **142**, 868.

[15] Baker, N. H., Moore, D. W. & Spiegel, E. A., 1971. *Q. Jl. Mech. appl. Math.*, **24**, 391 – 422.

[16] Baldry, I.K., Bedding, T.R., 2000, MNRAS, **318**, 341.

[17] Baldry, I.K., Viskum, M., Bedding, T.R., Kjeldsen, H., Frandsen, S., 1999, MNRAS, **302**, 381.

[18] Baldry, I.K., Bedding, T.R., Viskum, M., Kjeldsen, H., & Frandsen, S., 1998, MNRAS, **295**, 33.

[19] Balmforth, N.J., 1992, MNRAS, **255**, 639.

[20] Balmforth, N.J., Cunha, M.S., Dolez, N., Gough, D.O., Vauclair, S., 2001, MNRAS, **323**, 362.

[21] Balona, L.A., 1986a, MNRAS, **219**, 111.

[22] Balona, L.A., 1986b, MNRAS, **220**, 647.

[23] Balona, L.A., Stobie, R.S., 1979a, MNRAS, **187**, 187.

[24] Balona, L.A., Stobie, R.S., 1979b, MNRAS, **189**, 649.

[25] Basu, S., Antia, H.M., 1997, MNRAS, **287**, 187.

[26] Bedding, T.R., Butler, R.P., Kjeldsen, H., *et al.*, 2001, ApJ, **549**, L105.

[27] Bevington, P.R., & Robinson, D.K., 1992, Data reduction and error analysis for the physical sciences (2nd edition).

[28] Bigot, L., Provost, J., Berthomieu, Dziembowski, W.A., Goode, P.R., 2000, A&A, **356**, 218.

[29] Bigot, L., & Dziembowski, W.A., 2002, A&A, in press

[30] Borra, E.F., Landstreet, J.D., Mestel, L., 1982, ARA&A, **20**, 191.

[31] Bouchy, F., Carrier, F., 2001, A&A, **374**, L5.

[32] Breger, M., 1979, PASP, **91**, 539.

[33] Brown, T.M., Gilliland, R.L., 1990, ApJ, **350**, 839.

[34] Buta, R.J., Smith M.A., 1979, ApJ, **232**, 213.

[35] Carney, B.W., Peterson, R.C., 1985, MNRAS, **212**, 33.

[36] Carrier, F., Bouchy, F., Kienzle, F., *et al.* 2001, A&A,

[37] Chevalier, C., 1971, ApJ., **14**, 24.

[38] Christensen-Dalsgaard, J, 1981, MNRAS, **194**, 229.

[39] Christensen-Dalsgaard, 1998, *Lecture notes in Stellar Oscillations*, Fourth edition, ed. J. Christensen-Dalsgaard, Aarhus University, Denmark.

[40] Christensen-Dalsgaard, J., Frandsen, S., 1983, Sol. Phys, 82, 165.

[41] Christensen-Dalsgaard, J., Gough, D.O., Thompson, M.J., 1991, ApJ, **378**, 413.

[42] Christensen-Dalsgaard, J., Däppen, W., Ajukov, S.V, *et al.*, 1996, Science, **272**, 1286.

[43] Cowley, C.R., Cowley, A.P., Aikman, G.C.L., Crosswhite, H.M., 1977, ApJ, **216**, 37.

[44] Cox, J.P., Guilli, R.T., 1968, *Principles of Stellar Structure*, Gordon & Breach, New York, vol.2.

[45] Cugier, H., Dziembowski, W.A., Pamyatnykh, A.A., A&A, **291**, 143.

[46] Cunha, M.S., 2002, MNRAS, **333**, 47.

[47] Cunha, M.S., Gough, D.O., 2000, MNRAS, **319**, 1020.

[48] Deeming, T.J., 1975, Ap&SS, **36**, 137.

[49] Deleuil, M., Bouret, J.-C., Roberge, A., *et al.*, 2001, ApJ, **557**, L67

[50] Deubner, F.–L., Waldschik, Th., Steffens, S., 1996, A&A, **307**, 936.

[51] Deutsch, A.J., 1947, ApJ, **105**, 283.

[52] Dolez, N., Gough, D.O., 1982, in *Pulsations in Classical and Cataclysmic Variable Stars*, JILA, Boulder, CO, eds Cox, J.P. & Hansen C.J., p. 248.

[53] Dolez, N., Gough, D.O., Vauclair, S., 1988, *Advances in Helio– and Asteroseismology. Proc. IAU Symp.* No. 123, 291, ed. J. Christensen–Dalsgaard, S. Frandsen (Dordrech: Reidel).

[54] Dziembowski, W., 1977, Acta. Astr., **27**, 203.

[55] Dziembowski, W., Goode, P.R., 1996, ApJ, **458**, 338

[56] Dziembowski, W., Goode, P.R., 1986, In *Seismology of the Sun and Distant Stars*, ed. D.O. Gough, p 441. Dordrecht: Reidel.

[57] Dziembowski, W., Goode, P.R., 1985, ApJ, **296**, L27.

[58] Edmonds, A.R., 1957, *Angular Momentum in Quantum Mechanics.*, Princeton, NJ: Princeton University Press.

[59] Elsworth, Y., Howe, R., Isaak, G.R., McLeod, C.P., New, R., 1990, Nature, **345**, 322.

[60] Gautschy, A., Saio, H., Harzenmoser, H., 1998, MNRAS, **301**, 31

[61] Gelbmann, M., Ryabchikova, T., Weiss, W.W., Piskunov, N., Kupka, F., Mathys, G., 2000, A&Ap, **356**, 200.

[62] Gelbmann, M., Kupka, F., Weiss, W.W., Mathys, G., 1997, A&Ap, **319**, 630.

[63] Gelly, B., Grec, G., Fossat, E., 1986, A&A, **164**, 383

[64] Gelly, B., Grec, G., Fossat, E., 1988, In *Advances in Helio– and Asteroseismology. Proc. IAU Symp.* No. 123, 249, eds. J. Christensen–Dalsgaard, S. Frandsen (Dordrech: Reidel)

[65] Gilman, P.A., Miller, J., 1986, ApJS, **61**, 585.

[66] Goldreich, P., Kelley, D.A., 1977, ApJ, **212**, 243.

[67] Gough, D.O., 1986, *in Seismology of the Sun and the Distant Stars*, eds. D. O. Gough (Dordrecht: Reidel), p. 125

[68] Gough, D.O., 1977, *in IAU Colloquium* 36, *Energy Balance and Hydrodynamics of the Solar Chromosphere and Corona,* eds. R. M. Bonnet & P. Delache (Clermont-Ferrand: G. de Bussac), p.3.

[69] Gough, D.O., Leibacher, J.W., Scherrer, P.H., Toomre, J., 1996, Science, **272**, 1281.

[70] Gough, D.O., Kosovichev, A.G., and the GONG Team: 1996, Science, **272**, 1296.

[71] Handler, G., Paunzen, E., 1999, A&AS, **135**, 57.

[72] Handler, G., Weiss, W.W., Paunzen, E., Shobbrook, R.R., Garrido, R., Guzik, J.A., Hempel, A., Moalusi, M.B., Beach, T.E., Medupe, R., Chagnon, F., Matthews, J.M., Reegen, P., Granzer, T., 2002, MNRAS, **330**, 153.

[73] Hartoog, M.R., Cowley, C.R., Cowley, A.P., 1973, ApJ, **182**, 847.

[74] Heck, A., Manfroid, J., Renson, P., 1976, A&AS, **25**, 143.

[75] Heck, A., Mathys, G., Manfroid, J., 1987, A&AS, **70**, 33.

[76] Heller, C.H., Kawaler, S.D., 1988, ApJ., **329**, L43.

[77] Henden, A.A., Kaitchuk, R.H., 1982, Astronomical Photometry, Van Nostrand Reinhold Company Inc., 135 West 50^{th} Street, New York ,N.Y. 10020.

[78] Heynderickx, D., Waelkens, C., Smeyers, P., 1994, A&ApSS, **105**, 447.

[79] Houdek, G., Balmforth, N.J., Christensen-Dalsgaard, J., Gough, D.O., 1999, A&A, **351**, 582.

[80] Houk, N., Cowley, A.P., 1975, Michigan Spectral Catalogue, vol. 1., Department of Astronomy, University of Michigan, Ann Arbor.

[81] Houk, N., 1978, Michigan Spectral Catalogue, vol. 2., Department of Astronomy, University of Michigan, Ann Arbor.

[82] Houk, N., 1982, Michigan Spectral Catalogue, vol. 3., Department of Astronomy, University of Michigan, Ann Arbor.

[83] Houk, N., Smith-Moore, M., 1988, Michigan Spectral Catalogue, vol. 4., Department of Astronomy, University of Michigan, Ann Arbor.

[84] Hurly, P.R., Warner, B., 1983, MNRAS, **202**, 761.

[85] Iben, I., 1968, Phys. Rev. Letters, **21**, 1208.

[86] Jones, T.J., Wolff, S.C., Bonsack, W.K., 1974, Ap.J., **190**, 579.

[87] Kambe, E., Osaki, Y., 1988, PASJ, **40**, 313.

[88] Kemp, J.C., Wolstencroft, R.D., 1974, MNRAS, **166**, 1

[89] Kjeldsen, H., Bedding, T.R., 1995, A&A, **293**, 87.

[90] Kjeldsen, H., Bedding, T.R., Viskum, M., Frandsen, S., 1995, Astron. J., **109**, 1313.

[91] Kochukhov, O., Ryabchikova, T., 2001, A&Ap, **377**, L22.

[92] Koen, C., van Rooyen, R., van Wyk, F., Marang, F., 1999, MNRAS, 309, 1051.

[93] Kosovichev, J., Basu, S., *et al.*, 1997, in *Sounding Solar and Stellar Interiors.* Proc. IAU Colloq. No 181, p, Dordrecht: Reidl, ed. J. Provost, F.X. Schmider.

[94] Kreidl, T.J., 1985, IBVS, No. 2739.

[95] Kreidl, T.J., Kurtz, D.W., Schneider, H., van Wyk, F., Roberts, G., Marang, F., Birch, P.V., 1994, MNRAS, **270**, 115.

[96] Kupka, F., Gelbmann, U., Heiter, R., Kuschnig, R., Weiss, W.W., 1995, In *Astrophysical Applications of Stellar Pulsation*, ASPC, **83**, eds. R.S. Stobie, P.A. Whitelock.

[97] Kupka, F., Ryabchikova, T.A., Weiss, W.W., Kuschnig, R., Rogl, J., Mathys, G., 1996, A&A, **308**, 886.

[98] Kurtz, D.W., 1978, IBVS, No. 1436.

[99] Kurtz, D.W., 1980, MNRAS, **191**, 115.

[100] Kurtz, D.W., 1981, MNRAS, **196**, 61.

[101] Kurtz, D.W., 1982, MNRAS, **200**, 807.

[102] Kurtz, D.W., 1984, In *Proceedings of the Workshop on improvements to Photometry*, p. 56, ed. W.J. Borucki, A. Young, NASA Conference Publication 2350.

[103] Kurtz, D.W., 1985, MNRAS, **213**, 773.

[104] Kurtz, D.W., 1990, ARA&A, **28**, 607.

[105] Kurtz, D.W., 1991, MNRAS, **249**, 468.

[106] Kurtz, D.W., Balona, L.A., 1984, MNRAS, **210**, 779.

[107] Kurtz, D.W., Cropper, M.S., 1981, IBVS, No. 1987

[108] Kurtz, D.W., Kanaan, A., Martinez, P., Tripe, P., 1992, MNRAS, **255**, 289.

[109] Kurtz, D.W., Kanaan, A., Martinez, P., 1993b, MNRAS, **260**, 343.

[110] Kurtz, D.W., Kreidl, T.J., 1985, MNRAS, **216**, 987.

[111] Kurtz, D.W., Kreidl, T.J., O'Donoghue, D., Osip, D.J., Tripe, P., 1991, MNRAS, **251**, 152.

[112] Kurtz, D.W., Martinez, P., Ashley, R.P., 1993a, MNRAS, **264**, 529.

[113] Kurtz, D.W., Martinez, P., van Wyk, F., Marang, F., Roberts, G., 1994a, MNRAS, **268**, 641.

[114] Kurtz, D.W., Matthews, J.M., Martinez, P., Seeman, J., Cropper, M., Clemens, J.C., Kreidl, T.J., Sterken, C., Schneider, H., Weiss, H., Kawaler, S.D., Kepler, S.O., van der Peet, A., Sullivan, D.J., Wood, H.J., 1989, MNRAS, **240**, 881.

[115] Kurtz, D.W., Medupe, R., 1996, BAS. India, **24**, 291.

[116] Kurtz, D.W., Shibahashi, H., 1986, MNRAS, **223**, 557.

[117] Kurtz, D.W., Sullivan, D.J., Martinez, P., Tripe, P., 1994b, MNRAS, **270**, 674.

[118] Kurtz, D.W., Marang, F., van Wyk, F., Roberts, G., 1996, MNRAS, **280**, 1

[119] Kurtz, D.W., van Wyk, F., Roberts, G., Marang, F., Handler, G., Medupe, R., Kilkenny, D., 1997a, MNRAS, **287**, 69.

[120] Kurtz, D.W., Martinez, P., Tripe, P., Hanbury, A.G., 1997b, MNRAS, **289**, 645.

[121] Kurtz, D.W., Wegner, G., 1979, ApJ, **232**, 510.

[122] Kurucz, R.L., 1970, Smithsonian Ap. Obs. Spec. Rept., No. **309**.

[123] Kurucz, R.L., 1979, ApJS, **40**, 1.

[124] Kurucz, R.L., 1993a, In *Peculiar Versus Normal Phenomena in A-Type and Related Stars*, ASPC, **44**, p. 87, eds. M.M. Dworetsky, F. Castelli, R. Faraggiana.

[125] Kurucz, R.L., 1993b, Smithsonian Ap. Obs, CDROM 13.

[126] Kurucz, R.L., Peytremann, E., Avrett, E.H., 1974, *Blanketed Model Atmospheres for Early–Type Stars*, Washington, DC: Smithsonian Institution Press.

[127] Landolfi, M., Landi Degl'Innocenti, E., Landi Degl'Innocenti, M., Leroy, J.L., 1993, A&A, **272**, 285.

[128] Lavagnino, C.J., 1960, Bol.Assoc.Argent.Astron., **2**, 40.

[129] Ledoux, P., 1951, ApJ, **114**, 373.

[130] Leibacher, J.W., Stein, R.F., 1971, Astrophys.Lett., **7**, 191.

[131] Leighton, R.B., Noyes, R.W., Simon, G.W., 1962, ApJ, **135**, 474.

[132] Leroy, J.-L., Ratier, G., Bommier, V., A&A, **54**, 816.

[133] Leroy, J.-L., 1995, A&ASS, **114**, 79

[134] Leroy, J.-L., Landolfi, M., Landi Degl'Innocenti, M., Landi Degl'Innocenti, E., Bagnulo, S., Laporte, P., 1995, A&A, **301**, 797

[135] Leroy, J.-L., Landolfi, M., Landi Degl'Innocenti, E., A&A, **270**, 335.

[136] Libbrecht, K.G., Woodard, M.F., 1990, Nature, **345**, 779.

[137] Libbrecht, K.G., Kaufman, J.M., 1988, ApJ, **324**, 1172.

[138] Loumos, G.L., Deeming, T.J., 1978, Ap&SS, **56**, 285.

[139] Maitzen, H.M., 1984, A & A, **138**, 493.

[140] Martic, M., Schmitt, J., Lebrun, J.-C., *et al.*, 1999, A&A, **351**, 993.

[141] Martinez, P., 1993, PhD thesis, University of Cape Town.

[142] Martinez, P., 1996, BAS. India, **24**, 359.

[143] Martinez, P., Kurtz, D.W., 1990, MNRAS, **242**, 636.

[144] Martinez, P., Medupe, R., 1998, Ap&SS, **259**, 57.

[145] Matthews, J.M., 1988, MNRAS, **235**, 7_P.

[146] Matthews, J.M., 1991, PASP, **103**, 5.

[147] Matthews, J.M., Wehlau, W.H., Walker, G.A., Yang, S., 1988, ApJ, **324**, 1099.

[148] Matthews, J.M., Wehlau, W.H., Walker, G.A.H., 1990, ApJ, **365**, L81.

[149] Matthews, J.M., Wehlau, W.H., Rice, J., Walker, G.A.H., 1996, ApJ, **459**, 278.

[150] Matthews, J., Walker, R., 1970, *Methods of Mathematical Physics*, p. 177.

[151] Mathys, G., 1985, A&A **151**, 315.

[152] Mathys, G., 1991, A&AS, **89**, 121.

[153] Mathys, G., 1994, A&AS, **108**, 547.

[154] Mathys, G., 1995a, A&A, **293**, 733.

[155] Mathys, G., 1995b, A&A, **293**, 746.

[156] Mathys, G., Hubrig, S., 1997, A&AS, **124**, 475.

[157] Mathys, G., Stenflo, 1986, A&A, **168**, 184.

[158] Medupe, R., 1996, Msc thesis, University of Cape Town.

[159] Medupe, R., Kurtz, D.W., 1998, MNRAS, 299, 371.

[160] Medupe, R., Kurtz, D.W., Christensen-Dalsgaard, J., 2000, In *The impact of Large-Scale Surveys on Pulsating Star Research*, ASP Conf. Series, **203**, eds. L. Szabados & D. Kurtz, p.451.

[161] Medupe, R., Christensen-Dalsgaard, J., Kurtz, D.W., 1998, In *A half-Century of Stellar Pulsation Interpretations: A tribute to A.N Cox*, eds. P.A. Bradley & J.A. Guzik, 197.

[162] Michaud, G., 1970, ApJ, **160**, 641.

[163] Mihalas, D., 1978, *Stellar Atmospheres*, W.H. Freeman and Company, San Francisco.

[164] Mihalas, D., Mihalas, B. W., 1984, *Foundations of Radiation Hydrodynamics*, Oxford University Press.

[165] Nordlund, A., Stein, R.F., 1998, in *New Eyes to See Inside the Sun and Stars*, IAU Symposium No.185, eds Franz-Ludwig Deubner, Joergen Christensen-Dalsgaard & Don Kurtz, p.199.

[166] North, P., Jaschek, C., Hauck, B., Figueras, F., Torra, J., Kunzli, M., 1997, in *Hipparcos - Venice "97", ESASP - 402*, p. 239.

[167] Osaki, Y., 1993, In *Inside the Stars* IAU Colloq. 137, p. 512, ASP Conf. Series, eds. W.W Weiss & Baglin, A., vol. 40.

[168] Pesnell, W.D., 1989, ApJ, **339**, 1038.

[169] Pierce, A.K., Waddell, J., 1961, Mem. RAS, **68**, 89.

[170] Polosukhina, N.S., 1969, Izv. Krymsk. Astrof. Obs. **39**, 34

[171] Press, W.H., Teukolsky, S.A., Vetterling, W.T., Flannery, B.P., 1992, *Numerical Recipes in Fortran*, Cambridge University Press, p 364

[172] Preston, G.W., 1974, ARA&, **12**, 257.

[173] Raghavan, S., 1995, Science, **267**, 45.

[174] Renson, P., Manfroid, J., Heck, A., 1976, A&AS, **23**, 413.

[175] Roxburgh, I.W., 1996, BAS. India, **24**, 89.

[176] Ryabchikova, T.A., Adelman, S.J., Weiss, W.W., Kuschnig, R., 1997, A&Ap, **322**, 234.

[177] Ryabchikova, T.A., Landstreet, J.D., Gelbmann, M.J., Bolgova, G.T., Tsymbal, V.V., Weiss, W.W., 1997, A&Ap, **327**, 1137.

[178] Ryabchikova, T.A., Savanov, I.S., Hatzes, A.P., Weiss, W.W., Handler, G., 2000, A&Ap, **357**, 981.

[179] Saio, H., 1981, ApJ, **244**, 299.

[180] Serkovski, K., Chojnaki, W., 1969, A&A **1**, 442

[181] Shavrina, A. V., Polosukhina, N. S., Tsymbal, V., Khalak, V., 2000, Astronomy Reports, **44**, 235.

[182] Shibahashi, H., Saio, H , 1985, PASJ, **37**, 245.

[183] Shibahashi, H., Takata, H , 1993, PASJ, **37**, 245.

[184] Simon, T., Landsman, W.B., 1997, ApJ, **483**, 435.

[185] Sinachopoulos, D., 1989, A&AS, **81**, 103.

[186] Smart, W.M., 1977, Textbook on Spherical Astronomy (6^{th} edition), University Press, Cambridge.

[187] Smith, M.A., McCall, M.L., 1978, ApJ, **223**, 221.

[188] Smith, M.A., Fitch, W.S., Africano, J.L., Goodrich, B.D., Halbedel, W., Palmer, L.H., Henry, G.W., 1984, ApJ, **282**, 226.

[189] Stamford, P.A., & Watson, R.D., 1981, Ap&SS, **77**, 131.

[190] Stepien, K., 1968, ApJ., **154**, 945.

[191] Stibbs, D.W.N., 1950, MNRAS, **110**, 395.

[192] Takata, Shibahashi, H., 1993, PASJ, **37**, 245.

[193] Tassoul, J., 1978, Theory Of Rotating Stars, Princeton University Press, Princeton, New Jersey.

[194] Tassoul, M., 1980, ApJS, **43**, 469.

[195] Tassoul, M., 1990, ApJ., **358**, 313.

[196] Thompson, M.J., Toomre, J., and the GONG Team: 1996, Science, **272**, 1300.

[197] Tuominen, I., Piirola, V., 1978, Publ. Astr. Inst. Czech. Acad. Sci. 5, 25

[198] Turck-Chièze, S., Couvidat, S., *et al.*, 2001, ApJ, **555**, L69.

[199] Turcotte, S., Richer, J., & Michaud, G., 1998, ApJ, **504**, 559.

[200] Turcotte, S., Richer, J., Michaud, G., Christensen-Dalsgaard, J., 2000, A&A, **360**, 603

[201] Turcotte, S., Richer, J., Michaud, G., Iglesias, C.A., Rogers, F.J., 1998, ApJ, **504**, 539.

[202] Vogt, S.S., Penrod, G.D., 1983, ApJ, **275**, 661.

[203] Wade, R.A.& Rucinsky, S.M., 1985, A&ApS, **60**, 471.

[204] Walker, G.A.H, Yang, S., Fahlman, G.G., 1979, ApJ, **233**, 199

[205] Watson, R.D., 1988, Ap&SS, **140**, 255.

[206] Weiss, W.W., Schneider, H., 1984, A&A, **135**, 148.

[207] Weiss, W.W., 1986, In: *Upper Main Sequence Stars With Anomalous Abundances.* Proc. IAU Colloq. No 90, p. 219, Dordrecht: Reidl, ed. C.R. Cowley, M.M. Dworetsky, C. Megessier.

[208] Wolff, S.C., 1983, *The A–type Stars: Problems and Perspective.* NASA, SP–463. Washington, DC: NASA.

[209] Wolff, S.C., Wolff, R.J., 1971, AJ, **76**, 422.